

UNIVERSITÀ
DEGLI STUDI DI BARI
ALDO MORO

DIPARTIMENTO INTERATENEO DI FISICA
"MICHELANGELO MERLIN"

PhD course in Physics – Cycle XXXVIII
Nuclear, Subnuclear and Astroparticle Physics curriculum

Present and Future Constraints on Axion-Like Particles from Blazars

From current gamma-ray telescopes to the Cherenkov Telescope Array Observatory

Supervisor:
Prof. Francesco Giordano

Co-supervisor:
Dr. Leonardo Di Venere

Candidate:
Francesco Schiavone

ACADEMIC YEAR 2025–26



He who wonders discovers
that this is in itself a wonder.
— M. C. Escher

On the previous page: M. C. Escher, *The Fourth Day of the Creation* (1926). Quote from M. C. Escher, *The Graphic Work* (1959).

Summary

The field of very high energy (VHE) gamma-ray astrophysics has been revolutionized in the last few decades by the advent of stereoscopic imaging atmospheric Cherenkov telescope arrays, designed and operated by large international scientific collaborations. Astrophysical targets of various kinds have been routinely observed with increasing precision and sensitivity, in coordination with instruments working in other wavebands, with the common aim of providing a unified multi-wavelength view of the physical phenomena governing the behavior of these sources at all energy scales. Besides conventional astrophysics, VHE observations are also used to investigate the nature of the dark matter in the Universe and to study exotic physics effects related to the cosmological propagation of photons.

The jetted active galactic nuclei denoted as blazars are the most abundant class of sources detected outside our galaxy. Their relativistic jets, closely aligned to the line of sight from Earth, are a rich and complex environment, characterised by the presence of relatively strong magnetic fields over parsec-scale lengths. Owing to their cosmological distance from Earth, these sources serve as ideal targets to investigate effects of non-standard gamma-ray propagation. Among these, the existence of axion-like particles (ALPs) may be probed by exploiting their expected coupling to photons. The mechanism of ALP-photon conversions in external magnetic fields might lead to distinct signatures in the blazars' VHE spectra, which could be detected by the present or future generation of Cherenkov telescopes.

In this thesis, the present status of ALP searches and experimental constraints from the observation of blazars with Cherenkov telescopes is discussed. Focus is placed on the analysis of data from MAGIC and LST-1, the first Large-Sized Telescope prototype of the Cherenkov Telescope Array Observatory (CTAO). Once the full initial configuration of CTAO is operational, it will provide greatly improved flux sensitivity and energy resolution compared to current instruments. In order to estimate how these improvements will affect the attainable limits on ALPs from blazars in the near future, sensitivity projections based on simulated observations with CTAO are also presented and discussed.

The work is organized as follows. In Chapter 1, the topic of VHE astronomy is introduced historically, with a focus on the present generation of imaging Cherenkov telescopes and the CTAO. The basics of VHE data formats, reconstruction and analysis are also discussed. The observational characteristics and emission modeling of blazars are introduced in Chapter 2, highlighting the role of gamma-ray observations and future detection prospects with CTAO with a focus on flat-spectrum radio quasars (FSRQs). Chapter 3 describes ALPs and their mixing to photons in external magnetic fields, along with the modeling of the relevant magnetic environments in astrophysics. The basic statistical anal-

ysis techniques for ALP searches in gamma-ray data are discussed, along with some results from recent literature. In Chapter 4 the analysis of combined MAGIC and LST-1 data from observations of four bright blazars (Markarian 421, Markarian 501, BL Lacertae and 1ES 1959+650) is presented, and limits on the ALP parameter space are derived. A similar analysis is performed in Chapter 5 using simulated observations of Markarian 501 and PKS 2155−304 with the latest response functions for the Northern and Southern Arrays of CTAO, in order to obtain a projection of its sensitivity to an ALP signal from these blazars. In addition, a method based on the use of machine learning classifiers is proposed to derive the same results, as a first step towards the development of non-parametric techniques that might help in reducing model-dependent assumptions and systematic uncertainties. Finally, conclusions are drawn in Chapter 6, and some appendices complete the work.

Original contributions Original results of this work are presented in Section 2.6, in Chapter 4 and in Chapter 5, and will be the subject of future publications, currently in preparation. I contributed to various aspects of these works, including theoretical modeling, MAGIC data analysis, CTAO data simulation, statistical analysis, implementation of machine learning techniques and interpretation of results. Major inputs were provided by C. Bartolini, E. Lindfors and R. Mukherjee to Section 2.6 (*Fermi*-LAT data selection and analysis, interpretation and discussion of results), by I. Batković, G. D'Amico and M. Doro to Chapter 4 (LST-1 data analysis, signal modeling and statistical analysis, interpretation and discussion of results) and by L. Di Venere to Chapter 5 (interpretation and discussion of results). This work has been carried out within the CTAO, LST and MAGIC collaborations; some of the results reported in this thesis are part of ongoing analyses still under collaboration review.

Symbols and conventions Throughout this work, the following symbols and conventions are used. The speed of light in vacuum is denoted as $c \simeq 3 \times 10^8\,\mathrm{m\,s^{-1}}$, Newton's gravitational constant as $G \simeq 6.67 \times 10^{-11}\,\mathrm{m^3\,kg^{-1}\,s^{-2}}$, Planck's reduced constant as $\hbar \simeq 1.05 \times 10^{-34}\,\mathrm{J\,s}$ and the fine structure constant as $\alpha \simeq 1/137$. The proton and electron masses are given by $m_p \simeq 1.67 \times 10^{-27}\,\mathrm{kg}$ and $m_e \simeq 9.11 \times 10^{-31}\,\mathrm{kg}$, while the electron charge is given by $e \simeq 1.60 \times 10^{-19}\,\mathrm{C}$. The Thomson cross-section for photon-electron scattering is given by $\sigma_T \simeq 6.65 \times 10^{-29}\,\mathrm{m^2}$. The solar mass and luminosity are denoted by $M_\odot \simeq 1.99 \times 10^{30}\,\mathrm{kg}$ and $L_\odot \simeq 3.83 \times 10^{26}\,\mathrm{W}$. The present-day value of Hubble's constant is given by $H_0 \simeq 67\,\mathrm{km\,s^{-1}\,Mpc^{-1}}$, whereas $\Omega_\Lambda \simeq 0.68$ and $\Omega_m \simeq 0.32$ denote the cosmological density parameters of dark energy and nonrelativistic matter.

The relativistic speed of a particle in units of c is denoted as β, while its Lorentz factor is given by $\gamma = (1 - \beta^2)^{-1/2}$. The redshift parameter used to measure cosmological distances is denoted by z. The symbols δ_{ij}, $\delta(x)$ and $\epsilon_{\alpha\beta\mu\nu}$ denote the Kronecker and Dirac delta and the totally antisymmetric Levi-Civita tensor.

Energies are expressed in multiples of electronvolts ($1\,\mathrm{eV} \simeq 1.6 \times 10^{-19}\,\mathrm{J}$). Dates are expressed either following the day/month/year or the modified Julian day (MJD) formats. The expressions in Chapter 3 use the natural system of units where $c = G = \hbar = 1$.

Contents

Summary iii

List of acronyms ix

1 Very high energy gamma-ray astronomy 1
1.1 Historical perspective . . . 1
1.1.1 From the sky… . . . 1
1.1.2 …to the ground . . . 3
1.2 Imaging atmospheric Cherenkov telescopes . . . 5
1.3 Extensive air shower arrays . . . 9
1.4 The Cherenkov Telescope Array Observatory . . . 11
1.4.1 Concept and present status . . . 11
1.4.2 Scientific goals . . . 14
1.4.3 Dark matter and fundamental physics searches with CTAO . . . 16
1.5 Data analysis . . . 19
1.5.1 Event reconstruction and data formats . . . 19
1.5.2 Statistical significance of signal . . . 23
1.5.3 Model fitting and high level analysis . . . 24

2 Blazars 29
2.1 The unified model of active galactic nuclei . . . 29
2.2 Observational characteristics of blazars . . . 31
2.3 Emission modeling . . . 33
2.3.1 Leptonic and hadronic mechanisms . . . 33
2.3.2 One-zone, two-zone and multi-zone models . . . 35
2.4 Variability . . . 37
2.5 Gamma-ray observations . . . 38
2.5.1 Present status . . . 38
2.5.2 Observation prospects with CTAO . . . 39
2.6 Exploring the VHE spectral shape of FSRQs with CTAO . . . 39
2.6.1 Motivation and source selection . . . 39
2.6.2 *Fermi*-LAT data analysis . . . 40
2.6.3 Comparison of CTAO configurations . . . 42
2.6.4 Spectral discrimination . . . 44

3 Axion-like particles 47
3.1 The QCD axion and axion-like particles . . . 47
3.2 Propagation in constant magnetic fields . . . 48
3.2.1 ALP-photon oscillations . . . 48
3.2.2 Direct detection experiments . . . 52
3.3 Propagation in inhomogeneous magnetic fields . . . 53
3.4 Magnetized astrophysical environments . . . 55
3.4.1 Blazar jets . . . 55
3.4.2 Galaxy clusters . . . 58
3.4.3 Milky Way magnetic field . . . 59
3.4.4 Intergalactic magnetic field . . . 60
3.5 Constraints on ALPs from gamma-ray astrophysics . . . 61
3.5.1 General considerations . . . 61
3.5.2 Statistical framework . . . 62
3.5.3 ALP limits from NGC 1275 . . . 63
3.5.4 Constraints from different sources . . . 65

4 Limits on ALPs from blazars with MAGIC and LST-1 69
4.1 Source and data selection . . . 69
4.2 Data taking and analysis . . . 70
4.2.1 MAGIC . . . 70
4.2.2 LST-1 . . . 72
4.2.3 High-level analysis . . . 72
4.3 Signal modeling . . . 73
4.4 Statistical analysis . . . 75
4.5 Results and discussion . . . 79

5 CTAO sensitivity to ALPs from blazars 81
5.1 Source modeling and simulation . . . 81
5.1.1 Source selection . . . 81
5.1.2 Data simulation and analysis . . . 82
5.2 ALP sensitivity derivation using the likelihood-ratio test . . . 84
5.3 ALP sensitivity derivation using machine learning . . . 86
5.4 Discussion of results . . . 91

6 Conclusions and outlook 95

Appendix A Statistical notes 99
A.1 Derivation of the Li-Ma significance . . . 99
A.2 Model fitting and flux point estimation . . . 100

Appendix B Analysis and simulation of FSRQ data 103
B.1 *Fermi*-LAT lightcurves . . . 103
B.2 Results of CTAO simulations . . . 107

Appendix C Long-term blazar analysis with MAGIC 111
C.1 Lightcurves . . . 111
C.2 Spectral parameters . . . 111

Appendix D Systematic effects on ALP limits 115
D.1 MAGIC and LST-1 analysis 115
D.2 CTAO projections 116

Appendix E Machine learning performance metrics 119
E.1 Train-test splitting and cross-validation 119
E.2 ROC, learning and validation curves 120

References 123

Acknowledgements 151

List of acronyms

AGN Active galactic nucleus.

AIC Akaike information criterion.

ALP Axion-like particle.

BB Bayesian block.

BL Lac BL Lacertae object.

BLR Broad line region.

BPL Broken power law.

CDM Cold dark matter.

CL Confidence level.

CMB Cosmic microwave background.

CR Cosmic ray.

CTAO Cherenkov Telescope Array Observatory.

EAS Extensive air shower.

EBL Extragalactic background light.

EC External Compton.

ECPL Exponentially cut-off power law.

EHBL Extremely high synchrotron-peaked BL Lac.

FoV Field of view.

FSRQ Flat-spectrum radio quasar.

GBM Gamma-ray Burst Monitor.

GRB Gamma-ray burst.

H.E.S.S. High Energy Stereoscopic System.

HBL High synchrotron-peaked BL Lac.

HE High energy.

HSP High synchrotron-peaked blazar.

IACT Imaging atmospheric Cherenkov telescope.

IBL Intermediate synchrotron-peaked BL Lac.

IC Inverse Compton.

IGMF Intergalactic magnetic field.

IRF Instrument response function.

ISP Intermediate synchrotron-peaked blazar.

KSP Key Science Project.

LAT Large Area Telescope.

LBL Low synchrotron-peaked BL Lac.

LP Log-parabola.

LSP Low synchrotron-peaked blazar.

LST Large-Sized Telescope.

LSW Light shining through walls.

MAGIC Major Atmospheric Gamma-ray Imaging Cherenkov telescopes.

MJD Modified Julian day.

ML Machine learning.

MST Medium-Sized Telescope.

MWL Multi-wavelength.

NLR Narrow line region.

NSB Night sky background.

PL Power law.

PMT Photomultiplier tube.

PSF Point spread function.

SCT Schwarzschild-Couder Telescope.

SECPL Super-exponentially cut-off power law.

SED Spectral energy distribution.

SiPM Silicon photomultiplier.

SMBH Supermassive black hole.

SSC Synchrotron self-Compton.

SST Small-Sized Telescope.

TS Test statistic.

UHBL Ultra high synchrotron-peaked BL Lac.

UHE Ultra high energy.

VERITAS Very Energetic Radiation Imaging Telescope Array System.

VHE Very high energy.

VLBI Very long baseline interferometry.

WIMP Weakly interacting massive particle.

WISP Weakly interacting slim particle.

CHAPTER 1

Very high energy gamma-ray astronomy

1.1 Historical perspective

1.1.1 From the sky…

The field of gamma-ray astrophysics was born in the wake of radio and X-ray observations during the second half of the 20th century, with the common aim of understanding and characterizing the high-energy processes happening within astronomical sources. One such process was the acceleration of charged cosmic ray (CR) particles, which had been abundantly measured in the previous decades.

In the early 1900s, it was realized by means of increasingly sensitive electroscope experiments that of some unknown source of ionizing radiation had to exist [1–3]. This radiation was later confirmed to be of extraterrestrial origin by the pioneering balloon flights of Victor Hess [4, 5], as the ionization of air was found to *increase* with altitude, instead of decreasing as it would if the radiation were coming from the ground. Many subsequent experiments [5, 6] confirmed this discovery and measured the energies and distributions of these particles with increasing precision. Nowadays, it is known that the CR spectrum features an approximately broken power law shape extending from a few MeV to 10^{20} eV in energy [7, 8]. Its composition is dominated by atomic nuclei, in a vast majority H and He, followed by electrons and positrons and by a small fraction ($\sim 10^{-4}$) of diffuse gamma-rays and neutrinos (Figure 1.1).

One of the main drivers of multi-wavelength (MWL) astronomy, i.e. combined observations of astronomical objects in bands of the electromagnetic spectrum other than optical, was thus to try and understand the mechanisms that could accelerate CR particles to such extreme energies. The observed CR flux at Earth is practically isotropic, as the vast majority of CRs are charged particles whose trajectories get bent by the ubiquitous magnetic fields found at all scales in the Universe. However, the same processes responsible for CR acceleration are also expected to produce abundant photon fluxes at different frequencies, such as synchrotron radiation or bremsstrahlung from relativistic electrons. These photons would directly point to the sources where acceleration mechanisms took place, opening new "windows" on the high-energy physics of astronomical objects. While the question of where and how CR acceleration happens still does not have a definitive answer [6, 7], MWL observations have been widely successful in characterizing the emission

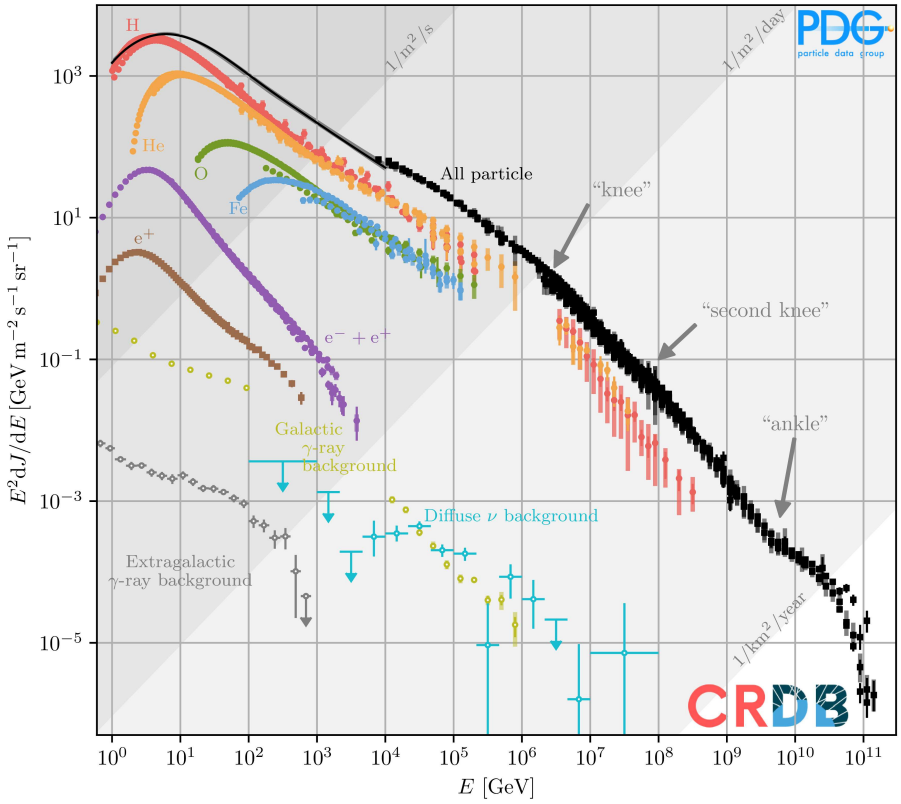


Figure 1.1: The cosmic ray spectrum and its composition. The points where the power-law spectral index changes are indicated as *knee*, *second knee* and *ankle*. Image from ref. [7].

of all sorts of cosmic objects and continue providing us with precious information on the physical processes happening therein.

Compared to other wavebands, the direct detection of astrophysical gamma-rays faces an additional issue. When interacting with atomic nuclei in the Earth's atmosphere, gamma-ray photons are converted into relativistic electron-positron pairs. These particles go on generating further gamma rays of lower energies via bremsstrahlung, which can again undergo pair production generating what is called an extensive air shower (EAS) or atmospheric cascade. The natural solution to this problem was to measure gamma rays outside of the atmosphere by means of detectors mounted on artificial satellites. After some early results by Explorer-11 [9], the first "map" of gamma-ray emission above 50 MeV from the Galactic plane was obtained by the Orbiting Solar Observatory 3 (OSO-3) in the early 1970s [10, 11]. The sensitivity and accuracy of these experiments were improved upon by the subsequent satellites SAS-2 [12] and COS-B [13], which were able to detect the first point sources. Greater developments came with the Compton Gamma-Ray Observatory (CGRO) [14], designated as one of NASA's "Great Observatories". Featuring the BATSE, EGRET, COMPTEL and OSSE detectors, CGRO paved the way for modern multi-instrumented satellites such as INTEGRAL [15], AGILE [16], and the *Fermi* Gamma-Ray Space Telescope equipped with the Large Area Telescope (LAT) [17] and Gamma-Ray Burst Monitor (GBM) [18] instruments. Among these space borne telescopes, all launched within the first decade of the 2000s, only *Fermi* is still operational, having survived way beyond its scheduled end of mission in 2013. After more than 15

years of uninterrupted operations, *Fermi* remains one of the main sources of high-energy (HE, $E \lesssim 100\,\mathrm{GeV}$) gamma-ray transient alerts, shared via the NASA General Coordinate Network (GCN) [19], which provide invaluable opportunities for detecting time-sensitive events such as gamma-ray bursts (GRBs) and blazar flares. Observations by *Fermi*-LAT have led to the compilation of a series of source catalogs, numbered from 0FGL to 4FGL-DR4 [20–27], which currently serve as standard references for virtually all known astrophysical gamma-ray sources.

1.1.2 ...to the ground

Despite the great success of space borne gamma-ray telescopes, they all share a common limitation. Gamma rays feature a similar spectral shape to charged CRs, with fluxes steeply decreasing with increasing energy. It follows that the typical effective area of satellite instruments, of order $\sim 1\,\mathrm{m}^2$, provides insufficient detection rates for measuring gamma rays of very high energies (VHE, $E \gtrsim 100\,\mathrm{GeV}$). Larger collection areas are needed to overcome this statistical limitation, which motivates the development of indirect ground-based detection techniques [28–33].

As mentioned above, astrophysical gamma rays do not reach the Earth's surface, getting absorbed by the atmosphere by producing extended air showers. As ultrarelativistic electron-positron pairs are produced in the shower, they travel faster than the speed of light in air, coherently polarizing and depolarizing the molecules of the medium. This results in the forward-beamed emission of electromagnetic radiation known as the Cherenkov effect [34, 35]. Such radiation is emitted along a cone with opening angle θ_c, defined by

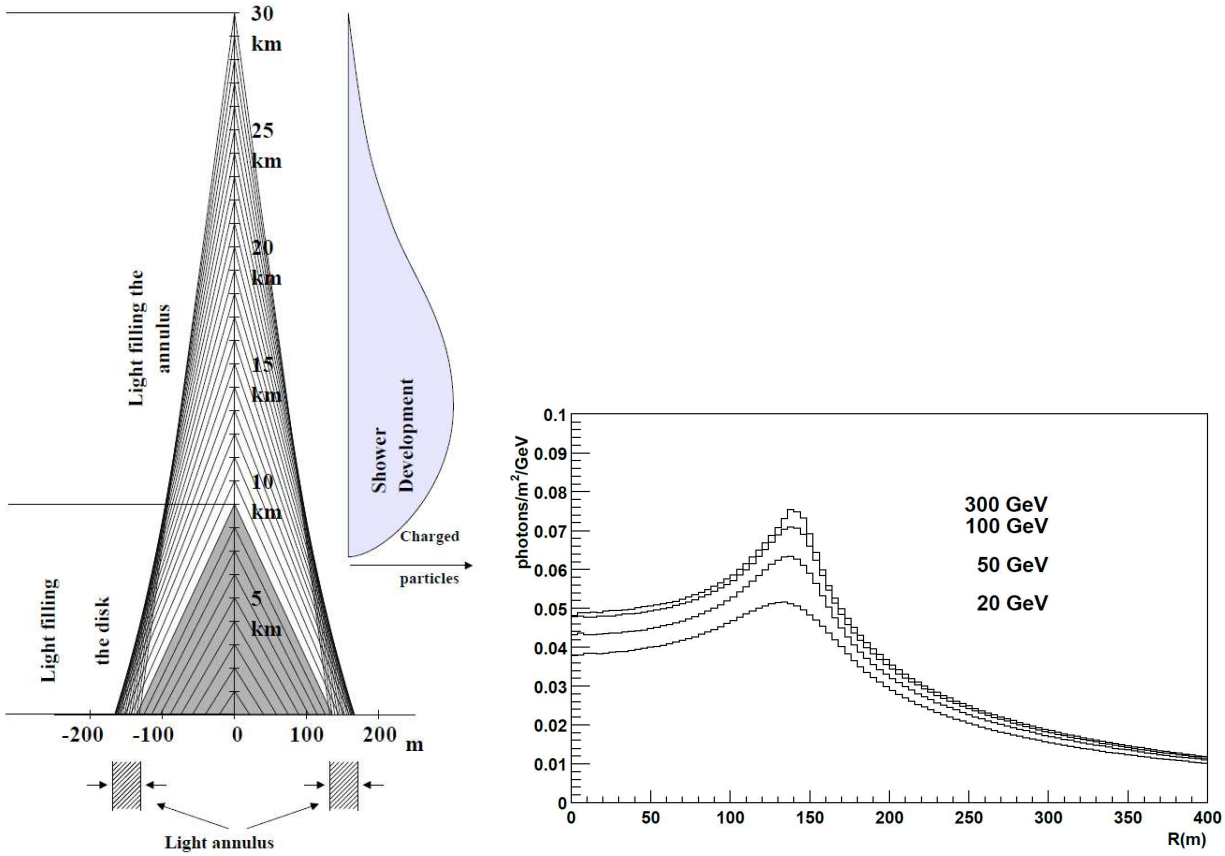
$$\cos\theta_c = \frac{1}{\beta n}\,, \tag{1.1}$$

where $\beta \approx 1$ is the relativistic speed of the particle (in units of the speed of light in vacuum, c) and n is the refractive index of the medium [36]. In the atmosphere, $n - 1$ varies with decreasing altitude between 10^{-5} and 10^{-4}, and the Cherenkov angle increases from about 0.2° to 1.5° [37]. One approach to ground-based gamma-ray detection aims to infer the cosmic gamma rays' direction and energy by measuring the feeble Cherenkov light emitted by the atmospheric cascades they generate. The number N of photons per unit wavelength λ and per unit track length z in the atmosphere is given by the Frank-Tamm formula [35, 37]

$$\frac{\mathrm{d}^2 N}{\mathrm{d}z\mathrm{d}\lambda} = 2\pi\alpha Z^2 \frac{\sin^2\theta_c}{\lambda^2}\,, \tag{1.2}$$

where α is the fine structure constant and Z is the atomic number of the medium. In atmospheric cascades, the Cherenkov photon spectrum peaks in the blue-ultraviolet, while the duration of the emission is of a few nanoseconds.

Starting from the top of the atmosphere the shower develops, reaching a maximum of 1200 secondary particles at around 9 km altitude for 1 TeV gamma rays. After this point, it begins to die out, as the energy of the individual secondary particles is no longer enough enough to support it. As the altitude decreases, the refractive index of air increases exponentially along with the density and the Cherenkov angle. Due to a compensation between these two effects, the shower produces an almost uniformly illuminated "light pool"



(A) (B)

Figure 1.2: (A) Diagram of the development of an atmospheric shower. (B) Cherenkov photon flux at ground level as a function of the distance from the shower axis, scaled for different energies of the primary gamma ray. The "hump" corresponds to the light annulus that forms at $R \sim 150\,\mathrm{m}$. Images taken from ref. [37].

surrounded by a brighter annulus with a radius of about 150 m at ground level [33, 37] (Figure 1.2). Consequently, gamma-ray detectors exploiting the air Cherenkov technique feature effective areas of order $\sim 10^4\,\mathrm{m}^2$ and above. This improvement upon satellite experiments by at least four orders of magnitude in collection surface allows ground-based Cherenkov telescopes to probe gamma rays of much higher energies, reaching into the TeV domain.

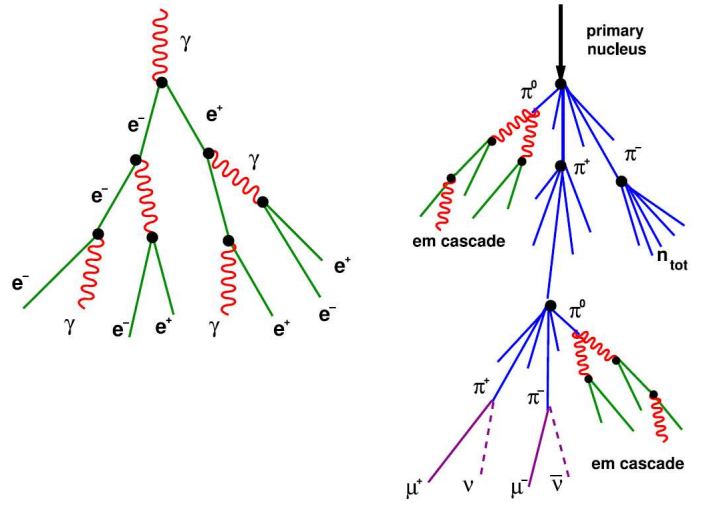
The number of produced photons per track length (*light yield*) is almost proportional to the primary gamma-ray energy [37]; for a 1 TeV gamma ray, this results around photons per square meter at ground level. The atmosphere is thus effectively used as a "natural calorimeter", as the nanosecond-long blue-ultraviolet flashes of the showers can give indirect information on the originating photon's energy. Air showers are produced by charged CRs as well, representing an important background source for gamma-ray Cherenkov detectors. However, an excess of Cherenkov light pulses from a certain direction in the sky (e.g. where a known radio source is located), compared to another "empty" region at the same zenith angle where only isotropic hadronic background is expected, indicates the presence of gamma-ray emission from that direction. This fact is the basis of the *ON-OFF technique* for background subtraction, which will be discussed in more detail in following

sections. While early rudimentary detectors succeeded to detect Cherenkov flashes associated with cosmic ray showers even before the launch of the first gamma-ray satellites [38–40], detecting a gamma-ray excess from specific sources proved to be a much harder task. A first, faint (3.1σ confidence level) detection of the Crab nebula — a supernova remnant considered now a "standard candle" in gamma-ray astronomy — was achieved in 1972 by the telescope installed at the Fred Lawrence Whipple Observatory in Arizona [41]. The Whipple telescope consisted of a 10 m multi-faceted mirror, with photomultiplier tubes (PMTs) installed in its focal plane to detect the reflected Cherenkov light, and represented the first prototype of a large atmospheric Cherenkov telescope.

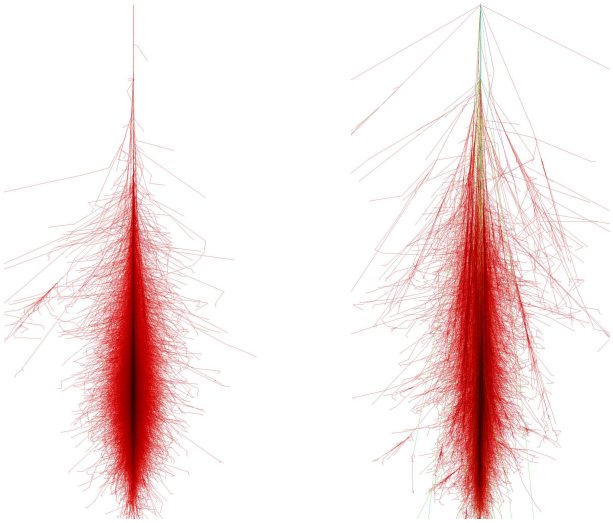
1.2 Imaging atmospheric Cherenkov telescopes

The first successful results by the Whipple telescope were produced by a very simple application of the ON-OFF technique. This consisted in having only two PMTs in the focal plane of the mirror, pointing respectively at the Crab nebula and a few degrees away from it, with the mirror alternatively focusing on either of them. The difference in the measured photoelectron counts represented the signal excess from the source. However, it was clear that a more refined approach was needed to improve the performance of the air Cherenkov technique and its sensitivity to hadronic background. While other minor experiments scanned the sky in search of gamma rays employing different techniques [33], a major breakthrough came from the suggestion of using cameras made up of several PMTs, in order to record 2-dimensional images of the air showers [42, 43]. This idea was put into practice by installing a 37-pixel camera in the focal point of the Whipple telescope, which thus became the first example of an *imaging atmospheric Cherenkov telescope* (IACT). With this improvement, a much more significant detection of the Crab nebula was achieved in 1989, at a confidence level of 9σ [44].

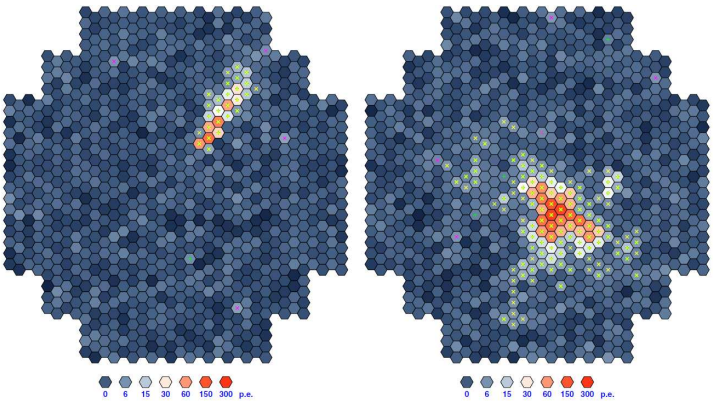
The working principle of IACTs is based on the fact that gamma-ray shower images are expected to possess several characteristics that should distinguish them from hadronic cascades. First, they should be approximately elliptical, with their major axis pointing towards the assumed source position (corresponding to the center of the camera frame), allowing the background images that do not fulfill this criterion to be excluded when pointing at a known object. In addition, detailed simulations of air shower development and detector response show that hadronic shower images have wider and more irregular shapes, mainly due to the emission of pions at large angles (Figure 1.3). These characteristics can be quantified by using *Hillas parameters* [45], obtained from the distribution of photoelectrons (p.e.) detected in the PMTs of the camera. Hillas parameters include the image *centroid* (first moment of the p.e. distribution), *length* and *width* (second moments), as well as the *distance* of the centroid from the expected source position and the angular distance α between the line connecting the source to the centroid and the major axis of the ellipse (Figure 1.4). These parameters can give information both on the direction of the shower, indicating whether the signal comes from a potential gamma-ray source, and on its morphology, helping to distinguish between gamma-ray and hadron images. The *azwidth* parameter, defined as the spread of the image perpendicular to the source-centroid line, initially proved to be particularly effective in the latter task [29, 44]. With an upgrade of the Whipple camera and more refined analysis techniques, a 49σ detection of the Crab nebula was obtained [46], while input from satellite experiments led to the detection of



(A)



(B)



(C)

Figure 1.3: (A) Schematic development of a gamma-ray and a hadronic shower, which features pion production and electromagnetic sub-cascades. Image taken from ref. [8]. (B) 1 TeV gamma-ray and proton showers simulated with the CORSIKA software (https://www.iap.kit.edu/corsika/). (C) Gamma-ray and proton showers as seen by the cameras of the H.E.S.S. telescopes, where the light intensity is represented by the number of photoelectrons. Image taken from ref. [32].

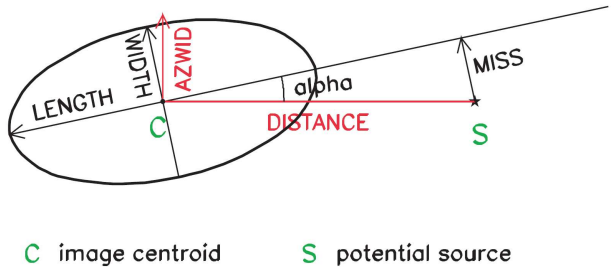


Figure 1.4: Schematic definition of the Hillas parameters. Image taken from ref. [29].

TeV gamma-rays from the first extragalactic objects observed with the Cherenkov imaging technique, the blazars Markarian 421 [47] and Markarian 501 [48].

Following the successes of the Whipple telescope and other experiments, such as repurposed solar power farms [29, 31, 33], work started towards a "third generation" [43] of ground-based detectors which would employ arrays of multiple IACTs. This would allow the gamma-ray direction to be accurately determined via stereoscopic recontruction, as multiple shower images from different points of view would be oriented towards the same source. Additionally, background events such as muon tracks from hadron showers passing close to one telescope, which would give very similar Cherenkov images to gamma rays, would be not seen by other telescopes far enough in the array and would thus be rejected. The first of such arrays was built within the High Energy Gamma-Ray Astronomy (HEGRA) experiment, which operated from 1987 to 2002 at the Roque de los Muchachos observatory on La Palma, in the Canary Islands, at an altitude of about 2200 m above sea level [49]. HEGRA initially consisted of a scintillator array to detect secondary charged particles from air showers directly on the ground, to which a grid of non-imaging photomultipliers (AIROBICC) was added to measure the associated Cherenkov light. The later integration of an array of six relatively small IACTs, which were progressively upgraded over the experiment's lifetime, allowed the system to reach a lower energy threshold of about 500 GeV and convincingly demonstrated the technical improvements brought about by stereoscopic imaging [50]. Contemporary arrays, such as the Italian CLUE [51] and the Japanese-Australian CANGAROO [52], further proved this point.

There are three major IACT systems currently in operation. Part of the HEGRA collaboration went on to form the High Energy Stereoscopic System (H.E.S.S.)[1] [53], built on the Khomas highlands in Namibia. H.E.S.S. I was initially made up of four identical IACTs with 12 m-diameter mirrors which began operations in 2003, achieving a low-energy threshold of about 100 GeV [54]. It was clear, however, that a much larger mirror area was necessary to detect faint showers from less-energetic photons, decreasing the energy threshold of the system and guaranteeing better overlap with satellite observations. This led to the design and construction of a telescope with a diameter of 28 m (H.E.S.S. II), installed in the middle of the array, which began operations in 2012 and brought the energy threshold down to 30 GeV [55, 56]. The 28 m telescope is the largest currently active IACT. Furthermore, H.E.S.S. is the only array of its kind currently operating in the Southern hemisphere, providing an unique view on the inner regions of the Milky Way, whose observations were collected in a comprehensive Galactic Plane survey [57].

[1] https://www.mpi-hd.mpg.de/HESS/



Figure 1.5: The MAGIC-I telescope during observations at the Roque de los Muchachos Observatory in March 2024. Photo by F. Schiavone.

A similar motivation led to the formation of another collaboration born from former members of HEGRA, the Major Atmospheric Gamma-ray Imaging Cherenkov (MAGIC)[2] telescope. Initially conceived as a single, very large 17 m telescope, MAGIC-I (Figure 1.5) was built on the HEGRA site at the Roque de los Muchachos Observatory in 2004 [58, 59]. A twin telescope, MAGIC-II, was added to the site in 2009 [60], and the system underwent a major hardware upgrade in 2014 to uniform the performance of the two instruments, reaching an overall energy threshold of 50 GeV [61, 62].

In the same period, another array was built alongside the Whipple telescope (which kept operating until its decommissioning in 2011). The Very Energetic Radiation Imaging Atmospheric System (VERITAS)[3] is made up of four 12 m IACTs, in a very similar configuration to H.E.S.S. I [63]. It has been in operation since 2007 at the Fred Lawrence Whipple observatory, with an energy threshold of about 85 GeV [64]. The different locations of these three systems allow them to observe sources only visible from the Northern or Southern hemispheres, respectively, with H.E.S.S. having a vantage point looking towards the central regions of the Milky Way.

Two more, mostly remotely operated IACTs are currently active in the Northern hemisphere. The First G-APD Cherenkov Telescope (FACT) [65], close to the MAGIC site, features a prototype camera mounted in the focus of a repurposed HEGRA mirror, based on Geiger-mode avalanche photodiode (G-APD) technology as an alternative to PMTs which is both more energy-efficient and less sensitive to moonlight. The 21 m Indian Major Atmospheric Cherenkov Experiment (MACE) [66] has been inaugurated in 2024 in Hanle, India, at an altitude of 4270 m above sea level.

[2] https://magic.mpp.mpg.de/
[3] https://veritas.sao.arizona.edu/

1.3 Extensive air shower arrays

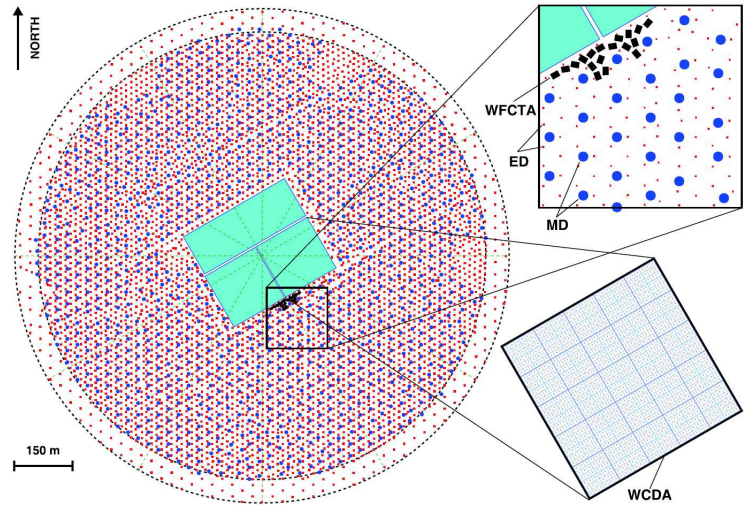
In parallel to IACTs, an alternative kind of detectors known as EAS arrays, or particle sampling detectors, was developed with the aim of directly detecting the charged particles reaching ground level from particle showers [28, 29, 67].

This approach to cosmic gamma-ray detection presents several differences compared to the imaging Cherenkov technique. IACTs require very clear night skies, with little or no moonlight, in order to detect the faint flashes of Cherenkov light from atmospheric showers. EAS arrays, on the other hand, can operate almost continuously, regardless of the time of day or weather conditions. In addition, while the field of view (FoV) of IACTs is typically limited by mirror and camera arrangements to a few degrees around the pointing direction, EAS arrays can easily detect gamma rays from much larger areas of the sky at once ($\sim 2\,\mathrm{sr}$) [28]. The characteristics of these arrays make them sensitive to higher gamma-ray energies than IACTs, being able to detect photons at hundreds of TeV or even PeV.

On the other hand, the lower energy threshold of a particle sampling array crucially depends on the altitude of the experiment, as low-energy showers die out in the higher layers of the atmosphere and never reach the ground. While this threshold can be lowered by placing the arrays at very high altitudes, it is typically difficult to go below the 100 GeV limit. In addition, angular resolution of at most a few tenths of a degree can be obtained by using the timing information of the array, compared to the more accurate directional reconstruction that can be provided by stereoscopic Cherenkov observations.

One of the first experiments to apply the particle sampling technique to gamma-ray observation was CASA-MIA (Chicago Air Shower Array/Michigan Muon Array) [68], built at 1600 m altitude in Utah, USA. The experiment was active from 1988 to 1999 and employed 1089 scintillator detectors over a $0.23\,\mathrm{km}^2$ surface, similarly in concept to the HEGRA particle detector. In addition, another scintillator array was located under the ground to detect penetrating muons from hadronic showers, making it possible to effectively reject CR background. Due to its low altitude and sparse layout, however, the system had an energy threshold of about 100 TeV which prevented any successful observations [28]. A similar approach was used in 1990 by the Tibet ASγ array [69], situated at 4300 m above sea level at the Yangbajing Observatory in Tibet, China. Its last upgraded version (Tibet-III) is still operational and consists of 789 detectors over a surface of $0.05\,\mathrm{km}^2$ [70]. The experiment lacked a muon veto system and only relied on count statistics to detect gamma-ray excesses above the isotropic CR background, until a muon detector (MD) was finally added to the array (Tibet AS+MD) in 2007 [71]. The denser layout and higher altitude of the Tibet experiment compared to CASA-MIA allowed it to sample a much larger fraction of shower particles, performing successful detections of the Crab nebula and several other sources [72]. The ARGO-YBJ experiment, in operation at the same Yangbajing site since 2007, uses a different technique based on a smaller $5800\,\mathrm{m}^2$ surface densely covered with resistive-plate chamber (RPC) detectors [73].

Another route was taken by the MILAGRO experiment, which operated between 2000 and 2008 at Fenton Hill in New Mexico, US, at an altitude of 2650 m [74]. MILAGRO was a water Cherenkov detector (WCD) consisting of a large $60\,\mathrm{m} \times 80\,\mathrm{m} \times 8\,\mathrm{m}$ water tank instrumented with PMTs, that would detect the Cherenkov light emitted inside the detector by passing particles. The central detector was surrounded by an array of smaller tanks,



(A)



(B)

Figure 1.6: (A) LHAASO layout. Figure from ref. [79]. (B) Photograph of the experiment. The WCDA can be seen in the center of the picture, with the WFCTA on its left side, surrounded by the KM2A (with MDs buried under small mounds of soil). Credits: Institute of High Energy Physics (Chinese Academy of Sciences).

covering a surface of about 0.4 km^2. A second, deeper layer of PMTs would detect penetrating muons to provide background rejection. The dense arrays of water tanks, compared to more sparsely spaced scintillator detectors, allowed MILAGRO to sample shower particles much more efficiently, reaching a 100 GeV energy threshold and sub-degree angular resolution even at a relatively moderate altitude [75]. MILAGRO was succeeded by the High Altitude Water Cherenkov (HAWC) experiment, consisting of 300 closely-spaced water tanks over a 0.22 km^2 surface, which started operating in 2015 on Sierra Negra, Mexico, at 4100 m altitude [76]. A next-generation WCD array, the Southern Wide-Field Gamma-Ray Observatory (SWGO), is currently in the research and development phase and will be installed in Pampa La Bola, Chile, at an altitude of 4770 m [77, 78].

The techniques described above were brought together by the Large High Altitude Air Shower Observatory (LHAASO, Figure 1.6), built on Mt. Haizi in Sichuan, China at a 4410 m altitude [79–81]. The experiment, which started observations in 2019, consists of three different arrays. A Kilometer Squared (1.3 km^2) Array (KM2A) of 5216 scintillator-

based electromagnetic particle detectors (EDs) and 1188 WCD muon detectors (MDs) covers the largest area. This part of the experiment is dedicated to the highest energies, from 10 TeV up to a few PeV, with the aim of studying ultra-high energy (UHE) gamma-ray sources. The KM2A surrounds a Water Cherenkov Detector Array (WCDA) of 78 000 m^2, made up of 3120 WCDs and sensitive to gamma-ray energies as low as 70 GeV. Finally, a Wide-FoV Cherenkov/Fluorescence Telescope Array (WFCTA) consisting of 18 small IACTs is primarily used for CR detection. Among its most important results, LHAASO performed the first discovery of a UHE gamma-ray source unassociated with any previously known astrophysical objects, LHAASO J2108+5157 [82].

1.4 The Cherenkov Telescope Array Observatory

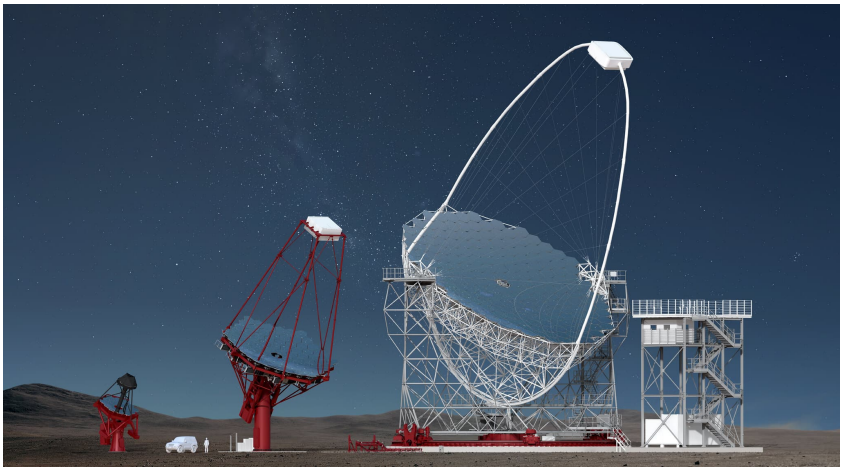
1.4.1 Concept and present status

While the current generation of IACTs was in its early stages, the concept of a future, worldwide observatory made up of arrays of different kinds of Cherenkov telescopes was already taking shape [83, 84]. The Cherenkov Telescope Array Observatory (CTAO[4]; formerly known as CTA) will be the first large-scale ground-based observatory for VHE gamma-ray astronomy employing the IACT technique, bringing together the experience from all international groups working on Cherenkov telescopes. A full view of the sky will be achieved by operating on two sites: the Northern Array will be located at the Roque de los Muchachos Observatory in La Palma, Canary Islands (on the same site as MAGIC and, formerly, HEGRA), while the Southern Array will be built in the Atacama Desert in Chile, at about 2600 m altitude. Contrary to the current generation of experiments, whose data access is restricted to the members of the respective collaborations, CTAO will be the first *open* gamma-ray observatory, accepting proposals from external investigators and providing public access to the resulting data products. Building on the knowledge gained with the present experiments, CTAO is expected to improve upon virtually all aspects of IACT performance. A major goal of the Observatory is to increase the energy range, lowering the energy threshold to about 20 GeV for a better overlap with satellite experiments, while being able to detect photons of energies up to 300 TeV thanks to the increased effective area. A target flux sensitivity of about one order of magnitude below the current standard is expected, along with a considerable improvement in angular and energy resolution. In addition, a short temporal resolution and fast response to external triggers will enable the CTAO telescopes to efficiently detect transient events such as GRBs or AGN flares. Finally, the multi-IACT composition of CTAO will enable it to operate in much more flexible configurations compared to present systems, with the possibility of targeting different sources with independent sub-arrays and implementing divergent pointing schemes [85, 86]. Such a flexibility will also allow unbiased galactic and extragalactic sky surveys to be carried out, without being restricted to known sources.

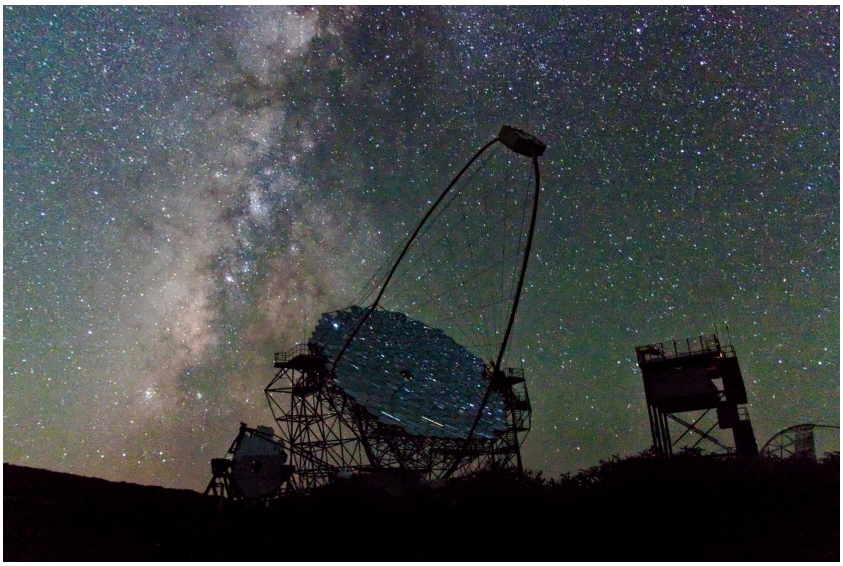
In order to achieve these performance goals, three different kinds of telescopes are foreseen for CTAO[5] (Figure 1.7a). In the low-energy range, approximately between 20 and 150 GeV, gamma-ray showers are frequent but faint, and thus observations are mainly

[4] https://www.ctao.org/

[5] For up-to-date technical specifications on the CTAO telescopes, see https://www.ctao.org/for-scientists/technical-specifications/.



(A)



(B)

Figure 1.7: (A) Digital rendering of the SST, MST and LST designs for CTAO. Image from https://www.ctao.org/it/emission-to-discovery/telescopes/. (B) The LST-1 prototype during observations at the Roque de Los Muchachos Observatory in March 2024. Photo by F. Schiavone.

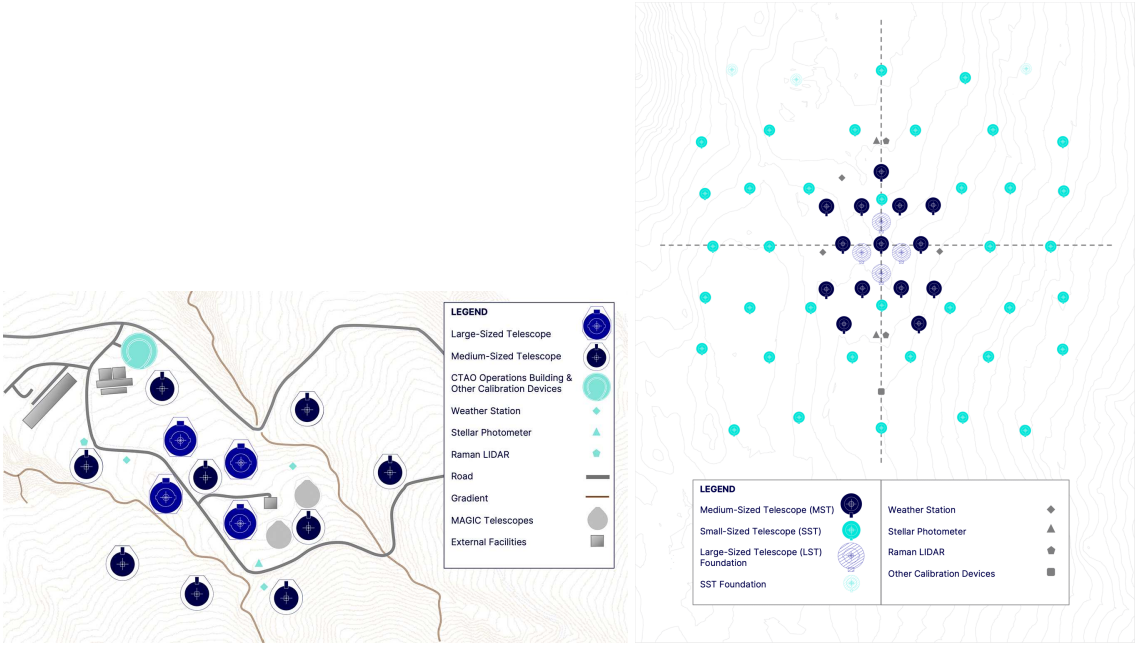
limited by background. For this reason, a relatively small number of closely-spaced Large-Sized Telescopes (LSTs) will be employed. These telescopes feature a parabolic segmented mirror of 23 m diameter, in order to efficiently collect the weak Cherenkov light from low-energy shower. A camera with 1855 PMTs is installed in the focal plane, forming a honeycomb structure of pixels with a total FoV radius of 4.3°. Another important characteristic of the LSTs is their lightweight structure, which allows them to repoint to any direction in the sky within 20 s for fast follow-up of transients. The first LST prototype (LST-1, Figure 1.7B) has been in operation at the Roque de los Muchachos Observatory since 2019 [87–89]. While officially still in the commissioning phase, LST-1 has already produced a large number of scientific results [90–97]. In 2023, the telescope performed the first detection of VHE gamma rays from OP 313, the farthest source observed in this energy range so far [98, 99]. An active observation proposal cycle is currently ongoing within the LST

collaboration. Due to the close proximity of the telescopes and large overlap in collaboration members, in recent years observations have often been performed jointly with the MAGIC telescopes, with a significant improvement in performance with respect to monoscopic operation [100].

In the "core energies" of CTAO, approximately between 150 GeV and 5 TeV, multiple Medium-Sized Telescopes (MSTs) with 11.5 m mirror diameters and PMT-based cameras with a FoV radius of about 7.5° will be dominant. Improvement in sensitivity compared to current systems will be obtained by increasing both the area over which the telescopes are spread and the quality of stereoscopic shower reconstruction, by imaging Cherenkov light with a larger number of telescopes. The current baseline design of MSTs features a single-mirror optics based on the Davies-Cotton design [101]. Two separate collaborations, NectarCAM [102] and FlashCam [103], are working on different implementations of the camera for the Northern and Southern MSTs, respectively. A MST prototype was in operation in Berlin between 2012 and 2020 [104], while the production of pathfinder telescopes to be installed in both CTAO sites is currently ongoing [105]. An alternative dual-mirror telescope using the Schwarzschild-Couder optical design [106] (Schwarzschild-Couder Telescope, SCT) has been proposed, with a primary mirror of 9.7 m diameter. The reduced aberration provided by this design allows for a wider FoV radius of 8° and a high resolution camera based on silicon photomultiplier (SiPM) technology. A prototype SCT (pSCT) has been in operation at the Whipple observatory since 2020 [107].

Finally, at the highest energies (5–300 TeV), observations are statistically limited as the gamma-ray fluxes become very low (Figure 1.1). Since large mirrors are not necessary to image the correlated rare, but bright, atmospheric showers, the chosen strategy will be to employ many (and relatively cheap) Small-Sized Telescopes (SSTs) distributed across a large area. Unlike LSTs and MSTs, and similarly to SCTs, this class of telescopes will feature a dual-mirror optics based on a modified Schwarzschild-Couder design with a primary mirror diameter of 4.3 m, as well as 2048-pixel SiPM cameras covering a wide FoV radius of 8.8°. Several SST prototypes with different characteristics have been developed. The GCT (Gamma-ray Cherenkov Telescope) prototype at the Paris-Meudon Observatory in France [108] and the ASTRI-Horn/SST-2M at the Serra La Nave Observatory in Sicily [109, 110] both feature a double-mirror optical structure and SiPM cameras that were used as the basis for the final SST design [111]. The ASTRI (Astrofisica con Specchi a Tecnologia Replicante Italiana) project, initially supposed to provide 9 pathfinder telescopes for the CTAO Southern Array, was later repurposed to operate as an independent "Mini-Array" located at the Teide Observatory on Tenerife, in the Canary Islands [112]. Two single-mirror SST (SST-1M) prototypes, with a Davies-Cotton mirror design and SiPM cameras, are currently operating as a stereoscopic system at the Ondřejov Observatory near Prague, in the Czech Republic [113].

The Northern and Southern arrays of CTAO will be optimized for different science cases. From the Northern hemisphere, mostly extragalactic sources such as AGNs are observable. Since gamma rays in the highest energy range detectable by the Observatory are not expected to be observed from these sources, due to the effective absorption over cosmological distance by the extragalactic background light (EBL) [114], the initial ("Alpha") confguration of the CTAO Northern Array will not feature any SSTs. It will instead consist of 4 LSTs surrounded by 9 MSTs (Figure 1.8a) focused on detecting lower-energy photons up to few TeV. The Southern Array, on the other hand, will be initially made up



(A) Northern Array. (B) Southern Array.

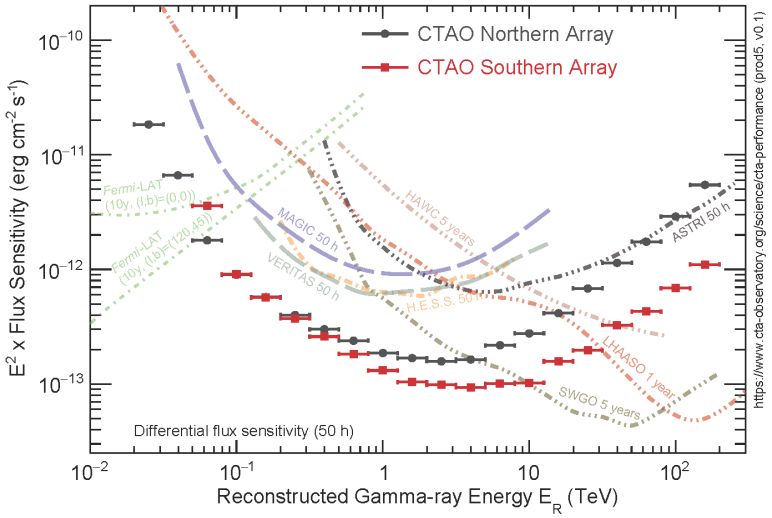
FIGURE 1.8: Plans for the Alpha configuration of the two CTAO arrays. Images from https://www.ctao.org/emission-to-discovery/array-sites/.

of 14 MSTs and 37 SSTs (FIGURE 1.8B) with the purpose of studying the highest-energy emission from the inner regions of the Milky Way. In total, 64 telescopes are expected to be built during the first construction phase of CTAO.

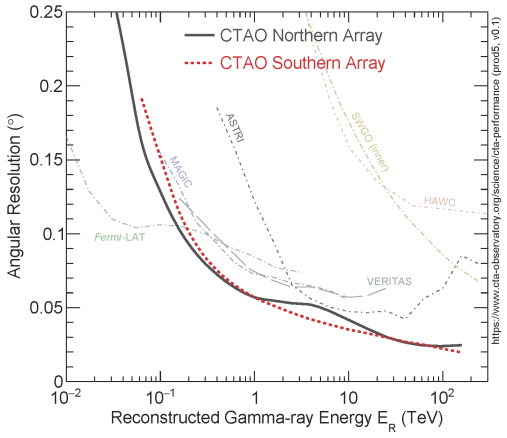
The site selection and layout optimization have been determined by dedicated Monte Carlo studies [115–117]. These require a detailed simulation of the shower development in the atmosphere and the emission of Cherenkov photons, typically performed using the CORSIKA (Cosmic Ray Simulations for KASCADE) software [118]. An equally thorough description of the telescopes' response, from the ray tracing in the optical structure to the electric signal generation in the camera, is provided by software programs such as `sim_telarray` [119], originally developed for the HEGRA and H.E.S.S. experiments. The estimated performance of both CTAO sites derived from these simulations is available in the form of instrument response functions (IRFs) [120]. The differential energy flux, angular resolution and energy resolution are shown in FIGURE 1.9 and compared to present gamma-ray experiments. Foreseen upgrades of this baseline configuration include the addition of 2 LSTs and 5 SSTs to the Southern Array ("Beta" configuration), along with several enhancements in terms of multiwavelength coordination and technological development, in the context of the Italian-funded CTA+ program [121, 122]. Simulations of a full-scope ("Omega") configuration, featuring 118 telescopes between the two sites, have also been performed [117, 123].

1.4.2 Scientific goals

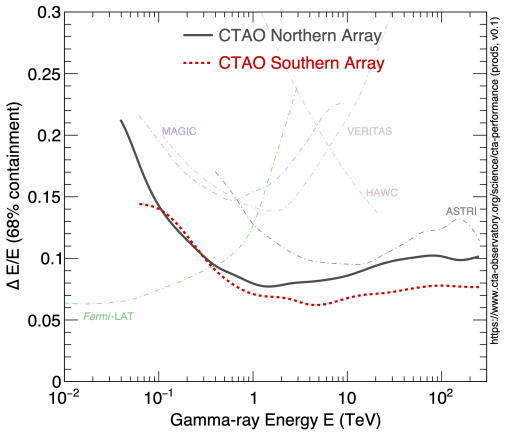
The main drivers behind the scientific program of CTAO are grouped in three main themes [83, 84]:



(A) Differential flux sensitivity.



(B) Angular resolution.



(C) Energy resolution.

Figure 1.9: Performance of the CTAO Alpha configuration compared to present gamma-ray experiments. Figures from https://www.ctao.org/for-scientists/performance/.

1. Understanding the origin of cosmic rays, their impact on the surrounding environments and the cumulative effects they produce on various scales;

2. Probing extreme environments, such as supermassive black holes, and understanding the particle acceleration processes within them;

3. Investigating the nature of dark matter and studying possible new fundamental physics effects on gamma-ray propagation.

In order to address these themes, a Core Programme organized in several Key Science Projects (KSPs) was developed in the context of the CTAO Consortium [124]. These projects were selected based on the scientific relevance and expected quality of results compared to the state of the art. As KSPs will typically require large amounts of time (hundreds or even thousands of observation hours), it is expected that approximately

40% of the available observation time will be dedicated to them during the first 10 years of CTAO operation, while the rest will remain open to external proposals.

Deep observations and surveys of the Galactic Center of the Milky Way are planned [125], as well as a survey of the Galactic Plane [126] and of the Large Magellanic Cloud [127], possibly disentangling the various components of the diffuse gamma-ray emission observed from these sources and providing hints on the CR acceleration happening therein. Particular attention will be devoted to cosmic PeVatrons [128], galactic sources where protons above PeV energies may be accelerated, and to star-forming systems both inside and outside the Milky Way. Extragalactic sources such as AGNs and clusters of galaxies [129] will be studied in detail, providing valuable information on their emission mechanisms and on possible non-standard effects on cosmological gamma-ray propagation [130], while an unbiased extragalactic survey will search for previously undetected sources (Section 2.5.2). A KSP is also dedicated to cosmic transients, such as GRBs, transients detected in other electromagnetic bands [131], as well as neutrino and gravitational-wave triggers.

1.4.3 Dark matter and fundamental physics searches with CTAO

The search for the nature of dark matter is one of the main scientific motivations behind the CTAO Core Programme. As such, a dedicated Dark Matter KSP is foreseen, which will employ observations from several sources where significant overdensities are expected.

It is well-known that about 32% of the energy density of the Universe consists of non-relativistic matter [132]. Various observational pieces of evidence show that only about 15% of this fraction is visible in the form of baryonic matter, i.e. astrophysical objects such as stars, galaxies and gas clouds, while the rest must be found in some form of gravitationally-interacting cold dark matter (CDM). While the precise particle nature of dark matter is still unknown, it should consist of particles which are either stable or with a decay time comparable to the age of the Universe, neutrally charged with respect to all fundamental interactions except for gravity, and whose presently observed abundance can be explained by some cosmological mechanism. Some of the best-motivated candidates fulfilling these requirements are represented by weakly-interacting massive particles (WIMPs). According to the WIMP paradigm, in the early Universe these particles would be able to self-annihilate into pairs of Standard Model particles, and vice versa. As a consequence of cosmological expansion, this process would gradually go out of equilibrium, leaving a relic WIMP abundance in a "freeze-out" process [133]. The reference value for the velocity-averaged annihilation cross section is given by the thermal estimate $\langle \sigma v \rangle \simeq 3 \times 10^{-26}\,\mathrm{cm^3\,s^{-1}}$, which reproduces the present dark matter density.

In gamma-ray astrophysics, WIMP searches are usually performed by looking for signatures of annihilation or decay in the spectra of massive targets, where the dark matter density is expected to be highest. In the case of annihilation, the expected contribution to the gamma-ray flux[6] is given by

$$\phi(E) = \frac{\mathrm{d}N}{\mathrm{d}E} = \frac{1}{8\pi} \frac{\langle \sigma v \rangle}{m_\chi^2} \frac{\mathrm{d}N_\gamma}{\mathrm{d}E} \times \int_{\Delta\Omega} \int_{\mathrm{l.o.s.}} \rho^2(\ell)\,\mathrm{d}\ell\,, \tag{1.3}$$

[6]Here and in the following, the gamma-ray flux ϕ is defined as the number of photons per unit time, surface and energy.

which is conventionally split in two factors. The particle physics factor involves the WIMP mass m_χ, the velocity-averaged annihilation cross-section $\langle \sigma v \rangle$ and the resulting photon spectrum $\mathrm{d}N_\gamma/\mathrm{d}E$, which depends on the specific particle physics model used. Typically, $\mathrm{d}N_\gamma/\mathrm{d}E$ is computed considering annihilation into a few benchmark channels such as W^+W^-, $\tau^+\tau^-$ or $b\bar{b}$ pairs [134]. The second factor, usually called astrophysical factor or J-factor, contains the squared dark matter density profile $\rho(\ell)$ integrated over the line of sight (l.o.s.) from Earth and the solid angle $\Delta\Omega$ covered by the detector. Common theoretically motivated density profiles are those by Einasto [135] and by Navarro, Frenk and White (NFW) [136].

Several hundreds of hours are expected to be allocated for observing sources of interest in the Dark Matter KSP. A paramount target for this kind of studies is the Galactic Center of the Milky Way, as its large mass and relative proximity to Earth would guarantee a strong dark matter signal. However, such a signal should be disentangled from the large background originated by the many gamma-ray sources present in this region. This, in turn, requires both accurate modeling of all its components and a high enough energy and spatial resolution, which will be one of CTAO's main improvements with respect to current IACT systems. Based on the KSP specifications, observations of the Galactic Center and surrounding regions have been simulated for a total of 825 hours, demonstrating that CTAO should be able to improve the current upper limits on $\langle \sigma v \rangle$ for TeV-scale WIMPs by about one order of magnitude within its first 10 years [125] (Figure 1.10). Similar studies were performed by simulating observations of the Large Magellanic Cloud for 340 hours [127] and for the Perseus Galaxy Cluster for 300 hours [129], where the case of WIMP decay was considered as well to place lower-limits on the WIMP lifetime. More recently, expected limits on WIMP annihilation have also been obtained for a selected sample of dwarf spheroidal galaxies, for a total of 600 hours [137]. While these targets would present a weaker dark matter signal compared to the Galactic Center, they are known to be almost completely free of astrophysical gamma-ray background, so that a detected signal in such band would represent a compelling evidence for dark matter annihilation.

A different approach to dark matter searches is implemented by looking for specific gamma-ray spectral features, e.g. monochromatic lines from direct WIMP annihilation into photon pairs, irrespective of the underlying particle physics model. In this case, simulated observations of the Galactic Center (500 hours) and of six dwarf spheroidal galaxies (100 hours each) with CTAO show that upper limits on $\langle \sigma v \rangle$ for TeV-scale WIMPs can be set even several orders of magnitude below the thermal benchmark [138].

Gamma-ray observations with CTAO will also be used to investigate questions related to cosmology and fundamental physics. Contrary to dark matter searches, which benefit from the relative proximity of the sources, this kind of studies aims to constrain effects on the propagation of gamma-ray photons over cosmological distances. For this reason, a privileged target is represented by gamma-ray emitting AGNs. The CTAO AGN KSP (discussed in Section 2.5.2) aims to perform in-depth observations of selected AGNs from different classes, as well as a monitoring campaign in search of high-intensity flares. These extragalactic sources are located at a distance from the Milky Way measured in terms of their cosmological redshift parameter z, which makes it possible to employ AGN data to investigate non-standard photon propagation effects [130].

As previously mentioned, VHE gamma rays propagating over cosmological distances are absorbed by the EBL, typically limiting the redshift of AGNs that can be observed in

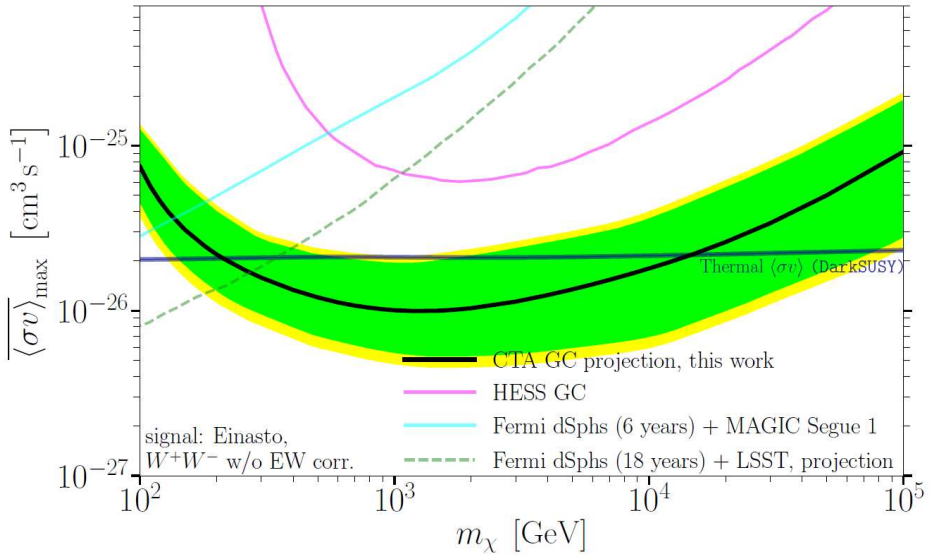


Figure 1.10: Projected limits on WIMP dark matter annihilating in W^+W^- pairs from the simulated CTAO observations of the Galactic Center, compared to previous constraints. Green and yellow bands represent 68% and 95% uncertainties on the limit, respectively. Figure taken from ref. [125].

this energy range to $z \lesssim 2$. The EBL is produced by the accumulated radiation in the infrared to ultraviolet over the history of the Universe due to star formation and emission processes. A VHE gamma ray can scatter on this soft photon background producing an electron-positron pair, according to the process

$$\gamma\gamma \to e^+e^- \tag{1.4}$$

known as Breit-Wheeler scattering [139]. The resulting effective absorption of gamma rays on their cosmological path defines an *optical depth* $\tau(E,z)$ dependent both on the gamma-ray energy E and on the cosmological redshift z of the emitting source [114]. The observed gamma-ray flux from a distant source will be thus given by

$$\phi_{\rm obs}(E) = \phi_{\rm int}(E)e^{-\tau(E,z)}\,, \tag{1.5}$$

where $\phi_{\rm int}(E)$ is the intrinsic flux emitted by the source. Various models of the EBL have been developed, both from first principles and phenomenological approaches, with a remarkable level of agreement between them [140–145]. CTAO observations of AGNs at various distances will help constrain the EBL intensity as a function of z, providing valuable information to disentangle between different models. Additionally, effects of the deflections of electron-positron pairs produced in the EBL can be used to improve current limits on the intergalactic magnetic field (IGMF) intensity. Finally, deviations from the predictions of standard EBL models in the VHE spectra of distant sources may give hints on new fundamental physics effects, such as the Lorentz invariance violation (LIV) predicted by some quantum gravity theories or the existence of axion-like particles (ALPs). ALPs will be discussed in much greater detail in Chapter 3 and in the rest of this work.

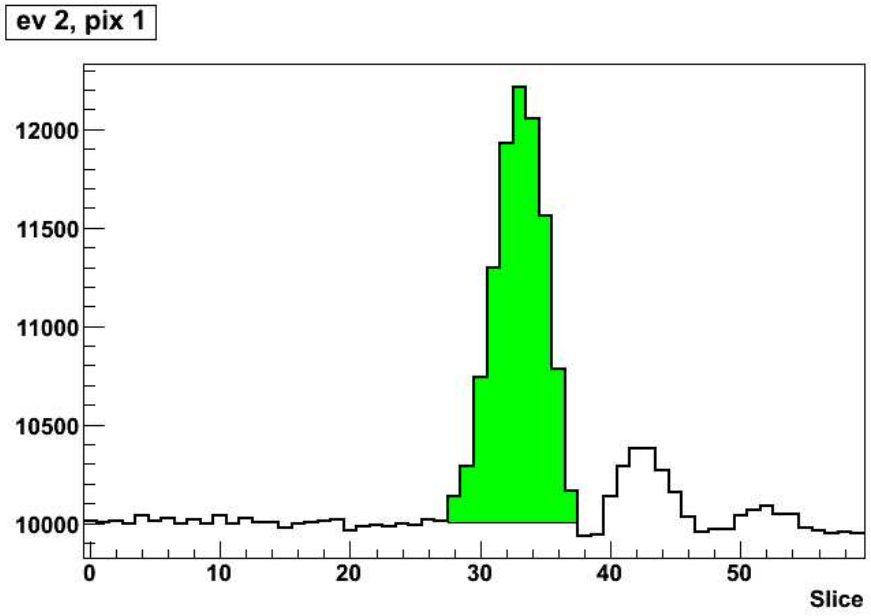


Figure 1.11: Typical waveform from a MAGIC camera PMT. The vertical axis represents ADC counts, while the horizontal axis represents time slices (depending on the readout chip sampling rate, 2 GHz in this case). The main pulse signal above pedestal noise is highlighted. Image credit: J. Sitarek, 1st CTAO Summer School (2024).

1.5 Data analysis

1.5.1 Event reconstruction and data formats

Unlike optical or radio astronomy, which typically deal with continuous radiation fluxes, the fundamental observed quantity in gamma-ray astronomy is represented by discrete photon counts. Furthermore, the observation of VHE gamma rays is an indirect process, and several steps need to be performed before information on the energy and direction of the incoming photons can be obtained.[7]

In the case of IACTs, the data acquisition (DAQ) starts at the level of camera pixels. A trigger system with a pre-set discrimination threshold (DT), which typically depends on the sky region and night-sky background (NSB) conditions such as moonlight, determines whether to store the incoming signal as a shower event. Different trigger strategies and multi-layer schemes can be implemented (e.g. [61]). Raw data from a shower event consist in waveforms (output voltage over time, Figure 1.11) from each photomultiplier in the camera, sampled and digitized by an analog-to-digital converter (ADC) system. The "pedestal" noise of the readout system is estimated and removed by dedicated dark runs, where the chips' output is recorded in the absence of external triggers. Furthermore, the output of the readout system is expressed in ADC counts, which need to be properly converted to photoelectron (p.e.) counts by appropriate calibration techniques. Typically, a ultraviolet laser shot from the center of the mirror is used to *flat-field* the camera, uniformly illuminating it in brief flashes. Assuming that one ADC count corresponds to C

[7] While the following description is meant to be as general as possible, many examples will refer to the MAGIC or LST-1 telescopes for clarity.

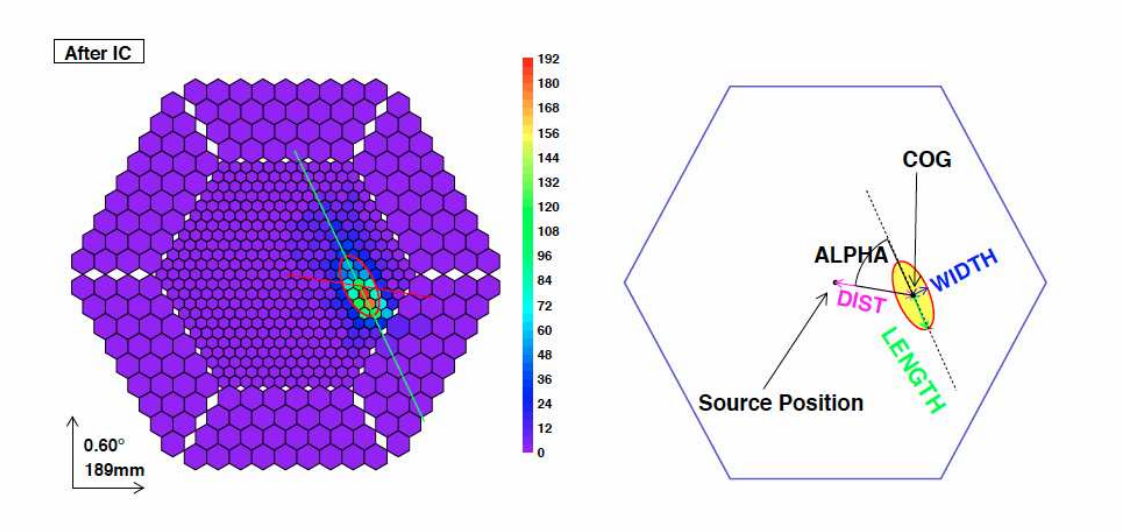
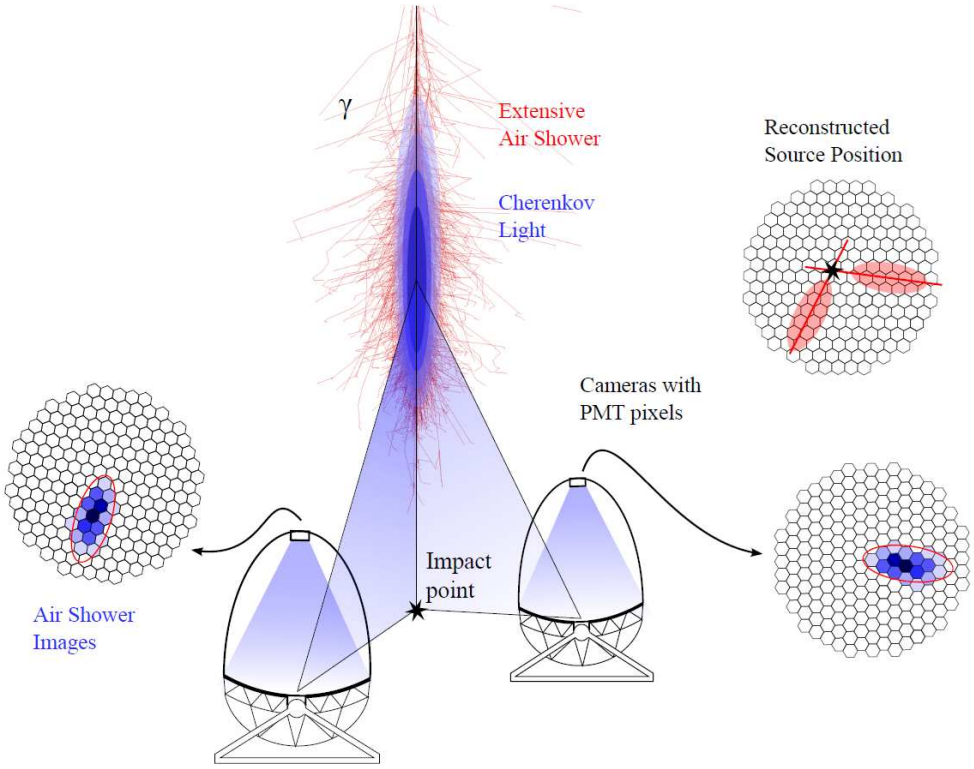


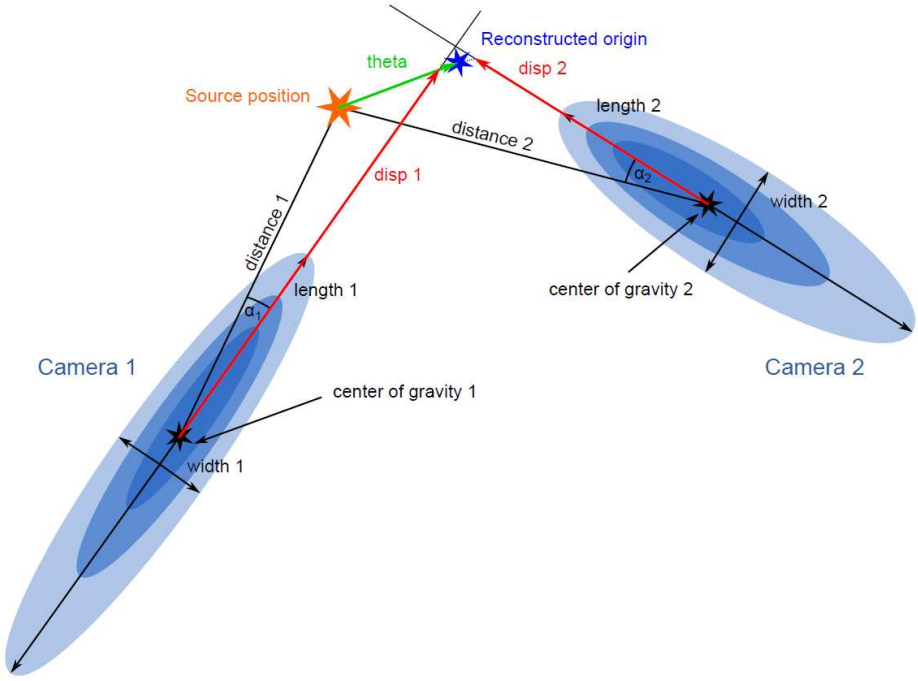
Figure 1.12: Example of a cleaned and parametrized image in the MAGIC-I camera, where the p.e. charge in the pixels not selected by the tail-cut method has been set to 0. Figure from the MAGIC Wiki (private).

p.e. and that a flatfield event produces on average N p.e., it follows that the mean ADC counts in one flash will be $\bar{x} = N/C$ with a Poissonian error of $\sigma = \sqrt{N}/C$. The p.e./ADC count conversion factor can thus be estimated from the measured average and variance of counts as $C = \bar{x}/\sigma^2$. Corrections to this simple method account for the non-Poissonian response of PMTs (F-factor), as well as the pedestal fluctuations and signal timing [146]. As the pedestal level and PMT gain tend to vary due to environmental conditions, such as temperature and humidity, interleaved pedestal and flatfield data are continuously taken during observation nights.

After pedestal subtraction and calibration, shower images such as those in Figure 1.3c are obtained by computing the total number of photoelectron (p.e. charge) deposited in each pixel; this corresponds to integrating the green area in Figure 1.11. At this stage, however, pixels contain electronic noise or background signal due to fluctuations in the NSB. The latter is typically due to effects such as starlight, moonlight, airglow and light pollution. Additionally, individual pixels may be illuminated by bright stars in the camera FoV. A common image cleaning procedure consists in applying a two-stage filtering process, the so-called *tail-cut* method, in order to efficiently reject all these sources of background and only retain the shower signal [148]. In the first step, one or more clusters of pixels with p.e. charge above a threshold Q_{core} are selected, forming the core of the image. Subsequently, all neighboring pixels with a charge above a second threshold $Q_{\text{boundary}} < Q_{\text{core}}$ are selected, forming the boundary of the image. In a standard analysis, typical values of 8 and 4 or 5 and 10 p.e. are used for Q_{core} and Q_{boundary}, respectively. More sophisticated techniques have also been developed for different analysis cases, employing signal timing information [149, 150] or charge information from multiple neighboring pixels (*sum-cleaning* method) [151]. After cleaning, the Hillas parameters described in Section 1.2 are extracted from the image's p.e. distribution (Figure 1.12). In the case of simultaneous operation of two or more telescopes, the camera images from different points of view can be combined to give a stereoscopic view of the shower (Figure 1.13a). The direction of



(A)



(B)

Figure 1.13: Diagram of stereoscopic shower reconstruction (A) and image parameters (B) with the MAGIC telescopes. Images from ref. [147].

the shower is thus reconstructed geometrically by the intersection of the image axes in the camera frame. New parameters can be introduced to describe the stereoscopic image, such as *disp*, indicating the distance between the centroids of each image and the shower direction, and θ, defined as the angular distance between the assumed and reconstructed source positions (Figure 1.13b).

The image parameters, either monoscopic or stereoscopic, are then used to discriminate whether the shower originated from a hadron or a gamma ray. This process, known as gamma-hadron separation, is typically implemented by feeding the parameters into a random forest (RF) algorithm [152–154]. The RF algorithm is an example of a ensemble machine-learning classifier, made up of individual decision trees [155–157]. Each tree acts on a sample, represented by set of parameters or *features*, to distinguish whether it belongs to one of two classes by operating sequential binary splits on the features' values. The splitting thresholds at each step (node) are referred to as the parameters of the tree; on the other hand, quantities such as the tree depth, maximum number of splits, etc. are called hyperparameters. During the "supervised training" of the tree the splits are chosen in order to minimize some loss function by operating on datasets whose class is known a priori. Once the tree has been trained and its parameters have been fixed, it can be used to classify previously unseen test datasets. A random forest is then "grown" by training several decision trees with random subsets of the training dataset (*bootstrapping*), and selecting the final prediction by majority voting.

In the case of gamma-hadron separation, RFs are trained with a large amount of detailed Monte Carlo simulations of the shower development and the Cherenkov photon detection by the telescopes, including all possible optical and electronic characteristics that might affect the signal, performed with tools such as CORSIKA and `sim_telarray` [119]. The simulated data, produced for both protons and gamma rays at different energies and zenith angles, are then processed and parametrized in the same way as real data. The shower parameters are then used for supervised training of the RF classifiers, which can then return a *gammaness* or *hadronness* score indicating how likely a set of parameters is to belong to a gamma-ray or hadronic shower. Besides gamma-hadron separation, RFs are used to estimate the energy of the primary particle in the shower, either directly or via look-up tables that correlate it with other shower parameters [158], or to estimate the shower direction (via the *disp* parameter) [62]. More advanced methods involving neural networks and deep learning have also been developed [159].

At this point, gamma-ray event lists with reconstructed energy and direction can then be compiled by applying appropriate cuts on gammaness. While the procedure outlined above is specific for IACTs, it has many points in common with event reconstruction in EAS arrays such as HAWC, where the calibrated signals from the PMTs in each detector are used to infer the shower properties [76].

In most cases, this data reduction process is applied to VHE data using proprietary software depending on the used telescope or array, and the data products are kept within the collaboration that produced them. A standardization of the data formats at each stage of the reduction process was first proposed in the context of the CTAO collaboration [160, 161]. According to this scheme, the data should be organized in several data levels numbered from DL0 to DL5 (Figure 1.14). Data level 0 (DL0) corresponds to the raw data output from the DAQ system. The calibrated and parametrized data constitute data level 1 (DL1), while data level 2 contains information about the reconstructed shower param-

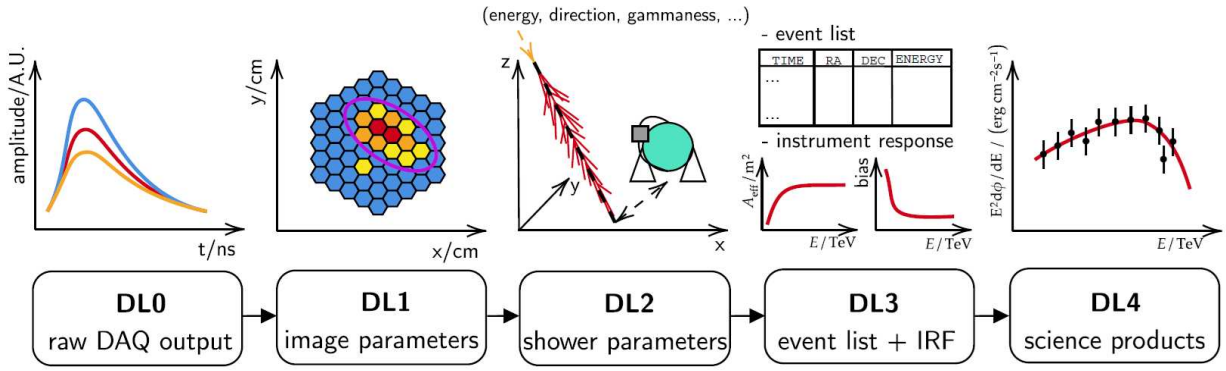


Figure 1.14: IACT data reduction levels (DL5 not shown). Figure from ref. [161].

eters. Data level 3 (DL3) consists of gamma-ray event lists (time, energy and direction), bundled with the IRFs necessary to perform any statistical analysis on the data. Higher-level data include science products, information related to the astrophysical emission and properties of the source such as fluxes and lightcurves, which are given at data level 4 (DL4), and observatory-level data such as catalogs and sky maps at data level 5 (DL5).

Starting from DL3, the information contained in the data is independent of the detection, calibration or reconstruction techniques. In order to make it possible to share and combine data between different experiments, a common data format has been proposed by the Gamma-Astro Data Formats (GADF) project [161, 162]. The format is based on the Flexible Image Transport System (FITS) [163] specifications. It will be officially adopted in the CTAO data analysis pipeline `ctapipe` [164], while being already employed in the LST-1 reconstruction software `lstchain` [165]. Other efforts to conform to the GADF standard by various collaborations include the `magicdl3` software [166, 167], which converts the standard MAGIC data format `melibea` to GADF-compliant DL3, the `V2DL3` converter tool for VERITAS data [168], and public data releases by H.E.S.S. [169] and HAWC [170]. The GADF is also natively adopted by the high-level gamma-ray data analysis package Gammapy [171], which will be the official science analysis tool for CTAO data. A complete workflow to analyze broadband multi-wavelength data with Gammapy was developed in ref. [172].

1.5.2 Statistical significance of signal

The main source of residual background in DL3 data is represented by cosmic rays misclassified as gamma-rays by the reconstruction algorithm. As mentioned in Section 1.2 this background is usually not modeled explicitly, but rather estimated by applying the ON-OFF observation technique. In modern IACTs, this can be achieved by pointing the telescopes at an offset from the source (*wobble* mode), so that both an ON region around the source and one or more OFF regions symmetrically distributed around the pointing direction can be observed in the same FoV (Figure 1.15). Compared to other methods, this *reflected regions* technique has the advantage that both ON and OFF regions can be observed simultaneously, without requiring additional time for OFF data taking. Other background estimation methods, especially used for extended sources, are described in ref. [173].

In order to estimate whether the gamma-ray excess in the ON region is statistically sig-

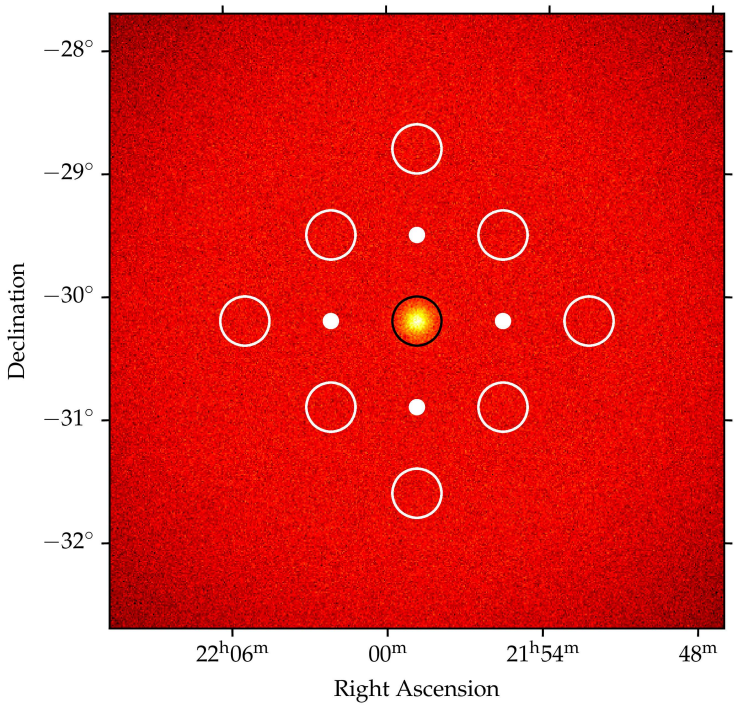


Figure 1.15: Counts map obtained from simulated observations of blazar PKS 2155−304 during the CTAO Internal Science Data Challenge (2024). The ON source region is shown in a black circle. The telescope pointings at a 0.7° offset from the source are shown as white dots, with three reflected OFF regions for each pointing (white circles).

nificant with respect to the background in the OFF regions, a likelihood-ratio hypothesis test is performed [174]. Given N_{on} and N_{off} counts in the ON and OFF regions, with an exposure ratio α, the Li-Ma significance [175]

$$S = \sqrt{2}\left\{ N_{\text{on}} \ln\left[\frac{\alpha}{1+\alpha}\left(\frac{N_{\text{on}}+N_{\text{off}}}{N_{\text{on}}}\right)\right] + N_{\text{off}} \ln\left[\frac{1}{1+\alpha}\left(\frac{N_{\text{on}}+N_{\text{off}}}{N_{\text{off}}}\right)\right]\right\}^{1/2}, \tag{1.6}$$

gives a measure of how unlikely it is that an observed excess in the ON region is due to background only, expressed in units of Gaussian standard deviations (see Appendix A). For one ON and n OFF regions of the same size observed during the same amount of time, the exposure ratio is simply $\alpha = 1/n$. Usually, a significance of at least 5σ is required to claim a detection. This quantity can be evaluated in different energy ranges for a given observation, applying different cuts on the θ^2 (Figure 1.16) and gammaness parameters and choosing those that yield the best significance [90]. In case of sources with a precisely known position, such as the Crab nebula, cuts on the α shower parameter (not to be confused with the acceptance ratio) can also be applied.

1.5.3 Model fitting and high level analysis

In the most general case, the gamma-ray flux from a source can be modeled by a function $\phi(\mathbf{p}, E)$ of the observation direction $\mathbf{p}$ and the photon energy E. A simple example of

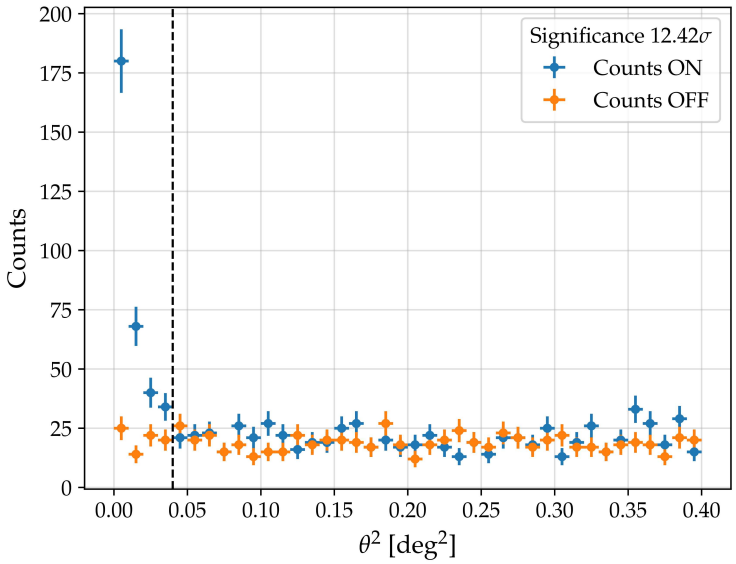


Figure 1.16: Example θ^2 plot generated with some of the data in Figure 1.15. The blue and orange points represent the distributions of θ^2 values in the ON and OFF regions, respectively. The excess of counts in the ON region below the cut $\theta^2 = 0.04\,\mathrm{deg}^2$, shown by a vertical dashed line, indicates a detection of the source. The significance is computed according to the Li-Ma formula.

energy dependence is a power law (PL) shape

$$\phi(E) = \phi_0 \left(\frac{E}{E_0} \right)^{-\Gamma}, \tag{1.7}$$

where E_0 is a suitable *reference energy*, ϕ_0 is the *amplitude* (corresponding to the flux at $E = E_0$) and Γ is the *spectral* or *photon index*, indicating how steeply the flux decreases with increasing energy. Other commonly used spectral models include broken power law(BPL)

$$\phi(E) = \phi_0 \begin{cases} \left(\frac{E}{E_{\mathrm{break}}} \right)^{-\Gamma_1} & E < E_{\mathrm{break}} \\ \left(\frac{E}{E_{\mathrm{break}}} \right)^{-\Gamma_2} & E \geq E_{\mathrm{break}} \end{cases}, \tag{1.8}$$

exponentially cut-off power law (ECPL)

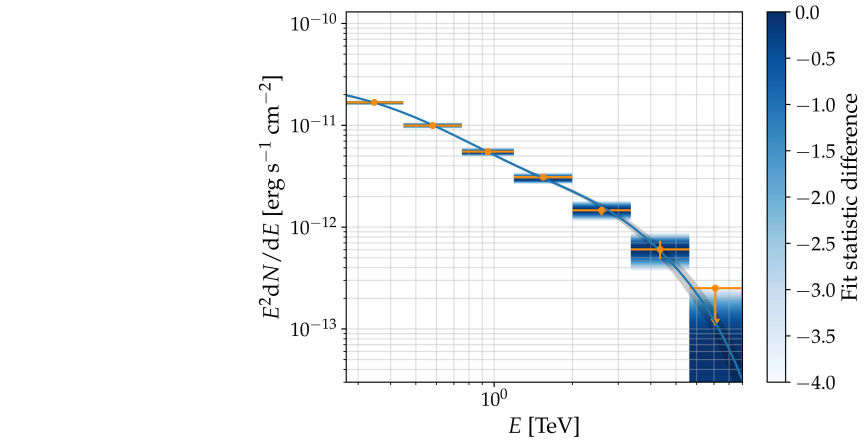
$$\phi(E) = \phi_0 \left(\frac{E}{E_0} \right)^{-\Gamma} e^{-E/E_{\mathrm{cut}}} \tag{1.9}$$

and log-parabola (LP)

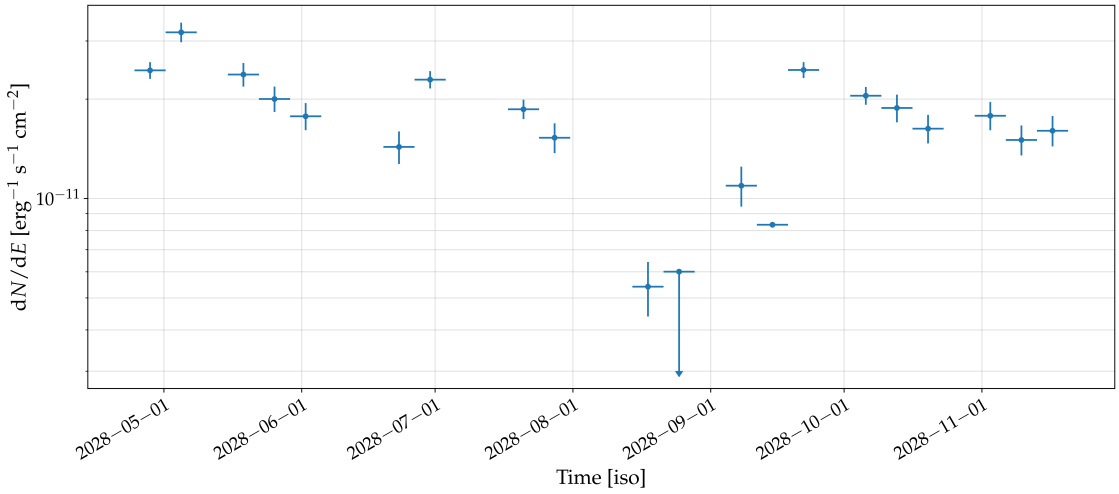
$$\phi(E) = \phi_0 \left(\frac{E}{E_0} \right)^{-\Gamma - \beta \ln(E/E_0)} \tag{1.10}$$

shapes.

The model parameters that define $\phi(\mathbf{p}, E)$ can be obtained by a maximum-likelihood fitting procedure (Appendix A). In an ON-OFF observation, this is implemented by min-



(A)



(B)

Figure 1.17: (A) Example SED for the simulated data shown in Figure 1.15, fit by a ECPL shape, accounting for EBL absorption. The fit statistic difference profiles are shown for each energy bin, with a upper limit shown at $2\Delta\phi$ above mean value. (B) Weekly-binned lightcurve generated for the same data.

imizing the fit statistic [176]

$$\mathrm{WSTAT} = 2\sum_{ik}[\mu_{ik} + (\alpha+1)b_{ik} - {N_{\mathrm{on}}}^{ik}\ln(\mu_{ik} + \alpha b_{ik}) - {N_{\mathrm{off}}}^{ik}\ln b_{ik}]\,, \tag{1.11}$$

where, for each i-th energy bin and k-th spatial bin, ${N_{\mathrm{on}}}^{ik}$ and ${N_{\mathrm{off}}}^{ik}$ are the observed counts of the ON and OFF regions, respectively, while μ_{ik} is the expected signal photon count and $b = \sum_{ik} b_{ik}$ is the expected background photon count in the OFF region(s).

After a global model fitting, higher-level estimates of the source properties can be derived. The spectral energy distribution (SED) of a source can be defined by means of *flux points* estimated by re-fitting the amplitude ϕ_0 of the global spectral model in each energy bin (see Appendix A). This defines the flux value and associated uncertainty (assumed Gaussian), $\phi(E) \pm \Delta\phi(E)$, in the bin centered at energy E. The significance of the signal in each bin is also computed according to the Li-Ma procedure. If a threshold value for

detection (e.g. 5σ) is not reached, a 95% confidence level upper limit can be set at the flux value $\phi(E) + 2\Delta\phi(E)$ (Figure 1.17a). By repeating this process for data binned in time or in direction, rather than energy, a *lightcurve* (Figure 1.17b) or a *flux map* can be obtained instead. Different estimators can be combined, yielding, for example, multiple lightcurves or flux maps in different energy ranges.

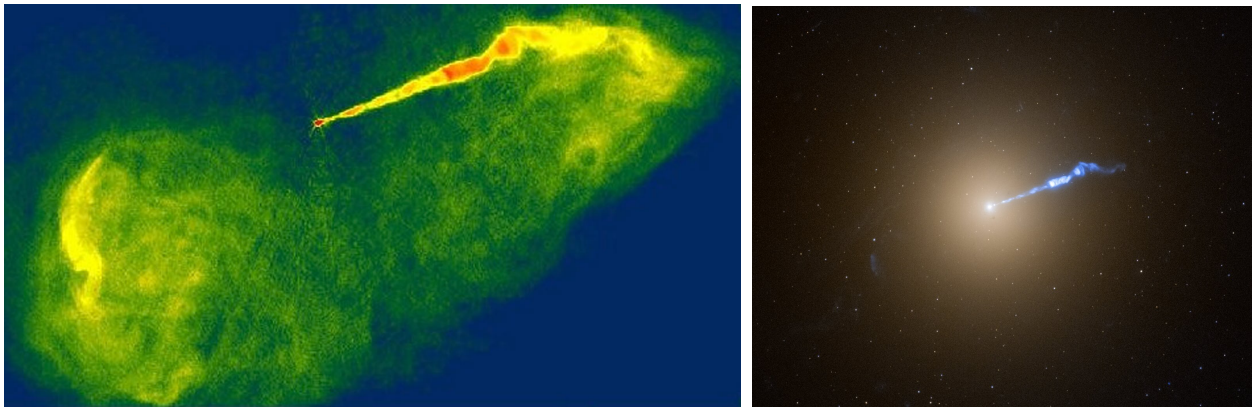
CHAPTER 2

Blazars

2.1 The unified model of active galactic nuclei

The study of active galactic nuclei (AGNs) historically began with the detection of emission spectral lines from optical observations of spiral galaxies (then referred to as "spiral nebulae"). These observations, most notably reported by Carl Seyfert [177] and later by Benjamin Markarian [178], showed evidence of non-thermal emission which could not be attributed to stellar activity in the galaxies. Several of these objects, with similar characteristics to the original sample, were classified based on the widths of their Doppler-broadened emission lines and finally confirmed as extragalactic objects, resulting in Seyfert 1 (broad-line) and Seyfert 2 (narrow-line) galaxies [179, 180]. In parallel, the evolution of radio astronomy led to the discovery of several quasi-stellar radio sources (*quasars*) characterised by powerful, variable radio luminosities and point-like optical images. The measurement of the cosmological redshift $z = 0.158$ of 3C 273 implied that it had to be located in the nucleus of a distant galaxy and to possess a luminosity about 100 times higher than galaxies such as the Milky Way [6, 181]. Similarly variable quasi-stellar objects (QSOs), but with no radio emission, were later found to represent a much larger fraction of active galaxies [182]. AGNs started to be separated between radio-quiet, such as Seyfert galaxies and QSOs, and radio-loud, representing about 10% of AGNs, in which radio emission is of non-thermal origin and significantly stronger than in normal galaxies [183]. This classification is correlated with the absence or presence of large relativistic jets originating from the nuclei, observed across different bands and reaching kpc or even Mpc scales [184] (Figure 2.1). According to a scheme proposed by Fanaroff and Riley [185], radio-loud galaxies can be further classified in *core-brightened* (FR-I) and *edge-brightened* (FR-II) based on whether their radio emission is concentrated in the galaxy nucleus or in lobes at the end of relativistic jets. Particularly luminous and variable radio-loud quasars were identified as *blazars* (a combination of *blaze* and *quasar*).

A wide and diversified "AGN zoo" emerged over time, with many, often overlapping, classes of AGNs being defined by observations in different bands of the electromagnetic spectrum [6, 186]. A common characteristic of these sources is their high variability in magnitude, on timescales ranging from minutes up to years. By a simple causality argument, the linear size R of the region from which the radiation is emitted should be compact and smaller than the distance travelled by the radiation itself in a proper time interval Δt,



(A) (B)

Figure 2.1: 20 cm radio interferometry (A) and optical (B) images of the relativistic jet in the AGN M87, taken by the Very Large Array and by the Hubble Space Telescope. Image credits: National Radio Astronomy Observatory/National Science Foundation and NASA/ESA.

i.e.

$$R \lesssim c\Delta t_{\rm var}\,, \tag{2.1}$$

in order to observe variability on a time scale $\Delta t_{\rm var}$. Furthermore, given the high observed brightness of these objects and their extragalactic nature, the magnitude-luminosity relationship implies large bolometric luminosities[1] of order $L \sim 10^{45}\,{\rm erg\,s^{-1}} \simeq 10^{12} L_\odot$ (where $L_\odot$ is the solar luminosity). A limit on the luminosity of a radiating compact object in a steady state is set by the *Eddington luminosity*, obtained by balancing the radiation pressure with the gravitational pull of the object [6]. For a mass M, the maximum value of the luminosity L is approximately given by

$$L_E = \frac{4\pi G M m_p c}{\sigma_T} \simeq 1.3 \times 10^{38} \left(\frac{M}{M_\odot}\right) {\rm erg\,s^{-1}}\,, \tag{2.2}$$

where G is Newton's gravitational constant, m_p is the proton mass, c is the speed of light in vacuum, $M_\odot$ is the solar mass and σ_T is the Thomson cross-section. This argument implies that in order to reproduce the typically observed luminosities of AGNs, these should have masses $M \gtrsim 10^5 M_\odot$.

From these basic considerations, requiring large masses confined in relatively compact regions, a unified model gradually emerged according to which AGNs consist in accreting supermassive black holes (SMBHs) at the centers of galaxies [187, 188]. Infalling matter around the black hole forms an accretion disk, which heats up due to dissipative processes and radiates energy in the ultraviolet/soft X-ray bands. Rapidly-moving gas clouds around the black hole may be present, forming the so-called broad-line region (BLR) which is responsible for the broader emission lines in the optical spectrum of the AGN. A dusty torus around the disk may be obscuring the BLR, while slower-moving gas clouds form a narrow-line region (NLR) where the Doppler-broadening of spectral lines is less pronounced. Finally, collimated jets of particles accelerated to relativistic velocities

[1] The bolometric luminosity L is defined as the total radiated power by an astronomical object. It is related to the observed energy flux as $\Phi = L/(4\pi d_L^2)$, where $d_L(z)$ is the luminosity distance given as a function of redshift [133].

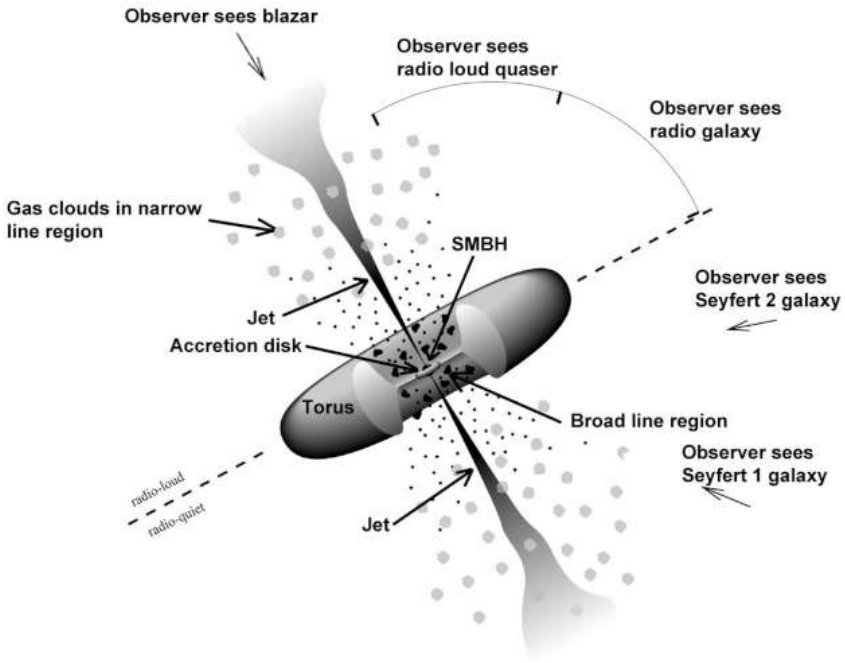


Figure 2.2: Diagram of the AGN unified model, displaying the main structure of the environment around the SMBHs as well as the various AGN classes originating from different observing angles. Figure from https://fermi.gsfc.nasa.gov/science/eteu/agn/, adapted from ref. [188].

can be emitted perpendicularly to the disk, extending to lengths of several kpc and possibly culminating in lobes. In this picture, the differences between the various AGN classes derive from structural differences (such as the presence or absence of strong jets, a BLR and/or an obscuring torus) and from the orientation of the AGN with respect to the line of sight from Earth (Figure 2.2). A radio-quiet AGN, whose emission is dominated by the accretion disk, will be classified as a Seyfert 1 galaxy if it is oriented in such a way that radiation from the BLR can reach Earth. On the other hand, if the BLR is obscured by the dusty torus, only radiation from the NLR can be detected and the galaxy will be classified as Seyfert 2. Similarly, a jet-dominated, radio-loud quasar will be classified as a FR-I or FR-II galaxy depending on the jet morphology if observed "sideways", and as a blazar if the jet forms a small angle ($\theta_{\text{obs}} \lesssim 20°$) with the line of sight from Earth. Notably, very long baseline interferometry (VLBI) observations of the AGN M87 by the Event Horizon Telescope collaboration produced the first ever radio image of a SMBH's event horizon, providing strong observational support for this model [189].

2.2 Observational characteristics of blazars

Blazars are the most extreme class of radio-loud jetted AGNs, featuring intense polarized emission and high variability. Their characteristic brightness is due to the close orientation of their relativistic jets to the line of sight from Earth, which produces strong *relativistic beaming*. Assuming that the jet has a bulk Lorentz factor

$$\gamma_{\text{bulk}} = \frac{1}{\sqrt{1-\beta^2}}\,, \tag{2.3}$$

where β is the relativistic speed of the jet, the Doppler factor [6]

$$\delta = \frac{1}{\gamma_{\text{bulk}}(1 - \beta \cos \theta_{\text{obs}})} \tag{2.4}$$

can be introduced. Relativistic beaming causes photons emitted in a solid angle element $\mathrm{d}\Omega$ to be detected in a smaller element

$$\mathrm{d}\Omega' = \frac{\mathrm{d}\Omega}{\delta^2}\,, \tag{2.5}$$

thus effectively making the jet appear more collimated. In addition, the observed energy E' and time interval $\Delta t'$ at which photons from the jet are detected can then be related to their values E, Δt in the comoving frame of the jet by

$$E' = \frac{\delta}{1+z} E\,, \quad \Delta t' = \frac{1+z}{\delta} \Delta t\,, \tag{2.6}$$

where z is the cosmological redshift of the source. The observed SED at Earth, defined as the measured energy per unit time and area, is then given by

$$E'^2 \frac{\mathrm{d}N'}{\mathrm{d}E'} = \frac{\delta^4}{(1+z)^2} E^2 \frac{\mathrm{d}N}{\mathrm{d}E}\,, \tag{2.7}$$

where N is the number of detected photons per unit time and area. For small observation angles $\theta_{\text{obs}} \lesssim 20°$ and highly relativistic jets ($\beta \simeq 1$), the beaming can become so strong as to outshine all other emission from the host galaxy of the blazar. Another peculiar consequence of relativistic beaming is the apparent superluminal motion observed in VLBI radio images of jets [6].

In the radio domain, blazars are defined as *flat spectrum* sources, with power-law spectral indices $-\Gamma \lesssim 0.5$ (see EQ. 1.7) [186]. Based on their optical properties, they can be classified as flat spectrum radio quasars (FSRQs) or BL Lacertae objects (BL Lacs). FSRQs display strong, broad emission lines in their optical spectra, indicating the presence of a broad line region in their environment. BL Lacs, on the other hand, present almost featureless optical spectra, which makes it difficult to measure their redshift. They were named after the prototypical source BL Lacertae, originally thought to be a variable star [190]. Observationally, FSRQs are intrinsically more powerful and brighter than BL Lacs [191, 192]. Typical blazar masses range between $10^7 M_\odot$ and $10^{10} M_\odot$ [193], with FSRQs being generally more massive by the Eddington criterion, as well as having a more complex structure due to the presence of a BLR and possibly a dusty torus around the SMBH. On average, FSRQs are found at larger redshifts than BL Lacs [194].

A striking characteristic of blazars, common to both FSRQs and BL Lacs, is the broadband shape of their SED, extending from radio waves up to gamma rays. When represented as a function of energy, it typically exhibits two peaks, one at low frequencies between the infrared and X-ray band, and one between X-rays and gamma rays. Depending on the peak ν_{sync} of the low-frequency component of the SED, typically attributed to synchrotron radiation emitted by accelerated relativistic electrons in the jet magnetic field, blazars can also be classified as low-synchrotron peaked (LSP, $\nu_{\text{sync}} \lesssim 10^{14}\,\text{Hz}$), intermediate-synchrotron peaked (ISP, $10^{14}\,\text{Hz} \lesssim \nu_{\text{sync}} \lesssim 10^{15}\,\text{Hz}$) and high-synchrotron

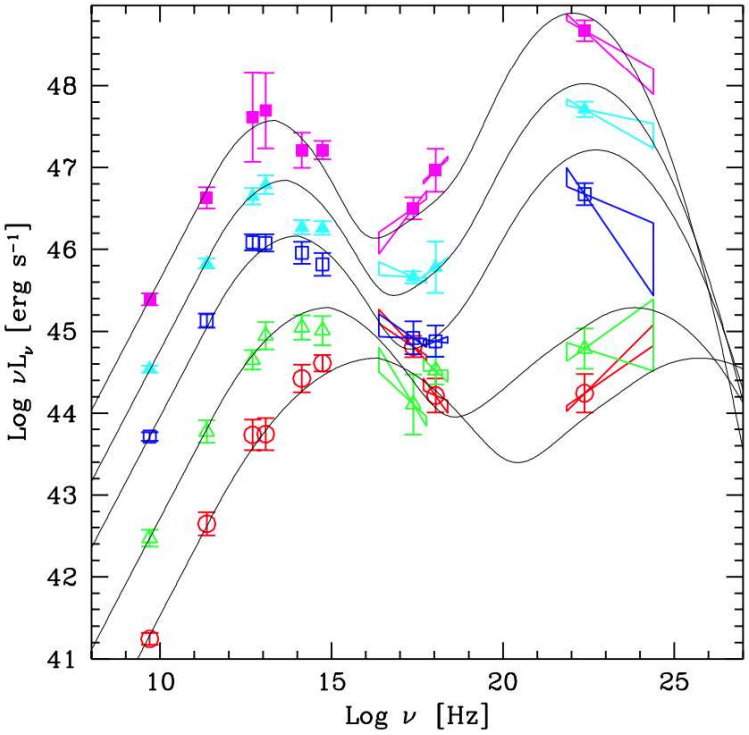


Figure 2.3: Average SEDs from the blazar sample considered in ref. [198], grouped by radio luminosity, clearly illustrating the blazar sequence. Figure from ref. [199].

peaked (HSP, $\nu_{\text{sync}} \gtrsim 10^{15}$ Hz) [195]. While FSRQs are most often LSP sources, BL Lac sources display a larger variety of synchrotron peak frequencies, and can be classified as low-, intermediate- and high-synchrotron peaked BL Lacs (LBLs, IBLs and HBLs) [196]. More recently, acronyms such as UHBL or EHBL (ultra-high or extremely-high frequency peaked BL Lacs) have also been introduced to describe blazars with even higher synchrotron peak frequencies, reaching into hard X-rays [197]. By considering the average broad-band SEDs of several blazars, grouped by luminosity, it can be shown that in brighter sources both peaks of the SED occur at lower frequencies. In addition, blazars with higher luminosity exhibit larger ratios between the peak intensities of high- and low-frequency SED components (Figure 2.3). This pattern is known as the *blazar sequence* [193, 194, 198, 199].

2.3 Emission modeling

2.3.1 Leptonic and hadronic mechanisms

The low-energy component of blazar spectra is usually attributed to synchrotron radiation from relativistic electrons in the jet. In the comoving frame of the jet, this component is usually computed analytically by assuming a power-law distribution of the electron number [200, 201]

$$N_e(\gamma_e) = N_0 \gamma_e^{-n}\,, \tag{2.8}$$

given in terms of the electron Lorentz factor γ_e and a spectral index n, or a broken power law with different spectral indices n_1 and n_2 above and below some break Lorentz fac-

tor $\gamma_{\rm break}$.

Both leptonic and hadronic models exist to describe the emission of high-energy radiation from blazars [201–203]. In leptonic models, this component is assumed to originate from inverse Compton (IC) scattering, in which high-energy electrons transfer part of their energy to low-energy photon fields, resulting in the production of X-rays and gamma rays. The general cross-section for the IC process is given by the Klein-Nishina formula [204], and the radiation produced by a given electron distribution $N_e(\gamma_e)$ over a target photon density $n(\varepsilon)$ can also be computed directly [200, 201]. The target photon field for IC scattering may be the synchrotron radiation emitted by the electrons themselves (synchrotron self-Compton, or SSC), or an external component (external Compton, EC). Sources of EC scattering include thermal photons from the accretion disk and dusty torus, and emission lines from the BLR and NLR. The cosmic microwave background (CMB), whose energy density scales with cosmological redshift as $(1+z)^4$, can represent a particularly important target for EC scattering in high-redshift blazars. The produced high-energy photons may also be absorbed in these environments by undergoing Breit-Wheeler scattering [139], which may give hints on the location of the gamma-ray emitting region [201].

In hadronic models, high-energy photons are assumed to be produced by a population of relativistic protons and other nuclei in the jet, either via synchrotron radiation, Bethe-Heitler pair production or photo-meson production [201]. At relatively low energies, Bethe-Heitler scattering of protons with ambient photons produces e^+e^- pairs [205], which then emit synchrotron or IC radiation as in the leptonic scenario. On the other hand, higher-energy protons interacting with external photon fields produce both charged and neutral mesons such as pions. Neutral pions then mainly decay to photon pairs in the gamma-ray band,

$$\pi^0 \to 2\gamma\,, \tag{2.9}$$

while charged pions follow the channels

$$\begin{aligned} \pi^+ &\to \mu^+\nu_\mu \to e^+\nu_e\bar{\nu}_\mu\nu_\mu\,, \\ \pi^- &\to \mu^-\bar{\nu}_\mu \to e^-\bar{\nu}_e\nu_\mu\bar{\nu}_\mu\,, \end{aligned} \tag{2.10}$$

with a decay fraction of almost 100% [7]. These models are considerably more complex than leptonic ones, since they should account for electromagnetic cascades generated by the highly energetic photons, electrons and positrons produced by pion decay, as well as for muon synchrotron radiation [201].

The main appeal of these models is the production of neutrinos alongside gamma rays, which can be probed experimentally to distinguish between hadronic and leptonic scenarios. A strong hint of hadronic acceleration in blazars was found in 2017 with the detection of a highly energetic astrophysical neutrino by the IceCube Neutrino Observatory, from a direction compatible with the BL Lac object TXS 0506+056 (IceCube-170922A event) [206]. The most probable reconstructed energy of the neutrino was 290 TeV, and the direction was 0.1° from the coordinates of the blazar. The detection was correlated with a gamma-ray flare detected in the same period by *Fermi*-LAT, with chance coincidence of the two events disfavored at the 3σ confidence level. The extensive multiwavelength coverage that followed, from radio to VHE gamma rays, resulted in a precise estimation of

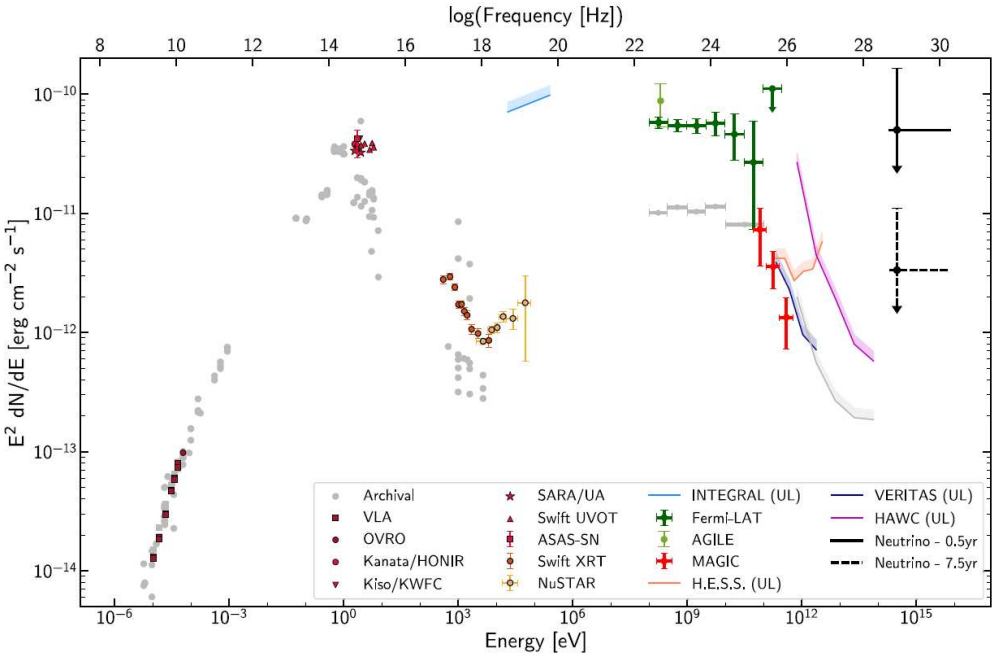


Figure 2.4: The multi-messenger SED of TXS 0506+056 after the IceCube-170922A event, showing upper limits on the neutrino flux. Figure from ref. [206].

the source redshift ($z = 0.3365$) and the measurement of a simultaneous SED over many orders of magnitude in photon energy (Figure 2.4). From the single neutrino event, upper limits on the neutrino flux from TXS 0506+056 could be computed, assuming either that the source had steadily emitted neutrinos for the full 7.5 years during which IceCube had been in operation, or that neutrinos were emitted during a 6-month flare. A neutrino luminosity of order 10^{45}–$10^{46}\,\mathrm{erg\,s^{-1}}$ could be estimated as well, compatible with typical blazar gamma-ray luminosities. Archival searches prompted by this observation later showed another neutrino excess from the direction of TXS 0506+056, detected between 2014 and 2015 at a 3.5σ confidence level, uncorrelated with gamma-ray emission [207, 208]. IceCube later published a list of potential neutrino sources, including BL Lac objects PKS 1424+240 and GB6 J1542+6129 and Seyfert galaxy NGC 1068 [209]. More recently, further evidence of neutrino emission by NGC 1068 was found [210], along with Seyfert galaxies NGC 4151, NGC 3079 [211] and NGC 7649 [212], further strengthening the connection between AGNs and astrophysical neutrino production.

2.3.2 One-zone, two-zone and multi-zone models

The simplest models of blazar emission assume all radiation to be emitted from a compact homogeneous region ("blob") with a tangled (i.e. randomly oriented) magnetic field, moving along the jet with some bulk Lorentz factor [200, 201]. Remarkably, in many instances these basic *one-zone* models provide good fits to blazar SEDs over a broad range of frequencies (e.g. [203]). While for LBLs and FSRQs the inclusion of EC is usually necessary [213], leptonic one-zone SSC models have been successfully used to constrain the emission regions in HBLs (e.g. [214, 215]), providing typical values of parameters such as the Doppler factor $\delta \simeq 10$–50, the size of the emitting region $R \simeq 10^{16-17}\,\mathrm{cm}$ and the

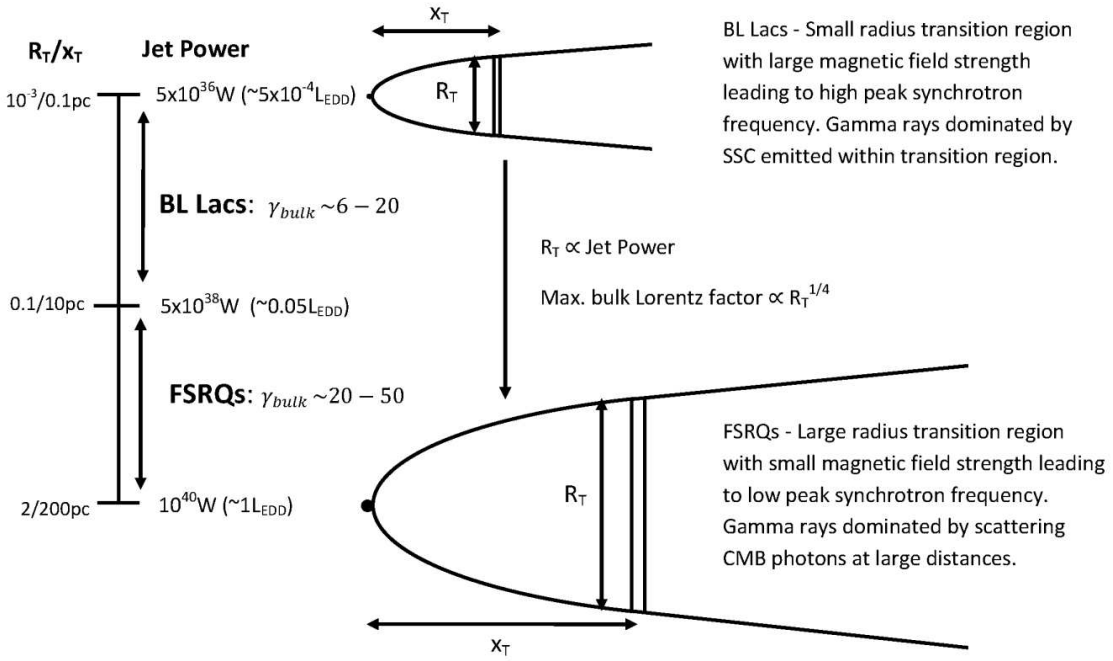


Figure 2.5: Schematic geometry of the Potter-Cotter model, with typical parameter values for BL Lacs and FSRQs. Figure from ref. [219].

magnetic field $B \simeq 0.01$–$0.1\,\mathrm{G}$ [201]. On the other hand, purely hadronic models typically require much higher magnetic fields ($B \simeq 10$–$100\,\mathrm{G}$) and Lorentz factors [203, 216]. Mixed lepto-hadronic models, where the high-energy emission is still mainly due to SSC with some contributions from proton synchrotron and photohadronic interactions, have been introduced to solve this discrepancy [201].

The main limitation of one-zone models lies in reproducing the radio component of SEDs. Synchrotron photons below a certain threshold can be re-absorbed by the electrons, thus making the emission region opaque to synchrotron radiation [200]. In order to correctly model radio emission, *two-zone* models can be employed, where the radio emission is assumed to come from a larger, less dense region optically thin to synchrotron photons. For example, spine-sheath models describe the jet as made up of an inner, faster flow surrounded by an external slower-moving layer, which is responsible for radio emission [217, 218].

A natural evolution of these models is represented by *multi-zone* or *inhomogeneous* models, where the entire jet structure is modeled as a more or less continuous series of interacting homogeneous zones within a given geometry. As a recent example, the purely leptonic Potter-Cotter model [220–223] considers a conical jet with a parabolic base, set by VLBI observations of M87 [224]. The radius R of the jet as a function of the jet length r is given by [221]

$$R(r) = \begin{cases} R_0 + A r^B & r \leq r_{\mathrm{con}}\,, \\ R_0 + A r_{\mathrm{con}}^B + (r - r_{\mathrm{con}}) \tan\left(\theta_{\mathrm{opening}}\right) & r > r_{\mathrm{con}}\,, \end{cases} \tag{2.11}$$

where r_{con} is the length at which the jet transitions from parabolic to conical and $\theta_{\mathrm{opening}}$ is the opening angle of the conical part (Figure 2.5). Both quantities refer to the lab frame.

The parabolic parameters R_0, A and B are fit to the M87 observation. The energy density in the region close to the black hole is assumed to be magnetically dominated, where the jet originates via the Blandford-Znajek process [200, 225] or similar mechanisms. The bulk Lorentz factor thus increases in the parabolic region as magnetic energy is converted to particle (electron) kinetic energy, accelerating the jet [226]. At equipartition between magnetic and particle energy, the jet becomes conical ($r = r_{\rm con}$) and begins to decelerate due to interaction with the surrounding environment. The evolution of the jet is modeled by applying relativistic energy-momentum conservation and considering the emission and absorption of synchrotron, SSC and EC radiation in each section. Target photons for EC scattering are those from the CMB, the accretion disk, starlight, BLR, NLR and dusty torus. The model includes radiative losses in the computation of electron energy, as well as adiabatic losses due to the jet's expansion. Finally, gamma-gamma absorption due to Breit-Wheeler scattering is also included [223].

In total, the Potter-Cotter model features 12 free parameters [221]. The jet has total power W_j, length L and opening angle $\theta_{\rm opening}$, and is observed at an angle relative to the line of sight $\theta_{\rm obs}$. The black hole mass is given by M, the accretion disk luminosity by $L_{\rm acc}$ and the outer radius of the dusty torus by $r_{\rm outer}$. The electron spectrum is assumed to follow a power law with spectral index α between energies $E_{\rm min}$ and $E_{\rm max}$. The jet is accelerated from an initial bulk Lorentz factor γ_0 to $\gamma_{\rm max}$ at the end of the parabolic section, and then decelerated down to $\gamma_{\rm min}$. Other dependent quantities such as the radius of the jet R_T or the magnetic field strength B_T at the transition region can be computed from the jet geometry and energetic considerations. The model has been successfully used to fit broadband quiescent SEDs of both FSRQs and BL Lacs [222, 223]. Most notably, parameters of the Potter-Cotter model have been reported in ref. [219] for a sample of 42 sources with simultaneous wavelength data [195], extracted from the list of sources detected by *Fermi*-LAT during the first three months of its operation [20, 227]. The differences in typical fit parameters for the two blazar classes are illustrated in FIGURE 2.5.

2.4 Variability

Blazar variability is typically observed across all wavelengths, both in flux and polarization [228, 229]. Variations in the spectral amplitude and index, which are often represented as hysteresis cycles in optical and X-ray observations, can be linked with the acceleration and cooling times of particles in the jets. The energy dependence of these processes causes measurable time delays between different wavebands as well [201, 229]. Hysteresis and multi-wavelength correlation with short time delays are a common prediction of time-dependent one-zone emission models, often confirmed by observations. There are however several cases of *orphan flares*, in which the expected multiwavelength correlation is not observed. One example is the VHE flare of FSRQ 3C 279 observed by H.E.S.S. in 2018, 11 days after the flare in the GeV band measured by *Fermi*-LAT [230, 231].

Extreme blazar variability over timescales of few minutes has been observed in VHE gamma rays, such as in the historical flares of Markarian 501 (Mrk 501) and PKS 2155−304, observed in 2005 and 2006 by MAGIC and H.E.S.S., respectively [232, 233]. By including the observed timescale $\Delta t'$ from EQ. 2.6 in the causality relation of EQ. 2.1, the constraint

$$R \lesssim c\Delta t' \frac{\delta}{1+z} \tag{2.12}$$

is obtained. It can be shown that, by assuming the emission region to be transparent to gamma rays, this relationship implies a lower limit on the Doppler factor δ [234] or on the bulk Lorentz factor [235]. In particular, the short variability scales observed in Mrk 501 and PKS 2155−304 would imply $\delta \gtrsim 50$, much higher than the typically inferred values $\delta \simeq 10$. A number of solutions have been proposed to this "bulk Lorentz factor crisis" [229, 236], such as two-zone models involving sub-jets or separate emitting blobs [237, 238]. In these models the zones may be interacting, so that e.g. photons produced in one zone can be EC scattered by electrons in the other.

The detection of periodic oscillations in the lightcurves of blazars may give hints on the presence of binary SMBH systems at their centers. As a notable case, a 12-year optical periodicity has been reported for blazar OJ 287 and interpreted as evidence for a SMBH binary [239, 240]. In the gamma rays, a 2.2-year periodicity was recently confirmed by *Fermi*-LAT observations of PG 1553+113 [241], while hints of 1.7-year quasi-periodic oscillations exist in both bands for PKS 2155−304 [242–245].

2.5 Gamma-ray observations

2.5.1 Present status

Despite being rare objects, due to their peculiar orientation, blazars make up the large majority of the detected extragalactic gamma-ray sources. Observation by *Fermi*-LAT have led to the compilation of several incremental AGN catalogs numbered from 1LAC to 4LAC-DR3 [246–251], derived from the corresponding gamma-ray source catalogs [21–26]. The 4LAC-DR3 catalog [251] reports a total of 3814 sources, among which 792 are associated with FSRQs, 1458 with BL Lacs and 1493 with blazars of uncertain type (BCUs), leaving only 71 non-blazar sources. FSRQs are mostly of the LSP class, with only 20 ISPs and 4 HSPs, while BL Lacs are more evenly distributed between the three classes.

This situation changes significantly in the VHE band. The *Fermi*-LAT catalogs of hard sources (1FHL to 3FHL [252–254]) are compiled in the energy range from 10 GeV to 2 TeV and mostly consist of extragalactic sources. The last version of the catalog reports 731 BL Lacs, 142 FSRQs and 290 BCUs, besides smaller numbers of non-blazar AGNs and galactic sources [254]. Sources detected by ground-based gamma-ray telescopes are listed in the online catalog TeVCat[2] [255], which at the time of writing features 68 BL Lacs (mostly HBLs) and only 11 FSRQs. The reason for this large observed abundance of BL Lacs in the VHE band can be explained by the fact that FSRQs feature an intrinsically weaker TeV emission, due both to being mostly LSP sources and to Breit-Wheeler scattering in the broad-line region, which is further dimmed down by EBL absorption.

EBL introduces an opacity of the Universe to gamma rays, parametrized by the optical depth $\tau(E; z)$, which increases both with energy and redshift [114]. The observation of blazars and any other extragalactic object is therefore limited by an energy-dependent "gamma-ray horizon", defined as the redshift z at which $\tau(E; z) = 1$ for a certain E [201]. The most distant blazar currently detected at in the VHE band is OP 313, at $z = 0.997$, whose emission above 100 GeV was discovered by LST-1 in 2023 [98, 99]. Gamma-ray observations of distant blazars can be used to perform cosmological measurements as

[2] https://tevcat2.tevcat.org/

well, such as providing estimates of the EBL spectrum or the Hubble constant [130, 256].

2.5.2 Observation prospects with CTAO

Blazars will be featured prominently in the foreseen scientific program of CTAO [124]. Representing the vast majority of extragalactic sources detected so far in the VHE gamma-ray band, blazars will be the most studied class in the AGN Key Science Project. CTAO will target a considerable number of these sources at various redshifts, sampled from different classes (LBL through UHBL and FSRQs, as well as some non-blazar AGNs), with the aim of providing high-quality spectra for population, classification and evolution studies. The total foreseen observation time, estimated by requiring that each source is detected at a 20σ significance above 60 GeV, will be split between 343 h for the Northern Array and 283 h for the Southern Array. From this relatively large source sample, a smaller selection will be chosen for long-term monitoring observations, with the aim of providing VHE lightcurves and time-resolved spectra. About 0.5 h per week per target will be spent on this project, totaling 132 h for the Northern Array and 48 h for the Southern Array per year. Finally, an AGN flare program will be set in place to trigger observations of blazars and other kinds of AGNs in the event of flaring episodes. While CTAO will have the capacity to self-trigger if a flare is detected during some other ongoing observation, it will also follow up upon external target of opportunity (ToO) alerts associated with multi-wavelength of multi-messenger triggers, such as GCN notices from *Fermi* or IceCube. This kind of coordination between different experiments and observatories will indeed be a key point for blazar observations with CTAO, and is among the improvement goals foreseen by the CTA+ project [122].

In addition to this project, the related Extragalactic Survey KSP will be dedicated to performing an unbiased scan of about 25% of the sky at high galactic latitudes. About 1000 h split between the two Arrays will be employed for this project, with the aim of revealing VHE emission from currently undetected sources. While these are mostly expected to include blazars, other extragalactic objects such as radio galaxies, starburst galaxies, GRBs and dark matter clumps might be detected within this KSP.

The expected scientific results of projects discussed above include understanding the mechanisms behind VHE emission, constraining relativistic jet modelling and studying the causes of variability at different time scales, from years down to minutes. The role of blazars as sites of UHE cosmic-ray accelerators will also be probed, as well as their gamma-ray luminosity function (given by the number density of blazars as a function of their flux). Finally, studies of different aspects of cosmology and fundamental physics will benefit from these observations as well (see Section 1.4.3). The final data products will be disseminated in the form of comprehensive VHE catalogs of extragalactic sources, including information on integral fluxes, spectra, and variability.

2.6 Exploring the VHE spectral shape of FSRQs with CTAO

2.6.1 Motivation and source selection

As mentioned in the previous Section, the majority of blazars detected in the VHE range belong to the BL Lac class. It is thus interesting to study how future instruments such

Source	z	R.A. [deg]	Dec [deg]	Hemisphere	Period [MJD]	LC binning [days]	Refs.
PKS 0736+01	0.19	114.82	1.61	North	56658 – 59215	7	[260, 261]
PKS 1222+216	0.43	186.23	21.38	North	54682 – 57082	3	[262, 263]
Ton 599	0.72	179.88	29.25	North	59137 – 60676	7	[264, 265]
OP 313	0.99	197.62	32.35	North	59580 – 60765	3	[98, 266]
PKS 1502+106	1.84	226.10	10.49	North	56658 – 58270	3	[267]
PKS 1510−089	0.36	228.21	−9.10	South	54682 – 57754	3	[268, 269]
3C 279	0.54	194.05	−5.79	South	56293 – 58849	7	[270, 271]
PKS 0346−27	0.99	57.16	−27.82	South	57754 – 59945	3	[272]

Table 2.1: List of sources selected to investigate CTAO's capability of detecting FSRQs and discriminating their gamma-ray spectral shape. For each source the redshift parameter, celestial coordinates, hemisphere from which we assume the source to be observed, analyzed *Fermi*-LAT time period, lightcurve binning and example references to past flares observed in the HE and VHE bands are given.

as CTAO will change the detection prospects of FSRQs and the present understanding of their VHE spectral shapes.

In models of leptonic acceleration, the SED of VHE gamma rays is linked to the electrons' Lorentz factor distribution, which in turn depends on the underlying acceleration mechanism [257]. First-order Fermi acceleration in the Thomson scattering regime [6] would give rise to an ECPL electron spectrum, and an equally shaped gamma-ray SED (eq. 1.9). In the case of different physical processes dominating in different energy ranges, the electron spectrum and the corresponding gamma-ray spectrum will generally follow a broken power law shape (eq. 1.8) [257]. More complex stochastic acceleration models predict log-parabolic spectra (LP, eq. 1.10), possibly featuring a simple power-law behaviour at low energies (PL-LP) [258, 259].

To assess CTAO's capability of detecting FSRQs, precisely determining their spectral parameters, and distinguishing between the different scenarios outlined above, we consider a sample of eight sources, listed in Table 2.1.[3] Each source was selected based on least one flare detection by *Fermi*-LAT and by a ground-based VHE telescope, reported in an Astronomer's Telegram (ATel) or similar publications [98, 260–272]. The source PKS 1502+106 represents an exception to this criterion, as it was never detected by a VHE instrument. It was however among the potentially detectable sources simulated during the CTAO Internal Science Data Challenge in 2024, and we decided to include it as an example of a blazar located at a comparatively very high redshift.

2.6.2 *Fermi*-LAT data analysis

We identified periods with high flaring activity in *Fermi*-LAT data for each source, reported in Table 2.1, using the publicly available *Fermi*-LAT Light Curve Repository.[4] The standard analysis on the corresponding *Fermi*-LAT Pass 8 data was performed using the FermiTools v2.2[5] and the `fermipy` v1.1 Python package[6] [273]. We used the `P8R3_SOURCE_V3`

[3]The results presented in this Section contain contributions by C. Bartolini and will be the subject of a future publication, currently in preparation within the CTAO Consortium.

[4]https://fermi.gsfc.nasa.gov/ssc/data/access/lat/LightCurveRepository/

[5]https://fermi.gsfc.nasa.gov/ssc/data/analysis/software/

[6]https://github.com/fermiPy/fermipy

IRFs, the 4FGL-DR4 catalog [26, 27], and the Galactic and isotropic diffuse gamma-ray emission models provided by standard templates.[7] The events were analyzed with reconstructed energy between 100 MeV and 500 GeV, selecting a region of interest (ROI) of $15 \times 15\,\mathrm{deg}^2$ centered on the source position and applying a standard quality cut (`DATA_QUAL>0 && LAT_CONFIG==1`). Furthermore, a zenith angle cut of 90 deg was used to reduce the contamination from the Earth limb. Following ref. [274], the data were organized in lightcurves, choosing either a 3-day or 7-day binning to minimize the number of temporal bins with no detection. The flux points in the lightcurves were grouped using the Bayesian blocks (BB) algorithm [275] as implemented in the Astropy Python package [276–278]. The algorithm identifies statistically significant temporal variations in a time series, by partitioning it into intervals (blocks) separated by change points. It can be applied to different data types, such as binned or unbinned times of discrete events (e.g. detector counts) or measurements of continuous quantities with associated Gaussian errors. In the Astropy implementation these are denoted as `events`, `regular_events` and `measures`, respectively.[8] In the first two applications, the segmentation is chosen so that the event rate in each block is consistent with a constant value. The latter version of the algorithm is the one of interest for the present case, as it allows intervals of approximately steady flux in the lightcurves to be identified. The optimal segmentation is found by maximizing a *fitness* function, corresponding to a block-wise log-likelihood balanced by a penalty term on the overall number of blocks.

After partitioning a lightcurve into BBs, the quiescent flux ϕ_q of the source can be estimated as the lowest mean flux in any of the blocks, under the condition that the number of data points in such a block is at least equal to half of the average number of data points in all other blocks [279]. Given the average uncertainty $\langle \phi_{\mathrm{err}} \rangle$ on the flux in the BBs, flares can be defined as groups of points in the lightcurve with fluxes higher than a threshold value

$$\phi_{\mathrm{th}} = \phi_q + s\langle \phi_{\mathrm{err}} \rangle \,, \tag{2.13}$$

where s corresponds to the minimum number of standard deviations above the quiescent level required to identify a flare [279]. For each flare, we then identified a rising and a decaying phase by using the Eisenstein-Hut HOP algorithm [280, 281], following the implementation given in ref. [282].[9] The algorithm identifies the peak time of each flare t_{peak} as a local maximum in the lightcurve. A "HOP group" is then defined by iteratively adding adjacent points in both directions until their flux values drop below ϕ_{th}, which in our case is computed with $s = 5$. This condition determines the start time t_{start} and the end time t_{end} of each flare. This procedure is referred to as the *baseline* method in ref. [282].

We selected the brightest flare for each source, defined as the flare with the highest flux at t_{peak} (Table 2.2). For each of these, we identified a *rising* phase between times t_{start} and t_{peak} and a *decaying* phase between times t_{peak} and t_{end}. The data from the rising and decaying phase of selected flares were then used to initialize a `MapDataset` object in Gammapy v1.3 [283], following the approach presented in ref. [172].[10] This makes it possible to bundle the *Fermi*-LAT event data in a single object with the instrument response (energy dispersion, exposure, PSF) and with the background and source models, accord-

[7] https://fermi.gsfc.nasa.gov/ssc/data/access/lat/BackgroundModels.html
[8] https://docs.astropy.org/en/stable/api/astropy.stats.bayesian_blocks.html
[9] https://github.com/swagner-astro/lightcurves
[10] https://github.com/mireianievas/gammapy_mwl_workflow

Source	Peak flux [$\mathrm{cm^{-2}\,s^{-1}}$]	t_{start} [MJD]	t_{peak} [MJD]	t_{end} [MJD]
PKS 0736+01	2.10×10^{-6}	58619.5	58623.0	58640.6
PKS 1222+216	8.19×10^{-6}	55271.2	55365.8	55595.5
Ton 599	3.10×10^{-6}	59910.0	59955.7	60043.5
OP 313	1.97×10^{-6}	60333.0	60369.0	60387.0
PKS 1502+106	1.28×10^{-6}	57165.3	57211.8	57498.5
PKS 1510−089	9.19×10^{-6}	55843.0	55853.5	55888.0
3C 279	1.18×10^{-5}	58078.7	58138.2	58295.8
PKS 0346−27	2.12×10^{-6}	58463.8	58622.9	58756.5

Table 2.2: Peak flux, start time, peak time, and end time of the most intense flare of each considered FSRQ.

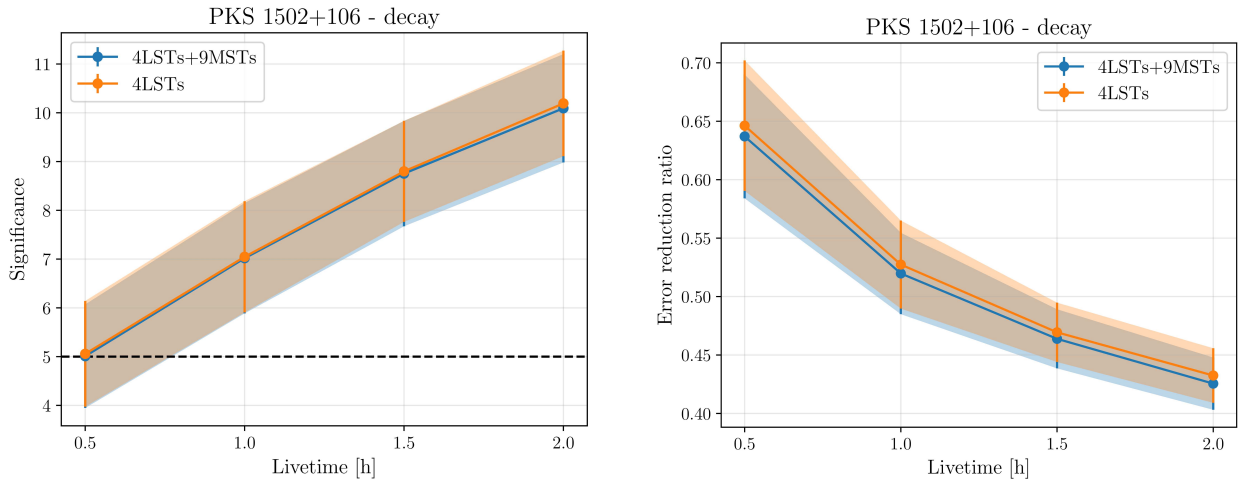
ing to GADF specifications, in order to easily analyze them jointly with simulated CTAO data. A reference ECPL model was initially fit to all datasets, taking into account EBL absorption using the model from ref. [145]. The complete *Fermi*-LAT lightcurves for each source and the spectral parameters obtained for each selected flaring state are reported in Appendix B.

2.6.3 Comparison of CTAO configurations

By extrapolating the spectral model defined above to higher energies, we used Gammapy to simulate ON-OFF observations of each flaring state with CTAO in wobble mode. We used an ON region radius of 0.11 deg and an offset of 0.5 deg. We considered a reconstructed energy axis of 15 bins from 30 GeV to 10 TeV. We repeated the procedure and compared results for sets of IRFs corresponding to different CTAO configurations. For the sources in the Northern hemispheres, we employed prod5 IRFs [120] based on the Alpha configuration, including either 4 LSTs or 4 LSTs and 9 MSTs and optimized for 0.5 h observations. For Southern sources, we used a modified version of the prod3b IRFs [123] including either 14 MSTs, 14 MSTs and 11 SCTs or 25 MSTs, only available for 50 h observations. The observation livetime of Northern sources was increased from 0.5 h up to a maximum of 2 h, to verify whether each source can be realistically detected soon after the trigger is received. For Southern sources, in case a 5σ detection was not obtained within the first 2 h, the livetime was increased up to a maximum of 5 h. The simulated data were obtained by applying Poissonian fluctuations around the expected photon counts, determined by the chosen flux model, IRFs and livetime (see Appendix A), while leaving all other observational conditions unchanged. The aim of this Section is to evaluate whether different CTAO configurations can provide a substantial difference in detection significance of the sources for the same amount of observation time. Furthermore, we wish to investigate the capability of these observations to reduce uncertainty on spectral parameters compared to that obtained from *Fermi*-LAT data only.

For almost all considered Northern sources, we find that the selected flaring states could be detected at a Li-Ma significance above 5σ within the first 0.5 h of observation, both with LSTs and MSTs and with LSTs only. The difference in results between the two configurations is generally negligible (see e.g. Figure 2.6a), suggesting that the contribution of MSTs in these observations will be marginal.

In estimating the improvement in the determination of spectral parameters, we choose



(A) (B)

Figure 2.6: Li-Ma significance (A) and error reduction ratio (B) as functions of the observation livetime, computed for the decaying flare of PKS 1502+106, comparing CTAO Northern Array configurations including 4 LSTs and 4 LSTs and 9 MSTs. The plotted values are the results of averaging 100 simulations for each point, with error bars representing one standard deviation from the mean value.

to focus on the spectral cutoff energy, as the precise measurement of this quantity is often interesting in FSRQ studies. To do so, we re-fit the ECPL model to the joint *Fermi*-LAT and CTAO dataset. The joint likelihood for *Fermi*-LAT and simulated CTAO data is defined as

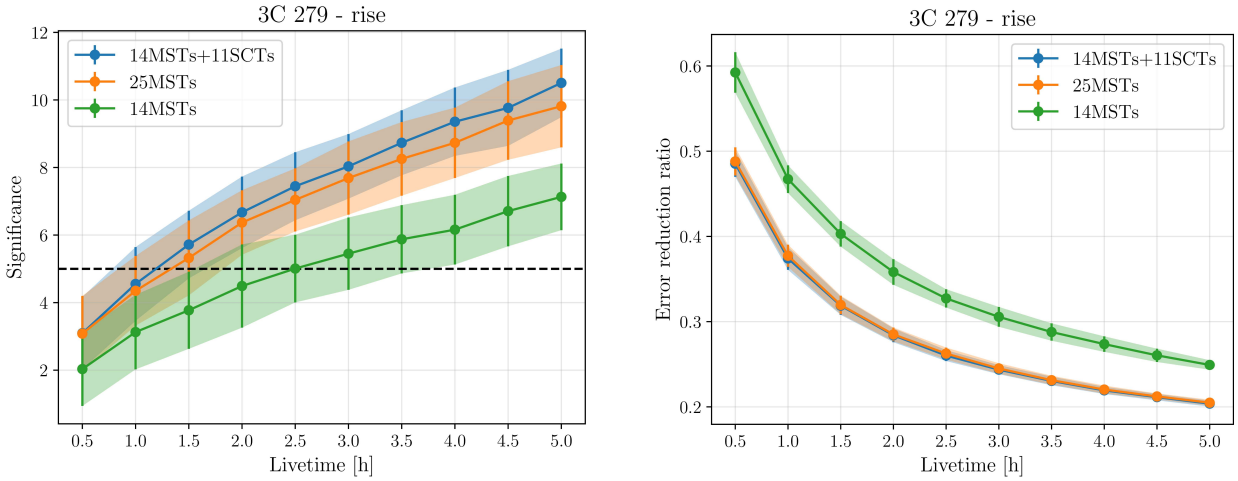
$$\mathcal{L}(\boldsymbol{m}, \boldsymbol{\mu}, \boldsymbol{b} | N, N_{\text{on}}, N_{\text{off}}) = \mathcal{L}_{\text{Fermi}}(\boldsymbol{m}|N) \times \mathcal{L}_{\text{CTAO}}(\boldsymbol{\mu}, \boldsymbol{b}|N_{\text{on}}, N_{\text{off}}) \,, \tag{2.14}$$

where the first term is given by EQ. A.11 and the second by EQ. A.6 (see APPENDIX A for definitions and notation). Maximizing this joint likelihood is equivalent to minimizing the sum of the Cash statistic (EQ. A.12) for *Fermi*-LAT data with N observed counts and the WSTAT (EQ. 1.11) for the CTAO simulated data with N_{on} and N_{off} counts. The maximum-likelihood estimator of the expected counts in the *Fermi*-LAT dataset is given by $\hat{\boldsymbol{m}}$, while those of the signal and background counts in the simulated CTAO datasets are given by $\hat{\boldsymbol{\mu}}$ and $\hat{\boldsymbol{b}}$.

We then compare the uncertainty on the spectral cutoff energy from an ECPL model fit to *Fermi*-LAT data only, $\Delta E_{\text{cut,Fermi}}$, to that obtained from a joint fit to *Fermi*-LAT and simulated CTAO data, $\Delta E_{\text{cut,Fermi+CTAO}}$. We define the error reduction ratio

$$r = \frac{\Delta E_{\text{cut,Fermi+CTAO}}}{\Delta E_{\text{cut,Fermi}}} \tag{2.15}$$

which can take values from 70% for 0.5 h down to 5% for 2 h observation time, indicating the ability of CTAO observations to help constrain this parameter. In all cases, we find no particular difference between results computed for CTAO configurations including 4 LSTs or 4 LSTs and 9 MSTs (e.g. FIGURE 2.6B), again suggesting that pointing MSTs at FSRQs in the CTAO Northern Array is not going to significantly improve the performance compared to LST-only observations. This result is explained by the fact that FSRQs generally feature soft spectra extending to relatively low energies. On the other hand, we have checked that



(A) (B)

Figure 2.7: Same as Figure 2.6 for the rising flare of 3C 279, comparing results for the CTAO Southern Array configurations including 14 MSTs, 14 MSTs and 11 SCTs, and 25 MSTs.

MSTs considerably contribute to both detection significance and error reduction on the spectral cutoff energy for BL Lac objects such as Mrk 421.

By repeating the simulations for FSRQs in the Southern hemispheres (e.g. Figure 2.7), we find that in general a longer time is required to reach a 5σ detection significance, due to the lower sensitivity at sub-TeV energies. While increasing the telescope multiplicity from 14 to 25 generally improves performance, no significant difference is found by employing 14 MSTs and 11 SCTs rather than 25 MSTs. The complete results for both sets of sources are reported in the form of tables in Appendix B.

2.6.4 Spectral discrimination

After selecting the optimal configurations for this scientific case in each array (4 LSTs in the North, 14 MSTs and 11 SCTs in the South), we consider how joint CTAO and *Fermi*-LAT can be used to distinguish between spectral shapes. As mentioned in Section 2.6.1, this discrimination would help identify the particle acceleration process underlying gamma-ray emission. In this case, we fit the *Fermi*-LAT data for each source to the model reported in the 4FGL-DR4 source catalog [27], which is a log-parabola for almost all considered sources. An exception is represented by 3C 279, which features instead a power law spectrum with super-exponential cutoff (SECPL) defined as in ref. [26]. We have checked that these models can fit reasonably well the considered datasets in the *Fermi*-LAT energy range.

We simulated more observations with CTAO by extending these models to VHE, using the configurations selected in the previous Section. The livetime was varied between 2 h and 10 h, which is a realistic observation duration for a detailed spectral study; for Northern sources, we employed IRFs optimized for either 0.5 h or 5 h depending on whichever value was closest to the simulated livetime. In the case of a real observation, however, the "true" source model would not be known. One would then select various models based on different physical assumptions and use statistical techniques to determine the model that

best describes the data. For observations simulated using a log-parabola spectral model, we choose an ECPL and broken power law as alternative models; for the case of 3C 279 we consider a log-parabola instead of an ECPL. We do not consider here the PL-LP model, as we checked that this spectral shape would be virtually indistinguishable from a simple log-parabola at VHE.

For each simulated observation, we fit the joint *Fermi*-LAT and CTAO datasets to the catalog model and to each of the alternative models. To assess how these joint observations might be used to distinguish between the different proposed models, we compute the corrected Akaike information criterion ($\mathrm{AIC_c}$) as [284, 285]

$$\mathrm{AIC_c} = 2(k - \ln \mathcal{L}) + \frac{2k(k+1)}{n-k-1}\,, \tag{2.16}$$

where $\mathcal{L}$ is the maximum likelihood given by EQ. 2.14, k is the number of free model parameters and n is the number of reconstructed energy bins over which the fit is performed. The model that yields the smallest value of $\mathrm{AIC_c}$ is selected as the one favored by the data; the presence of terms proportional to k adds a natural penalty for more complex models. In order to compare different models, which do not need to be nested, the difference

$$\Delta\mathrm{AIC}_i = \mathrm{AIC}_i - \mathrm{AIC}_{\mathrm{min}} \tag{2.17}$$

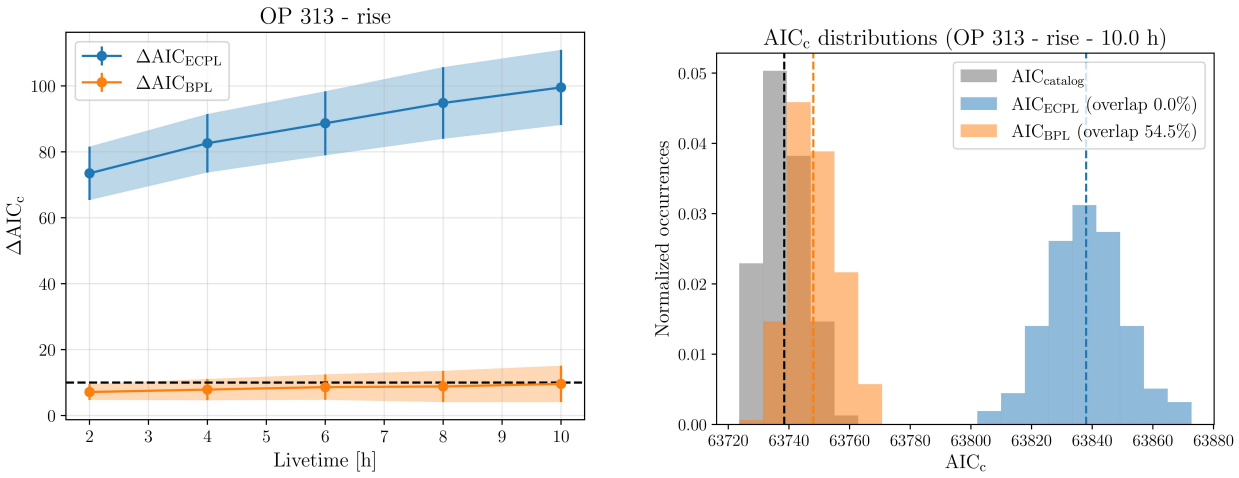
can be computed, where AIC_i is the $\mathrm{AIC_c}$ value computed using EQ. 2.16 for a generic model i and $\mathrm{AIC}_{\mathrm{min}}$ is the minimum $\mathrm{AIC_c}$ value over all tested models. In general, the relative likelihood of a model i with respect to the one that minimizes $\mathrm{AIC_c}$ can be expressed as $\exp(-\Delta\mathrm{AIC}_i/2)$ [285]. A typical requirement to exclude model i in favor of the one with minimum $\mathrm{AIC_c}$ is that $\Delta\mathrm{AIC}_i \gtrsim 10$, corresponding to a relative likelihood of less than $\sim 1/150$.

In this setting, we consider the $\mathrm{AIC_c}$ difference between each alternative model and the catalog model given by

$$\Delta\mathrm{AIC}_{\mathrm{alt}} = \mathrm{AIC}_{\mathrm{alt}} - \mathrm{AIC}_{\mathrm{cat}}\,, \tag{2.18}$$

where $\mathrm{AIC}_{\mathrm{alt}}$ and $\mathrm{AIC}_{\mathrm{cat}}$ are the $\mathrm{AIC_c}$ values corresponding to the alternative and catalog models, respectively. A value $\Delta\mathrm{AIC}_{\mathrm{alt}} > 10$ indicates that a combined *Fermi*-LAT and CTAO observation can confidently exclude the alternative model in favor of the catalog model, thus correctly identifying the model used to simulate the data. If $0 < \Delta\mathrm{AIC}_{\mathrm{alt}} < 10$, the catalog model is still favored by the data but the alternative model cannot be rejected. Conversely, if $\Delta\mathrm{AIC}_{\mathrm{alt}} < 0$, the alternative model is favored instead of the catalog model, with relative likelihood given by $\exp(-|\Delta\mathrm{AIC}_{\mathrm{alt}}|/2)$.

As an example of our results, FIGURE 2.8A displays the evolution of the $\Delta\mathrm{AIC_c}$ with the observation livetime for the rising flare of OP 313. The CTAO data were simulated assuming a log-parabola spectral model, which was tested against ECPL and BPL spectral models. It can easily be seen from the plotted $\mathrm{AIC_c}$ values, averaged over 200 simulations for each point, that for this particular case the ECPL model can be confidently disentangled from the log-parabola. The average $\Delta\mathrm{AIC_c}$ value for the BPL model, on the other hand, barely reaches 10 after a 10 h observations, making it harder to distinguish the two models. This is also reflected by the $\mathrm{AIC_c}$ distributions shown in FIGURE 2.8B, which illustrates how the $\mathrm{AIC_c}$ values corresponding to the ECPL model are systematically higher



(A) (B)

Figure 2.8: (A) ΔAIC_c values for the alternative models compared to the catalog model (log-parabola) as a function of time, computed for the rising flare of OP 313. The plotted values are the results of averaging 200 simulations for each point, with error bars representing one standard deviation from the mean value. (B) AIC_c distributions for each tested spectral model, displaying the overlap of the distributions corresponding to each alternative model with the catalog one. The vertical dashed lines indicate the mean of each distribution.

than those computed for the catalog model, while there is significant overlap between the catalog and BPL models. This result in general holds true for all tested sources, where the ECPL model (or SECPL in the case of 3C 279) almost always displays large ΔAIC_c values relative to the LP model, with small or vanishing overlap between the two AIC_c distributions. A comparison between LP and BPL spectra on the other hand gives less decisive results, with ΔAIC_c only barely reaching the threshold of 10 after 10 h of observations for most sources. In a few cases, ΔAIC_c values less than or compatible with 0 are obtained, indicating that one or both alternative models fits the data as well or better than the model used to simulate them. This typically corresponds to soft or dim spectra, which likely contribute less to CTAO observation, so that the fit essentially depends on the *Fermi*-LAT data. A negative or null ΔAIC_c then simply indicates that the alternative model fits the *Fermi*-LAT data better or as well as the catalog model shape, while additional CTAO data at VHE would not contribute to this discrimination. Tables with ΔAIC_c values computed at 10 h for both sets of sources are given in Appendix B.

CHAPTER 3

Axion-like particles

3.1 The QCD axion and axion-like particles

The original axion model was introduced as a solution to the strong $\mathcal{CP}$ problem arising in quantum chromodynamics (QCD). This problem is essentially related to the invariance of the Lagrangian operators representing fundamental interactions in the quantum field theory of the Standard Model (SM) of particle physics. While all interactions should be invariant under the simultaneous operations of charge conjugation $\mathcal{C}$, parity $\mathcal{P}$ and time reversal $\mathcal{T}$ ($\mathcal{CPT}$ theorem [286]), some interactions can "violate" symmetry under separate applications of these transformations. The best-known case is that of weak interactions, which violate both $\mathcal{P}$ [287, 288] and $\mathcal{CP}$ [289] symmetries. A $\mathcal{CP}$-violating term is also present in the QCD Lagrangian,

$$\mathcal{L}_{\rm QCD} \subset \theta \frac{g_s^2}{32\pi} G^{a\mu\nu} \tilde{G}^a_{\mu\nu} \,, \tag{3.1}$$

where g_s is the strong gauge coupling, $G^{a\mu\nu}$ is the gluon field strength tensor, $\tilde{G}^a_{\mu\nu} = (1/2)\epsilon_{\alpha\beta\mu\nu} G^{a\alpha\beta}$ is its dual, and θ is a pure number. [1] It can be shown that this term gives rise to an electric dipole moment for the neutron [290]

$$d_n \simeq 1.2 \times 10^{-16}\, \theta\, e \cdot \text{ cm} \,, \tag{3.2}$$

where e is the electron charge. This quantity is however experimentally constrained to be $d_n \lesssim 1.8 \times 10^{-26}\, e \cdot$ cm [291], which implies the extremely tight bound $\theta \lesssim 10^{-10}$. The strong $\mathcal{CP}$ problem is that of why (or how) the θ parameter should be tuned to such a small value. In order to avoid this inconvenience, Peccei and Quinn suggested to promote θ to a dynamical field, which would naturally relax to zero via a spontaneous symmetry breaking mechanism [292]. Weinberg [293] and Wilczek [294] later defined the *axion* (denoted with a) as the pseudo-Nambu-Goldstone boson arising from the Peccei-Quinn (PQ) symmetry breaking. These original axions were predicted to have a mass $m_a \simeq$ 100 keV–1 MeV and were soon ruled out experimentally [295]. In these early models, the axion mass and its coupling to mesons were taken to be proportional to the square root of the Fermi coupling $1/f_a \simeq G_F^{1/2} \simeq 3.4 \times 10^{-3}$ GeV^{-1}, where f_a is the energy scale at which

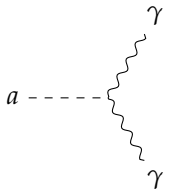
[1] All equations in this Chapter are expressed in natural units, with $c = \hbar = 1$.

the PQ symmetry breaks down. By increasing this energy to higher values, however, the axion mass and couplings could be made almost arbitrarily small, such as in the KSVZ [296, 297], DFSZ [298, 299], and other models [300]. The resulting "invisible axions" could thus still be defined as a viable solution to the strong $\mathcal{CP}$ problem, while escaping experimental constraints thanks to their extremely weak couplings to SM particles.

In these generalized models, the axion mass is given by

$$m_{a,\mathrm{QCD}} \simeq 5.7 \left(\frac{10^{12}\,\mathrm{GeV}}{f_a} \right) \mu\mathrm{eV}\,, \tag{3.3}$$

as obtained from detailed QCD calculations [301]. A common feature of QCD axion models is their effective coupling to nucleons and photons. In particular, the effective coupling to photons may be represented by the Feynman diagram



and its strength is regulated by a coupling constant given by [301]

$$g_{a\gamma,\mathrm{QCD}} = \frac{\alpha}{2\pi} \frac{C_{a\gamma}}{f_a} \simeq 2.0 \times 10^{-16} C_{a\gamma} \left(\frac{m_{a,\mathrm{QCD}}}{1\,\mu\mathrm{eV}} \right) \mathrm{GeV}^{-1}\,, \tag{3.4}$$

where $C_{a\gamma}$ is a model-dependent $\mathcal{O}(1)$ constant. For QCD axions, the axion mass m_a is thus proportional to axion-photon coupling constant $g_{a\gamma}$.

As will be discussed below, this coupling is widely exploited in experimental searches for axions. Most of these searches, however, do not rely on any particular relationship between m_a and $g_{a\gamma}$ and can thus be extended to *any* light spinless boson with a two-photon coupling [302]. This leads to the definition of *axion-like particles* (ALPs), featuring a similar phenomenology to the QCD axion but unrelated to the solution of the strong $\mathcal{CP}$ problem. As a relevant example, string theory predicts a spectrum of ALPs over a wide mass range, sometimes called an *axiverse* [303, 304]. ALPs represent an example of weakly interacting slim particles (WISPs) [305], and are often quoted along with WIMPs as well-motivated dark matter candidates [306]. The current experimental constraints on the ALP parameter space spanned by m_a and $g_{a\gamma}$ are summarized in FIGURE 3.1.

3.2 Propagation in constant magnetic fields

3.2.1 ALP-photon oscillations

The effective Lagrangian of a photon-ALP system contains a term of the form

$$\mathcal{L}_{a\gamma} \subset \frac{g_{a\gamma}}{4} F_{\mu\nu} \tilde{F}^{\mu\nu} a = g_{a\gamma} \mathbf{B} \cdot \mathbf{E}\, a\,, \tag{3.5}$$

where $F_{\mu\nu}$ is the electromagnetic field strength tensor and $\tilde{F}^{\mu\nu}$ is its dual [308]. From the complete expressions of these tensors (e.g. [309]) it can easily be seen that their product

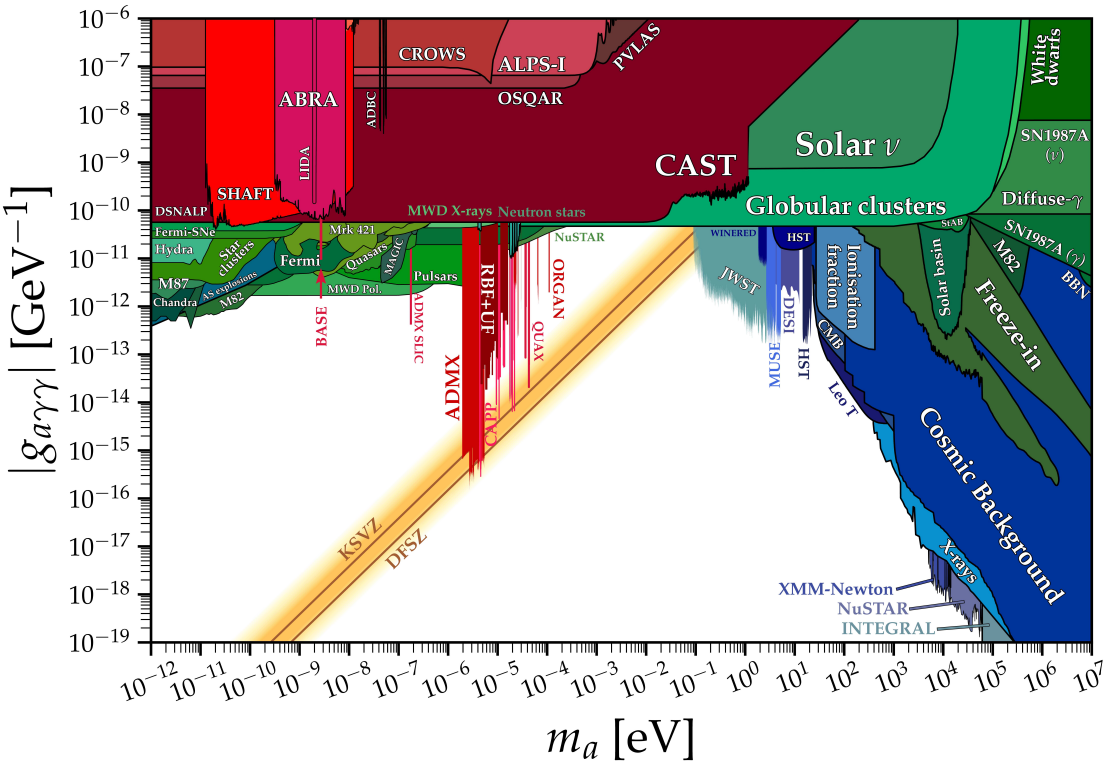
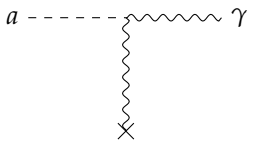


Figure 3.1: Present experimental constraints on the ALP parameter space spanned by m_a and $g_{a\gamma}$, obtained from astrophysical observations (green), cosmological probes (blue) and direct detection experiments (red). The yellow diagonal lines highlight the relationship between the two parameters in QCD axion models (eq. 3.4), such as KSVZ and DFSZ. Figure from ref. [307].

amounts to the scalar product between the electric and magnetic field vectors **E** and **B**. This allows for the mixing of ALPs and photons in the presence of external magnetic fields, represented by the diagram



where $\times$ represents the magnetic field source.

The ALP-photon system can be represented by a three-dimensional quantum state

$$\Psi(x) = \begin{pmatrix} A_\perp(x) \\ A_\parallel(x) \\ a(x) \end{pmatrix} \tag{3.6}$$

where $A_\perp$ and $A_\parallel$ represent the components of the photon vector potential field perpendicular and parallel, respectively, to the external magnetic field transversal to the propagation direction B_T (Figure 3.2). The stationary equation of motion for this system can be written in linearized form as [308]

$$(\omega - i\partial_x + \mathcal{M}_0)\Psi(x) = 0\,, \tag{3.7}$$

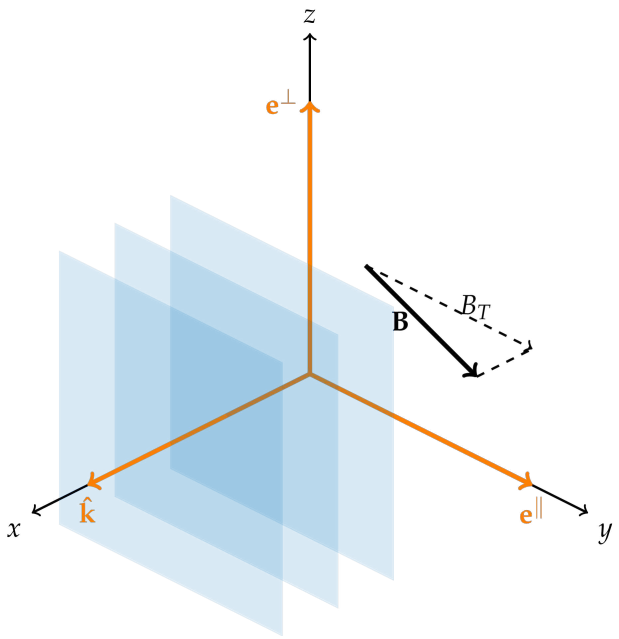


Figure 3.2: Reference frame for ALP-photon mixing, showing the polarization vectors of the electromagnetic field $\mathbf{e}^{\perp}$ and $\mathbf{e}^{\parallel}$, as well as the propagation direction $\hat{\mathbf{k}}$. Also shown are plane wavefronts propagating along the x axis and the external magnetic field $\mathbf{B}$, with its transverse projection B_T.

where $\omega = E/\hbar$ is the photon frequency, E being its energy, ∂_x is the derivative along the propagation direction, and

$$\mathcal{M}_0 = \begin{pmatrix} \Delta_\perp & 0 & 0 \\ 0 & \Delta_\parallel & \Delta_{a\gamma} \\ 0 & \Delta_{a\gamma} & \Delta_a \end{pmatrix} . \tag{3.8}$$

It can be seen that eq. 3.7 is formally similar to Schrödinger's equation, with $\mathcal{M}_0$ playing the role of the Hamiltonian matrix. The Δ symbols are defined as

$$\Delta_{\perp,\parallel} = \omega(n_{\perp,\parallel} - 1) = \Delta_{\mathrm{QED}\perp,\parallel} + \Delta_{\mathrm{pl}} + \Delta_{\mathrm{CMB}} , \tag{3.9}$$

$$\Delta_a = -\frac{m_a^2}{2\omega} = -7.8 \times 10^{-2} \left(\frac{m_a}{1\,\mathrm{neV}}\right)^2 \left(\frac{1\,\mathrm{GeV}}{E}\right) \mathrm{kpc}^{-1} , \tag{3.10}$$

$$\Delta_{a\gamma} = \frac{g_{a\gamma} B_T}{2} = 1.52 \times 10^{-2} \left(\frac{g_{a\gamma}}{10^{-11}\,\mathrm{GeV}^{-1}}\right) \left(\frac{B_T}{1\,\mu\mathrm{G}}\right) \mathrm{kpc}^{-1} , \tag{3.11}$$

where B_T is the transverse magnetic field intensity, here assumed constant, and $n_\perp$ and $n_\parallel$ are the refraction indices for the two polarization states. Higher-order photon-photon interactions in the Euler-Heisenberg effective Lagrangian [310]

$$\mathcal{L}_{\mathrm{EH}} = -\frac{1}{4} F_{\mu\nu} F^{\mu\nu} + \frac{\alpha^2}{90 m_e^4} \left[(F_{\mu\nu} F^{\mu\nu})^2 + \frac{7}{4} (F_{\mu\nu} \tilde{F}^{\mu\nu})^2 \right] \tag{3.12}$$

introduce polarization-dependent dispersion effects (vacuum birefringence) given by

$$\Delta_{\mathrm{QED}\perp} = 2\Delta_{\mathrm{QED}}\,, \quad \Delta_{\mathrm{QED}\parallel} = \frac{7}{2}\Delta_{\mathrm{QED}}\,, \tag{3.13}$$

$$\Delta_{\mathrm{QED}} = \frac{\alpha}{45\pi}\left(\frac{B_T e}{m_e^2}\right)^2 \omega = 4.14\times10^{-9}\left(\frac{B_T}{1\,\mu\mathrm{G}}\right)^2\left(\frac{E}{1\,\mathrm{GeV}}\right)\mathrm{kpc}^{-1}\,, \tag{3.14}$$

where e and m_e are the electron charge and mass [308, 311]. The analogous effect of magnetically-induced birefringence in a medium (Cotton-Moutton effect [312]), is usually considered negligible in astrophysical contexts [313]. The photon dispersion effect produced by a ionized plasma is parametrized by

$$\Delta_{\mathrm{pl}} = -\frac{\omega_{\mathrm{pl}}^2}{2\omega} = -1.06\times10^{-4}\left(\frac{n_e}{1\,\mathrm{cm}^{-3}}\right)\left(\frac{1\,\mathrm{GeV}}{E}\right)\mathrm{kpc}^{-1}\,, \tag{3.15}$$

where ω_{pl} is the plasma frequency

$$\omega_{\mathrm{pl}} = \sqrt{4\pi\alpha\frac{n_e}{m_e}} \tag{3.16}$$

and n_e is the volume density of free electrons in the medium (e.g. [313]). Finally, an important effect on cosmological propagation is given by the CMB, contributing to photon dispersion with a term [314]

$$\Delta_{\mathrm{CMB}} = \frac{44\alpha^2}{135}\frac{\rho_{\mathrm{CMB}}}{m_e^4}\omega = 8.08\times10^{-8}\left(\frac{E}{1\,\mathrm{GeV}}\right)\mathrm{kpc}^{-1}\,, \tag{3.17}$$

where $\rho_{\mathrm{CMB}} = 0.261\,\mathrm{eV\,cm}^{-3}$ is the present-day CMB energy density.

It can be seen from the mixing matrix in EQ. 3.8 that only the $A_\parallel$ photon state mixes with the ALP state a. The equation of motion is thus simplified as that of a 2-dimensional system

$$[\omega - i\partial_x + \mathcal{M}]\psi(x) = 0\,, \tag{3.18}$$

where

$$\mathcal{M} = \begin{pmatrix}\Delta_\parallel & \Delta_{a\gamma}\\ \Delta_{a\gamma} & \Delta_a\end{pmatrix}\,, \quad \psi(x) = \begin{pmatrix}A_\parallel(x)\\ a(x)\end{pmatrix}\,. \tag{3.19}$$

In order to easily solve this system with an analogous treatment to neutrino oscillations [315], the matrix $\mathcal{M}$ can be diagonalized with a rotation by a mixing angle [313]

$$\theta = \frac{1}{2}\arctan\left(\frac{\Delta_{a\gamma}}{\Delta_\parallel - \Delta_a}\right)\,, \tag{3.20}$$

represented by the unitary transformation

$$\mathcal{U} = \begin{pmatrix}\cos\theta & \sin\theta\\ -\sin\theta & \cos\theta\end{pmatrix}\,. \tag{3.21}$$

The general solution of EQ. 3.18 is then

$$\psi(x) = \mathcal{U}^T \exp\left(i\mathcal{M}'x\right)\mathcal{U}\,\psi(0)\,, \tag{3.22}$$

where $\mathcal{M}' = \mathcal{U}\mathcal{M}\mathcal{U}^T$ is diagonal. For an initial photon-only state, $\psi(0) = \begin{pmatrix}1 & 0\end{pmatrix}$, the probability of finding an ALP after propagating over a distance x is given by [313]

$$P_{a\gamma}(x) = |a(x)|^2 = \sin^2(2\theta)\sin^2(\Delta_{\rm osc}x/2) = (\Delta_{a\gamma}x)^2\left(\frac{\sin(\Delta_{\rm osc}x/2)}{\Delta_{\rm osc}x/2}\right)^2, \tag{3.23}$$

with an oscillation wavenumber set by

$$\Delta_{\rm osc} = \sqrt{(\Delta_\parallel - \Delta_a)^2 + 4\Delta_{a\gamma}^2}\,. \tag{3.24}$$

The probability in EQ. 3.23 becomes maximal and energy-independent when $4\Delta_{a\gamma}^2 \gg (\Delta_\parallel - \Delta_a)^2$ and $\Delta_{\rm osc} \simeq 2\Delta_{a\gamma}$, reaching the value

$$P_{a\gamma,\rm max}(x) \simeq \sin^2(\Delta_{a\gamma}x) \tag{3.25}$$

which is referred to as the *strong mixing regime*. By using the expressions in EQ. 3.9 to EQ. 3.17, EQ. 3.24 can be rewritten as

$$\Delta_{\rm osc} = g_{a\gamma}B_T\sqrt{\left(\frac{E}{E_{\rm max}} \pm \frac{E_{\rm min}}{E}\right)^2 + 1}\,, \tag{3.26}$$

where [316–318]

$$E_{\rm min} = \frac{|m_a^2 - \omega_{\rm pl}^2|}{2g_{a\gamma}B_T} = 2.56\,{\rm GeV}\,\frac{|m_{\rm neV}^2 - 1.37\times10^{-3}n_{\rm cm^{-3}}|}{g_{11}B_{\rm \mu G}}\,, \tag{3.27}$$

$$E_{\rm max} = \frac{g_{a\gamma}B_T}{\dfrac{7\alpha}{90\pi}\dfrac{B_T^2e^2}{m_e^4} + \dfrac{44\alpha^2}{135}\dfrac{\rho_{\rm CMB}}{m_e^4}} = \frac{2.14\times10^6\,{\rm GeV}}{B_{\rm \mu G}^2 + 5.69}g_{11}B_{\rm \mu G} \tag{3.28}$$

and the $\pm$ sign depends on the sign of $m_a^2 - \omega_{\rm pl}^2$. In the above expressions, the shorthands $B_{\rm \mu G} = (B_T/1\,{\rm \mu G})$, $g_{11} = (g_{a\gamma}/10^{-11}\,{\rm GeV}^{-1})$, $m_{\rm neV} = (m_a/1\,{\rm neV})$ and $n_{\rm cm^{-3}} = (n_e/1\,{\rm cm}^{-3})$ have been introduced for brevity. The strong mixing regime is thus realized at energies $E_{\rm min} \ll E \ll E_{\rm max}$, while the oscillatory behaviour of $P_{a\gamma}$ dominates outside this range. A typical plot of $P_{a\gamma}$ as a function of energy is shown in FIGURE 3.3.

3.2.2 Direct detection experiments

The effects discussed above are the basis of experiments aimed at directly detecting ALPs [301, 308, 319]. An example of this kind of experiments is represented by beam regeneration (or "light shining through walls", LSW) setups, such as the Any Light Particle Search II (ALPS-II [320]), where a laser beam is shot against an opaque screen. In the presence of a strong $\mathcal{O}(\rm T)$ magnetic field, typically produced by superconducting magnets, some photons in the beam should be able to convert into ALPs, pass through the screen and oscillate back to photons on the other side. ALP signatures may also be searched in experiments looking to measure vacuum birefringence effects, such as PVLAS [321].

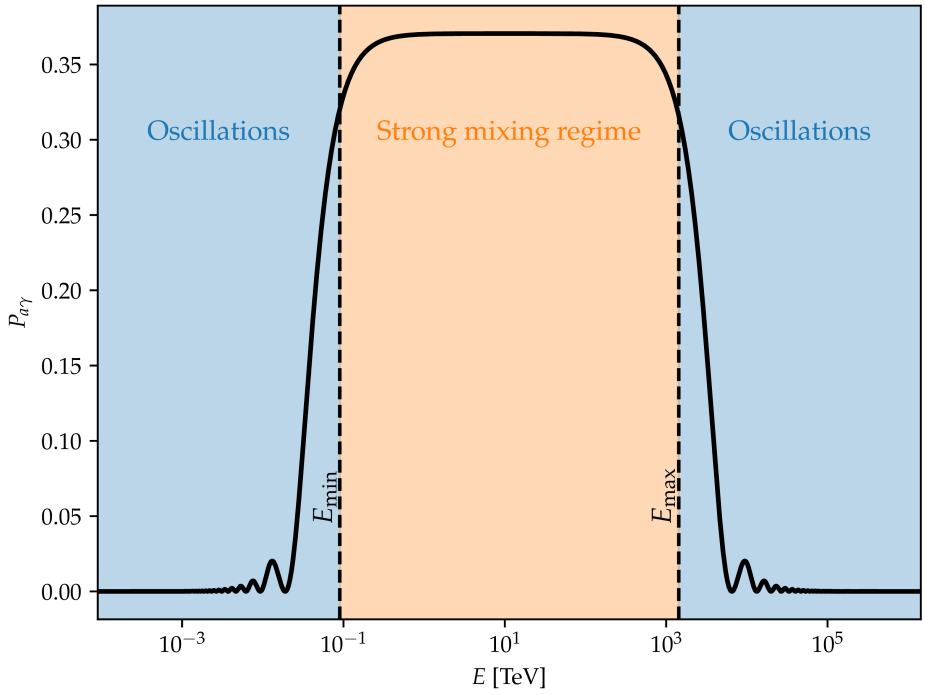


Figure 3.3: Example axion-photon oscillation probability $P_{a\gamma}$ as a function of energy, computed for $m_a = 12.2\,\mathrm{neV}$, $g_{a\gamma} = 4.3 \times 10^{-11}\,\mathrm{GeV}^{-1}$, $B_T = 1\,\mu\mathrm{G}$ and $n_e = 10^{-3}\,\mathrm{cm}^{-3}$. The oscillatory and strong mixing regimes are highlighted, along with the critical energies E_{min} and E_{max}.

A copious ALP flux at Earth is expected to be emitted from the Sun, where ALPs would be produced by the Primakoff process $\gamma\gamma \to a$ [301, 319]. *Axion helioscopes* aim at detecting these solar ALPs by pointing strong hollow magnets towards the Sun, which would trigger the conversion of the incoming ALPs to X-ray photons in the keV band. The CERN Axion Solar Telescope (CAST) experiment, employing a $\sim$ 9 T decommissioned magnet from the Large Hadron Collider (LHC), recently provided the 95% CL upper limit $g_{a\gamma} \lesssim 5.8 \times 10^{-11}\,\mathrm{GeV}^{-1}$ for $m_a \lesssim 0.2\,\mathrm{eV}$ [322], which represents the leading constraint from direct detection over a wide mass range (see Figure 3.1). The future International Axion Observatory (IAXO) will build on this concept, aiming to improve the CAST limit by about one order of magnitude [323].

Finally, *axion haloscopes* work under the hypothesis that nonrelativistic ALPs constitute all or most of the dark matter in the Milky Way halo. By exploiting resonant conversion effects in microwave cavities, these experiments can be tuned to provide strong limits for specific values of the ALP mass. Examples of this approach are found in ADMX [324], RADES [325], ABRACADABRA [326] and the future MADMAX [327].

3.3 Propagation in inhomogeneous magnetic fields

While the picture outlined above gives a good overview of the general characteristics of ALP-photon mixing, it is often necessary to consider the more general case of propaga-

tion in a non-uniform magnetic field while interacting with the surrounding environment. This problem is naturally solved by treating the ALP-photon beam as an open quantum system and studying the evolution of its density matrix, given by [316, 328]

$$\rho(x) = \Psi(x) \otimes \Psi^{\dagger}(x) = \begin{pmatrix} A_{\perp}(x) \\ A_{\parallel}(x) \\ a(x) \end{pmatrix} \otimes \begin{pmatrix} A_{\perp}(x) & A_{\parallel}(x) & a(x) \end{pmatrix}^{*} . \tag{3.29}$$

In analogy with the Schrödinger-like EQ. 3.7, $\rho(x)$ satisfies the Von Neumann equation

$$i\frac{\mathrm{d}\rho}{\mathrm{d}x} = [\rho, \mathcal{M}_0] , \tag{3.30}$$

with $\mathcal{M}_0$ given by EQ. 3.8.

As the direction of the magnetic field is in general not constant and the beam is not polarized, the 2-dimensional simplification of SECTION 3.2.1 can no longer be applied. Instead, the propagation length is typically subdivided in domains where the magnetic field can be regarded as uniform. In each k-th domain, $A_{\perp}$ and $A_{\parallel}$ can always be regarded as perpendicular and parallel polarization states, respectively, with respect to the transverse magnetic field. This is done by the transformation

$$\mathcal{V}_k = \begin{pmatrix} \cos\psi_k & -\sin\psi_k & 0 \\ \sin\psi_k & \cos\psi_k & 0 \\ 0 & 0 & 1 \end{pmatrix} , \tag{3.31}$$

representing a rotation of an angle ψ_k in field space.

In this framework, photon absorption effects from the environment can also be easily accounted for by by including non-Hermitian terms in the mixing matrix $\mathcal{M}_0$, as is commonly done in the Hamiltonian of an open quantum system [329]. The photon absorption rate is defined as

$$\Gamma_k = \frac{\tau_k - \tau_{k-1}}{\Delta x_k} , \tag{3.32}$$

where Δx_k is the size of the k-th domain and τ_k is the optical depth for the relevant absorption process, such as EBL scattering, at the corresponding point in space [317]. It should be noted that, when considering propagation over cosmological distances, the discretization in length x corresponds to a discretization in the redshift parameter z via the relationship

$$\frac{\mathrm{d}x}{\mathrm{d}z} = \frac{c}{H_0} \frac{1}{(1+z)\sqrt{\Omega_\Lambda + \Omega_m (1+z)^3}} , \tag{3.33}$$

where $H_0 \simeq 67\,\mathrm{km\,s^{-1}\,Mpc^{-1}}$, $\Omega_\Lambda \simeq 0.68$ and $\Omega_m \simeq 0.32$ [132]. The k-th domain will therefore be characterised by a redshift parameter z_k, and all quantities such as photon energy, particle density and magnetic field intensity should be scaled by the appropriate power of $(1 + z_k)$ (e.g. [330, 331]). Photon absorption effects can then be included in the ALP-photon propagation equation by substituting the photon polarization terms as $\Delta_{\perp,\parallel} \to \Delta_{\perp,\parallel} + i\Gamma_k/2$ [317].

The density matrix in the k-th domain is then recursively given by [316]

$$\rho_k = \mathcal{T}_k \rho_{k-1} \mathcal{T}_k^\dagger \,, \tag{3.34}$$

where the *transfer matrix* $\mathcal{T}_k$ is defined as

$$\mathcal{T}_k = \mathcal{V}_k^T \, \mathcal{U}^T \, e^{i\mathcal{M}_0' \Delta x_k} \, \mathcal{U} \, \mathcal{V}_k \,. \tag{3.35}$$

Here, $\mathcal{U}$ denotes the 3-dimensional generalization of the rotation matrix given by EQ. 3.21

$$\mathcal{U} = \begin{pmatrix} 1 & 0 & 0 \\ 0 & \cos\theta & \sin\theta \\ 0 & -\sin\theta & \cos\theta \end{pmatrix} \tag{3.36}$$

and $\mathcal{M}_0' = \mathcal{U}\mathcal{M}_0\mathcal{U}^T$ is the diagonalized version of $\mathcal{M}_0$. An explicit expression of the transfer matrix $\mathcal{T}$ as a function of θ and ψ_k is given e.g. in refs. [316, 328]. Starting from an initial state represented by the density matrix ρ_0, the state after N domains will be given by

$$\rho_N = \mathcal{T}(\psi_0, \ldots, \psi_N) \rho_0 \mathcal{T}^\dagger(\psi_0, \ldots, \psi_N) \,, \tag{3.37}$$

where

$$\mathcal{T}(\psi_0, \ldots, \psi_N) = \prod_{k=0}^{N} \mathcal{T}_k \,. \tag{3.38}$$

In particular, considering a completely unpolarized photon initial state $\rho_0 = (1/2)\,\mathrm{diag}(1,1,0)$, the *photon survival probability* can be determined as the probability of detecting a photon in either polarization final state $\rho_1 = \mathrm{diag}(1,0,0)$ or $\rho_2 = \mathrm{diag}(0,1,0)$. This amounts to projecting the final state ρ_N onto any of the polarization states, ρ_1 or ρ_2, summing the outcomes and computing the trace

$$P_{\gamma\gamma} = \mathrm{Tr}[(\rho_1 + \rho_2)\rho_N] = \mathrm{Tr}\Big[(\rho_1 + \rho_2)\, \mathcal{T}(\psi_0, \ldots, \psi_N) \rho_0 \mathcal{T}^\dagger(\psi_0, \ldots, \psi_N)\Big] \,. \tag{3.39}$$

In general, the photon survival probability has a non-trivial dependence on energy, redshift and any other parameter entering in the magnetic field configuration and mixing dynamics, and must be evaluated numerically. In the absence of photon-ALP mixing ($g_{a\gamma} = 0$), $P_{\gamma\gamma}$ reduces to the EBL absorption factor $e^{-\tau(E,z)}$ (EQ. 1.5).

3.4 Magnetized astrophysical environments

3.4.1 Blazar jets

Many different classes of astrophysical objects are characterized by magnetic fields of varying intensities and morphologies, which offer a natural framework to probe large-scale effects related to ALP-photon mixing. In blazar jets, for example, the collimation of relativistic jets implies the presence of a magnetic field whose flux is conserved along the jet trajectory (*flux freezing*) [332]. Assuming a conical jet, a poloidal component of this field (directed along the jet axis) would decrease as $B \sim r^{-2}$ with the distance from the galactic nucleus, by the argument of flux conservation. Similarly, a toroidal component

(transverse to the jet axis) would decrease as $B \sim r^{-1}$. Thus, at large enough distances from the central SMBH, the poloidal component can be neglected and the magnetic field in the blazar jet can be considered as purely transverse.

The simplest models of ALP-photon conversions in BL Lac jets, where any possible photon absorption by the BLR or dusty torus can be neglected, consider a randomly oriented domain-like magnetic field with constant $\mathcal{O}(\mathrm{G})$ intensity over the gamma-ray emission region, which is assumed to be small compared to the overall extension of the jet [333]. Similarly, the electron density (necessary to compute the photon dispersion term in plasma) is taken as constant in these models. Other models consider a coherent, analytical large-scale transverse field [334–336]

$$B_{\mathrm{jet}}(r) = B_0 \left(\frac{r}{r_0} \right)^{-1} , \tag{3.40}$$

where B_0 is the magnetic field strength in the VHE emitting region, located at a $\mathcal{O}(\mathrm{pc})$ distance r_0 from the central black hole. Similarly, the electron density in a conical jet decreases as

$$n_e(r) = n_0 \left(\frac{r}{r_0} \right)^{-2} , \tag{3.41}$$

where n_0 is the electron density at r_0, of order $\mathcal{O}(10^4\,\mathrm{cm}^{-3})$. These relations hold in the jet comoving frame, and thus the ALP/photon energy should be scaled according to EQ. 2.6 when using them to compute conversions in blazar jets.

A more sophisticated model of the jet magnetic field was introduced by Davies, Meyer and Cotter (DMC) in ref. [337], based on the leptonic Potter-Cotter (PC) jet model described in SECTION 2.3.2 [219–223]. The original PC model considers a jet with total power W_j which evolves according to the geometry described by EQ. 2.11 while enforcing relativistic energy-momentum conservation. An isotropic tangled (i.e. randomly oriented) magnetic field is assumed, whose strength $B(r)$ along the jet is computed by requiring that magnetic and electron energy densities reach equipartition at the transition region between the parabolic and conical sections of the jet ($\rho_B(r_{\mathrm{con}}) = \rho_e(r_{\mathrm{con}})$) [221]. The DMC model expands on this concept by assuming the jet magnetic field to be made up of a tangled component B_t and an helical component B_h, which starts as poloidal at the base of the jet and gradually turns to toroidal up to a jet length r_T. The energy density fraction of the tangled component relative to the helical component is defined as

$$\frac{B_t^2}{B_h^2} = \frac{f}{1-f} , \tag{3.42}$$

where $f \in [0,1]$ is a free parameter of the model. Knowing the total magnetic field intensity $B(r)$ along the jet from the PC model, the intensities of the two components can then be determined as

$$B_t(r) = B(r)\sqrt{f} , \quad B_h(r) = B(r)\sqrt{1-f} . \tag{3.43}$$

The transverse component of the helical field is assumed to scale with jet length for $r \leq r_T$, while the field is fully toroidal for $r > r_T$, so that

$$B_{h,\mathrm{transverse}}(r) = \begin{cases} B_h(r_T) \left(\dfrac{r}{r_T} \right)^{\alpha} & r \leq r_T \\ B(r)\sqrt{1-f} & r > r_T \end{cases} , \tag{3.44}$$

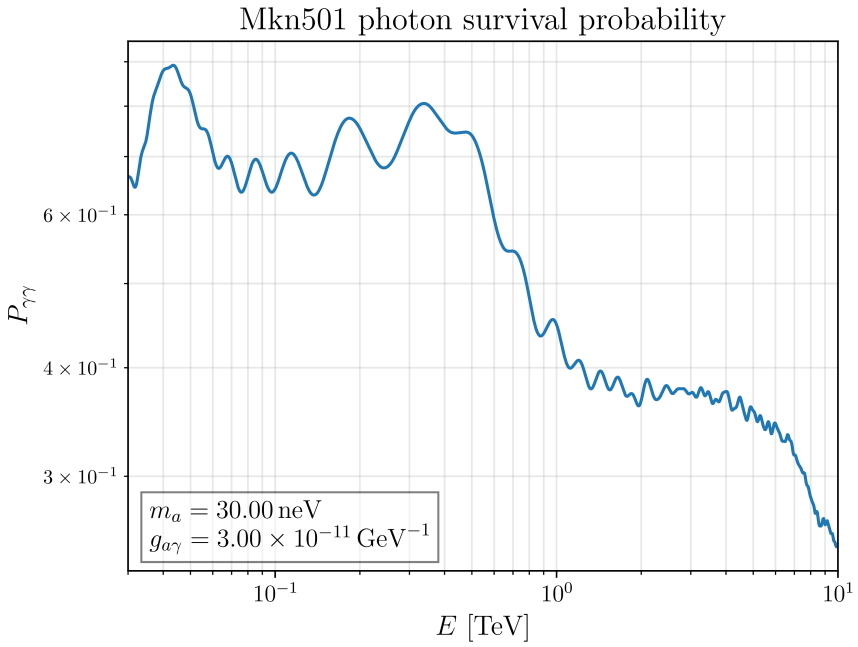


Figure 3.4: Example photon survival probability computed for ALP parameters $m_a = 30\,\mathrm{neV}$ and $g_{a\gamma} = 3 \times 10^{-11}\,\mathrm{GeV}^{-1}$, including ALP-photon conversions in the jet of blazar Mrk 501 (using the model from ref. [337] with parameters from ref. [219]) and in the Milky Way (using the model from ref. [339]). The plot was produced with gammaALPs.

where the exponent α is another free parameter of the model which generalizes the power-law scaling of eq. 3.40. From the previous equation, it is easy to see that for $r = 0$ the transverse component of the helical field is zero, (the field is fully poloidal), while for $r \geq r_T$ it coincides with $B_h(r)$ (the field is fully toroidal). On the other hand, the transverse components of the tangled field are determined in each domain by two random angles θ and ϕ, with a coherence length that can be sampled from a chosen distribution.

As the transition region in the jet is where most gamma rays are produced according to the PC model, r_T can be set equal to the location of the VHE emission region r_{VHE} [337]. Furthermore, these quantities can both be used as the jet length r_0 at which the magnetic field in eq. 3.40 and the electron density in eq. 3.41 are normalized. This reduces the additional parameters of the magnetic field to (r_T, α, f) in addition to those obtained by the PC model. The relative importance of these parameters in different regions of the ALP parameter space was discussed in ref. [337].

The DMC model was originally implemented in the gammaALPs Python package [338].[2] The relevance of the jet magnetic field in determining photon-ALP mixing was discussed in ref. [337], concluding that in general this component provides a significant contribution over large areas of the ALP parameter space and cannot be neglected. An example of the photon survival probability computed with this model for the blazar Markarian 501 is shown in Figure 3.4.

[2]The gammaALPs source code is available at https://github.com/me-manu/gammaALPs/, from which the above description of the model was partially derived.

3.4.2 Galaxy clusters

Active galactic nuclei may be located inside galaxy clusters, which are thought to be permeated by $\mathcal{O}(\mu\mathrm{G})$ magnetic fields over $\mathcal{O}(\mathrm{kpc})$ scales [340]. The overall intensity of the magnetic field is typically assumed to be given by (e.g. [341])

$$B(r) = B_0 \left(\frac{n_e(r)}{n_0} \right)^{\eta} , \tag{3.45}$$

where $n_e(r)$ is the free electron density in the intra-cluster medium. The latter is given as a function of the distance r from the center of the cluster by

$$n_e(r) = n_0 \left(1 + \frac{r}{r_c} \right)^{-3\beta/2} \tag{3.46}$$

with n_0 of order $\mathcal{O}(10^{-3}\,\mathrm{cm}^{-3})$. Typical values of the other parameters in the above expressions include $r_c \simeq 100\,\mathrm{kpc}$ for the radius of the cluster core, $\eta \simeq 1$ and $\beta \simeq 2/3$ [334]. Simple domain-like models with the magnetic field orientation randomly changing from one cell to the next exist in this case as well, with a $\mathcal{O}(10\,\mathrm{kpc})$ correlation length, roughly the size of a galaxy in the cluster (e.g. [342, 343]).

A commonly used model, also implemented in gammaALPs, involves a divergence-free, homogeneous, isotropic magnetic field with Gaussian turbulence described in detail in ref. [334]. The magnetic field components can be expressed by the Fourier decomposition

$$B_i(\mathbf{x}) = \int \frac{\mathrm{d}^3 k}{(2\pi)^3} \tilde{B}_i(\mathbf{k}) e^{i\mathbf{k}\cdot\mathbf{x}} , \tag{3.47}$$

where $\tilde{B}_i(\mathbf{k}) = \tilde{B}_i(-\mathbf{k})$ is a real even function. The correlation function between modes is given by

$$\langle \tilde{B}_i(\mathbf{k}) \tilde{B}_j(\mathbf{k}') \rangle \propto M(k) \left(\delta_{ij} - \frac{k_i k_j}{k} \right) \delta^3(\mathbf{k} - \mathbf{k}') , \tag{3.48}$$

where $k = |\mathbf{k}|$. The turbulence power spectrum $M(k) \sim k^q$, defined in the wavenumber interval $k_L < k < k_H$, is normalized so that the field has root mean square $\mathcal{B}$ of order $\mathcal{O}(\mu\mathrm{G})$. From the above expressions, it can be checked that the field has zero mean and divergence. The random transversal components along a given line of sight can be expressed by a discrete Fourier expansion

$$B_i(x) = \sum_n b_n (\xi_n \cos k_n x + \eta_n \sin k_n x) , \tag{3.49}$$

where i denotes either of the axes transverse to the line of sight, while (ξ_n, η_n) are pairs of standard-distributed Gaussian random numbers. Under the given assumptions, the coefficients b_n in the above expression can be derived as functions of the parameters $\mathcal{B}$, q, k_H and k_L (see ref. [334]). Finally, the resulting transverse field is scaled with r according to EQ. 3.45. Owing to the intrinsic randomness in this model, the photon survival probability $P_{\gamma\gamma}$ obtained with the same choice of parameters can vary widely depending on the specific realization of the magnetic field (see FIGURE 3.5).

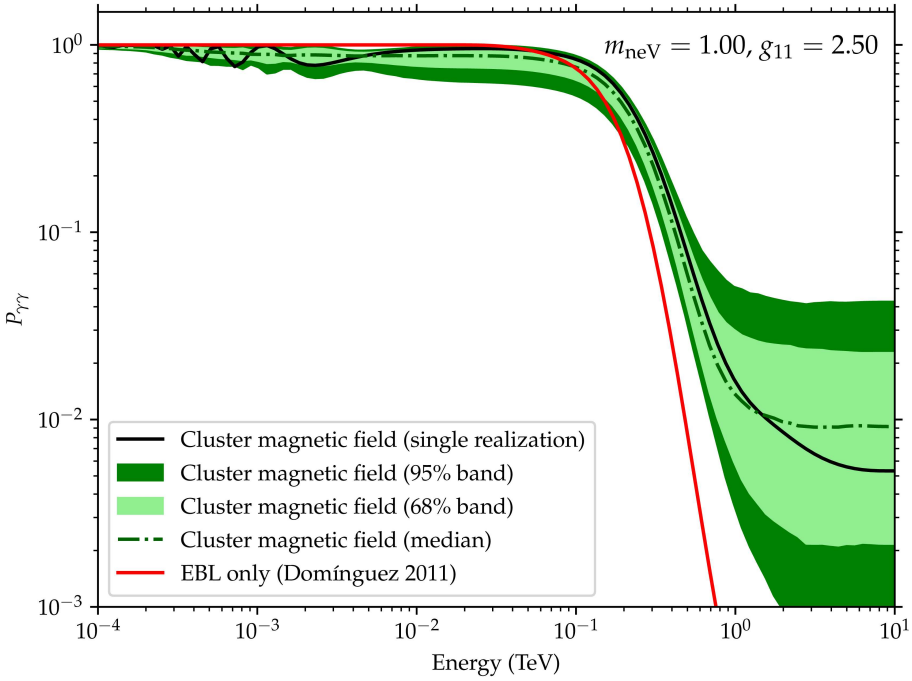


Figure 3.5: Example photon survival probability $P_{\gamma\gamma}$ computed for ALP parameters $m_a = 1\,\mathrm{neV}$, $g_{a\gamma} = 2.5 \times 10^{-11}\,\mathrm{GeV}^{-1}$. The plot was produced with gammaALPs, considering ALP-photon conversions in the magnetic field of a galaxy cluster located at the coordinates of PG 1553+113 (using the parameters reported in ref. [344]) and in the Milky Way magnetic field (modeled according to ref. [339]). The green bands show the 68% and 95% deviations of $P_{\gamma\gamma}$ around the median values for 1000 realizations of the cluster magnetic field, one of which is shown in black, highlighting the large variability exhibited by different realizations of the same turbulent magnetic field. The red line represents the gamma-ray absorption due to the EBL (modeled according to ref. [142]).

3.4.3 Milky Way magnetic field

Spiral galaxies such as the Milky Way are known to harbor magnetic fields with strengths of order $\mathcal{O}(\mu\mathrm{G})$, which can be detected through radio synchrotron emission and polarization or Faraday rotation measures (e.g. [345]).

The structure of the magnetic field in our galaxy can be inferred from accurate measurements from a large number of radio observatories and satellite instruments such as the Wilkinson Microwave Anisotropy Probe (WMAP) and *Planck*. A popular model used to fit these data with great accuracy was proposed by Jansson and Farrar [339]. The Jansson-Farrar (JF) model defines the Galactic magnetic field of the Milky Way as a superposition of three different components: a large-scale regular field, a small-scale random field and a "striated" field which is ordered on large scales but randomly oriented locally. The regular component is in turn obtained by summing contributions from a disk field restricted to the galactic plane, a purely toroidal halo field, and an out-of-plane, X-shaped field motivated by edge-on radio observations of similar galaxies. The analysis reported in ref. [339] only focuses on the regular and striated components, the latter of which is parametrized by a simple multiplicative factor which denotes its relative impact with respect to the former. Nonetheless, the JF model provides very good agreement with experimental data and has been widely used to model ALP-photon conversions in the Milky Way.

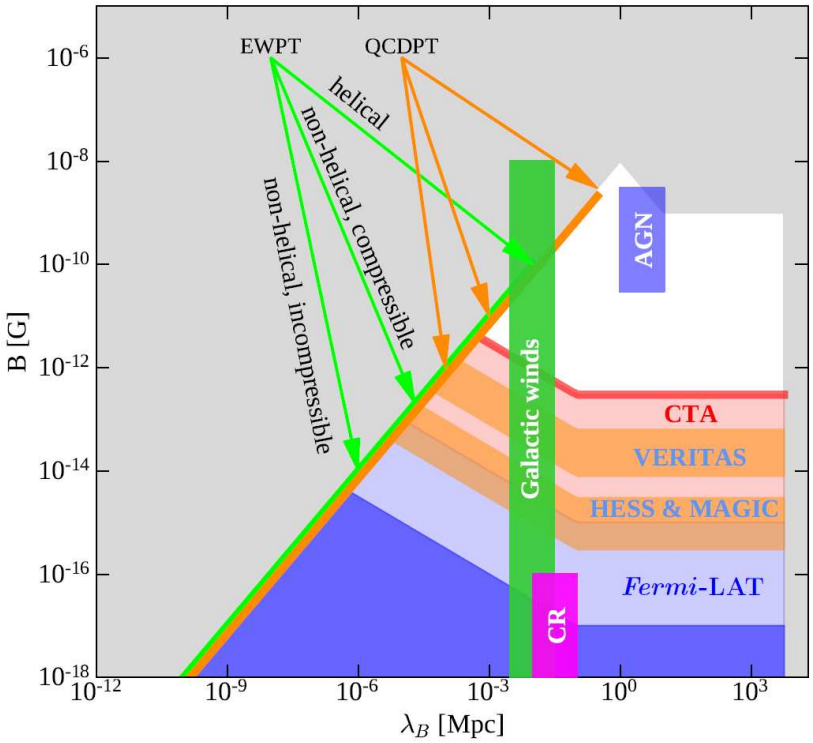


Figure 3.6: Experimental limits and favored regions for the present IGMF intensity and coherence length, with a focus on gamma-ray observations. Figure from ref. [130].

Other models of the Galactic magnetic field include those by Pshirkov et al. [346] and by Unger and Farrar [347]. The latter is essentially an updated version of the JF model, which makes use of several "auxiliary models" to enhance the flexibility of the model and account for different sources of uncertainty. All three models have been implemented in the gammaALPs package.

3.4.4 Intergalactic magnetic field

The fact that large-scale magnetic fields are almost ubiquitously observed in galaxies and galaxy clusters suggests that they may have a primordial origin, connected to cosmological structure formation [348]. In this scenario, a relic intergalactic magnetic field (IGMF) would permeate space, possibly leaving imprints on several astrophysical and cosmological processes. For example, the electron-positron pairs produced by gamma-ray scattering over the EBL would be deflected by the IGMF and eventually produce lower-energy gamma rays inverse Compton scattering over the CMB. This would result in the emission of a time-delayed and spatially extended signal, which for a small enough magnetic field strength could be detected by gamma-ray telescopes as a "halo" around otherwise point-like sources, such as blazars [349]. Non-detection of these emission components allowed observations by *Fermi*-LAT [350], MAGIC [351], H.E.S.S. [352] and VERITAS [353] to constrain the present IGMF strength to $B_0 \gtrsim 10^{-14}\,\mathrm{G}$ for coherence lengths $\lambda_B \sim 1$–$1000\,\mathrm{Mpc}$, a limit that is expected to be improved by CTAO [130] (Figure 3.6). A primordial magnetic field would also have effects on the CMB anisotropy spectrum, which constrains its present intensity to $B_0 \lesssim 1\,\mathrm{nG}$ over $\mathcal{O}(1\,\mathrm{Mpc})$ coherence lengths [354].

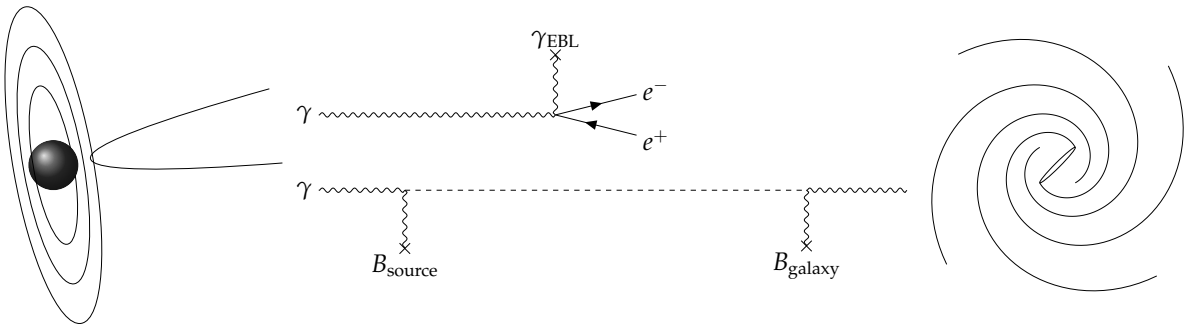


Figure 3.7: Schematic representation of astrophysical VHE gamma-ray propagation in the presence of ALPs. The upper diagram represents the standard scenario, where a gamma ray emitted from a distant source (left) interacts with the EBL and is converted into an electron-positron pair, never reaching the Milky Way (right). When crossing the source magnetic field $B_{\rm source}$, however, the gamma ray might be converted into an ALP, which would traverse the EBL and convert back into a photon in the Galactic magnetic field $B_{\rm galaxy}$ as shown in the lower diagram.

ALP-photon mixing in the IGMF has been widely considered in literature since early times. As its structure is almost completely unknown, this field is modeled in most cases with randomly oriented domains at varying redshifts (e.g. [313, 328, 330, 331, 342, 355]). For a given present-day value B_0, the IGMF intensity at redshift epoch z is obtained as $B(z) = B_0(1+z)^2$, under the assumption that the field lines are frozen in the cosmic medium and that the net magnetic flux across a closed comoving surface is zero [348]. More recently, results on cosmological ALP-photon mixing using realistic IGMF morphologies from magneto-hydrodynamic simulations have also been obtained [356].

3.5 Constraints on ALPs from gamma-ray astrophysics

3.5.1 General considerations

The effects on ALP-photon conversions on gamma-ray astrophysical observations have been extensively discussed in literature [313, 317, 328, 342, 343, 357–359]. Gamma-ray polarization effects could in principle be observed, as ALPs only couple to the photon state parallel to the external transverse magnetic field; however, such effects are not detectable with present-day instruments [316, 360]. On the other hand, for a given intrinsic photon flux at the source $\phi_{\rm int}(E)$, the observed flux in the presence of ALPs would be given by

$$\phi_{\rm obs}(E) = P_{\gamma\gamma}(E)\phi_{\rm int}(E)\,, \tag{3.50}$$

where $P_{\gamma\gamma}(E)$ is the photon survival probability given by eq. 3.39. Two main measurable spectral features may be investigated, whose extent generally depends on the field strength and topology, ALP parameters, source distance, and energy range of interest. A spectral *hardening* at VHE might be observed, due to gamma-ray photons converting into ALPs in the magnetic field of the source and back into photons in the Milky Way (Figure 3.7). This mechanism would allow the ALP-photon beam to travel cosmological distances, eluding the absorption that is normally experienced by VHE gamma rays due to pair production on the soft photons making up the EBL. The resulting effect, analogous to a "cosmic LSW

experiment", is expected to be more significant in the spectral tails of distant sources, for which the EBL absorption in the absence of ALPs would be strongest. The second observable effect is the presence of energy-dependent irregularities (*wiggles*) superimposed on the spectral shape, due to the peculiar shape of the photon survival probability $P_{\gamma\gamma}$ as a function of energy (see e.g. FIGURE 3.4).

The typical ALP parameter ranges that can be probed by gamma-ray observations can be estimated by requiring that the lower energy threshold for strong mixing regime (EQ. 3.27) falls in the GeV–TeV range. For typical astrophysical magnetic fields $B \sim 1\,\mu\text{G}$–$1\,\text{mG}$, this condition results in a mass interval $m_a \sim 1\,\text{neV}$–$1\,\text{meV}$ [344, 357]. The ALP-photon coupling in this range is experimentally constrained by CAST to be $g_{a\gamma} \lesssim 5.8 \times 10^{-11}\,\text{GeV}^{-1}$ [322]. On the other hand, the requirement that the oscillatory term in EQ. 3.25 is large enough ($g_{a\gamma} B_T x/2 \gtrsim 1$) results in an estimate of the lowest detectable ALP photon coupling $g_{a\gamma} \gtrsim 10^{-12}\,\text{GeV}^{-1}$ for typical magnetic field intensities and conversion lengths [357].

3.5.2 Statistical framework

A number of gamma-ray observations have been used to constrain ALPs, employing different statistical techniques (see ref. [359] for a review). The most common approach is to perform a hypothesis test based on a likelihood-ratio test statistic (TS) of the general form

$$\text{TS} = -2 \ln \frac{\mathcal{L}(H_0|D)}{\mathcal{L}(H_1|D)}\,, \tag{3.51}$$

where H_0 and H_1 are two hypotheses applied to the data D, and $\mathcal{L}$ is a suitably-defined likelihood function (e.g. EQ. A.6). For example, hypothesis H_0 (the *null hypothesis*) may be that according to which the data are best described by a smooth spectral model including EBL absorption, while under hypothesis H_1 (*alternative hypothesis*) the data might follow a model including ALPs with best-fit parameters $(m_a, g_{a\gamma})$. In this case, the test statistic will have a form given by (e.g. [361, 362])

$$\text{TS} = -2 \sum_i \ln \frac{\mathcal{L}(\mu_{0,i}, \hat{\boldsymbol{\theta}}_0|D_i)}{\mathcal{L}(\hat{\mu}_i, \hat{\boldsymbol{\theta}}|D_i)}\,, \tag{3.52}$$

where the sum is performed over energy bins, $\mu_{0,i}$ represents the number of expected photon counts in the i-th bin according to the null hypothesis, while $\hat{\mu}_i$ is the expected number of counts in the i-th bin that maximizes the likelihood $\mathcal{L}$ in the alternative hypothesis (obtained in practice by finding the maximum likelihood over all the scanned ALP parameters). See APPENDIX A for an explicit definition of the likelihood and the notation used. The symbol $\boldsymbol{\theta}$ denotes the set of all *nuisance parameters*, such as the spectral parameters, background rates or magnetic field configuration. In the numerator, $\hat{\boldsymbol{\theta}}_0$ is the set of values that maximizes the likelihood given the set of counts $\boldsymbol{\mu}_0$, while in the denominator $\hat{\boldsymbol{\theta}}$ is the overall maximum-likelihood estimator. This technique is known as *likelihood profiling* [362].

In order to assess the confidence level (CL) at which the null hypothesis can be excluded, the distribution of the TS under the null hypothesis should be known. Under suitable assumptions, this is given by Wilks' theorem as a χ^2 distribution with a number

of degrees of freedom equal to the difference between the numbers of free parameters in the two hypotheses [363]. However, there are several arguments according to which this theorem cannot be applied to the case of ALPs. The main point of these arguments is that Wilks' theorem requires that the null hypothesis is represented by a subset of the parameter space of the alternative hypothesis, obtained by fixing the values of certain parameters to well-defined values. In the case of ALP-photon mixing, the null hypothesis is obtained by setting $g_{a\gamma} = 0$. However, in this case the values of other parameters (such as the ALP mass or the magnetic field parameters) are not constrained by the data, as the likelihood does not depend on them. Other arguments are related to the irregular dependence of the likelihood on the ALP parameters and to the degeneracy between ALP-photon coupling and magnetic field, due to the oscillation probability only depending on the product $g_{a\gamma}B$ (e.g. [334, 364, 365]). Therefore, the TS distribution in the null hypothesis typically has to be obtained by running a large number of Monte Carlo simulations or pseudo-experiments. From the obtained probability distribution function $f(x)$, the confidence level for excluding the null hypothesis will be given by

$$\mathrm{CL} = \int_0^{\mathrm{TS}_{\mathrm{obs}}} f(x)\,\mathrm{d}x = 1 - p\,, \tag{3.53}$$

where $\mathrm{TS}_{\mathrm{obs}}$ is the TS value obtained from the observed data, while p is the probability (p-value) that the TS is greater than or equal to $\mathrm{TS}_{\mathrm{obs}}$ under the null hypothesis. For any given p-value and distribution, a threshold $\mathrm{TS}_{\mathrm{thr}}$ can be computed so that the null hypothesis is excluded if $\mathrm{TS}_{\mathrm{obs}} > \mathrm{TS}_{\mathrm{thr}}$. The typical requirement for excluding the null hypothesis is $p = 5.7 \times 10^{-7}$, corresponding to 5 Gaussian standard deviations (5σ). If this criterion is not met, a detection of ALPs cannot be claimed and only upper limits on $g_{a\gamma}$ can be reported. In this case, a different TS can be defined as

$$\mathrm{TS}(m_a, g_{a\gamma}) = -2\sum_i \ln \frac{\mathcal{L}(\mu_i(m_a, g_{a\gamma}), \hat{\boldsymbol{\theta}}(m_a, g_{a\gamma})|D_i)}{\mathcal{L}(\hat{\mu}_i, \hat{\boldsymbol{\theta}}|D_i)}\,, \tag{3.54}$$

where $\mu_i(m_a, g_{a\gamma})$ is the expected number of counts in the i-th bin for ALP parameters $(m_a, g_{a\gamma})$, and $\hat{\boldsymbol{\theta}}(m_a, g_{a\gamma})$ is the corresponding set of nuisance parameters that maximizes the likelihood. To get the confidence level for exclusion, a TS distribution for each $(m_a, g_{a\gamma})$ should in principle be obtained, though in some cases a "representative" distribution can be chosen to set threshold values. ALP upper limits are usually reported at 95% or 99% CL (2σ or 3σ level, respectively).

3.5.3 ALP limits from NGC 1275

The method described above was applied to derive constraints on ALPs based on several gamma-ray observations of the AGN NGC 1275 in the Perseus galaxy cluster. In these works, the turbulent intra-cluster magnetic field was modeled following the technique first introduced in ref. [334], with parameter choices motivated by observations of Perseus or similar clusters. Conversions in the galactic magnetic field of the Milky Way were also taken into account, while the effect of the IGMF was usually neglected. As discussed in Section 3.4.2, due to the intrinsic randomness in the intra-cluster magnetic field, different realizations of the same field can give very different $P_{\gamma\gamma}$ values, resulting in better

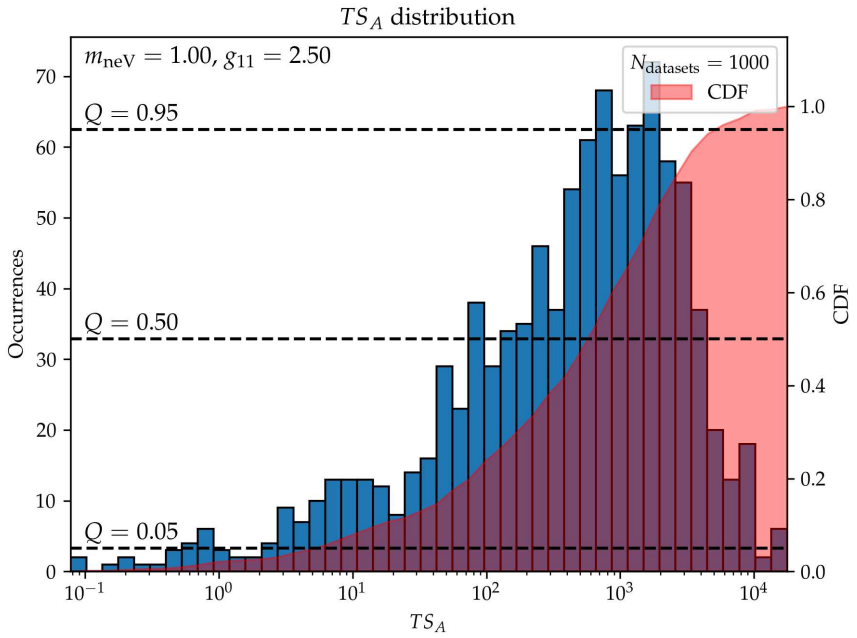


Figure 3.8: Example TS distribution computed for ALP parameters $m_a = 1\,\mathrm{neV}$, $g_{a\gamma} = 2.5 \times 10^{-11}\,\mathrm{GeV}^{-1}$ for different realizations of the same turbulent magnetic field, using the parameters from ref. [344]. The TS values were computed for 1000 Asimov datasets resulting from simulated observations of PG 1553+113, using the CTAO response functions.

or worse fits to the data and thus different likelihood values. These effects are not easily parametrized, and thus it is not possible to profile over the magnetic field as with the other nuisance parameters. The adopted strategy in these cases is usually to compute the TS in eq. 3.52 for many different realizations of the magnetic field, and choose that corresponding to a certain quantile Q in the resulting TS distribution [334] (see Figure 3.8).

This analysis was performed using six years of *Fermi*-LAT data, which resulted in a 95% CL upper limit on the ALP photon coupling $g_{a\gamma} \lesssim 5 \times 10^{-12}\,\mathrm{GeV}^{-1}$ for $m_a \in [0.5, 5]\,\mathrm{neV}$ [364] (Figure 3.9a). To account for the TS dependence on the specific realization of the intra-cluster turbulent magnetic field, a quantile $Q = 0.95$ was chosen. The distribution of the TS in the null hypothesis (eq. eq. 3.52) was estimated by Monte Carlo simulations, and it was assumed to hold for the TS of eq. 3.54 as well in order to obtain upper limits. A similar study was performed with 41.3 h of MAGIC data, with a more careful estimation of the point-to-point TS distributions over the considered ALP parameter space. Interestingly, the null hypothesis of no ALPs could be excluded at the 2.03σ level in favor of an ALP model with $m_a = 21.5\,\mathrm{neV}$ and $g_{a\gamma} = 3.81 \times 10^{-12}\,\mathrm{GeV}^{-1}$. As this significance is still too low to claim detection, 99% CL upper limits at $g_{a\gamma} \lesssim 3 \times 10^{-12}\,\mathrm{GeV}^{-1}$ for $m_a \simeq 50\,\mathrm{neV}$ were reported [365] (Figure 3.9b). Both the *Fermi*-LAT and MAGIC limits are shown in Figure 3.1. A similar but more conservative approach was recently adopted by VERITAS in ref. [366], where no ALP parameters could be excluded at a significant level.

The capability of CTAO of constraining an ALP signal from NGC 1275 was estimated in ref. [130]. Following the specifications given in the Clusters of Galaxies KSP [124], simulated observations of a quiescent state of this source were performed for a total of 300 h, to which a 10 h observation of a flaring state was added, based on previous observa-

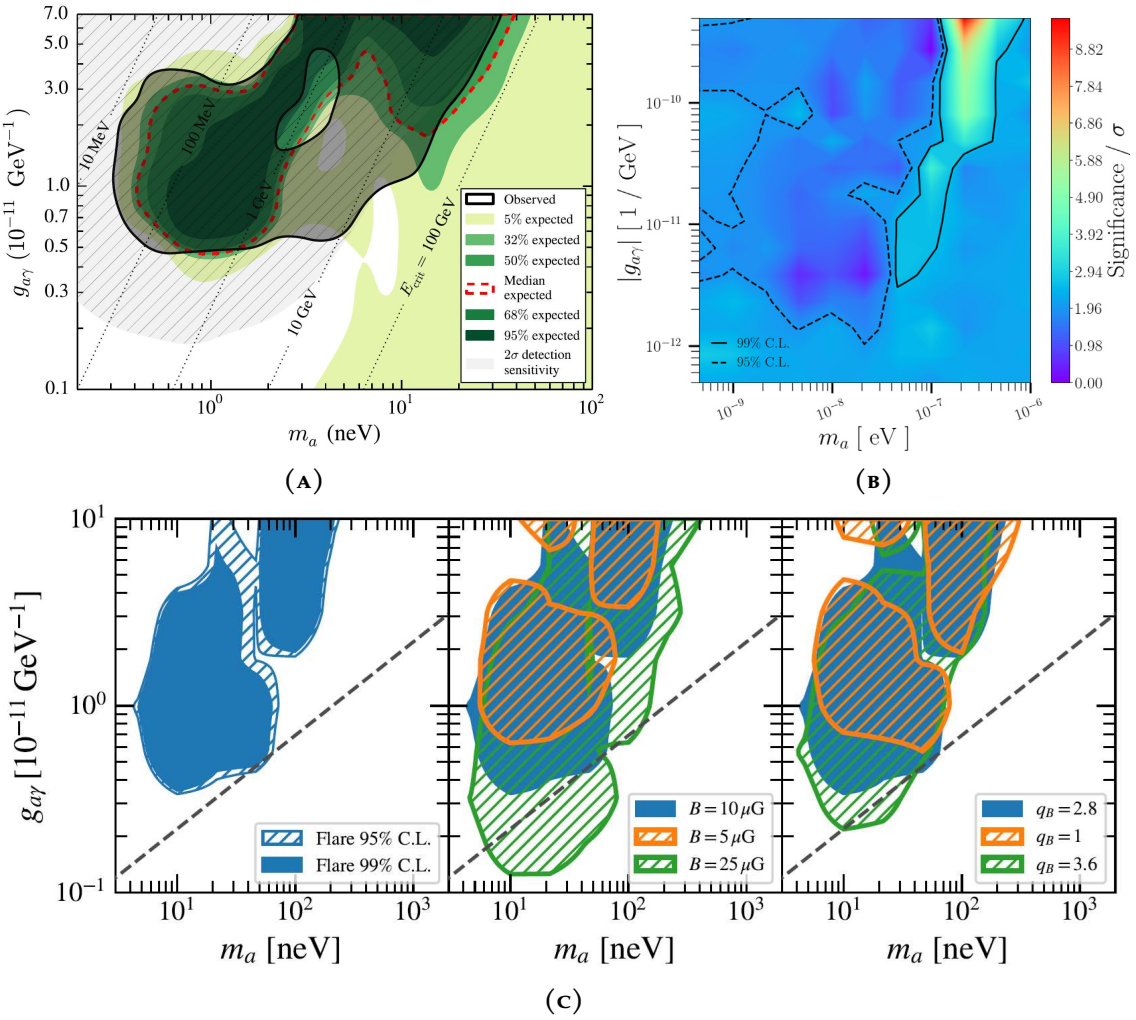


Figure 3.9: Observed and projected limits on the ALP parameter space from real and simulated observations of NGC 1275. (A) Expected and observed 95% CL limits from six years of *Fermi*-LAT observations. The grey shading indicates the region of the parameter space where ALPs could have been detected. Figure from ref. [364]. (B) ALP exclusion significance from 42 h observations with MAGIC. As the null hypothesis is excluded at 95% CL, limits at 99% CL are reported instead. Figure from ref. [365]. (C) Projected limits on the ALP parameter space derived from a 10 h simulated observation of a NGC 1275 flare with CTAO. Variations on the 95% CL limits are shown by changing the central magnetic field strength in the cluster or the turbulence spectral index. Figure from ref. [130].

tions by MAGIC. In order to provide a median estimate of the sensitivity, Asimov datasets were used, with the number of observed counts set equal to the expected one [367]. By performing a similar analysis to that outlined above, only the flaring state was found to significantly contribute to the limits, yielding the projected exclusion region shown in Figure 3.9c.

3.5.4 Constraints from different sources

Several other gamma-ray observations were used to constrain ALP parameters, employing a variety of sources and instruments [359]. Recent results include combined limits from

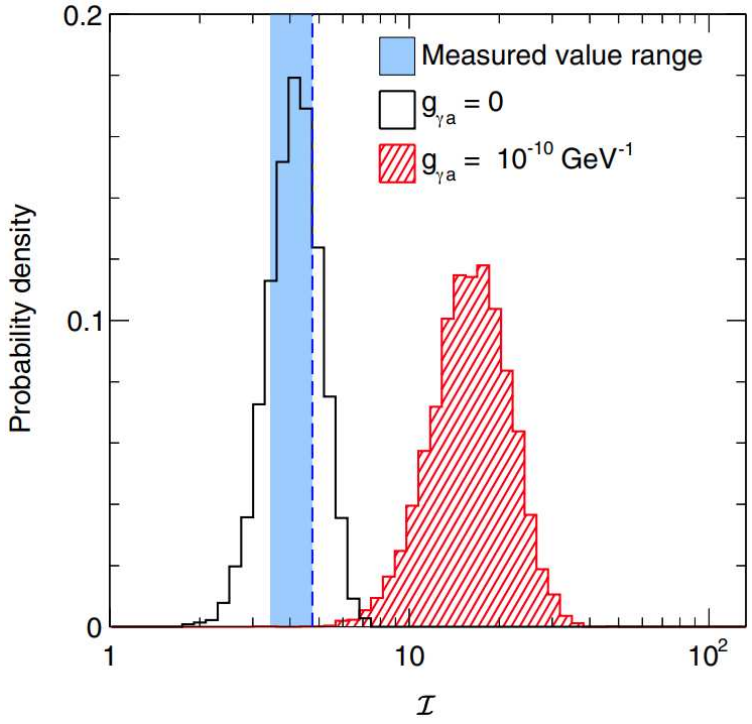


Figure 3.10: Example distributions of the irregularity estimator $\mathcal{I}$ used to set limits on ALP parameters with H.E.S.S. observations of PKS 2155−304, where the variation in the measured value depends on the choice of energy binning. Figure from ref. [370].

observations of selected BL Lacs with HAWC [368] and of FSRQs observed by *Fermi*-LAT [369], though these limits are typically weaker or comparable to previously published ones. Early CTAO projections were also derived for a combination of blazars, considering ALP-photon conversions both in the magnetic fields of the blazar jets and of the host galaxy clusters [344].

In cases where spectral wiggles are the relevant features to be searched in the data, an estimator can be defined to give a measure of how irregular the spectrum compared to a smooth EBL-absorbed model, such as a power law. This approach was used, for example, to constrain ALP parameters from observations of the blazar PKS 2155−304 with H.E.S.S. [370]. The irregularity estimator was defined as

$$\mathcal{I}^2 = \sum_i \frac{(\tilde{\phi}_i - \phi_i)^2}{d_i^T C_i d_i}\,, \tag{3.55}$$

where ϕ_i and $\tilde{\phi}_i$ are the measured and expected flux according to a power-law model in the i-th energy bin, C_i is the covariance matrix for the triplet $(\phi_{i-1}, \phi_i, \phi_{i+1})$, and $d_i^T = (\partial\tilde{\phi}_i/\partial\phi_{i-1}\,, -1, \partial\tilde{\phi}_i/\partial\phi_{i+1}\,)$. This estimator, analogous to a χ^2 test statistic, gives for each i-th bin a measure of how much the data in adjacent bins deviate from a simple power-law spectrum. By computing $\mathcal{I}$ for the observed data and comparing its value to the distributions one would obtain from many different realizations of the observation for a given magnetic field model, different sets of ALP parameters can be excluded (Figure 3.10). Both the cases of a galaxy cluster and intergalactic magnetic field were considered in ref. [370], with the latter providing a 95% CL upper limit $g_{a\gamma} \lesssim 2.1 \times 10^{-11}\,\mathrm{GeV}^{-1}$ for $m_a \in [15, 60]$ neV.

Finally, a different class of bounds on ALPs comes from the observations of astrophysical objects such as supernovae and neutron stars [371]. In these cases, ALPs are expected to be abuntantly produced in the sources by the Primakoff process, similarly to solar axions. By crossing the magnetosphere of the source or the magnetic field of the Milky Way, these ALPs would be converted to gamma rays, which would be detectable by current instruments. The most notable case is that of SN 1987A, from which the non-detection of gamma rays by the Solar Maximum Mission (SMM) satellite led to stringent upper limits down to $g_{a\gamma} \lesssim 10^{-12}\,\mathrm{GeV}^{-1}$ over a wide mass range for light ALPs [372–374].

CHAPTER 4

Limits on ALPs from blazars with MAGIC and LST-1

4.1 Source and data selection

As discussed in the previous Chapters, a significant portion of the parameter space of ALPs can be probed by means of observations of extragalactic gamma-ray sources. In the magnetic fields of the source, Milky Way, and possibly intergalactic space, ALP-photon oscillations could be triggered, leaving observable imprints on the measured gamma-ray spectra. The non-detection of such features makes it possible to constrain the ALP parameters in regions not easily accessible by other means (such as direct detection experiments).

In this Chapter we focus on the analysis of data from observations of blazars, performed with the MAGIC telescopes between 2014 and 2024 and with LST-1 between 2020 and 2024.[1] We search for ALP-induced irregularities in the gamma-ray spectra of four bright and well-studied sources, all belonging to the BL Lac class: Markarian 421 (Mrk 421), Markarian 501 (Mrk 501), 1ES 1959+650 and BL Lacertae (the archetypal BL Lac). We then discuss statistical and systematic effects, and we derive constraints on the ALP parameter space assuming ALP-photon conversions to primarily happen in the relativistic jets of the blazars and in the galactic magnetic field of the Milky Way. The first three sources are classified as HBLs (see Section 2.2), with significant TeV emission and variability. During their most intense flaring activity, these sources were also characterised as EHBLs [375–377]. BL Lac typically features a softer VHE spectrum and is classified as a LBL source. All four sources were regularly and abundantly observed with both instruments, yielding a large amount of archival data available for our study.

We restrict our analysis to data of optimal quality, obtained under low night-sky background (NSB) and good weather conditions. This comprises most of the data from the selected targets from each experiment, constituting the largest datasets analyzed for each target and for ALP searches with ground-based gamma-ray observations[359]. A summary of the selected data for each source and instrument is given in Table 4.1.

[1] The results presented in this Chapter contain contributions by I. Batković, G. D'Amico and M. Doro and will be the subject of a future publication, currently in preparation within the MAGIC and LST collaborations.

Target	Class	z	MAGIC				LST-1			
			Period	Duration	TS	BBs	Period	Duration	TS	BBs
Mrk 421	HSP	0.031	2014.12–2024.12	250.1 h	429.1	139	2020.12–2024.02	81.3 h	69.5	33
Mrk 501	HSP	0.034	2015.07–2024.09	233.7 h	85.7	31	2020.03–2023.06	48.5 h	17.1	12
BL Lac	LSP	0.069	2015.06–2024.11	82.9 h	69.7	9	2021.08–2022.11	27.8 h	31.6	14
1ES 1959+650	HSP	0.048	2015.03–2024.12	210.2 h	231.6	51	2020.08–2023.09	14.6 h	5.2	5

Table 4.1: Summary of MAGIC and LST-1 observations of the selected blazars. The name, class and redshift z is reported for each source, as well as the observation period, total selected observation time, Li-Ma test statistic (TS) value and number of Bayesian blocks selected for each instrument.

4.2 Data taking and analysis

4.2.1 MAGIC

MAGIC is a stereoscopic system of two 17 m diameter Cherenkov telescopes located at the Roque de los Muchachos Observatory on La Palma, in the Canary Islands, at an altitude of about 2200 m above sea level (Figure 1.5). As of the latest major upgrade in 2012, each telescope features a PMT-based camera with 1039 pixels, covering a total field of view of 3.5° [61]. Operations are carried out over approximately month-long data-taking shifts, with a central building (Counting House, CH) serving both as a control room and as a data processing and storage center. The schedule of nightly observations is decided in order to accommodate a series of scientific proposals made by members of the collaboration at the beginning of each observation cycle and evaluated by a time allocation committee (TAC). Several subsystems are present on the top of the CH, on and around the telescopes to monitor weather and atmospheric conditions during operations. A dedicated LIDAR system performs a real-time range-resolved measurement of the atmospheric transmission, while a pyrometer and an all-sky camera help in estimating cloudiness in the field of view of the telescopes [378]. The data taken each night are subdivided in *runs*, usually lasting about 20 min each.

The low-level gamma-ray reconstruction pipeline, whose general steps are outlined in Section 1.5.1, is implemented in the MAGIC Analysis and Reconstruction Software (MARS) [379], a suite of C++ programs based on the ROOT framework [380]. The basic stereo analysis workflow of MARS is shown in Figure 4.1. The program `sorcerer` performs pixel calibration, while `star` returns the calibrated images and the relative Hillas parameters for each telescope. These are then used by the `superstar` program to reconstruct stereoscopic images and shower parameters. Processed `star` and `superstar` files for all observations are produced automatically by on-site analysis (OSA) and stored at the Port d'Informació Cientifica (PIC) data center in Barcelona, Spain, where they can be accessed online.[2] The `coach` program trains a random forest algorithm to distinguish between OFF data, selected by the analyzer among low-significance observations performed under the same conditions as the analyzed data, and simulated gamma-ray images for each zenith range. The Monte Carlo simulations used to train the RFs are regularly produced after changes in the operational characteristics of the telescopes during a certain time (such as hardware upgrades or modifications in the reflectivity of the mirrors), based on which different analysis periods are defined. Finally, the `coach` and `superstar` output

[2] https://magic.pic.es/

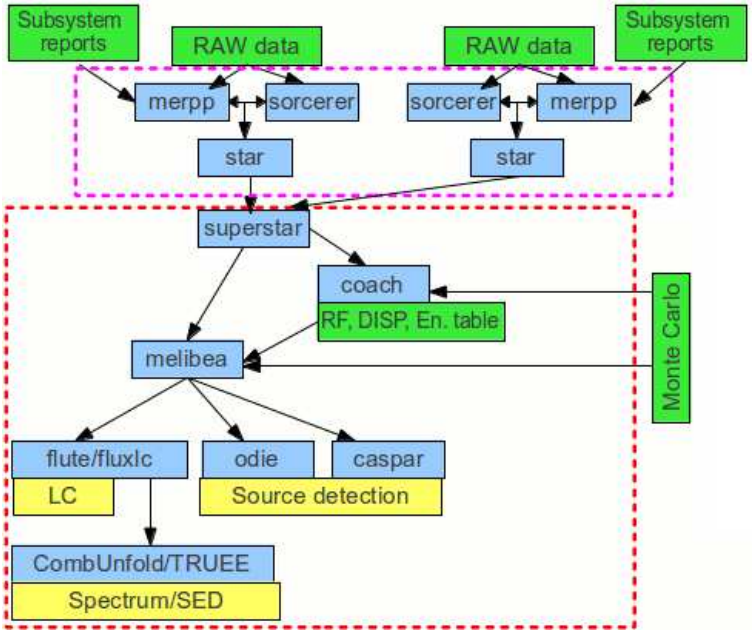


Figure 4.1: MARS stereo analysis workflow. The reduction from raw data up to `star` or `superstar` level is usually performed automatically by an on-site analysis pipeline or mass reprocessing at PIC, while the rest of the analysis is handled manually. Figure from the MAGIC Wiki (private).

files are used as input to `melibea`, which produces high-level gamma-ray event lists. While MARS contains programs for high-level analysis, such as `odie` and `flute`, the `magicDL3` software tool has been developed to convert `melibea` files to the GADF-compliant DL3 format [166]. This makes it possible to manipulate MAGIC data, bundled with the appropriate IRFs, with Gammapy and similar high-level analysis packages, as well as to perform joint analyses with data from other instruments in the same unified framework.

The steps described above can be executed almost automatically by the `autoMAGIC` software [161, 167]. Starting from a simple configuration file where the source, dates, and data selection cuts are specified, `autoMAGIC` simplifies the analysis pipeline by retrieving the relevant `star` or `superstar` files archived on the PIC and tracking the execution of the various necessary MARS and `magicDL3` programs, returning DL3 files in FITS format at the end of the process. A relational database keeps track of the execution process and allows `autoMAGIC` to reuse results of previously run analyses, thus making it particularly effective in analyzing large amounts of data.

We used `autoMAGIC` to select and analyze good-quality data from the four blazars listed above, focusing on a 10-year period between 2014 and 2024. We required data to be taken during dark time (defined by an average pixel current of less than 2200 nA) in runs of at least 300 s. Cuts on weather conditions were imposed by selecting data with an atmospheric transmission at 9 km of at least 80% measured by the LIDAR or, where not available, cloudiness of less than 45% as measured by the pyrometer. Finally, a cut on the zenith angle between 5° and 62° was applied. This relatively strict data selection was defined in order to apply an uniform, non-tailored pipeline to the data, with the aim of generating an algorithm to extend ALP-oriented analysis to large datasets. The process resulted in the MAGIC selected observation times reported in Table 4.1.

In order to ensure the good quality of the analysis, we cross-checked our results by

comparing them with previously published lightcurves and SEDs from selected periods.

4.2.2 LST-1

LST-1 is the first prototype of a Large-Sized Telescope to be used in the CTAO Northern Array (Figure 1.7b). It is located at the Roque de los Muchachos Observatory, at a close distance from the MAGIC telescopes, where it has been in commissioning since 2018. LST-1 features a PMT camera with 1855 pixels and 4.3° field of view. The large size of the mirror, with a diameter of 23 m, allows it to reach an energy threshold of about 20 GeV, significantly lower than MAGIC. While awaiting for the construction of a CTAO Operations Building, a temporary commissioning container is used as a control room and a small computer cluster handles on-site data processing and storage. Operations are carried out with a similar schedule and in close coordination with MAGIC, given both the proximity of the telescopes and the large overlap in the collaboration members. Observations are often scheduled and performed jointly, with MAGIC and LST-1 effectively working as a three-IACT stereoscopic system [100].

The analysis of monoscopic LST-1 data is performed with the `lstchain` software [165], based on the official CTAO reconstruction pipeline `ctapipe` [164]. The basic analysis steps implemented in `lstchain` are the same described above for MAGIC (minus stereoscopic reconstruction), with a greater effort towards data standardization and native DL3 support.

We produced DL3 files for the selected observations starting from official DL2 files by the LST collaboration, available at the on-site IT cluster. These were subsequently cross-checked with the official DL3 production, which was made available at a later time during the analysis. We selected data from the sources of interest by applying similar cuts to those used for MAGIC data selection, focusing on the period between 2020 and 2024. The resulting selected observation time is reported in Table 4.1.

4.2.3 High-level analysis

Starting from DL3 files, the analysis of data from different instruments can be carried out identically. Gammapy v1.3 [283] and v1.1 [381] were used for the MAGIC and LST-1 analyses, respectively. Observations were performed in wobble mode, pointing the telescopes at an offset from the source position (ON region) in order to include signal-free regions (OFF regions) in the field of view. The background is estimated by the reflected regions method (Section 1.5.2), by using three ($\alpha = 1/3$) and one ($\alpha = 1$) background regions for the MAGIC and LST-1 datasets, respectively.

The first step of this analysis consists in reducing the data from each run into a dataset consisting of photon counts binned according to energy. We consider a reconstructed energy axis with 10 bins per decade defined between 50 GeV and 50 TeV for MAGIC data and between 10 GeV and 100 TeV for LST-1 data, respectively. The effects of choosing a different energy binning on the final results are discussed in Appendix D, where the impact of the finite energy resolution of the instruments is also evaluated by applying a constant energy bias to the source spectra. For fitting, we set low-energy thresholds of 25 GeV and 70 GeV for observations performed at a zenith distance smaller than 35° with LST-1 and MAGIC, respectively, while we adopt a common value of 100 GeV for both instruments at

larger zenith distances [62, 97]. We set the upper energy bound at 20 TeV.

We then produce a lightcurve for each source and instrument, in order to characterize spectral variability over the considered observation periods. Blazars are highly variable sources, exhibiting sudden flares during which their gamma-ray flux can increase by factors of 10–100 compared to their baseline (quiescent) state. We compute lightcurves by estimating the flux above 200 GeV in each run. For runs where the source is not detected at a statistical significance of at least 2σ, 95% CL upper limits are reported instead.

Depending on its activity state, the gamma-ray SED of a blazar can be typically best fit by different smooth spectral models, such as a power law (EQ. 1.7), exponentially cut-off power law (EQ. 1.9) or log-parabola (EQ. 1.10), including the absorption effect of EBL (EQ. 1.5). To identify different activity periods, we use the Bayesian blocks (BB) algorithm described in ref. [275] (see SECTION 2.6.2). We use the `measures` version of the algorithm to subdivide the run-wise lightcurves into temporal bins of similar flux levels. We set the *false alarm probability*, or false positive rate for the detection of a change point in the time series, to $p_0 = 0.0027$ (corresponding to the area under the tails of a standard Gaussian distribution computed at the 3σ level). Decreasing the value of p_0 increases the accuracy of the splits but decreases their number, thus reducing the temporal resolution of the data. The numbers of BBs for each MAGIC and LST-1 dataset are reported in TABLE 4.1.

The data in each BB are stacked by summing the counts in each energy bin across all runs in the BB. They are then fit to a ECPL and to a LP spectral model, including EBL absorption as given in ref. [142]. The model giving the lowest χ^2 is chosen as the favorite one for that particular block.

Full lightcurves and spectral parameters for the analyzed MAGIC data are reported in APPENDIX C.

4.3 Signal modeling

To model ALP-photon mixing along the line of sight from the sources to Earth, we start by considering the magnetic fields of the selected blazars' jets. We use the jet magnetic field based on the Potter-Cotter model and described in ref. [337] (see SECTION 3.4.1). Relatively simple leptonic models can often describe the VHE emission of BL Lacs such as those selected in our sample, which typically feature weaker internal gamma-ray absorption compared to FSRQs, along with smaller emission regions and stronger magnetic fields. The values used for the jet parameters are reported in TABLE 4.2 and adapted from ref. [219], except for the electron density normalization n_0 which is taken from ref. [382]. The location of the transition region along the jet is computed as $r_T = 10^5 r_S$, where $r_S = 2GM/c^2$ is the Schwarzschild radius of the supermassive black hole [221]. This value is taken to be equal to the reference radius r_0, where the magnetic field strength B_0 and the electron density n_0 are computed, and to the location of VHE emission r_{VHE}. The relative impact of these parameters was evaluated in refs. [337, 383], and we consider it as a systematic effect in APPENDIX D.

After accounting for propagation across the EBL, whose optical depth to gamma rays is modeled according to Domínguez et al. [142], we consider ALP-photon oscillation in the magnetic field of the Milky Way. The latter is assumed to follow the `neCL` model introduced by Unger and Farrar [347]. A comparison between the different Unger-Farrar models and the related effects to ALP-photon conversions was performed in ref. [384],

Target	Mrk 421	Mrk 501	BL Lac	1ES 1959+650
r_0 [pc]	6.02	0.3	0.12	0.10
B_0 [G]	0.03	0.8	2.68	1.88
n_0 [cm^{-3}]	8.5×10^3	4.5×10^4	8×10^5	7×10^2
$r_{\rm jet}$ [10^3 pc]	9.72	3.24	16.20	32.41
$\gamma_{\rm min}$	9	2	5	4
$\gamma_{\rm max}$	12	9	8	8
α	1.55	1.68	1.95	1.60

Table 4.2: Parameters of the jet magnetic field model; radius r_0 where B field is equal to B_0, electron density n_0 at r_0, jet length $r_{\rm jet}$, jet Lorentz factors $\gamma_{\rm min}$ and $\gamma_{\rm max}$ at $r_{\rm jet}$ and r_0, respectively, power-law index of electron energy distribution function α, radius at which helical field becomes toroidal r_T and distance of gamma-ray emission region from BH $r_{\rm VHE}$. Here we assume $r_T = r_{\rm VHE} = r_0$. Values are taken from ref. [219], with exception of n_0 which are provided in ref- [382].

where `neCL` was shown to provide the most consistent results compared to previous models (e.g. the one by Jansson and Farrar [339]). We therefore take this model as a reference, whereas the `base` and `expX` models can be used to bracket its uncertainty.

There is no evidence that any of the targets in our sample are located in strongly magnetized galaxy clusters, which would contribute with an additional turbulent magnetic field. Furthermore, as these are relatively close sources ($z < 0.1$), we also expect the effect of IGMF to be subleading. In order to explicitly verify the latter assumption, we computed $P_{\gamma\gamma}$ for BL Lac, the most distant source in our sample, considering different values of the ALP parameters. We assumed a cell-like structure of the IGMF with present-day coherence length $l_0 = 1\,$Mpc and intensity $B_0 = 10^{-12}\,$G, compatible with current constraints (Figure 3.6). While the IGMF introduces some additional spectral irregularities, we have estimated these effects to be subleading in comparison to those introduced by the magnetic fields of the jet and the Milky Way (Figure 4.2). We note however that a stronger IGMF strength $B_0 \simeq 1\,$nG, the maximum value allowed by the most recent upper limits [354], might introduce more relevant spectral deformations and would not necessarily be negligible. In any case, the IGMF would not be strong enough to introduce a spectral hardening at high energies and would only modify the irregularities in the spectrum.

For each BB, the intrinsic gamma-ray spectrum $\phi_{\rm int}(E)$ is taken to follow a ECPL or log-parabola shape as determined in the previous Section. The expected measured flux in the presence of ALPs is then obtained by multiplying the intrinsic flux by the photon survival probability (eq. 3.50), which can be computed as explained in Section 3.3. The computation of the photon survival probability $P_{\gamma\gamma}$ is performed using the gammaALPs software package [338]. This package defines a `ModuleList` class where different magnetic field environments can be added in sequence. The `ModuleList` can then be run to automatically compute $P_{\gamma\gamma}(E)$ following eq. 3.39, for initial state ρ_0 and fixed ALP parameters $(m_a, g_{a\gamma})$, over the line of sight from a given source. The mixing in the jets and in the galactic magnetic fields is implemented in the `MixJetHelicalTangled` and `MixGMF` classes, respectively. Examples of $P_{\gamma\gamma}$ as a function of energy for the four blazars considered and for different values of the ALP parameters are shown in Figure 4.3.

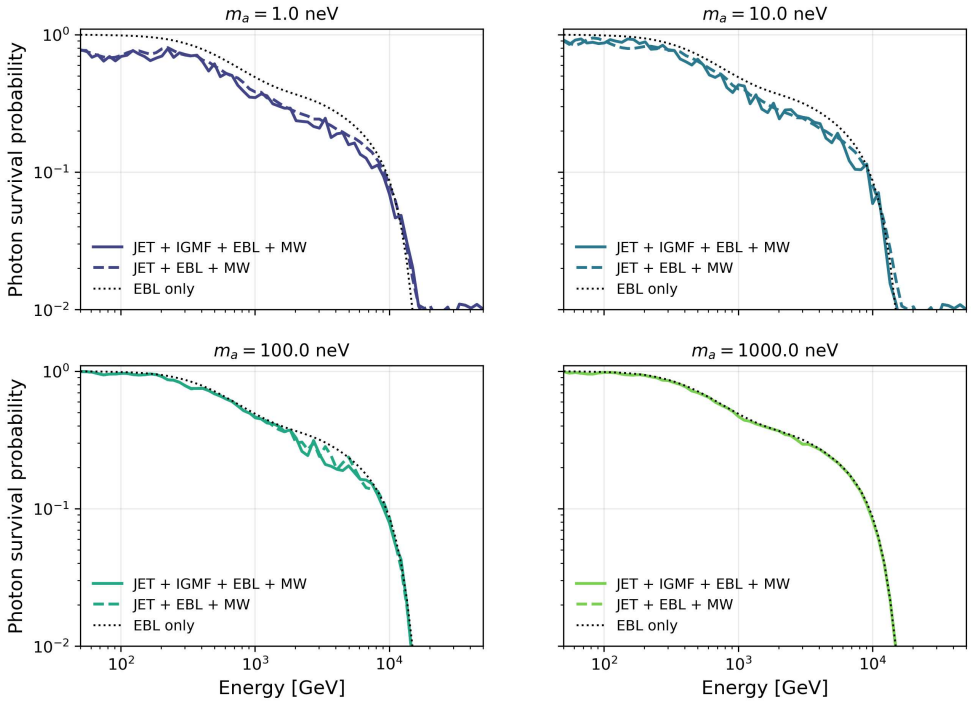


Figure 4.2: Photon survival probability for BL Lac, assuming $g_{a\gamma} = 2.0 \times 10^{-11}\text{GeV}^{-1}$ and $B_0 = 10^{-12}\,\text{G}$, for four different ALP masses and three magnetic field configurations. The solid lines correspond to photon–ALP mixing in the jet, the IGMF, and the Milky Way, where EBL attenuation is included in the IGMF modeling. The dashed lines represent the same scenario, but without the IGMF contribution. For comparison, the finely dashed line shows the photon survival probability considering EBL attenuation only.

4.4 Statistical analysis

To investigate whether ALP signatures are present in our data, we define for each i-th BB the Poisson ON/OFF likelihood

$$\mathcal{L}(m_a, g_{a\gamma}, \boldsymbol{\mu}_i, \boldsymbol{b}_i, \boldsymbol{\theta}_i | N_{\text{on}}, N_{\text{off}}) = \prod_{j=1}^{N_i} \left[\frac{\left(\mu_{ij} + \alpha_i b_{ij}\right)^{{N_{\text{on}}}^{ij}}}{{N_{\text{on}}}^{ij}!} e^{-(\mu_{ij}+\alpha_i b_{ij})} \frac{{b_{ij}}^{{N_{\text{off}}}^{ij}}}{{N_{\text{off}}}^{ij}!} e^{-b_{ij}} \right], \tag{4.1}$$

analogous to EQ. A.6, where N_i is the number of energy bins. The symbols $\boldsymbol{\mu}_i$ and $\boldsymbol{b}_i$ denote the sets of signal and background counts over all energy bins in the i-th BB. For clarity, the dependence of the likelihood on $(m_a, g_{a\gamma})$ and on the SED parameters $\boldsymbol{\theta}_i$ is indicated explicitly. In practice, it enters the likelihood via the signal expectation

$$\mu_{ik} = \int_{\Delta E_j} dE \int_{\Delta E'} dE'\; \phi^i_{\text{int}}(E'; \boldsymbol{\theta}_i)\; P_{\gamma\gamma}(E'; m_a, g_{a\gamma})\; \text{IRF}^i(E \mid E')\,, \tag{4.2}$$

defined analogously to EQ. A.7.

The values $\hat{\boldsymbol{\theta}}_i(m_a, g_{a\gamma})$ that maximize the likelihood at each point in the ALP parameter space are obtained by fitting each spectral model to the data with Gammapy. We then

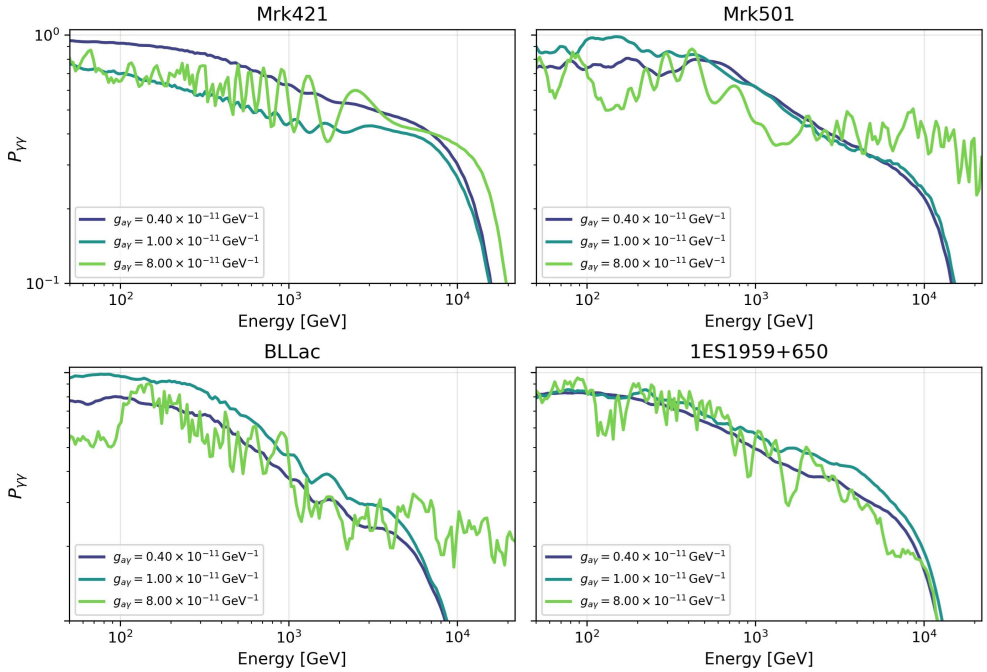


Figure 4.3: Photon survival probability for the four sources considered in this analysis, shown for $m_a = 50\,\mathrm{neV}$ and three representative values of $g_{a\gamma}$. The comparison illustrates both the dependence of the survival probability on the ALP parameters and the differences arising from the intrinsic jet magnetic-field modeling and source distance.

define the WSTAT variable

$$\begin{aligned} W_i(m_a, g_{a\gamma}) &= -2\log\mathcal{L}(m_a, g_{a\gamma}, \mu_{ij}, b_{ij}, \boldsymbol{\theta}_i | N_{\mathrm{on}}, N_{\mathrm{off}}) + 2\log\hat{\mathcal{L}}_i \\ &= 2\sum_{j=0}^{N_i}\left(\mu_{ij} + (1+\alpha_i)\hat{b}_{ij} - {N_{\mathrm{on}}}^{ij}\ln\left(\mu_{ij} + \alpha_i\hat{b}_{ij}\right) - {N_{\mathrm{off}}}^{ij}\ln\hat{b}_{ij} - C\right), \end{aligned} \tag{4.3}$$

where $\hat{\mathcal{L}}_i$ is the analytical maximum of the likelihood and C is a constant term that can be expressed in terms of N_{on} and N_{off} (see eq. 1.11).

This quantity can be considered as being asymptotically distributed as a χ^2 random variable with effective number d_i of degrees of freedom, approximately given by

$$d_i \;\approx\; N_i - p_i\,, \tag{4.4}$$

where $p_i = 3$ is the number of free SED parameters fit in block i. These could be, e.g., $(\phi_0, \Gamma, E_{\mathrm{cut}})$ for ECPL or (ϕ_0, Γ, β) for LP. However, low numbers of counts resulting in empty or nearly empty bins can induce non-negligible deviations from these theoretical values.

The number of degrees of freedom $d_i(m_a, g_{a\gamma})$ for each BB is then calibrated over the $(m_a, g_{a\gamma})$ plane by dedicated Monte Carlo simulations in the following way. For a given BB i and for a fixed point $(m_a, g_{a\gamma})$ in the ALP parameter space, the corresponding spectral model is fit to the data and used to simulate a number of ON-OFF observations. Each of these simulated datasets is fit again to the spectral model and the corresponding $W_i^{\mathrm{MC}}(m_a, g_{a\gamma})$ statistic is computed. The resulting distribution of W_i^{MC} is then fit with

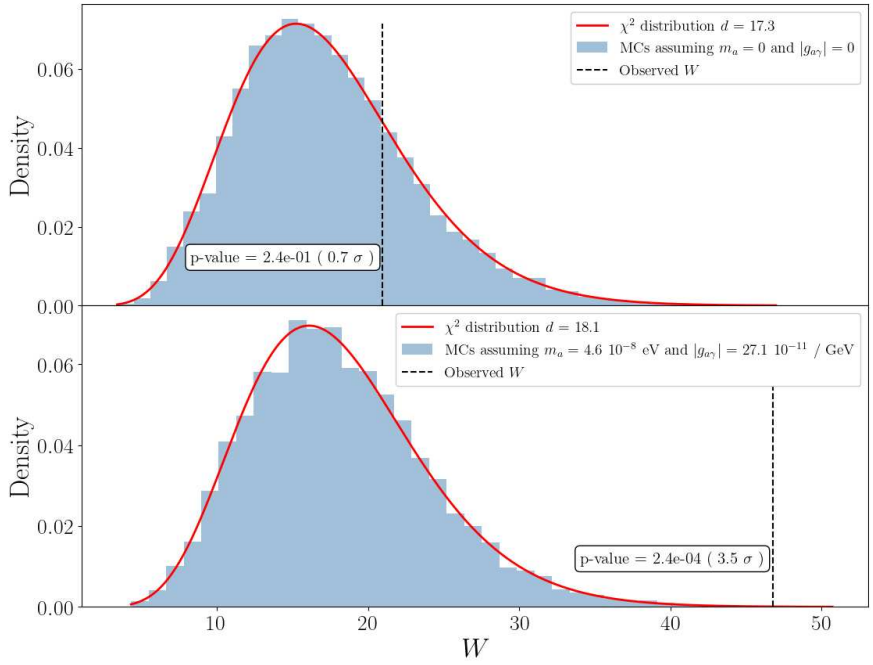


Figure 4.4: Distribution of the MC-simulated test statistic W_i^{MC} for a given BB both in the null hypothesis ($m_a = 0$, $g_{a\gamma} = 0$) and in the ALP hypothesis ($m_a = 4.6 \times 10^{-8}\,\mathrm{eV}$, $g_{a\gamma} = 27.1 \times 10^{-11}\,\mathrm{GeV}^{-1}$). The histograms show the W_i^{MC} values obtained from pseudo-experiments, while the red curves represent the best-fit χ^2 distributions. The vertical dashed lines indicate the observed W_i value from real data. The reported p-values and corresponding Gaussian significances quantify the level of disagreement between the model and data.

a χ^2 distribution, and the number of degrees of freedom is given by the expected value of the distribution (Figure 4.4).

After computing the block-wise test statistic $W_i(m_a, g_{a\gamma})$, the global test statistic is obtained by summing over all blocks,

$$W(m_a, g_{a\gamma}) = \sum_i W_i(m_a, g_{a\gamma})\,, \tag{4.5}$$

and can be treated as χ^2-distributed with number of degrees of freedom

$$d(m_a, g_{a\gamma}) = \sum_i d_i(m_a, g_{a\gamma})\,. \tag{4.6}$$

The statistical significance for excluding a point $(m_a, g_{a\gamma})$ in the ALP parameter space is then given by the p-value

$$p(m_a, g_{a\gamma}) = Q\left(\frac{d(m_a, g_{a\gamma})}{2}, \frac{W(m_a, g_{a\gamma})}{2}\right), \tag{4.7}$$

where

$$Q\left(\frac{s}{2}, \frac{x}{2}\right) = \frac{1}{\Gamma(s/2)} \int_{x/2}^{\infty} t^{s/2-1} e^{-t} \mathrm{d}t \tag{4.8}$$

represents the probability that a χ^2 variable with s degrees of freedom takes on a value larger than x. The integral in eq. 4.8 is also known as the *regularized upper incomplete gamma*

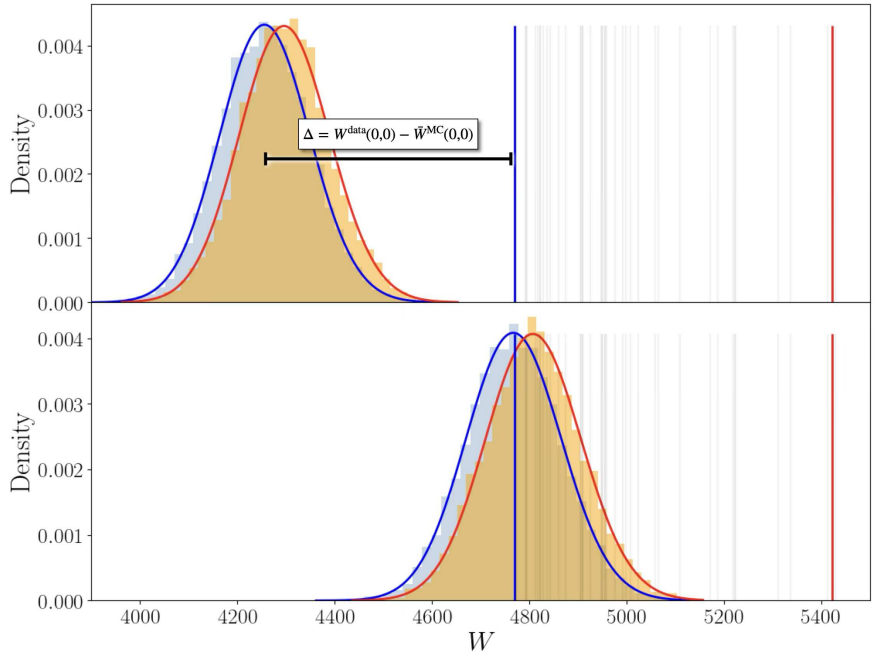


Figure 4.5: Original (top) and corrected (bottom) distributions of the test statistic W. The histograms show the distribution of W^{MC} values obtained under two hypotheses: the null hypothesis (blue) with $m_a = 0$ and $g_{a\gamma} = 0$, and an ALP benchmark hypothesis (red) with $m_a = 2.2 \times 10^{-8}$ eV and $g_{a\gamma} = 0.4 \times 10^{-11}\,\text{GeV}^{-1}$. Solid curves represent the best-fit χ^2 distributions, while vertical lines indicate the corresponding observed W values for each hypothesis (blue for null, red for benchmark ALP). Light grey vertical lines show observed W values for other ALP hypotheses.

function. Thus, smaller p-values computed according to the previous equations indicate stronger exclusion of the corresponding ALP parameters. We express the exclusion significance in terms of an equivalent number of Gaussian standard deviation (z-score), given by

$$z = \sqrt{2}\,\text{Erf}^{-1}(1-p)\,, \tag{4.9}$$

where $\text{Erf}^{-1}(x)$ is the inverse of the error function

$$\text{Erf}(x) = \frac{2}{\sqrt{\pi}} \int_0^x e^{-t^2}\,\text{d}t\ . \tag{4.10}$$

The procedure outlined above was repeated over a grid of 11×11 logarithmically spaced points in the ALP parameter space spanning a mass range $m_a \in [1, 1000]$ neV with ALP-photon coupling $g_{a\gamma} \in [0.1, 50] \times 10^{-11}\,\text{GeV}^{-1}$, which is motivated by the arguments given in Chapter 3.

In cases where the intrinsic SED model provides a poor fit to the data, leading to large observed W values under the null hypothesis, a further calibration step is applied. In order to do so, we first check that $W(m_a, g_{a\gamma}) \gtrsim W(0,0)$ for all tested ALP parameters, indicating that the mismatch between model and data under the null hypothesis not due to the presence of an ALP signal. We then shift the simulated W distributions as

$$W^{\text{MC}}(m_a, g_{a\gamma}) \to W^{\text{MC}}(m_a, g_{a\gamma}) + \Delta\,, \tag{4.11}$$

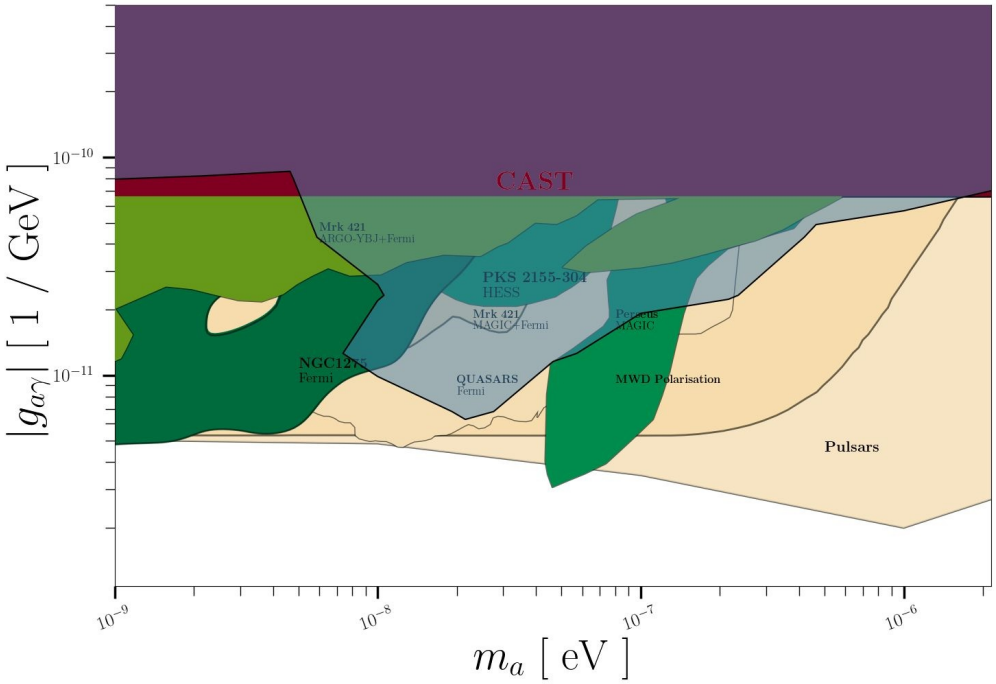


Figure 4.6: ALP exclusion region at 95% confidence level (2σ) obtained from the MAGIC and LST-1 blazar analysis (shaded in blue), compared with other experimental limits from the literature collected in ref. [307]. The contour is drawn by linear interpolation of the values on the ALP parameter grid.

where

$$\Delta = W(0,0) - \bar{W}^{\mathrm{MC}}(0,0) \tag{4.12}$$

is the discrepancy between the observed W value under the null hypothesis and the average of the simulated distribution (Figure 4.5). This shift effectively accounts for the observed discrepancy when estimating the number of degrees of freedom from simulations.

We highlight here the *modularity* of this block-wise approach. By computing the statistic $W_i(m_a, g_{a\gamma})$ and calibrated degrees of freedom $d_i(m_a, g_{a\gamma})$ separately for each data block, it is possible to combine data from different sources, instruments and observation periods in an incremental fashion, thus allowing for integration of new data as soon as they are available.

4.5 Results and discussion

Figure 4.6 shows the region of the parameter space that can be excluded above a confidence level of 95%, determined as described above, compared with reference limits from the literature.

While no previously unconstrained ALP parameters can be excluded by this analysis, VHE gamma rays represent a complementary probe for studying the effect of ALPs on cosmological photon propagation. In this respect, our limits sit between those obtained from observations of NGC 1275 with *Fermi*-LAT [364] and MAGIC [365], and broadly agree with those obtained from the observation of FSRQs with *Fermi*-LAT [369].

Nevertheless, these results highlight some interesting points. The block-wise statistical method presented above is flexible to the addition of new data, allowing new values of W_i and d_i to be summed into the global test statistic W and total degrees of freedom d without having to recompute likelihoods for the entire dataset. This potentially provides an easy way of improving these limits in the future by considering more sources or recent observations.

The blazar datasets used here are the largest yet analyzed for the purpose of ALP searches in the context of VHE astronomy. Despite this, by plotting the individual exclusion contours obtained from each BB, we conclude that the contribution to the overall limits is mostly due to very bright flaring states, and consequently there is no great benefit in adding large amounts of data taken during quiescent states given the performance of currently operating telescopes. It should be noted that this situation might considerably improve with the advent of CTAO, thanks to its greater sensitivity to lower photon fluxes and enhanced energy resolution. This is discussed in detail in the next Chapter.

On the other hand, we also argue that the modeling of the magnetic field in the blazar jets used in this work is affected by large systematic errors, and that it is based on a model of the jet whose aim is to describe the average states of the sources. Therefore, rather than by adding more data, these limits might be made more accurate with a better knowledge of the field strength and morphology. We discuss some of these systematic effects and how they impact our final results in Appendix D. Building on these preliminary results, a next phase in this study will involve a dedicated modeling of the magnetic field parameters in each BB, using multiwavelength data provided by tools such as the Markarian Multiwavelength Data Center [385].

We finally stress the importance of producing "legacy" high-level datasets for each experiment by efficiently and uniformly analyzing large amounts of data. In the context of collaborations such as MAGIC, products like the 10-year data samples presented in Appendix C can be made available to all members (and, possibly, to a more extended astrophysical community) to be used in the study of different science cases.

CHAPTER 5

CTAO sensitivity to ALPs from blazars

5.1 Source modeling and simulation

5.1.1 Source selection

As discussed in Section 2.5.2, the observation of AGNs is one of the Key Science Projects (KSPs) proposed for CTAO, to be carried out within the first 10 years of operation of the observatory. One of the declared goals of the AGN KSP is to study possible imprints of new fundamental physics on the cosmological propagation of gamma-rays, including ALP searches (see Section 1.4.3). In this Chapter, we present simulated CTAO observations of two bright BL Lacs and the subsequent derivation of projected exclusion regions in the ALP parameter space.[1]

To estimate CTAO's capability of constraining an ALP signal from blazars, we focus on two of the most well-known and studied TeV emitters: Mrk 501 and PKS 2155−304. Both are high-synchrotron peaked BL Lac objects (HBLs), featuring significant emission at TeV-scale energies, and are included in the plans for long-term monitoring and high-quality spectral measurements of the KSP described above [124]. This guarantees that CTAO will be able to gather a large amount of good quality data from these sources, which will be available for applying our proposed analysis.

For the baseline states of our sources, we adopt the best-fit spectral models reported in the 4th *Fermi*-LAT Source Catalog Data Release 4 (4FGL-DR4) [26, 27]. For Mrk 501 and PKS 2155−304, these are simple log-parabola functions (eq. 1.10). Since there are no observational constraints on the gamma-ray emission of blazars above a few tens of TeV, we conservatively assume that the validity of these models can be extended up to 10 TeV (thus not fully exploiting the CTAO energy range). In other works, an exponential cutoff factor around 1 TeV in rest-frame energy was added to these spectra (e.g. [130]). We have checked that this modification does not significantly impact the extent of our final results.

Since the effect of EBL absorption is negligible in the *Fermi*-LAT energy range, we take the 4FGL models as representative of the intrinsic spectra of the sources, and apply the EBL absorption factor to account for flux reduction at higher energies. We employ tabulated values of the optical depth as computed in the model of Domínguez et al. [142]. We

[1] The work presented in this Chapter has been carried out within the CTAO Consortium and will be the subject of a future publication, currently undergoing peer review.

Source	Model	ϕ_0	E_0	Γ	β	$E_{\rm cut}$	Ref.
	Baseline	$[10^{-12}\,\mathrm{MeV^{-1}\,cm^{-2}\,s^{-1}}]$	[MeV]				
Mrk 501	LP	3.76 ± 0.05	1535.09	1.75 ± 0.01	0.019 ± 0.004	–	[27]
PKS 2155−304	LP	12.59 ± 0.13	1160.97	1.77 ± 0.01	0.042 ± 0.004	–	[27]
	Flaring	$[10^{-10}\,\mathrm{TeV^{-1}\,cm^{-2}\,s^{-1}}]$	[TeV]			[TeV]	
Mrk 501	LP	18.6 ± 0.06	0.3	1.73 ± 0.06	0.13 ± 0.03	–	[232]
PKS 2155−304	ECPL	4.51 ± 0.36	1.0	2.16 ± 0.05	–	1.74 ± 0.24	[386]

Table 5.1: Parameters of the spectral models used for the sources considered in this work. We note that the β parameter for the Mrk 501 flaring state is scaled by a factor $\ln(10)$ with respect to ref. [232] after the conversion from base-10 logarithm to natural logarithm.

Source	z	RA [deg]	Dec [deg]	gammaALPs parameters						
				`r_0` [pc]	`B0` [G]	`gmax`	`gmin`	`n0` [$\mathrm{cm^{-3}}$]	`rjet` [pc]	`alpha`
Mrk 501	0.034	253.47	39.76	0.36	0.81	9	2	4.5×10^4	3.2×10^3	1.68
PKS 2155−304	0.116	329.72	−30.23	0.33	0.82	15	7	1.65×10^4	3.2×10^3	1.70

Table 5.2: Summary table of the astrophysical parameters of the selected blazars. The gammaALPs parameters used for modeling the jet magnetic field are adapted from refs. [219] and [382]. Additionally, the parameters `rvhe` and `r_T` are used, both set equal to `r_0` and taken to be ~ 100 times the size of the transition region R_T. Unspecified parameters are set to their default values.

will discuss the impact of this choice on our final results in Appendix D.

In addition to the *Fermi*-LAT baseline states, we consider for each source a flaring state taken from previous VHE measurements. Specifically, we take the Mrk 501 flare observed by the MAGIC-I telescope on 30 June 2005 [232], which is again well-fit by a LP shape, and the historical PKS 2155−304 flare observed by H.E.S.S. on 29 July 2006 [386], which follows an ECPL (eq. 1.9). These spectra are corrected for EBL absorption and, as in the previous case, we assume their validity up to 10 TeV and we extrapolate them down to 30 GeV.

The selection of spectral parameters for each source and activity state is reported in Table 5.1. The flaring spectrum chosen for PKS 2155−304 corresponds to the data taken with the lowest energy threshold (200 GeV), labeled as `T200` in ref. [386].

5.1.2 Data simulation and analysis

The effect of ALP-photon oscillations on the gamma-ray spectra of the selected sources is modeled as described in Section 4.3. We use gammaALPs v0.3.0 to compute the photon survival probability $P_{\gamma\gamma}$ as a function of energy for different sources and ALP parameter set. The astrophysical parameters for each blazar are given in Table 5.2, included those used for modeling the jet magnetic field according to the Potter-Cotter model, while the magnetic field of the Milky Way is modeled according to Jansson and Farrar [339]. Examples of the selected blazar spectra with and without ALP effects are shown in Figure 5.1.

CTAO observations are simulated using the Gammapy v1.0.1 Python package [171, 387]. For each source, we generate 50 hours of mock data for the baseline state and 5 hours (corresponding to about a night of observations) for the flaring state. We assume observations to be taken in wobble mode, by pointing the telescopes at an offset from the

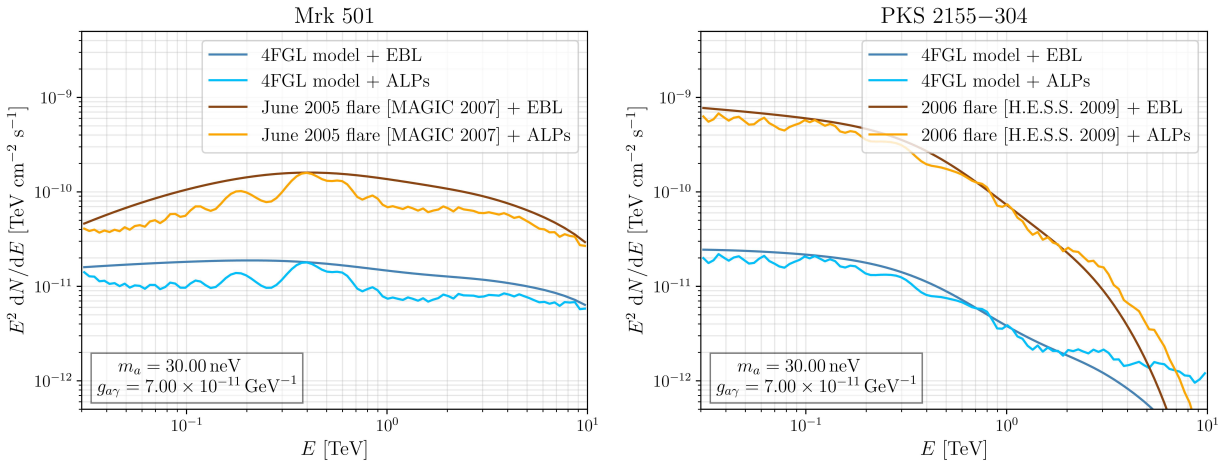


Figure 5.1: ALP effects on the baseline and flaring spectral shapes chosen for the sources in this work. For large enough values of $g_{a\gamma}$, both spectral distortions ("wiggles") and a hardening at high energies are visible.

Source	Livetime [h]	IRFs	Reference spectrum
Mrk 501 (baseline)	50	`Prod5-North-20deg-AverageAz-4LSTs09MSTs.180000s`	LP [27]
PKS 2155−304 (baseline)	50	`Prod5-South-20deg-AverageAz-14MSTs37SSTs.180000s`	LP [27]
Mrk 501 (flaring)	5	`Prod5-North-20deg-AverageAz-4LSTs09MSTs.18000s`	LP [232]
PKS 2155−304 (flaring)	5	`Prod5-South-20deg-AverageAz-14MSTs37SSTs.18000s`	ECPL [386]

Table 5.3: Observation times, IRF file names and reference spectra for the selected blazars.

source (the ON region) and estimating the background from a number of OFF regions symmetrically distributed around the center of the field of view. For this setup, we consider an offset from the source of 0.7 degrees, taking ON and OFF regions with a radius of 0.2 degrees. We choose 3 OFF regions, or equivalently, an acceptance ratio $\alpha = 1/3$. The redshift parameters reported in TeVCat[255] are used, and the source coordinates are fetched directly by using the `SkyCoord` class in Astropy.

We subdivide the measured energy axis with 20 bins per energy decade, in order to resolve the fine spectral irregularities that may be introduced by ALP effects. For each energy bin i, the expected number of signal counts μ_i is obtained by convolving the observed flux ϕ_{obs} with the instrument response functions (IRFs), and then integrating over the energy bin width and observation time (eq. A.7). For our simulations we use the publicly available CTAO prod5 v0.1 IRFs [120], computed for the CTAO "Alpha" configuration. These include effective area, point spread function (PSF) and energy dispersion, as well as the background rates that can be used to compute the expected number of background counts per energy bin b_i. Different IRF files are available for 0.5, 5 and 50 hours of observations, both for the Northern and Southern Arrays in distinct subarray configurations, and for different values of zenith and azimuth angles. We simulate observations of Mrk 501 and PKS 2155−304 with the Northern and Southern Arrays, respectively, assuming all observations to be taken at a zenith angle of 20 degrees while averaging over the azimuth angle. The observational parameters used in simulating the datasets, as well as the chosen IRFs and spectral models, are summarised in Table 5.3.

Datasets are simulated by sampling the signal and background counts in each energy

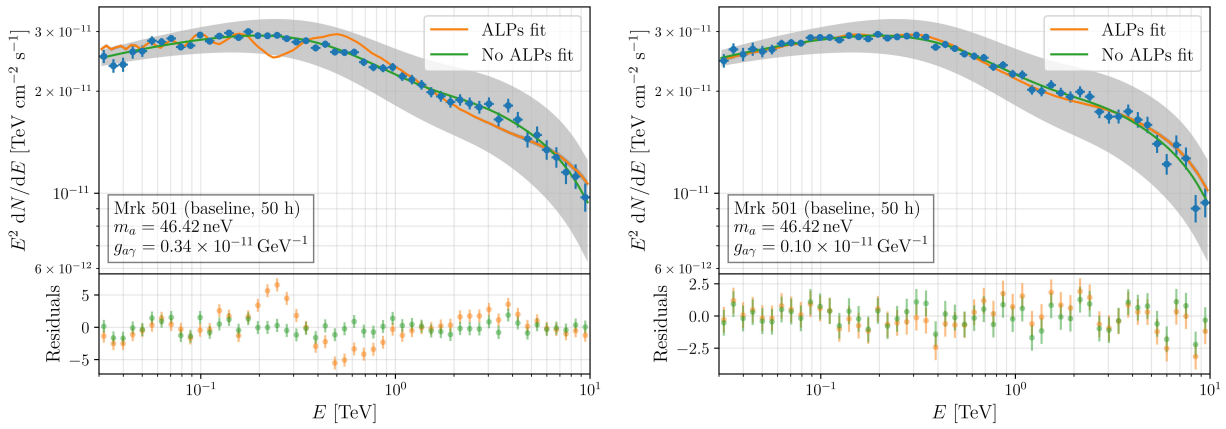


Figure 5.2: Example simulated SEDs for two 50-hour observations of the Mrk 501 baseline state. Spectral fits are shown for the ALP-less case and for two different ALP parameter sets. The residuals for both cases are computed as $(f - \phi)/\sigma_f$, where f is the measured flux with uncertainty σ_f and $\phi(E)$ is the model prediction (see ref. [130]).

bin from Poisson distributions, with average values $\mu_i + \alpha b_i$ in the ON region and b_i in the OFF regions respectively, using the `fake()` method provided by the `Dataset` class in Gammapy. Example simulated SEDs for the baseline state of Mrk 501 are shown in Figure 5.2.

5.2 ALP sensitivity derivation using the likelihood-ratio test

We consider a grid of 10×10 logarithmically spaced points over the ALP parameter space, with $m_a \in [0.1, 1000]$ neV and $g_{a\gamma} \in [0.03, 7] \times 10^{-11}\,\mathrm{GeV}^{-1}$. The choice of the mass interval is commonly adopted in similar studies, and roughly corresponds to the region where the critical energy for the strong mixing regime falls within the CTAO energy range (see Section 3.5). On the other hand, the upper bound on $g_{a\gamma}$ is motivated by the most recent experimental limit set by the CAST helioscope [322].

Given the intrinsic spectrum of each source, we compute the photon survival probability $P_{\gamma\gamma}$ for each $(m_a, g_{a\gamma})$ pair with gammaALPs, and obtain the expected observed spectrum as in eq. 3.50. The likelihood function is given by

$$\mathcal{L}(m_a, g_{a\gamma}, \boldsymbol{\mu}, \boldsymbol{b}, \boldsymbol{\theta} | N_{\mathrm{on}}, N_{\mathrm{off}}) = \prod_i \mathcal{L}(m_a, g_{a\gamma}, \mu_i, b_i, \boldsymbol{\theta} | {N_{\mathrm{on}}}^i, {N_{\mathrm{off}}}^i) \tag{5.1}$$

for a given dataset, following the notation introduced in the previous Chapters and in Appendix A. Each i-th energy bin contributes with a Poissonian term of the form given by eq. A.6, with ${N_{\mathrm{on}}}^i$ and ${N_{\mathrm{off}}}^i$ photon counts observed in the ON and OFF regions, respectively. The expected signal photon count in the i-th bin according to the ALP model with parameters $(m_a, g_{a\gamma})$ is indicated by μ_i, while b_i is the expected background photon count in the OFF regions. The expected signal count μ_i depends on the SED nuisance parameters (amplitude, spectral indices and cutoff energy), collectively denoted by $\boldsymbol{\theta}$. The nuisance parameters $\boldsymbol{\theta}$ and b_i, and consequently μ_i, are set to the values $(\hat{\mu}_i, \hat{b}_i, \hat{\theta})$ that maximize the likelihood for a given choice of $(m_a, g_{a\gamma})$. As in Section 4.4, we explicitly indicate the dependence of the likelihood on m_a, $g_{a\gamma}$) and $\boldsymbol{\theta}$.

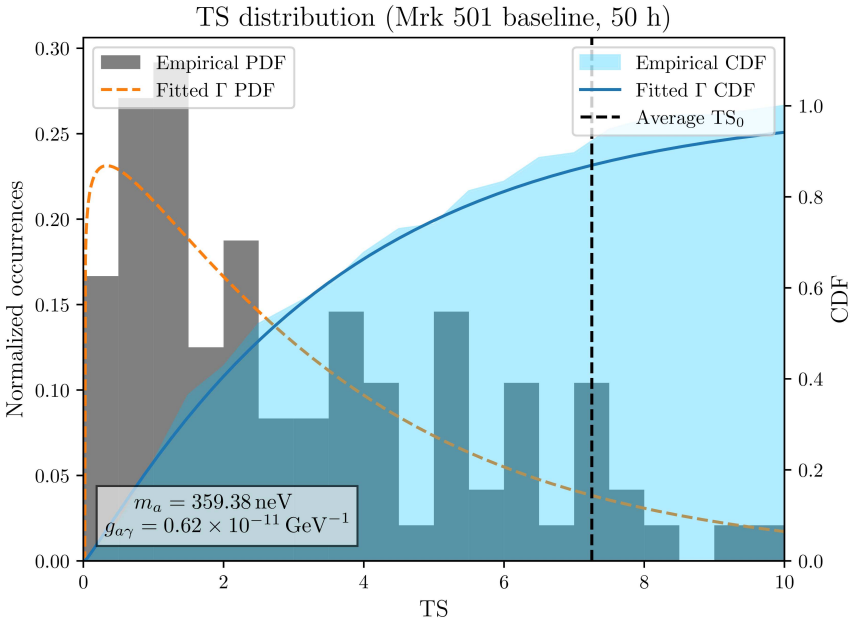


Figure 5.3: Example likelihood-ratio TS distribution obtained for the baseline state of Mrk 501. The empirical probability distribution function (PDF) and cumulative distribution function (CDF) are shown along with the best fits with a Γ distribution. The average value of the TS in the absence of ALPs, TS_0, is shown with a vertical dashed line.

We define the test statistic

$$\mathrm{TS}(m_a, g_{a\gamma}|N_{\mathrm{on}}, N_{\mathrm{off}}) = -2\ln\frac{\mathcal{L}(m_a, g_{a\gamma}, \hat{\boldsymbol{\mu}}, \hat{\boldsymbol{b}}, \hat{\boldsymbol{\theta}}|N_{\mathrm{on}}, N_{\mathrm{off}})}{\hat{\mathcal{L}}(N_{\mathrm{on}}, N_{\mathrm{off}})}\,, \tag{5.2}$$

where $\hat{\mathcal{L}}(N_{\mathrm{on}}, N_{\mathrm{off}})$ is the maximum likelihood for the given dataset over the considered ALP parameter space. In practice, maximizing the likelihood is equivalent to minimizing the WSTAT (eq. 1.11). This quantity is computed and returned by Gammapy when fitting each spectral model to the dataset D. Therefore, eq. 5.2 is equivalent to

$$\mathrm{TS}(m_a, g_{a\gamma}|N_{\mathrm{on}}, N_{\mathrm{off}}) = \mathrm{WSTAT}(m_a, g_{a\gamma}|N_{\mathrm{on}}, N_{\mathrm{off}}) - \mathrm{WSTAT}_{\mathrm{min}}(N_{\mathrm{on}}, N_{\mathrm{off}})\,, \tag{5.3}$$

and can be intuitively regarded as a measure of the discrepancy between any ALP model $(m_a, g_{a\gamma})$ and the one that best fits the data.

For each source (considered in both baseline and flaring states) we simulate 100 observations without including ALP effects, following the prescriptions outlined in Section 5.1.2, and compute the average TS for each $(m_a, g_{a\gamma})$ pair, denoted with $\mathrm{TS}_0(m_a, g_{a\gamma})$. In order to obtain the statistical significance for excluding the ALP hypothesis with parameters $(m_a, g_{a\gamma})$, one then needs to compare the obtained average against the TS distribution expected under the ALP hypothesis. As Wilks's theorem cannot be applied to the case of ALPs [130, 344, 365] and thus the shape of the TS distribution cannot be assumed a priori, we estimate it with a Monte Carlo approach. Therefore, for each $(m_a, g_{a\gamma})$ point and each considered source, we simulate 100 datasets including ALP effects and compute the corresponding TS values according to eq. 5.3. An example of a TS distribution obtained in this

way is shown in FIGURE 5.3. Following ref. [365], we fit these data to a Gamma distribution, generalizing of the χ^2 distribution used in the previous Chapter, whose probability distribution function (PDF) is given by

$$f(x, \alpha, \beta) = \frac{\beta^\alpha x^{\alpha-1} e^{-\beta x}}{\Gamma(\alpha)} . \tag{5.4}$$

In the previous expression, α and β are strictly positive parameters and $\Gamma(\alpha)$ is the gamma function

$$\Gamma(\alpha) = \int_0^\infty t^{\alpha-1} e^{-t} \, \mathrm{d}t \ . \tag{5.5}$$

The confidence level (CL) for excluding the ALP hypothesis $(m_a, g_{a\gamma})$ is then given by the cumulative distribution function (CDF) evaluated at $\mathrm{TS}_0(m_a, g_{a\gamma})$, i.e.

$$\mathrm{CL} = 1 - p = \mathrm{CDF}(\mathrm{TS}_0) \equiv \int_0^{\mathrm{TS}_0} f(x, \alpha, \beta) \, \mathrm{d}x \ , \tag{5.6}$$

where p is the corresponding p-value. Finally, the exclusion significance is expressed as the equivalent number of standard deviations (z-score) following EQ. 4.9 All the statistical computations discussed above were performed using the Scipy Python package [388].

Intuitively, it can be understood that for any $(m_a, g_{a\gamma})$ pair the TS distribution will generally be concentrated around small values: since the best-fitting ALP model will most likely be close to the model that was used to generate the datasets, the difference between the two log-likelihood values (measured by the TS) should be small and only due to statistical fluctuations. Conversely, the average of ALP-less datasets may present much larger TS_0 values for certain $(m_a, g_{a\gamma})$ pairs, which in turn would allow them to be excluded. We stress here that, since we are testing datasets *without* ALP effects and we are computing the significance for excluding the ALP hypothesis, our results should be interpreted as an estimate of CTAO's capability of constraining ALPs (i.e., placing upper limits on their parameter space) rather than discovering them.

5.3 ALP sensitivity derivation using machine learning

As mentioned above, the effects of ALP-photon conversions on gamma-ray spectra are highly nonlinear and not easily parametrized. The energy and amplitude at which spectral features appear depend in a nontrivial way from the morphology and intensity of the magnetic fields encountered by the ALP-photon beam along the line of sight from Earth. It is therefore interesting to see how non-parametric statistical methods can address this task, such as those provided by machine learning (ML) classification algorithms. A first step in this direction is to verify that a ML-based method can reproduce the results obtained by the classical likelihood-ratio test (LRT) discussed above.

Machine learning algorithms such as the random forest are extensively used in VHE gamma-ray astronomy, especially for the task of gamma-hadron discrimination (SECTION 1.5.1). These algorithms can act on a *sample*, identified by a vector of features $\mathbf{X} = (X_1, \ldots, X_n)$, and output a set of scores indicating how likely the given sample is to belong to each of the classes. In the following we shall focus on XGBoost (eXtreme Gradient Boosting) [389], a similar algorithm to the RF, which leverages a technique called *gradient boosting*

to efficiently minimise the loss function. Implementations of the XGBoost algorithm are available in several programming languages and generally exhibit reasonably good performance "out of the box", with minimal tweaking compared to RFs.

Given a simulated observation by CTAO, we consider the corresponding feature vector $\mathbf{X}$ whose elements are the excess photon counts in each energy bin above background. In the case of a real analysis, we assume the background to have already been subtracted by conventional methods (e.g. by reflected regions). For each of our selected sources and activity states, we define a grid of classifiers over the points of the ALP parameter space considered in the previous Section. The classifier corresponding to each $(m_a, g_{a\gamma})$ pair is trained to distinguish between 20 000 simulated datasets including ALP effects and 20 000 only accounting for EBL absorption. A similar approach was applied in ref. [390] to the case of X-ray data.

The excess counts are then normalised to the $[0, 1]$ interval, so that the only relevant characteristic for classifying the spectra is their *shape*, given by the intrinsic differences between adjacent bins rather than the overall number of counts. In order to allow for some variability in the intrinsic spectrum, avoiding to overfit the classifiers to a specific model, the training datasets are simulated by uniformly sampling values of each spectral parameter π in the range $[\pi - \Delta\pi, \pi + \Delta\pi]$, according to the values reported in Table 5.1. We have checked that the classifier performance only improves slightly by further increasing the number of training datasets.

The classifiers in the grid are based on the Python implementation of the XGBoost algorithm, using the following fiducial hyperparameters:

```
n_estimators=100, max_depth=3, reg_alpha=10., reg_lambda=500., eta=0.3
```

The first two hyperparameters represent, respectively, the number of trees in the ensemble and the maximum depth of each tree (i.e., the maximum number of sequential splits). The other hyperparameters correspond to the the α and λ parameters used in L1 and L2 regularization, which add penalty terms to the loss function in order to reduce overfitting, and the learning rate η, which controls the contribution of each new tree added during training. For complete definitions, refer to the XGBoost Python documentation.[2] While this choice is arbitrary to a certain extent, we computed the values of several metrics over the grid to check that the performance is reasonably good in the same regions of the parameter space where we expect ALP signatures to be stronger. These metrics are computed by training the classifiers on a subset of all labeled data (*training dataset*) and then checking how it performs on another subset (*test dataset*). As the values of these metrics can slightly change by changing the samples selected for the test dataset, *cross-validation* can be used to average over different training and test datasets.

A decrease in performance is indeed observed at large m_a and small $g_{a\gamma}$ values, in the lower right corner of the grid, where the spectral distortions due to ALPs are weaker and less distinguishable from the ALP-less case. As an example we consider *accuracy*, defined as the fraction of true negative (TN) and true positive (TP) identifications over the total number of samples S

$$\text{Accuracy} = \frac{\text{TN} + \text{TP}}{S}\,, \tag{5.7}$$

[2] https://xgboost.readthedocs.io/en/stable/

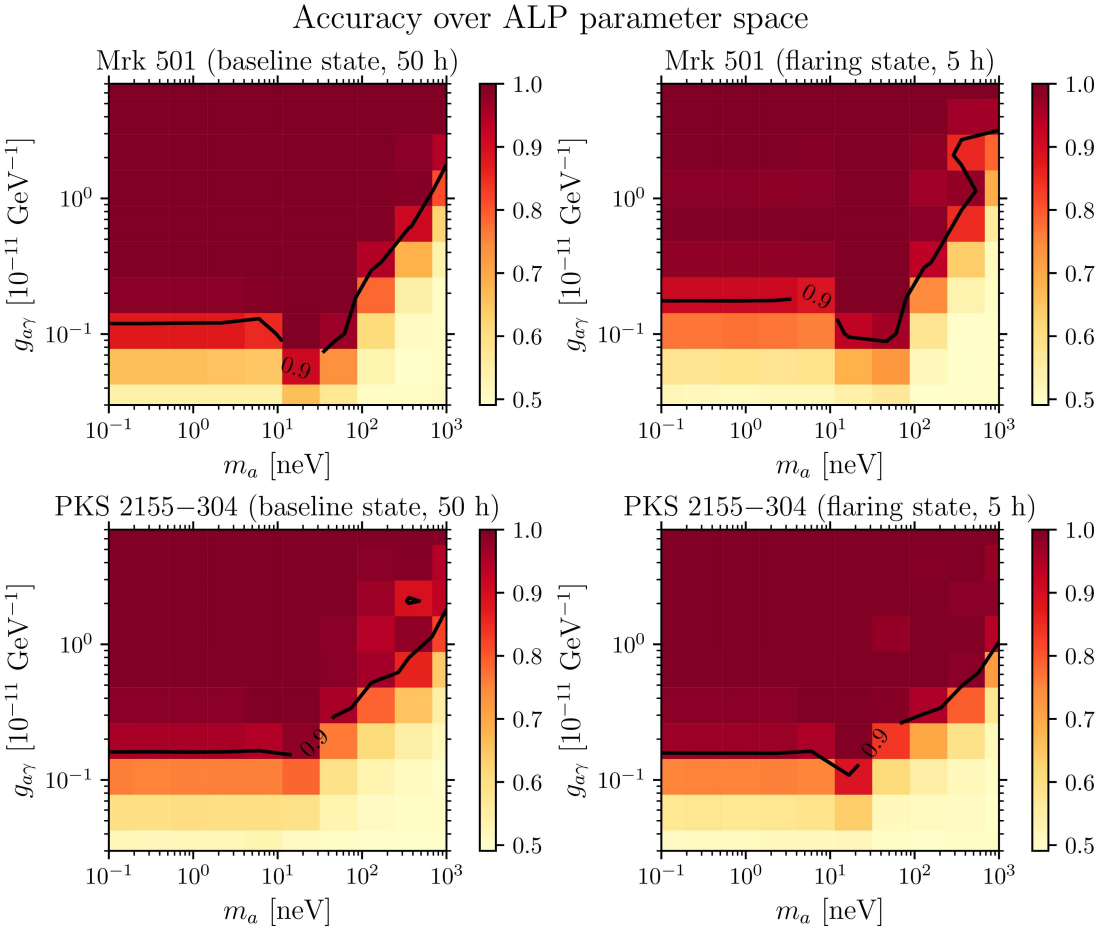


Figure 5.4: Accuracy of the XGBoost classifier grids defined over the ALP parameter space, with the 90% contours highlighted.

which is shown in Figure 5.4. In Appendix E we give definitions of several other metrics (precision, recall, F1 score) and show that they all follow a similar behavior over the ALP parameter space. These metrics were computed with Scikit-learn [391], using a 80-20 train-test split.

Once the classifier grid for each source and spectral state has been trained, it is applied to 100 simulated datasets without ALP effects generated as described in Section 5.1.2. For each dataset D, the classifier corresponding to each $(m_a, g_{a\gamma})$ pair returns a score $p_{\mathrm{ALP}}(m_a, g_{a\gamma}|D)$ representing how likely the dataset is to be classified as ALP-like[3]. We then define the quantity

$$\Pi(m_a, g_{a\gamma}|D) = 1 - p_{\mathrm{ALP}}(m_a, g_{a\gamma}|D) \tag{5.8}$$

and, similarly to the previous case, we denote the average value obtained from the 100 ALP-less datasets with $\Pi_0(m_a, g_{a\gamma})$.

We then search a Π distribution for each $(m_a, g_{a\gamma})$ pair, evaluating the Π statistic in eq. 5.8 for 2 000 simulated ALP-like datasets. Since Π is always valued between 0 and 1, we

[3]We note that in general this score is not a probability in a strict statistical sense, unless it is appropriately calibrated.

fit the resulting distribution to a Beta PDF

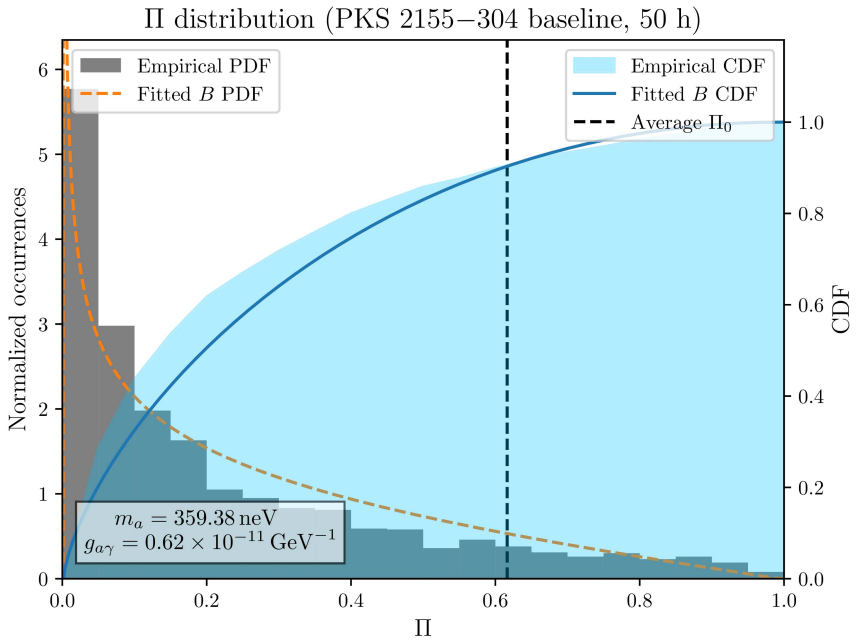
$$f(x, \alpha, \beta) = \frac{\Gamma(\alpha+\beta)x^{\alpha-1}(1-x)^{\beta-1}}{\Gamma(\alpha)\Gamma(\beta)}\,, \tag{5.9}$$

with $0 \leq x \leq 1$ and $\alpha, \beta > 0$. Using this distribution, the confidence level for excluding the ALP hypothesis and the z-score are computed using EQ. 5.6 and EQ. 4.9, respectively. The quality of the fit is generally good for medium and low values of $g_{a\gamma}$, as can be seen from FIGURE 5.5, but it worsens for higher ones.

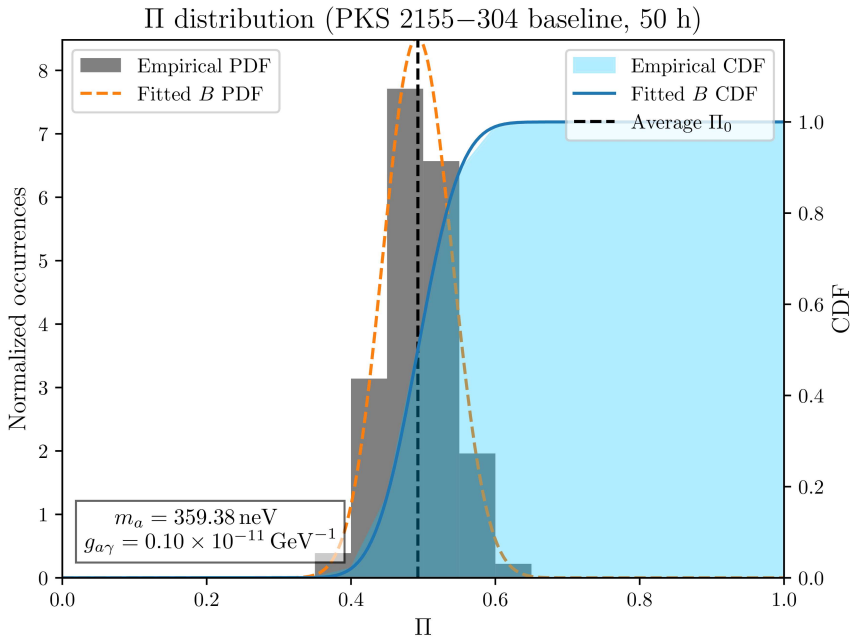
In cases where the classifier accuracy is maximal, i.e. for large $g_{a\gamma}$ values, the resulting Π distribution is largely peaked around very small values. In such extreme occurrences, the fit to the Beta distribution is typically poor. Moreover, the average value Π_0 obtained from the ALP-less datasets is usually close to 1, resulting in a confidence level for excluding the ALP hypothesis of essentially 100%, and consequently in a divergent z-score; see eqs. (5.6) and (4.9). A possible explanation of this behavior is found in the binary nature of the classifier algorithm, whose result is determined by averaging the predictions of several decision trees. When $g_{a\gamma}$ is small, the size of Poissonian fluctuations in the datasets is comparable with the ALP-related spectral features. In classifying the datasets, a decision tree applies splits on the features (in this case, photon counts in each bin) based on thresholds set during the learning process. Poissonian fluctuations may then cause the photon counts in certain bins to lie above or below these decision thresholds, leading different datasets to follow different splits along the tree and consequently forming a continuous distribution of Π values. On the other hand, in regions of the ALP parameter space where spectral features are large, the difference between different datasets due only to Poissonian fluctuations may be too small compared to the decision thresholds in the trees. This leads almost all datasets to follow the same splits in each classification tree, ultimately resulting in very similar predictions. As a consequence, when computing the Π statistic for 2 000 test datasets at high $g_{a\gamma}$, a highly peaked distribution is found.

In order to determine whether our main results hold under these limitations, we recomputed the exclusion confidence levels for each point in the ALP parameter space simply as the fraction of the 2 000 simulated $\Pi(m_a, g_{a\gamma})$ values smaller than $\Pi_0(m_a, g_{a\gamma})$. This approach is in fact equivalent to eq. (5.6), but it does not require to assume a specific distribution for Π. By doing so, we have explicitly checked that the 95% CL (2σ) sensitivity region on the ALP parameter space remain unchanged. On the other hand, without the smoothing provided by a fitting function, the z-score diverges to infinity much more quickly as $g_{a\gamma}$ increases. We conclude that higher-confidence limits (e.g. $3\sigma, 5\sigma$) obtained with the classifier-based method should be regarded as less reliable and more dependent on the quality of the fit.

Clearly, for a well-performing classifier, the Π distribution obtained in this way should be largely concentrated around small values, i.e. an ALP-like dataset is likely to be classified correctly. On the other hand, the Π_0 value from the ALP-less datasets should be quite high (close to 1), thus leading to exclusion of the ALP hypothesis. There are, however, some regions of the ALP parameter space where the spectra with and without ALP effects are hardly distinguishable, typically for large m_a and small $g_{a\gamma}$ values. The accuracy of the classifiers in these cases is then very low (FIGURE 5.4), as can be seen from a Π distribution peaked around 0.5, and no exclusion is expected. Example of distributions corresponding to these two situations are shown in FIGURE 5.5A and FIGURE 5.5B, respectively.



(A)



(B)

Figure 5.5: (A) Example distribution of the Π statistic defined in eq. (5.8). The distribution is concentrated around values of $\Pi < 0.5$ while the average value obtained in the no-ALP hypothesis (Π_0) is larger than 0.5. This behavior corresponds to a classifier correctly identifying ALP signatures. (B) The same distribution for a low-accuracy classifier. In this case, both the Π distribution obtained in the presence of ALPs and the average value Π_0 in the no-ALP hypothesis are around 0.5, indicating that the classifier cannot distinguish between the two scenarios.

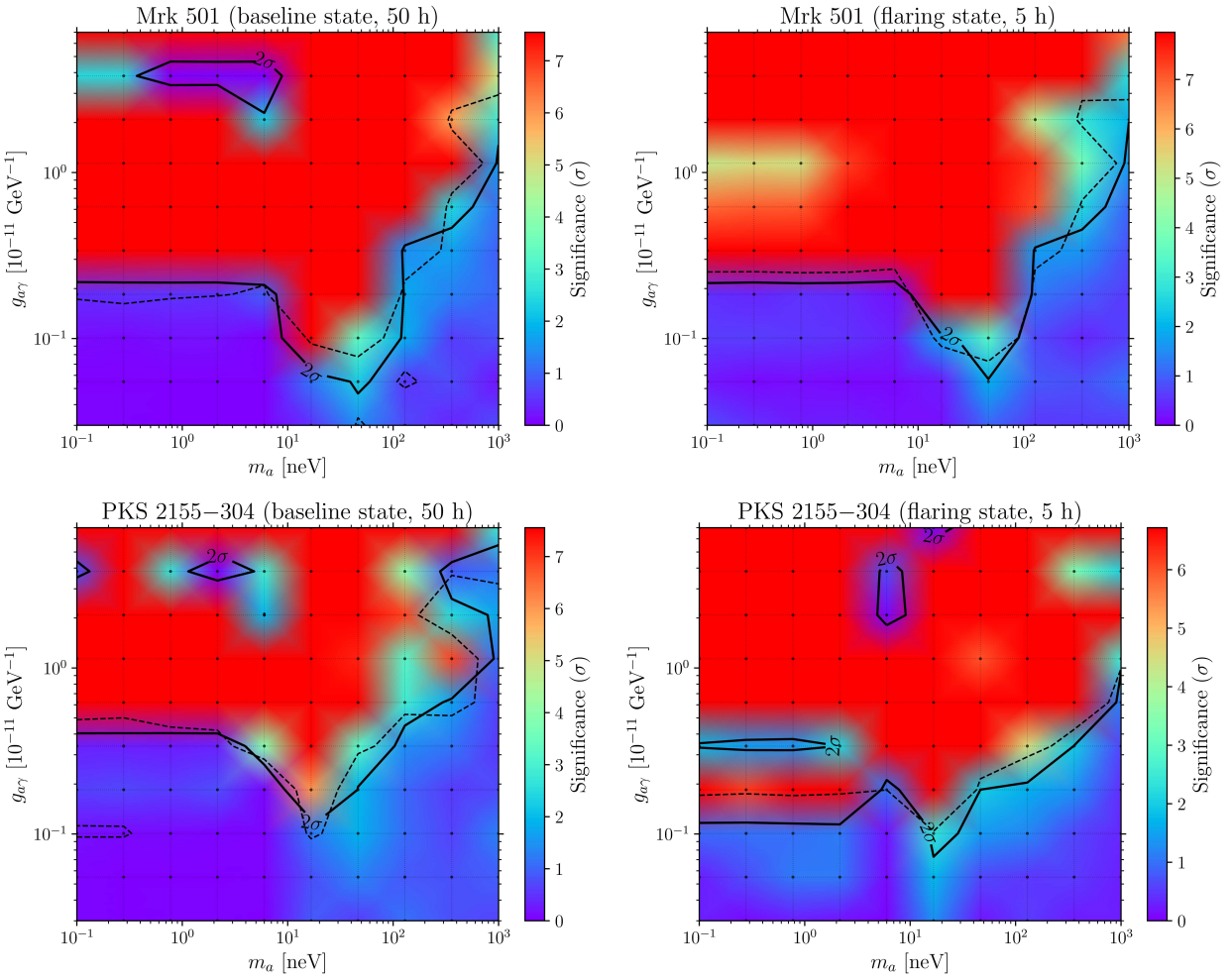


Figure 5.6: ALP exclusion significance computed with the ML-based method, with the 2σ contours highlighted (solid lines). The contours obtained at the same confidence level with the LRT method are shown as dashed lines for comparison. A linear interpolation was applied between the points in the parameter space for which the exclusion confidence level was computed, which are indicated as black dots.

5.4 Discussion of results

Our main results are presented in Figure 5.6, where a color map is used to represent the exclusion significance obtained with the ML classifier method in units of Gaussian standard deviations over the ALP parameter space. We note that, for both methods, the exclusion significance may be infinite for those points where the confidence level computed by eq. 5.6 is equal to 1. For plotting, these values are clipped to the highest finite significance.

The 2σ sensitivities obtained with the method of ML classifiers, shown as solid lines, are comparable with that resulting from the LRT (dashed lines). For all sources, the overall shapes and extensions of the projected exclusion regions are in agreement between the two methods, with occasional low-significance "holes" or high-significance "islands" in both sets of contours. Such features are common to other analyses of this kind [130, 364] and do not affect the expected upper bounds on $g_{a\gamma}$, which represent our main results.

The excluded region of the parameter space in the case of Mrk 501 is almost the same for both the baseline and flaring states. An explanation for this is the fact that the spectral shapes considered for the two states are fairly similar (see FIGURE 5.1), and that the increased brightness of the flaring state is compensated by the longer exposure used for the baseline state. Given this, we can assume that the photon counts in the considered energy ranges are above the CTAO sensitivity for both states and are equally affected by ALPs, thus leading to similar exclusions in the parameter space. Conversely, PKS 2155−304 exhibits a spectral curvature and a stronger EBL absorption effect that significantly reduce the flux at higher energies. In this case, a flaring state can indeed bring the flux of higher-energy photons above the CTAO sensitivity, thus improving the constraining power of the observations. These qualitative considerations are confirmed by computing the Li-Ma significance S of the signal (EQ. 1.6). While for Mrk 501 both observations yield $S \sim 300$, in the case of PKS 2155−304 a 5-hour flaring observation results in a significance $S \sim 800$, compared to $S \sim 200$ for a 50-hour observation in the baseline state.

These projections, representing the mean expected CTAO sensitivity to ALPs from each considered source, are obtained by averaging the results from many different simulated observations. A different approach for estimating such a mean sensitivity, employed in various studies on ALPs [130, 334, 344] and WIMPs [125, 127, 138], would be to use "Asimov datasets" [367] instead. These datasets are generated by simply setting the numbers of counts in the ON and OFF regions equal to their expected values, in order to eliminate Poissonian fluctuations and directly provide a median estimate of the sensitivity. We have checked explicitly that the contours obtained from a single Asimov dataset using the LRT method are very close to those resulting from averaging over many "noisy" datasets. On the other hand, we found that applying the ML classifiers to Asimov datasets causes a significant overestimation of the exclusion regions, as the total absence of noise in photon counts almost always produces low p_{ALP} values even for extremely small $g_{a\gamma}$. In a realistic analysis, these points of the parameter space would not be excluded, as the unavoidable Poissonian fluctuations in photon counts could easily mimic ALP effects at very low couplings. We thus conclude that Asimov datasets cannot be reliably used in estimating ALP sensitivities with ML classifiers.

As a final remark, we note that these results may be affected by several systematic effects, such as the choice of energy binning, magnetic field parameters and EBL model. We discuss these effects in APPENDIX D. We note, in particular, that recent measurements of the cosmic infrared background by the CIBER experiment might extend the allowed parameter space for ALPs to a wider region than what is expected from the commonly adopted EBL models [392].

In FIGURE 5.7 we compare the projections derived in this work with previously published constraints on the ALP parameter space[4]. Most of these are computed at the 2σ confidence level [130, 322, 364, 370, 374, 393, 394], except for the limits by MAGIC which are reported at the 3σ level [365]. In particular, ref. [130] represents the only previous estimate of ALP sensitivity officially published by the CTAO Consortium, derived from simulated observations of the AGN NGC 1275 inside the Perseus galaxy cluster. With these targets, we expect that CTAO will be able to place limits on a much wider portion of previously unconstrained ALP parameter space in the 0.1–100 neV mass range. We remark that, while already competitive, the limits derived from a Southern source like PKS 2155−304

[4]The reference limits are mostly taken from the online repository at ref. [307].

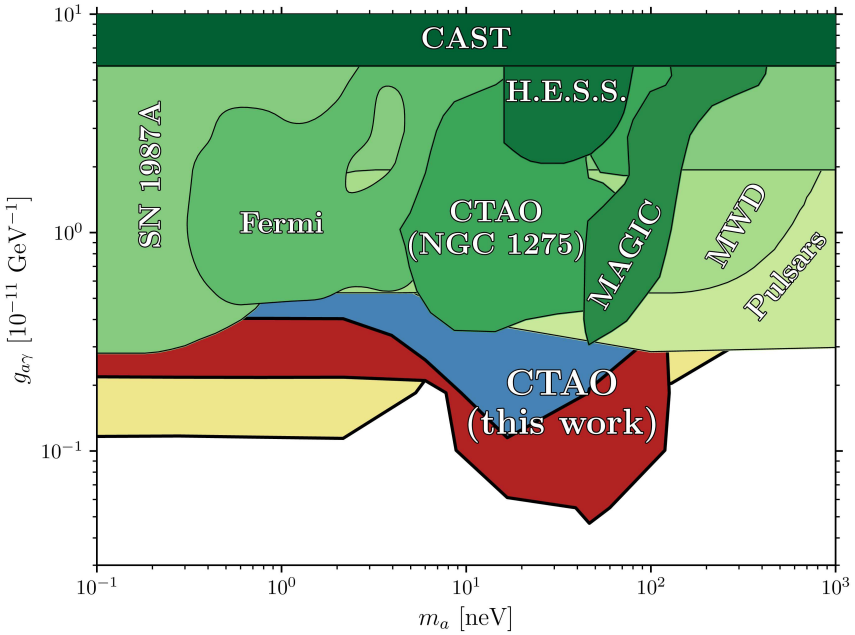


Figure 5.7: Comparison of the CTAO 2σ exclusion regions on the ALP parameter space obtained in this work with reference constraints from the literature [130, 322, 364, 370, 374, 393, 394], shown in green. The projected sensitivities obtained from 50-hour observations of Mrk 501 (red) and PKS 2155−304 (blue) in their baseline states, as well as that from a 5-hour observation of a PKS 2155−304 flare (yellow) are shown. We do not explicitly include the results obtained from the Mrk 501 flare as they largely overlap with those from the baseline observation.

could be further improved with the foreseen addition of 2 LSTs to the CTAO Southern Array [121, 122], whose contribution would increase the sensitivity to low-energy spectral oscillations.

CHAPTER 6

Conclusions and outlook

In this thesis work, an overview of the capabilities of the present and future generations of Cherenkov telescopes has been discussed. Particular emphasis has been placed on the potential of these instruments to study effects of new fundamental physics, such as the nature of the dark matter in the Universe or deviations from the standard cosmological propagation of photons.

Highly variable and luminous jetted active galactic nuclei, collectively known as blazars, are among the ideal targets to perform these searches. Their cosmological distance offers a natural baseline to probe ALP-photon conversions, while their extreme brightness allows for clear detection and accurate spectral analyses. The latter aspect is particularly evident during flaring episodes, where the observed flux can increase by factors of 10–100 compared to the average level. Blazars have been studied since the very beginning of VHE astronomy, but the understanding of the complex mechanisms behind their gamma-ray and broad-band emission still represents a formidable challenge. Extensive multi-wavelength observational campaigns are routinely carried out by space and ground-based observatories, often triggered by flaring states, in the effort to constrain or validate different emission models. Blazars dominate the extragalactic gamma-ray sky, with a large majority of BL Lacs in the VHE regime, and will be consistently targeted by the upcoming scientific program of the Cherenkov Telescope Array Observatory. CTAO aims to observe these objects with greater sensitivity and resolution than ever before, performing detailed spectral studies and long-term monitoring of selected sources. Observations of FSRQs with CTAO will most likely lead to new detections of sources of this class, typically under-represented in VHE blazar catalogs. In addition, a better determination of their spectral shapes will be possible, which in turn will provide useful information on the acceleration processes that regulate gamma-ray emission (Section 2.6).

A prominent example of a fundamental physics case that can be probed by these observations is represented by axion-like particles, hypothetical pseudo-scalar particles predicted by several extensions of the Standard Model of particle physics. While the original axion model was introduced to solve the strong $\mathcal{CP}$ problem in quantum chromodynamics, a plethora of ALPs has since emerged from different physical frameworks, such as string theory (*string axiverse*). This makes the search of these particles a paramount effort in modern theoretical and experimental physics, that is being pursued by astrophysical and cosmological means as well as by laboratory experiments (Figure 3.1).

In the context of VHE gamma-ray astronomy, hints of the existence of ALPs can show

up in the photon spectra of distant sources. ALPs mixing with photons in the presence of external magnetic fields of astrophysical origin, ubiquitous at all scales in the Universe, can introduce spectral irregularities on the otherwise smooth spectral shapes predicted by conventional physics, which could be detected by present and future gamma-ray instruments. In addition to this, the conversion of VHE photons into ALPs at the source would allow an ALP-photon beam to travel through the EBL without being absorbed (Figure 3.7). The reconversion of ALPs into photons in the magnetic field of the Milky Way would be observed as a photon recovery process, producing a hardening of the spectra of distant sources.

These effects were studied in Chapter 4 on a large sample of data from observations of four bright blazars (Markarian 421, Markarian 501, BL Lacertae and 1ES 1959+650) performed with the MAGIC and LST-1 imaging Cherenkov telescopes. The data from both instruments were analyzed by applying the method of Bayesian blocks to the lightcurves of each source and combining the individual results obtained for each block. No significant evidence of ALP signatures was found, and the outcome of the analysis was consequently expressed as an exclusion region on the ALP parameter space computed at the 95% confidence level (Figure 4.6). No previously unconstrained ALP parameters could be excluded by this analysis, which however still provides complementary limits to other searches. Furthermore, the "modular" approach employed allows for the easy integration of new data, even from different sources or instruments, in order to improve existing results. This is to be expected especially in the case of particularly bright flares, while no great benefit is foreseen from adding data taken during low states of the sources.

In Chapter 5, projections of the sensitivity of CTAO to constrain an ALP signal from blazars are presented. Observations of two blazars, Mrk 501 and PKS 2155−304, were simulated using the instrument response functions of the planned configurations of the CTAO Northern and Southern arrays, respectively. Both quiescent and flaring states were considered for each source, showing that in all cases a significant portion of the ALP parameter space could be newly excluded by these observations (Figure 5.7). This improvement can be interpreted in light of the greatly enhanced point source sensitivity and energy resolution that CTAO will possess compared to current instruments (Figure 1.9), which will make it possible to detect much fainter signals and weaker spectral signatures with unprecedented sensitivity. Furthermore, the recently proposed addition of 2 LSTs to the Southern Array in the context of the CTA+ project will contribute to further enhancing its sensitivity to low-energy spectral features, such as those that could be induced by ALPs.

All the results presented above are affected by large systematic errors, as discussed in Appendix D. These mainly stem from the uncertainty in the modeling of the morphology and intensity of the magnetic fields along the line of sight from the source. The magnetic field structure in blazar jets, in particular, is almost unconstrained experimentally and can only be estimated from theoretical arguments, thus making ALP searches from blazars somewhat model-dependent. In the absence of a more precise determination of this structure, turning to different computational approaches that could detect ALP-induced spectral features in a model-independent fashion might be a viable strategy. To probe this possibility, the CTAO sensitivity projections of Chapter 5 were computed both with the classical likelihood-ratio test and with a newly proposed method making use of machine-learning classifiers. While in the present context the classifier-based method uses the same modeling assumptions as the traditional method, thus not really solving the issue of sys-

tematic uncertainties, a promising result is shown by the fact that the sensitivities obtained by the two results broadly agree with each other (FIGURE 5.6). This is a first step in the direction of exploring different non-parametric methods for ALP searches in astrophysical data, in line with other recent works [390, 395]. Future developments of this concept will involve dedicated studies focused on the application of more complex and optimized algorithms, such as neural networks, with the aim of maximizing the attainable experimental sensitivity to ALPs while reducing the amount of model-dependent assumptions.

APPENDIX A

STATISTICAL NOTES

A.1 Derivation of the Li-Ma significance

In a gamma-ray observation performed with the ON-OFF technique, it can be assumed that the counts in the ON and OFF regions are random variables $N_{\rm on}$ and $N_{\rm off}$ following Poisson statistics, depending on unknown parameters $\langle N_S \rangle$ and $\langle N_B \rangle$ representing the expected number of signal and background counts in the ON region. The likelihood function is the probability of observing values $(N_{\rm on}, N_{\rm off})$ conditioned to the parameter values $(\langle N_S \rangle, \langle N_B \rangle)$, taken as a function of the parameters. It is given by[1]

$$\mathcal{L}(\langle N_S \rangle, \langle N_B \rangle | N_{\rm on}, N_{\rm off}) = \frac{(\langle N_S \rangle + \langle N_B \rangle)^{N_{\rm on}}}{N_{\rm on}!} e^{-(\langle N_S \rangle + \langle N_B \rangle)} \frac{(\langle N_B \rangle / \alpha)^{N_{\rm off}}}{N_{\rm off}!} e^{-\langle N_B \rangle / \alpha}, \quad \text{(A.1)}$$

where α is the exposure ratio between ON and OFF regions. If the regions are of the same size, this is given by the ratio of exposure times, while if multiple regions are observed simultaneously in a single FoV it is simply the ratio between the numbers of ON and OFF regions. In the hypothesis H_1 of a signal the maximum-likelihood estimates of the parameters are

$$\langle \hat{N}_S \rangle = N_{\rm on} - \alpha N_{\rm off}\,, \qquad \langle \hat{N}_B \rangle = \alpha N_{\rm off}\,, \quad \text{(A.2)}$$

while in the hypothesis H_0 of no signal (*null hypothesis*)

$$\langle N_S \rangle = 0\,, \qquad \langle \hat{N}_B \rangle = \frac{\alpha}{1+\alpha}(N_{\rm on} + N_{\rm off})\,. \quad \text{(A.3)}$$

By replacing these values in EQ. A.1, the maximum likelihood values under the two hypotheses $\mathcal{L}(H_0|N_{\rm on}, N_{\rm off})$ and $\mathcal{L}(H_1|N_{\rm on}, N_{\rm off})$ can be obtained. The maximum-likelihood ratio λ is given by [175]

$$\lambda = \frac{\mathcal{L}(H_0|N_{\rm on}, N_{\rm off})}{\mathcal{L}(H_1|N_{\rm on}, N_{\rm off})} = \left[\frac{\alpha}{1+\alpha}\left(\frac{N_{\rm on}+N_{\rm off}}{N_{\rm on}}\right)\right]^{N_{\rm on}} \left[\frac{1}{1+\alpha}\left(\frac{N_{\rm on}+N_{\rm off}}{N_{\rm off}}\right)\right]^{N_{\rm off}} \quad \text{(A.4)}$$

[1] It should be noted that the likelihood is sometimes written as $\mathcal{L}(\text{data}|\text{model})$ instead of $\mathcal{L}(\text{model}|\text{data})$, e.g. in ref. [175]. This notation emphasizes the definition of the likelihood as the probability of observing the data conditioned to the model. However, it should always be interpreted as a function of the model parameters, while the data are taken to be fixed.

and a likelihood-ratio test statistic (TS) of the form

$$\mathrm{TS} = -2 \ln \lambda \tag{A.5}$$

can be defined. The likelihood under the H_1 hypothesis depends on two parameters, while under the null hypothesis H_0 it depends only on $\langle N_B \rangle$, since $\langle N_S \rangle = 0$ by definition. According to Wilks' theorem [363], under the null hypothesis the TS is then distributed as a random variable following a χ^2 distribution with 1 degree of freedom. The variable $S = \sqrt{\mathrm{TS}}$, known as the Li-Ma significance [175] and given in EQ. 1.6, therefore follows a standard normal distribution with mean 0 and standard deviation 1. It can be directly interpreted as an equivalent number of standard deviations, meaning that if an observation yields, e.g., $S = 5$, the signal has a significance of 5σ. In other words, the probability (p-value) that a value $S \geq 5$ is observed under the null hypothesis is equal to that of observing a value greater than or equal to 5 in a standard normally distributed variable, i.e. $p \simeq 5.7 \times 10^{-7}$. The null hypothesis (no signal) is then rejected at the 5σ level in favor of the alternative hypothesis.

A.2 Model fitting and flux point estimation

Given a flux model $\phi(\mathbf{p}, E)$, the model parameters that best describe the observed data can be determined by a model fitting procedure. In the case of ON-OFF observations, each i-th energy bin and k-th spatial bin contributes with a Poissonian term similar to that used to define the Li-Ma significance (EQ. A.1)

$$\mathcal{L}(\mu_{ik}, b_{ik} | {N_{\mathrm{on}}}^{ik}, {N_{\mathrm{off}}}^{ik}) = \frac{(\mu_{ik} + \alpha\, b_{ik})^{{N_{\mathrm{on}}}^{ik}}}{{N_{\mathrm{on}}}^{ik}!} e^{-(\mu_{ik} + \alpha\, b_{ik})} \frac{{b_{ik}}^{{N_{\mathrm{off}}}^{ik}}}{{N_{\mathrm{off}}}^{ik}!} e^{-b_{ik}}\,, \tag{A.6}$$

where ${N_{\mathrm{on}}}^{ik}$ and ${N_{\mathrm{off}}}^{ik}$ are the observed counts in each energy and spatial bin in the ON and OFF regions, while μ_{ik} are the expected signal photon counts in the ON region and b_{ik} are the expected background photon counts in the OFF region(s). The expected number of signal counts is given by the convolution (*folding*) [130]

$$\mu_{ik} = t_{\mathrm{obs}} \int_{\Delta E_i} \mathrm{d}E \int_{\Delta \mathbf{p}_k} \mathrm{d}\mathbf{p} \int_{\Delta E'} \mathrm{d}E' \int_{\Delta \mathbf{p}'} \mathrm{d}\mathbf{p}'\, R(\mathbf{p}, E | \mathbf{p}', E') \phi(\mathbf{p}', E')\,, \tag{A.7}$$

where t_{obs} is the observation time, E and $\mathbf{p}$ are the reconstructed energy and direction with bin widths ΔE_i and $\Delta \mathbf{p}_k$. The actual physical values of these quantities are denoted as E' and $\mathbf{p}'$ and integrated over suitable intervals $\Delta E'$ and $\Delta \mathbf{p}'$. The IRF $R(\mathbf{p}, E | \mathbf{p}', E')$, connecting true and reconstructed quantities, is assumed to be factorised as

$$R(\mathbf{p}, E | \mathbf{p}', E') = A_{\mathrm{eff}}(\mathbf{p}', E') \times \mathrm{PSF}(\mathbf{p} | \mathbf{p}', E') \times E_{\mathrm{disp}}(E | \mathbf{p}', E')\,, \tag{A.8}$$

where $A_{\mathrm{eff}}(\mathbf{p}', E')$ is the effective area, given by the product of the collection area of the detector and its efficiency at a given energy and direction, while $\mathrm{PSF}(\mathbf{p} | \mathbf{p}', E')$ and $E_{\mathrm{disp}}(E | \mathbf{p}', E')$ are the point spread function and energy dispersion, which give the probability of reconstructing the direction and energy of a photon as $\mathbf{p}$ and E for given true values $\mathbf{p}'$ and E'. It should be noted that, in general, the instrument response may also depend on time.

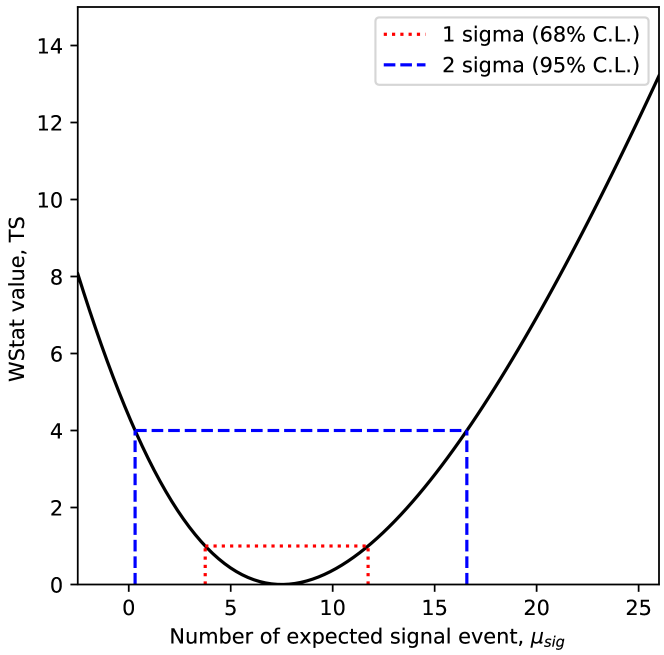


Figure A.1: Example WSTAT profile as a function of the expected number of signal counts. The best-fitting value is the one that minimizes the WSTAT, while 1σ and 2σ uncertainties are determined by the values of μ that increase the WSTAT by 1 or 4, respectively. This example can be easily translated to the case of flux point fitting, where the expected number of counts in the i-th bin μ_i only depends on the signal amplitude ϕ_0, while all other spectral parameters are fixed. Figure from https://docs.gammapy.org/2.0.1/tutorials/details/fitting.html.

Finally, the binned likelihood function

$$\mathcal{L}(\boldsymbol{\mu}, \boldsymbol{b}|N_{\text{on}}, N_{\text{off}}) = \prod_{ik} \mathcal{L}(\mu_{ik}, b_{ik}|{N_{\text{on}}}^{ik}, {N_{\text{off}}}^{ik}) \tag{A.9}$$

can be defined. The function $\mathcal{L}$ depends individually on the signal and background counts in each energy and spatial bin; the sets of counts across all bins are denoted as $\boldsymbol{\mu}$ and $\boldsymbol{b}$, respectively. Similarly, N_{on} and N_{off} denote the sets of observed counts in each bin of the ON and OFF regions. In addition, it is important to note that the likelihood is ultimately a function of the spectral model parameters (such as normalization, spectral index, or cutoff energy), which determine the expected signal counts $\boldsymbol{\mu}$ and background counts $\boldsymbol{b}$.

The model parameters that define $\phi(\mathbf{p}, E)$, such as the amplitude and spectral index of a power law, should be those corresponding to the values $(\hat{\boldsymbol{\mu}}, \hat{\boldsymbol{b}})$ that maximize the likelihood in eq. A.9. For computational reasons it is often preferred to *minimize* instead the quantity $-2\ln\mathcal{L}$. By neglecting terms that do not depend on $\boldsymbol{\mu}$ and $\boldsymbol{b}$, this is equivalent to minimizing the WSTAT given in eq. 1.11.[2] Using minimization algorithms such as Minuit [396], the model parameters are varied and the WSTAT is recomputed until a minimum is reached. At each iteration, the expected signal counts μ_{ik} are computed as in eq. A.7.

[2]The Gammapy implementation of WSTAT is detailed at https://docs.gammapy.org/dev/user-guide/stats/wstat_derivation.html

In the absence of a background model, the expected counts b_{ik} are set to the value $\hat{b}_{ik}(\boldsymbol{\mu})$ that maximizes likelihood for a given set $\boldsymbol{\mu}$ by imposing $\partial \ln \mathcal{L}/\partial b_{ik} = 0$ analytically. In this way, b_{ik} is treated as an additional parameter with no physical interest (nuisance parameter), and the resulting likelihood is referred to as a profile likelihood [362].

After fitting a global model to the data, the flux points in SEDs and light curves are estimated by re-fitting the amplitude ϕ_0 of the model in each energy bin (e.g. [24]). The best-fit value that minimizes the fit statistic defines the flux value $\phi(E)$ in the bin centered at energy E. The difference between a generic fit statistic value, with one free parameter ϕ_0, and its minimum

$$\Delta\mathrm{WSTAT} = \mathrm{WSTAT}(\boldsymbol{\mu}, \hat{\boldsymbol{b}}(\boldsymbol{\mu})|N_{\mathrm{on}}, N_{\mathrm{off}}) - \mathrm{WSTAT}(\hat{\boldsymbol{\mu}}, \hat{\boldsymbol{b}}|N_{\mathrm{on}}, N_{\mathrm{off}}) \tag{A.10}$$

follows approximately a χ^2 distribution with one degree of freedom, with its square root following a standard normal distribution [362]. Therefore, the 1σ error on the flux is given by the variation $\Delta\phi(E)$ such that the fit statistic difference is equal to 1. In case of low-significance bins, flux upper limits at 95% confidence level can be shown at $\phi(E) + 2\Delta\phi(E)$, corresponding to a fit statistic difference equal to 4 (Figure A.1).

If a background gamma-ray flux model is available, as e.g. in *Fermi*-LAT analyses, a simple Poissonian likelihood of the form

$$\mathcal{L}(\boldsymbol{m}|N) = \prod_{ik} \frac{m_{ik}}{N_{ik}!} e^{-m_{ik}} \tag{A.11}$$

can be used. The observed gamma-ray counts in each energy and spatial bin are given by N_{ik}, while $m_{ik} = m^{ik}_{\mathrm{sig}} + m^{ik}_{\mathrm{bkg}}$ is the expected number of counts according to both the signal and the background models. The symbols $\boldsymbol{m}$ and N denote the sets of expected and observed counts over all bins. The fit statistic to be used in this case is the Cash statistic [397]

$$C(\boldsymbol{m}|N) = 2\sum_{ik}(m_{ik} - N_{ik}\ln m_{ik})\,, \tag{A.12}$$

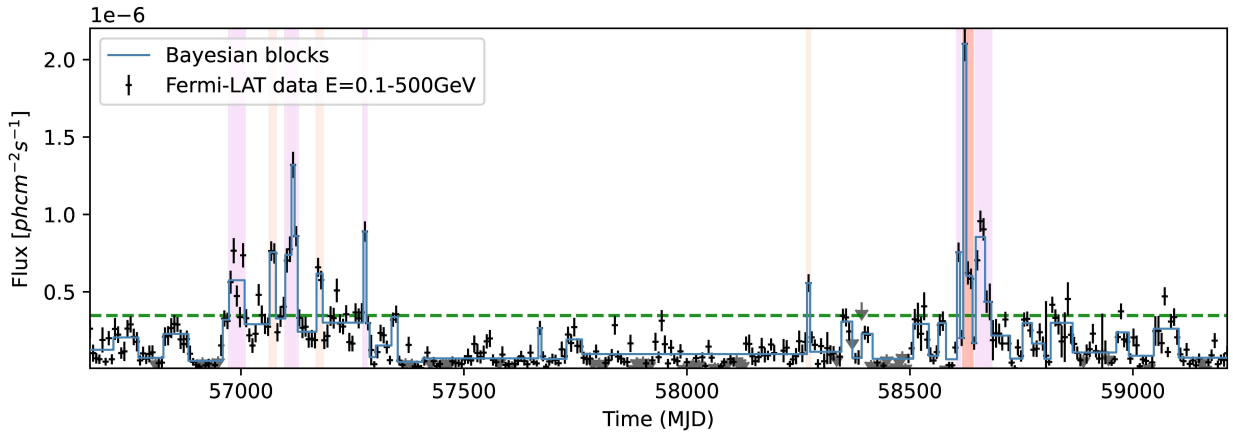
to which the same arguments as above can be applied.

APPENDIX B

Analysis and simulation of FSRQ data

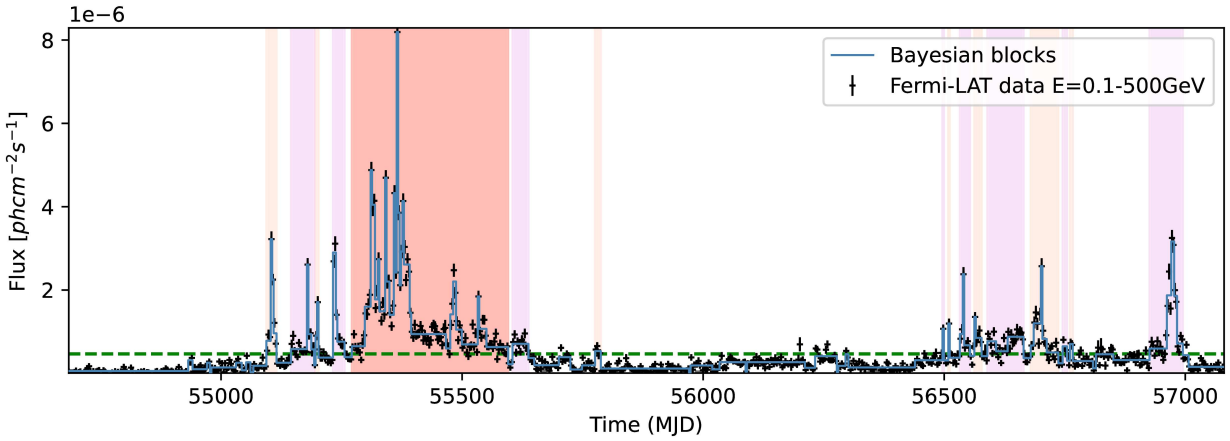
B.1 *Fermi*-LAT lightcurves

The *Fermi*-LAT lightcurves of the eight blazars considered in Section 2.6 are reported in Figure B.1, representing the integral flux between 0.1 GeV and 500 GeV in 3- or 7-day bins (see Table 2.1). Flaring periods above a mean flux threshold were identified using the HOP algorithm [280], following the approach presented in [282]. The brightest flare of each source was split into a rising and decaying phase (see Table 2.2) and used as a basis to simulate CTAO observations. The parameters obtained by fitting a ECPL spectral model to each flaring state are reported in Table B.1.

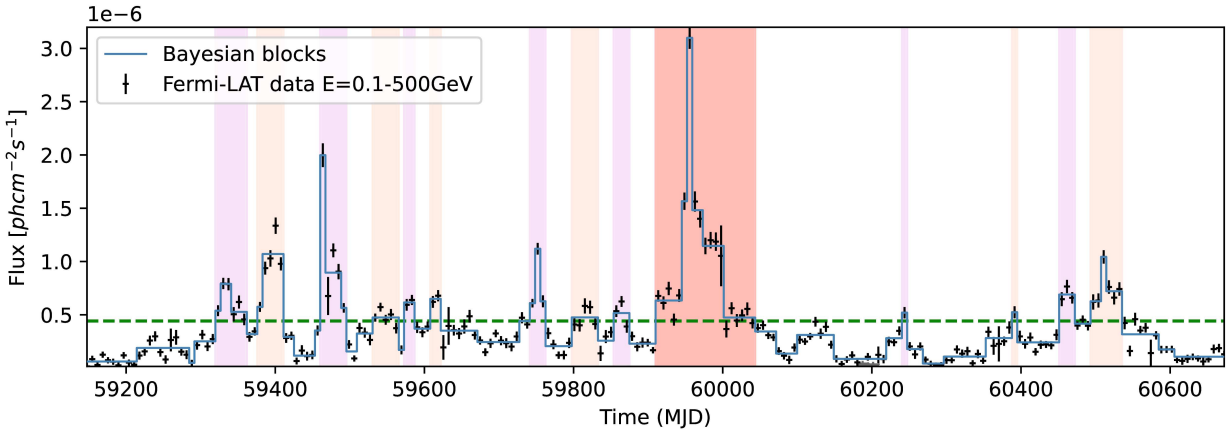


(a) PKS 0736+01.

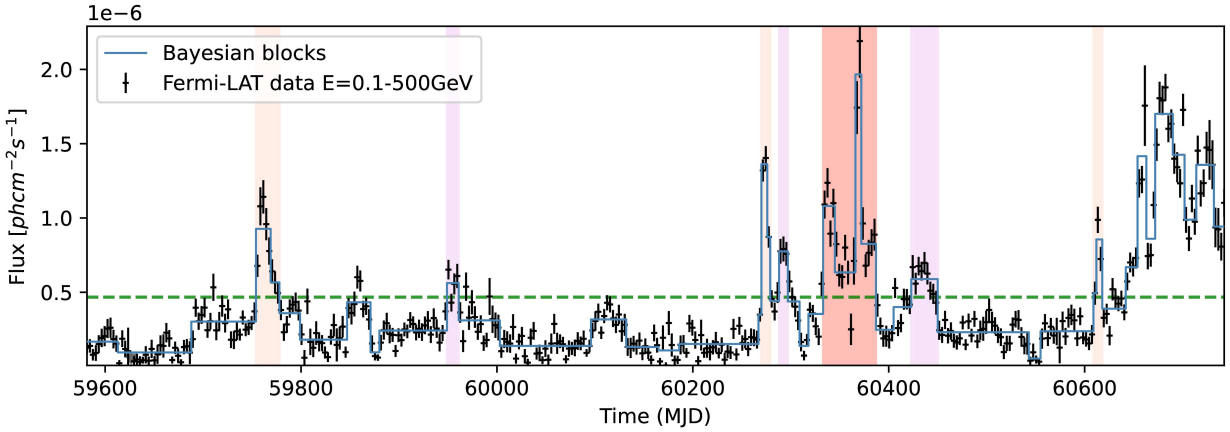
Figure B.1: *Fermi*-LAT lightcurves analyzed as described in Section 2.6. The red area indicates the flare that was used to model CTAO observations. Other flares detected by the HOP algorithm above the flux threshold represented by the green dashed line are highlighted in pink and orange.



(B) PKS 1222+216.

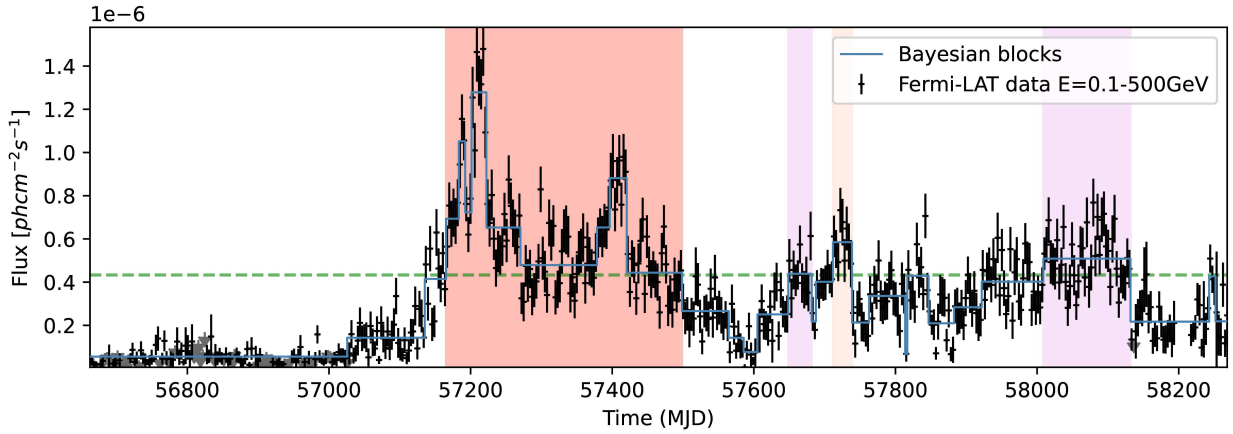


(C) Ton 599.

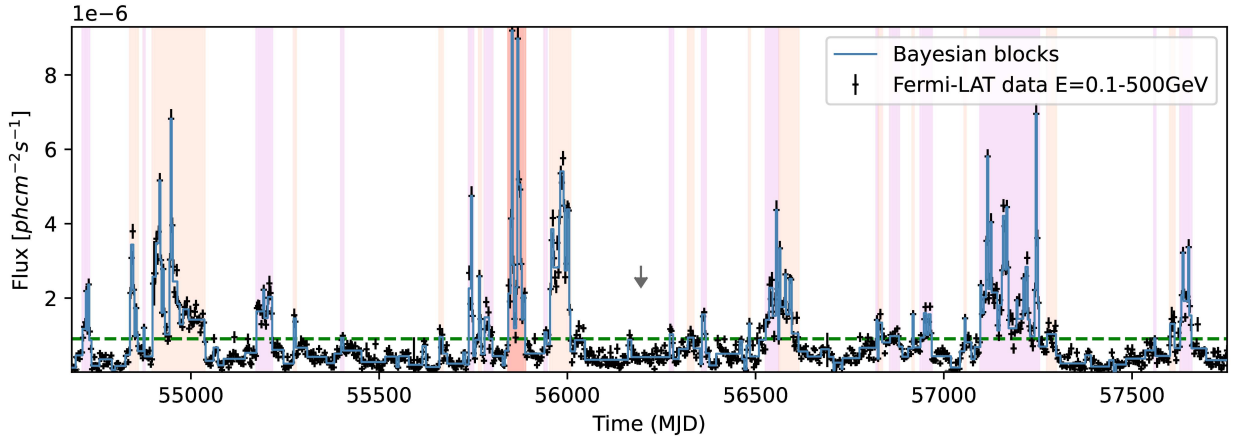


(D) OP 313.

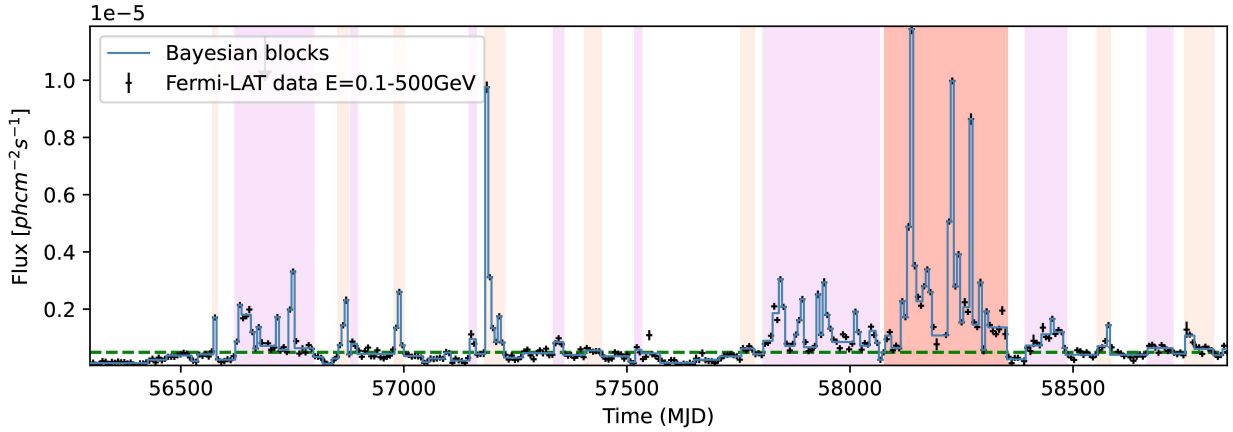
Figure B.1: *Fermi*-LAT lightcurves analyzed as described in Section 2.6. The red area indicates the flare that was used to model CTAO observations. Other flares detected by the HOP algorithm above the flux threshold represented by the green dashed line are highlighted in pink and orange.



(E) PKS 1502+106.

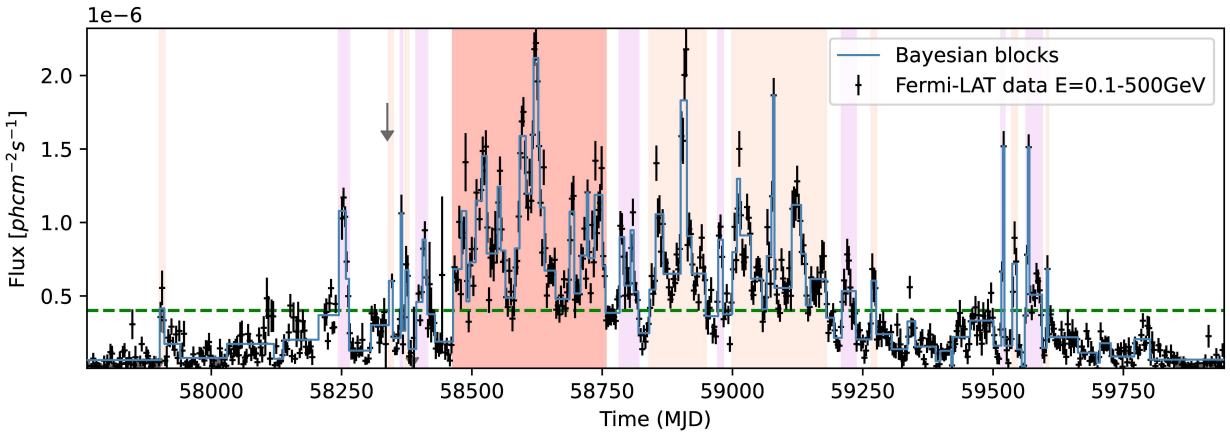


(F) PKS 1510−089.



(G) 3C 279.

Figure B.1: *Fermi*-LAT lightcurves analyzed as described in Section 2.6. The red area indicates the flare that was used to model CTAO observations. Other flares detected by the HOP algorithm above the flux threshold represented by the green dashed line are highlighted in pink and orange.



(H) PKS 0346−27.

Figure B.1: *Fermi*-LAT lightcurves analyzed as described in Section 2.6. The red area indicates the flare that was used to model CTAO observations. Other flares detected by the HOP algorithm above the flux threshold represented by the green dashed line are highlighted in pink and orange.

Source	Flaring period	ϕ_0 ($\mathrm{MeV^{-1}s^{-1}cm^{-2}}$)	E_{cut}(GeV)	Γ
PKS 0736+01	rising	$(7.47 \pm 0.54) \times 10^{-10}$	9.10 ± 5.35	1.93 ± 0.10
	decaying	$(2.36 \pm 0.15) \times 10^{-10}$	9.27 ± 5.00	2.07 ± 0.08
PKS 1222+216	rising	$(8.80 \pm 0.11) \times 10^{-10}$	29.98 ± 6.59	2.09 ± 0.01
	decaying	$(4.46 \pm 0.05) \times 10^{-10}$	27.78 ± 7.42	2.32 ± 0.02
Ton 599	rising	$(3.38 \pm 0.12) \times 10^{-10}$	9.14 ± 2.47	1.88 ± 0.05
	decaying	$(4.00 \pm 0.14) \times 10^{-10}$	31.79 ± 15.76	1.90 ± 0.04
OP 313	rising	$(5.06 \pm 0.20) \times 10^{-11}$	15.79 ± 3.13	1.65 ± 0.03
	decaying	$(4.45 \pm 0.26) \times 10^{-11}$	21.63 ± 8.06	1.76 ± 0.05
PKS 1502+106	rising	$(3.34 \pm 0.09) \times 10^{-10}$	12.82 ± 3.34	1.92 ± 0.04
	decaying	$(1.95 \pm 0.03) \times 10^{-10}$	10.95 ± 1.64	1.98 ± 0.02
PKS 1510-089	rising	$(2.84 \pm 0.15) \times 10^{-10}$	12.60 ± 6.28	2.22 ± 0.05
	decaying	$(3.20 \pm 0.08) \times 10^{-10}$	15.84 ± 3.95	2.13 ± 0.02
3C 279	rising	$(1.51 \pm 0.03) \times 10^{-8}$	16.46 ± 2.81	2.06 ± 0.02
	decaying	$(3.64 \pm 0.03) \times 10^{-10}$	14.67 ± 1.04	2.04 ± 0.01
PKS 0346-27	rising	$(3.79 \pm 0.08) \times 10^{-11}$	25.70 ± 4.12	1.92 ± 0.01
	decaying	$(3.07 \pm 0.07) \times 10^{-11}$	23.11 ± 4.08	1.89 ± 0.02

Table B.1: Spectral parameters of the ECPL model used to fit the *Fermi*-LAT data of each flaring state.

B.2 Results of CTAO simulations

Table B.2 and Table B.3 summarize the evolution of Li-Ma detection significance ($\sqrt{\mathrm{TS}}$) with CTAO evaluated at two representative values of the observation livetime, for Northern and Southern sources, respectively. Similarly, Table B.4 and Table B.5 display the evolution with livetime of the error reduction ratio r on the spectral cutoff energy defined in eq. 2.15 for both sets of sources. Finally, Table B.6 and Table B.7 show the $\Delta\mathrm{AIC_c}$ values computed between the catalog model of each source and various alternative models. The catalog model is LP for all sources except for 3C 279, where a SECPL is used instead. The $\Delta\mathrm{AIC_c}$ are reported for an observation time of 10 h with the selected CTAO configurations (4 LSTs for sources in the Northern hemisphere, 14 MSTs and 11 SCTs for those in the Southern). The overlap between $\mathrm{AIC_c}$ distributions for each alternative model with the catalog model is also reported.

Source	Flaring period	4 LST 30 min	4 LST + 9 MST 30 min	4 LST 2 h	4 LST + 9 MST 2 h
PKS 0736+01	rising	17.86 ± 1.09	17.82 ± 1.13	35.71 ± 1.11	35.63 ± 1.14
	decaying	3.63 ± 1.11	3.92 ± 0.97	7.62 ± 1.12	7.56 ± 1.11
PKS 1222+216	rising	48.40 ± 1.03	50.26 ± 1.11	97.06 ± 1.16	100.59 ± 1.18
	decaying	10.41 ± 1.13	10.88 ± 1.17	21.07 ± 1.05	21.73 ± 1.06
Ton 599	rising	9.62 ± 1.19	9.69 ± 1.15	19.53 ± 1.12	19.51 ± 1.03
	decaying	67.57 ± 1.14	70.13 ± 1.13	135.26 ± 1.10	140.50 ± 1.06
OP 313	rising	57.29 ± 1.20	58.25 ± 1.24	114.75 ± 1.10	116.67 ± 1.19
	decaying	58.52 ± 1.23	59.95 ± 1.21	117.00 ± 1.04	119.99 ± 1.03
PKS 1502+106	rising	13.74 ± 1.13	13.79 ± 1.14	27.51 ± 1.04	27.54 ± 1.08
	decaying	5.05 ± 1.08	5.00 ± 1.06	10.19 ± 1.08	10.09 ± 1.11

Table B.2: Detection significance ($\sqrt{\mathrm{TS}}$) of the rising and decaying flare states of each Northern source for different CTAO configurations and two representative values of the livetime.

Source	Flaring period	14 MST 2 h	14 MST + 11 SCT 2 h	14 MST 5 h	14 SCT + 11 MST 5 h
PKS 1510−089	rising	0.85 ± 1.16	1.09 ± 1.02	1.16 ± 1.11	1.85 ± 0.99
	decaying	3.03 ± 1.15	4.59 ± 1.06	4.94 ± 1.07	7.54 ± 1.09
3C 279	rising	4.49 ± 1.23	6.67 ± 1.06	7.13 ± 0.99	10.50 ± 1.01
	decaying	4.17 ± 1.13	6.40 ± 1.09	6.65 ± 1.03	10.26 ± 1.12
PKS 0346−27	rising	10.28 ± 1.16	14.49 ± 1.10	–	–
	decaying	7.14 ± 1.13	10.18 ± 1.06	–	–

Table B.3: Detection significance ($\sqrt{\mathrm{TS}}$) of the rising and decaying flare states of each Southern source for different CTAO configurations and two representative values of the livetime. Values for PKS 0346−27 at 5 h are not reported as the source was detected above 5σ within 2 h.

Source	Flaring period	4 LST 30 min	4 LST + 9 MST 30 min	4 LST 2 h	4 LST + 9 MST 2 h
PKS 0736+01	rising	0.21 ± 0.03	0.20 ± 0.02	0.16 ± 0.02	0.15 ± 0.01
	decaying	0.25 ± 0.03	0.26 ± 0.03	0.2 ± 0.02	0.20 ± 0.02
PKS 1222+216	rising	0.23 ± 0.01	0.21 ± 0.01	0.16 ± 0.01	0.14 ± 0.01
	decaying	0.43 ± 0.06	0.41 ± 0.05	0.29 ± 0.02	0.27 ± 0.02
Ton 599	rising	0.28 ± 0.02	0.28 ± 0.02	0.23 ± 0.01	0.23 ± 0.01
	decaying	0.12 ± 0.01	0.10 ± 0.01	0.06 ± 0.01	0.05 ± 0.01
OP 313	rising	0.26 ± 0.02	0.23 ± 0.01	0.16 ± 0.01	0.14 ± 0.01
	decaying	0.17 ± 0.01	0.15 ± 0.01	0.09 ± 0.01	0.08 ± 0.01
PKS 1502+106	rising	0.33 ± 0.03	0.33 ± 0.03	0.27 ± 0.02	0.27 ± 0.02
	decaying	0.65 ± 0.06	0.64 ± 0.05	0.43 ± 0.02	0.43 ± 0.02

Table B.4: Error reduction ratio (r) on the spectral cutoff energy of the rising and decaying flare states of each Northern source for different CTAO configurations and two representative values of the livetime.

Source	Flaring period	14 MST 2 h	14 MST + 11 SCT 2 h	14 MST 5 h	14MST + 11 SCT 5 h
PKS 1510−089	rising	0.41 ± 0.06	0.32 ± 0.04	0.31 ± 0.04	0.23 ± 0.03
	decaying	0.32 ± 0.02	0.25 ± 0.01	0.22 ± 0.01	0.18 ± 0.01
3C 279	rising	0.36 ± 0.02	0.28 ± 0.01	0.25 ± 0.01	0.2 ± 0.01
	decaying	1.08 ± 0.02	0.88 ± 0.02	0.78 ± 0.02	0.61 ± 0.01
PKS 0346−27	rising	0.27 ± 0.01	0.22 ± 0.01	–	–
	decaying	0.32 ± 0.01	0.26 ± 0.01	–	–

Table B.5: Error reduction ratio (r) on the spectral cutoff energy of the rising and decaying flare states of each Southern source for different CTAO configurations and two representative values of the livetime. Values for PKS 0346−27 at 5 h are not reported as the source was detected above 5σ within 2 h.

Source	Flaring period	Alternative model	ΔAIC_c	Overlap
PKS 0736+01	rising	ECPL	65.01 ± 12.43	0.01
		BPL	14.49 ± 6.11	0.33
	decaying	ECPL	23.11 ± 6.33	0.16
		BPL	3.13 ± 2.84	0.81
PKS 1222+216	rising	ECPL	216.26 ± 21.04	0
		BPL	25.8 ± 6.55	0.15
	decaying	ECPL	34.26 ± 12.42	0.10
		BPL	-2.49 ± 3.50	0.82
Ton 599	rising	ECPL	75.77 ± 10.62	0
		BPL	11.20 ± 2.95	0.40
	decaying	ECPL	43.82 ± 9.24	0.02
		BPL	9.62 ± 5.89	0.54
OP 313	rising	ECPL	99.47 ± 11.45	0
		BPL	9.61 ± 5.54	0.55
	decaying	ECPL	53.38 ± 8.12	0.01
		BPL	21.24 ± 5.44	0.14
PKS 1502+106	rising	ECPL	46.05 ± 11.04	0.01
		BPL	11.00 ± 5.57	0.44
	decaying	ECPL	26.85 ± 11.52	0.16
		BPL	-11.55 ± 2.50	0.37

Table B.6: AIC_c differences between the catalog (LP) model and each alternative model in the table. The values correspond to a 10 h observation performed with 4 LSTs of the selected Northern hemisphere sources. The overlap between AIC_c distributions for each alternative model with the catalog model is also reported.

Source	Flaring period	Alternative model	ΔAIC	Overlap
PKS 1510−089	rising	ECPL	37.05 ± 6.24	0.02
		BPL	6.10 ± 3.00	0.66
	decaying	ECPL	172.2 ± 12.74	0
		BPL	20.11 ± 4.90	0.23
3C 279	rising	LP	64.48 ± 37.28	0.10
		BPL	76.97 ± 31.05	0.02
	decaying	LP	370.96 ± 44.76	0
		BPL	220.64 ± 37.69	0
PKS 0346−27	rising	ECPL	133.14 ± 17.14	0
		BPL	0.23 ± 6.61	0.79
	decaying	ECPL	111.16 ± 13.93	0
		BPL	3.61 ± 6.60	0.84

Table B.7: AIC_c differences between the catalog model (LP for PKS 1510−089 and PKS 0346−27, SECPL for 3C 279) and each alternative model in the table. The values correspond to a 10 h observation performed with 14 MSTs and 11 SCTs of the selected Southern hemisphere sources. The overlap between AIC_c distributions for each alternative model with the catalog model is also reported.

APPENDIX C

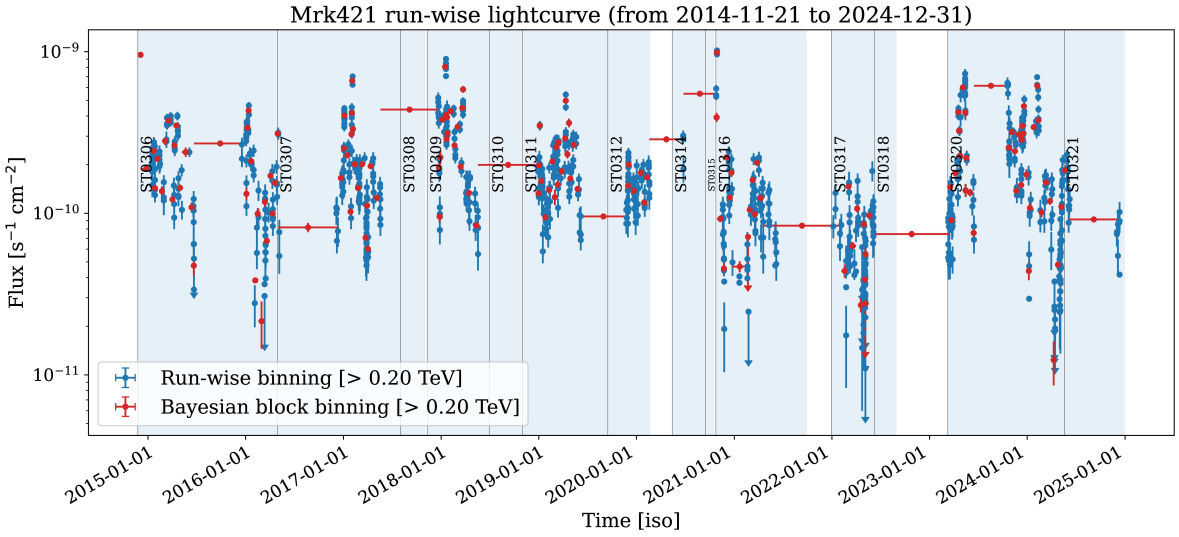
Long-term blazar analysis with MAGIC

C.1 Lightcurves

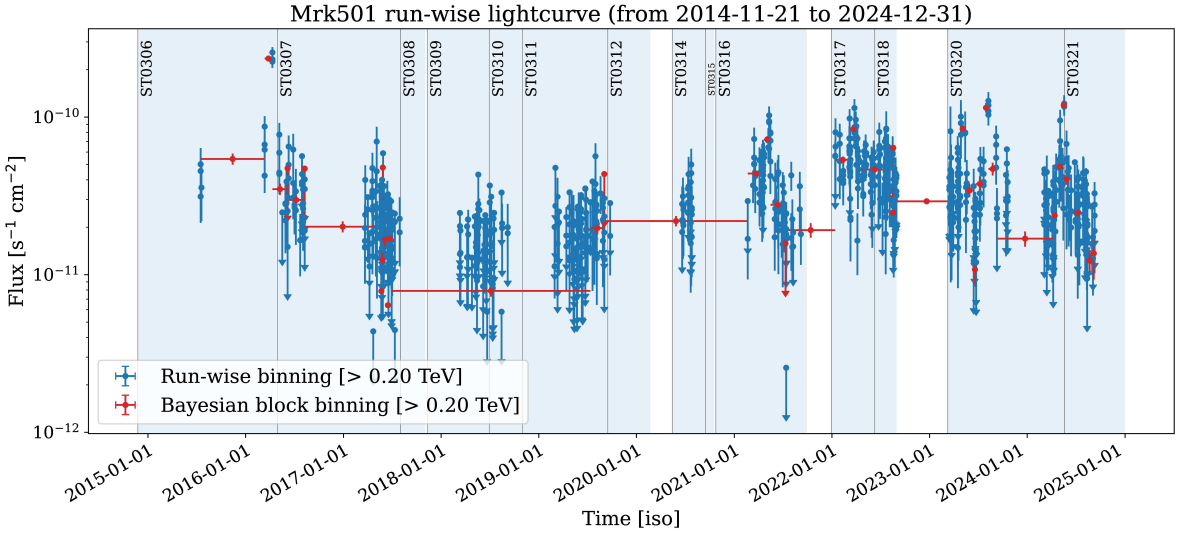
In this Appendix, the main results of the MAGIC data analysis discussed in Chapter 4 are reported. Figure C.1 shows the long-term lightcurves, covering approximately 10 years of stereoscopic, dark-time observations between 2014 and 2024. The blue points in the lightcurves show the integral flux above 200 GeV estimated for each selected run, while the red points represent the flux above the same threshold in each Bayesian block. The selected MAGIC analysis periods are also highlighted, ranging between ST0306 and ST0321. Each analysis period is associated with a specific set of Monte Carlo simulations, representing the hardware performance of the telescopes during that time; periods with known data quality issues were excluded.

C.2 Spectral parameters

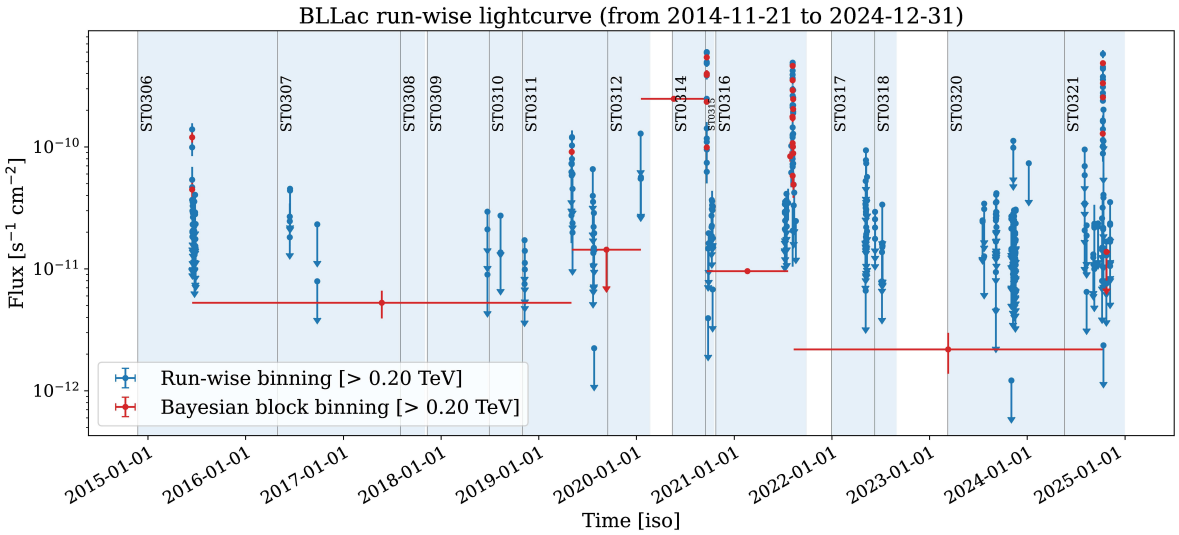
Figure C.2 shows the spectral parameters (amplitude and spectral index) for the Bayesian blocks identified in each source's lightcurve. An ECPL or log-parabola shape is chosen over a simple power law in case it is favored by a likelihood-ratio test by at least 3σ, as described in ref. [24]. The color of each point indicates the preferred spectral model for that block. For visualization purposes, spectral parameters with large uncertainties are not shown in the plots, but they are still included in the statistical analysis (see Section 4.4). A "harder-when-brighter" trend cannot be clearly identified in the data, which justifies the analysis of each Bayesian block individually instead of grouping them by flux level or spectral index.



(A) Mrk 421.

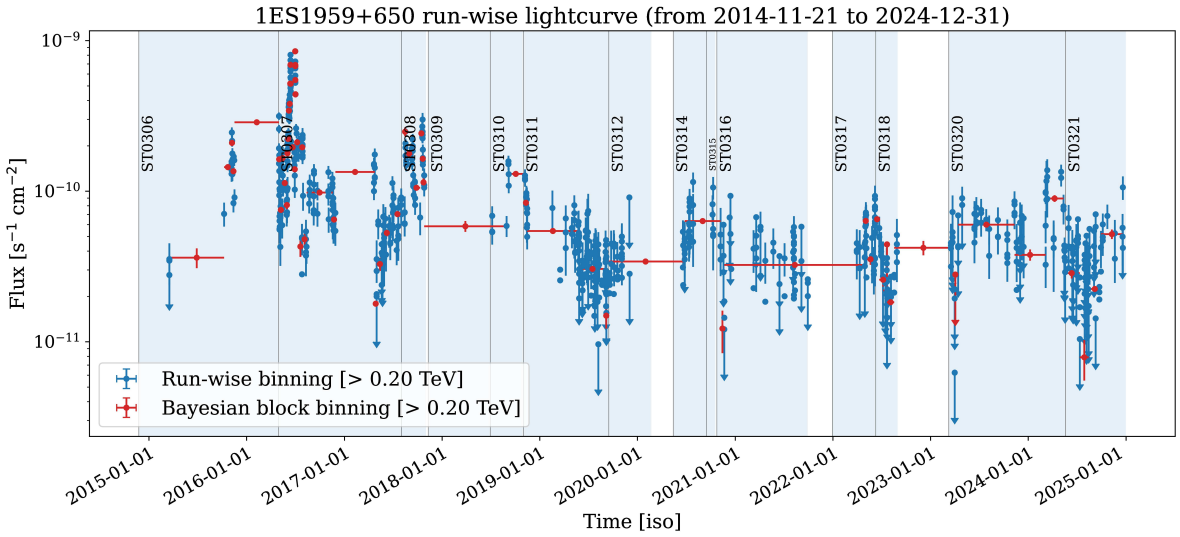


(B) Mrk 501.



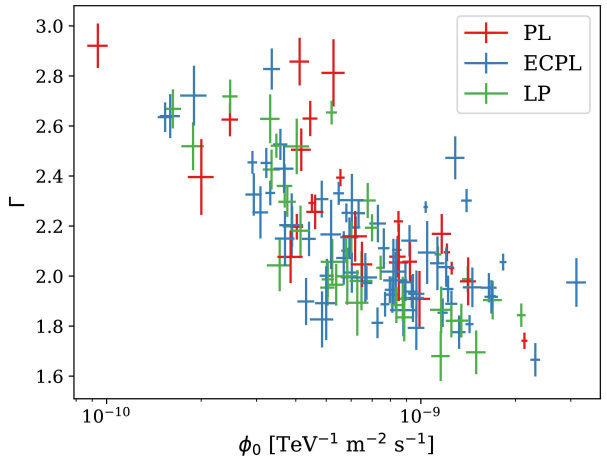
(C) BL Lac.

FIGURE C.1: Long-term MAGIC lightcurves for the four blazars analyzed in CHAPTER 4.

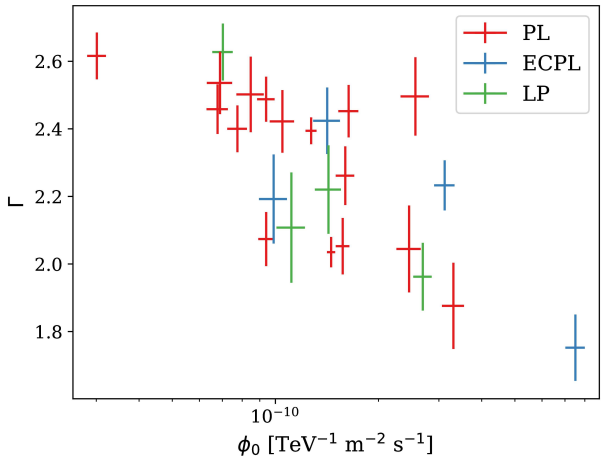


(D) 1ES 1959+650.

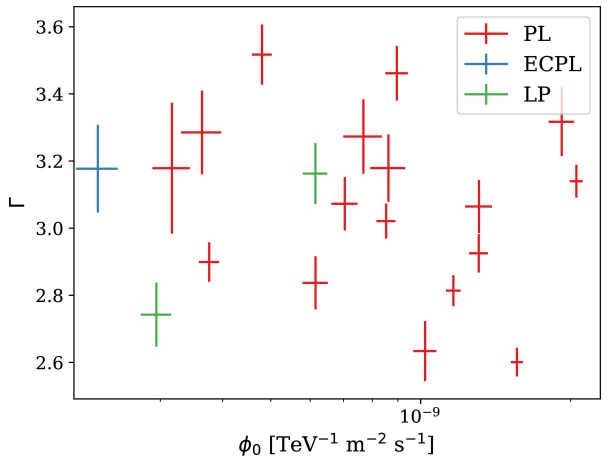
FIGURE C.1: Long-term MAGIC lightcurves for the four blazars analyzed in CHAPTER 4. (*cont.*)



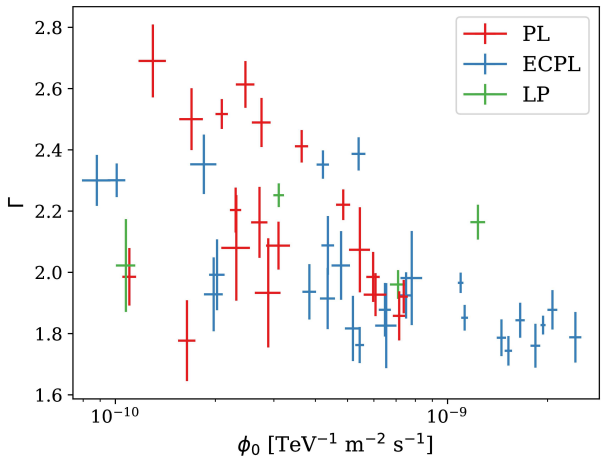
(A) Mrk 421.



(B) Mrk 501.



(C) BL Lac.



(D) 1ES 1959+650.

FIGURE C.2: Spectral parameters for the Bayesian blocks in the lightcurve of each blazar.

APPENDIX D

Systematic effects on ALP limits

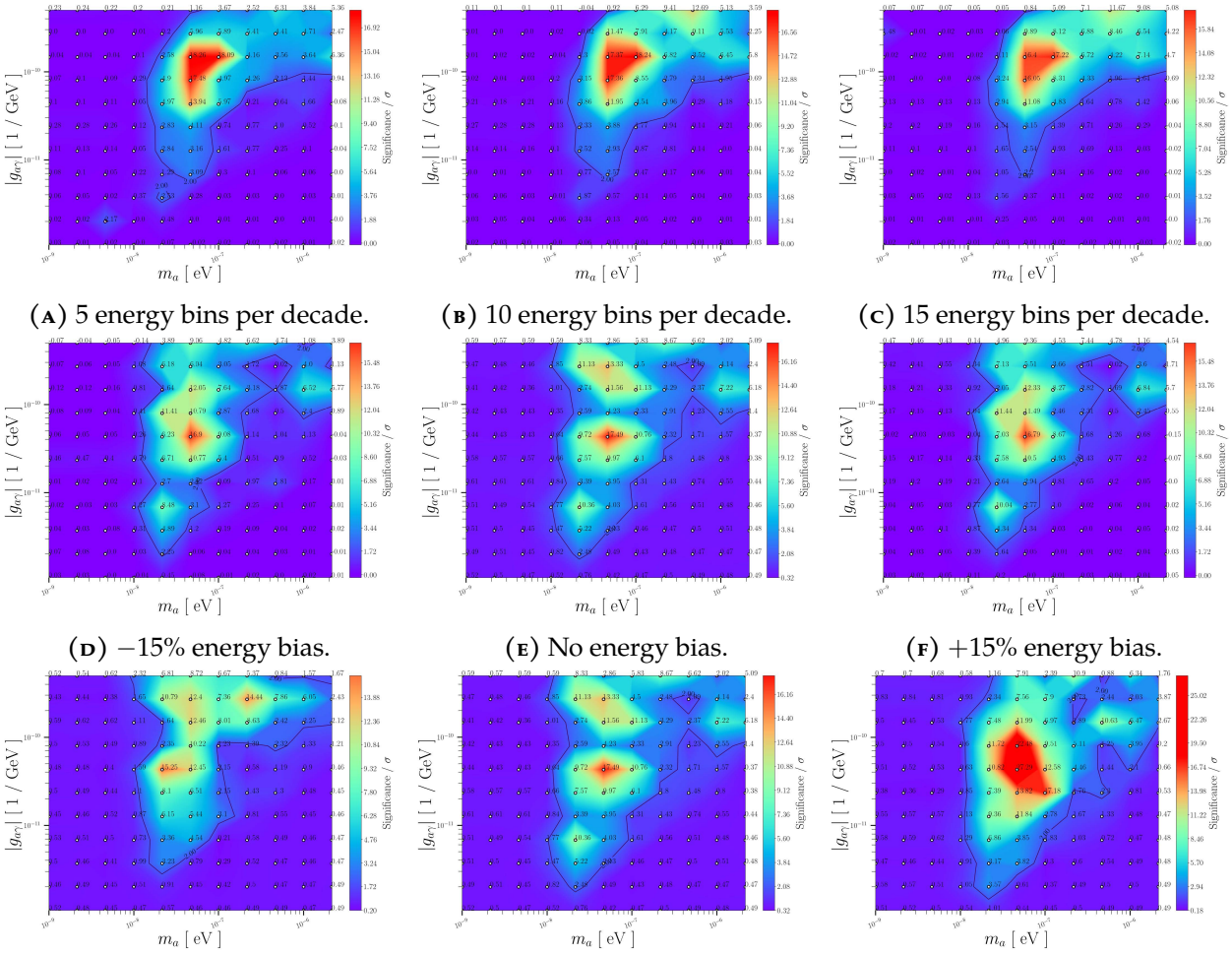
D.1 MAGIC and LST-1 analysis

The evaluation of various systematic effects on the ALP limits from the analysis of MAGIC and LST-1 data presented in Chapter 4 is shown in Figure D.1. It should be noted that these are preliminary results evaluated at different times during the analysis and using different assumptions on the jet parameters, galactic magnetic field and data segmentation than those finally adopted. As such, they only serve as a qualitative illustration of how different choices in both physical and analysis parameters can impact the final limits. We choose to focus on Mrk 421, as it was found to be the most constraining source in our sample.

Figure D.1a to Figure D.1c illustrate the effect of changing the reconstructed energy binning between 5, 10 and 15 bins per decade on the limits obtained from LST-1 data only. Similarly, Figure D.1d and Figure D.1f show how limits from combined MAGIC and LST-1 change by shifting the spectral features by $\pm 15\%$ in energy compared to the reference values, as a possible effect of the finite energy dispersion of the instruments (as done e.g. in ref. [365]).

To bracket the uncertainty on physical jet parameters, Figure D.1g and Figure D.1i show the impact of decreasing and increasing r_0 by $\pm 30\%$ compared to its reference value of $r_0 = 6.02\,\mathrm{pc}$ (Figure D.1h). This parameter was found in ref. [383] to be the most relevant for the adopted jet model, and indeed it is the one that changes the limits in the most significant way. Indeed, we note that energy binning and bias do not have a large impact on the final limits, while changing the value of r_0 considerably changes both the shape of the constrained region as well as the significance at which points are most strongly excluded.

Besides those reported in Figure D.1, more comparisons were performed by changing the galactic magnetic field model between Janson-Farrar [339] and Unger-Farrar [347], and by grouping data based on night-wise rather than run-wise lightcurves. The final choices adopted for the analysis and signal modeling are reported in Chapter 4.



(A) 5 energy bins per decade. (B) 10 energy bins per decade. (C) 15 energy bins per decade.

(D) −15% energy bias. (E) No energy bias. (F) +15% energy bias.

(G) $r_0 = 4.21$ pc. (H) $r_0 = 6.02$ pc. (I) $r_0 = 7.83$ pc.

FIGURE D.1: Illustration of various systematic effects on ALP limits from MAGIC and LST-1 observations of Mrk 421. Figures (A) to (C) were obtained for LST-1 data only, while figures (D) to (I) show results from combined MAGIC and LST-1 data. Varying assumptions on magnetic field models and data segmentation were taken in producing each set of plots.

D.2 CTAO projections

We report here how the projections of the CTAO sensitivity to ALPs from blazars presented in CHAPTER 5 are affected by changes in energy binning, magnetic field strength or EBL model. While the former effects are similar between the sources considered in this work, we focus our discussion on PKS 2155−304 as it is the most strongly affected by EBL absorption.

FIGURE D.2A shows the average 2σ sensitivity on the ALP parameter space from a 50-hour observation of PKS 2155−304 in its baseline state for different choices of the energy binning. We compare the results presented in the main text, obtained for 20 bins per decade, with those resulting from considering either half or double the number of bins per decade (10 or 40, respectively). The latter choice of binning, in particular, was employed in ref. [130]. While there is very little difference between these results, halving the number of bins seems to reduce the size of the hole-like features around $g_{a\gamma} \sim 4 \times 10^{-11}\,\mathrm{GeV}^{-1}$,

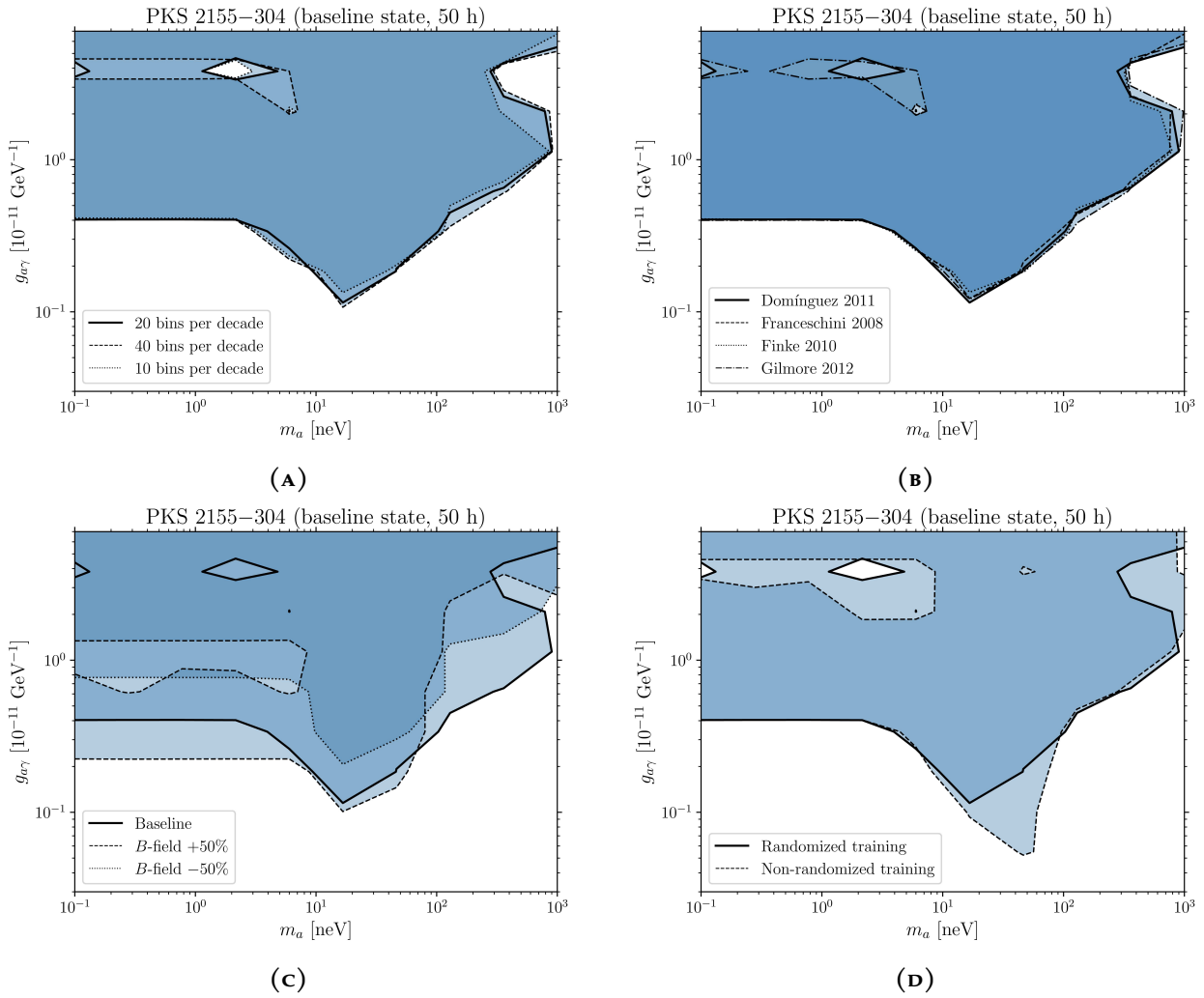


Figure D.2: CTAO sensitivity to the ALP parameter space obtained from a 50-hour simulated observation of PKS 2155−304 in its baseline state for different choices of the energy binning, EBL model, magnetic field strength and training strategy.

while doubling it turns the feature into a continuous band. A similar outcome is found by comparing the results from different EBL models [140, 141, 143] to the one used in the main text [142], with the sensitivity to ALP parameters almost unaffected by this choice (Figure D.2b).

We consider in Figure D.2c how our results are affected by changing the average magnetic field strength B_0 in the jet, either increasing it by 50% ($B_0 = 1.23\,\mathrm{G}$) or decreasing it by the same amount ($B_0 = 0.41\,\mathrm{G}$) with respect to the value reported in Table Table 5.2 ($B_0 = 0.82\,\mathrm{G}$). As the ALP effects on the photon spectrum depend on the product between the coupling constant $g_{a\gamma}$ and the magnetic field, it is easy to see that increasing the latter allows to set more stringent limits on the former, and vice versa. We remark that this uncertainty comes not only from the large experimental difficulty in determining the value this parameter, but also from the fact that such value is unlikely to remain constant while the source goes through different activity states.

Finally, in Figure D.2d we compare our main results with those we find by not randomizing the intrinsic spectral parameters within their error bands in the training datasets (see

Section 5.3) and only using their average values. As expected, the sensitivity derived in this way is stronger, as the ML classifiers become overfit to a specific spectral model, but less generalizable. On the other hand, in a "randomized" training, the variations on the spectral parameters should not be larger than a few percent in order to maintain a solid performance of the classifiers.

APPENDIX E

Machine learning performance metrics

E.1 Train-test splitting and cross-validation

Several approaches exist to estimate the performance of a machine-learning classification algorithm, based on how well it can identify samples in a labeled dataset. The dataset is then subdivided in a *training dataset*, used to train the algorithm, and a *test dataset*, used to estimate how well its performance can be generalized to previously unseen data (*train-test splitting*). The definitions that follow are based on ref. [157] and implemented in the Scikit-learn Python package [391].

A test dataset for binary classification problems generally consists of S samples, with P samples belonging to a "positive" class and N to a "negative" one (e.g., ALP-like and ALP-less observations in the application of Chapter 5). When a machine learning classifier is applied to these samples, it will correctly classify a certain number of them as positive (true positive, TP) or as negative (true negative, TN). On the other hand, some positive samples will be misclassified as negative, and vice versa (false negative, FN, and false positive, FP). The following relations then hold:

$$\begin{aligned} S &= P + N\,, \\ P &= \mathrm{TP} + \mathrm{FN}\,, \\ N &= \mathrm{TN} + \mathrm{FP}\,. \end{aligned} \tag{E.1}$$

Based on these quantities, the *accuracy* of the algorithm can be estimated as

$$\mathrm{Accuracy} = \frac{\mathrm{TN} + \mathrm{TP}}{S}\,, \tag{E.2}$$

representing the overall capability of the algorithm to correctly classify positive samples. The true and false positive rates are respectively defined as

$$\mathrm{TPR} = \frac{\mathrm{TP}}{P}\,, \quad \mathrm{FPR} = \frac{\mathrm{FP}}{N}\,. \tag{E.3}$$

True and false negative rates can be defined in an analogous way. These four quantities are often represented visually in a normalized *confusion matrix* (Figure E.1).

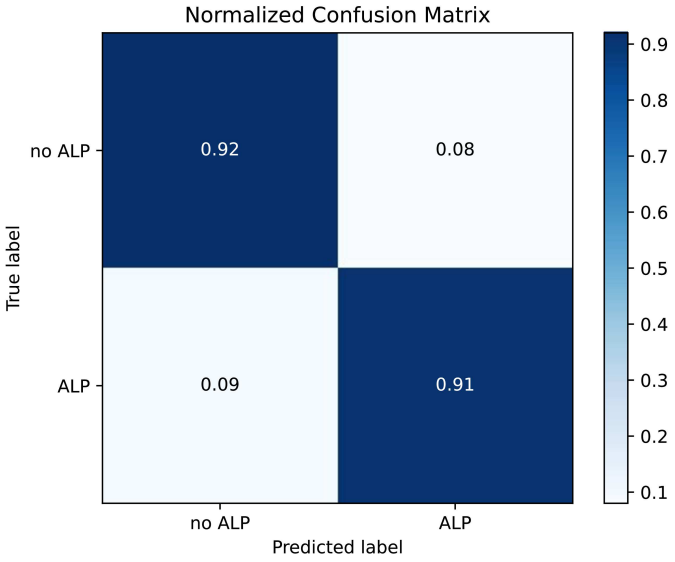


Figure E.1: Example normalized confusion matrix applied to the problem of spectral classification based on the presence of ALP signatures. This example was produced with a non-optimized XGBoost classifier trained to distinguish blazar spectra with and without spectral features due to ALPs with $m_a = 1\,\mathrm{neV}$, $g_{a\gamma} = 3 \times 10^{-11}\,\mathrm{GeV}^{-1}$, applying a 30-70 train-test split.

Two closely related quantities are *recall* (actually equivalent to TPR) and *precision*, defined as

$$\mathrm{Recall} = \frac{\mathrm{TP}}{\mathrm{TP} + \mathrm{FN}} = \mathrm{TPR}\,, \quad \mathrm{Precision} = \frac{\mathrm{TP}}{\mathrm{TP} + \mathrm{FP}}\,. \tag{E.4}$$

Finally, the *F1 score* is an often used metric defined as

$$\mathrm{F1} = 2\,\frac{\mathrm{Precision} \times \mathrm{Recall}}{\mathrm{Precision} + \mathrm{Recall}}\,. \tag{E.5}$$

Accuracy, precision, recall and F1 score were compared for the analysis of CTAO sensitivity to ALPs discussed in Chapter 5. As can be seen from Figure E.2, all four metrics display a very similar behavior over the ALP parameter space.

Average metrics can be computed via k-fold cross-validation. This technique consists in splitting the original dataset in k subsets and evaluating the performance metrics k times, each time using a different subset as the test dataset and the others as training datasets. In this way, mean values with their relative uncertainties can be provided for each metric.

E.2 ROC, learning and validation curves

Classifier performance can also be evaluated by shifting the values of the algorithm's hyperparameters. For example, a classifier typically outputs a score describing the how likely a certain sample is to belong to the positive class. If the score falls below a certain threshold the sample is classified as negative, otherwise as positive. By changing this threshold value, the evolution of the true positive rate as a function of the false positive rate can be represented in a *receiver operating characteristic* (ROC) curve (Figure E.3). A classifier with

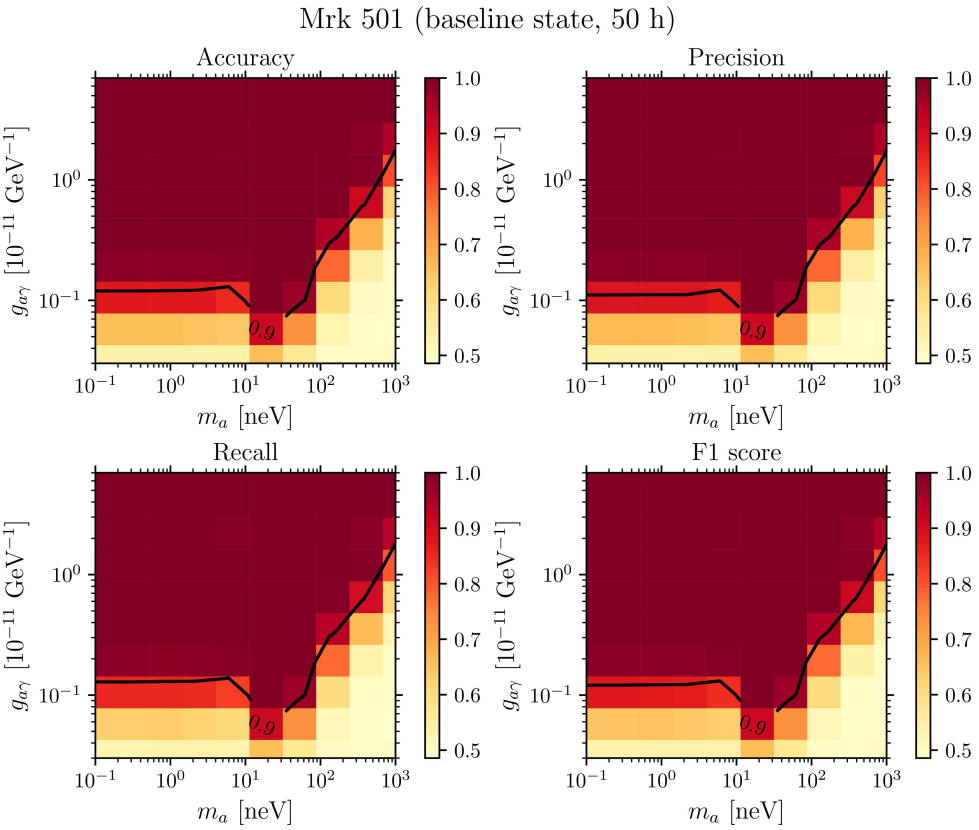


Figure E.2: XGB metrics for the baseline state of Mrk 501 considered in Chapter 5 over the ALP parameter space.

perfect performance would always have TPR = 1, so that the area under the curve (AUC) would also be equal to 1. On the other hand, a classifier taking random guesses would have TPR = FPR, and thus AUC = 0.5. Therefore, the ROC AUC score (between 0.5 and 1) can be used as another descriptor of the performance of a classifier.

Similarly, the impact of the size of the training dataset on performance can be studied by computing a cross-validated metric, such as accuracy, for training and test datasets comprising increasing fractions of the total dataset. The resulting curve is called a *learning curve* (Figure E.4a). As the size of the training dataset increases and the model becomes more generalized, the training accuracy decreases, while the accuracy on test data increases. These curves eventually tend to converge around a common value. If this value is too low, the classifier is said to have *high bias* or to *underfit* the data. On the other hand, if the overall accuracy is high but the difference between the training and test accuracy is too large, the classifier has *high variance* and is *overfitting* the data (as it is too fine-tuned to the training dataset to properly generalize to the test dataset). Both these cases highlight a non-optimal performance of the classifier, which can be corrected by changing the values of other hyperparameters. Similar curves (*validation curves*, Figure E.4b) can be used to study the evolution of accuracy (or other metrics) as a function of each hyperparameter. All these techniques can be used to diagnose issues in the classifier training and perform *model selection*, choosing the hyperparameters that optimize performance while achieving adequate bias-variance trade-off.

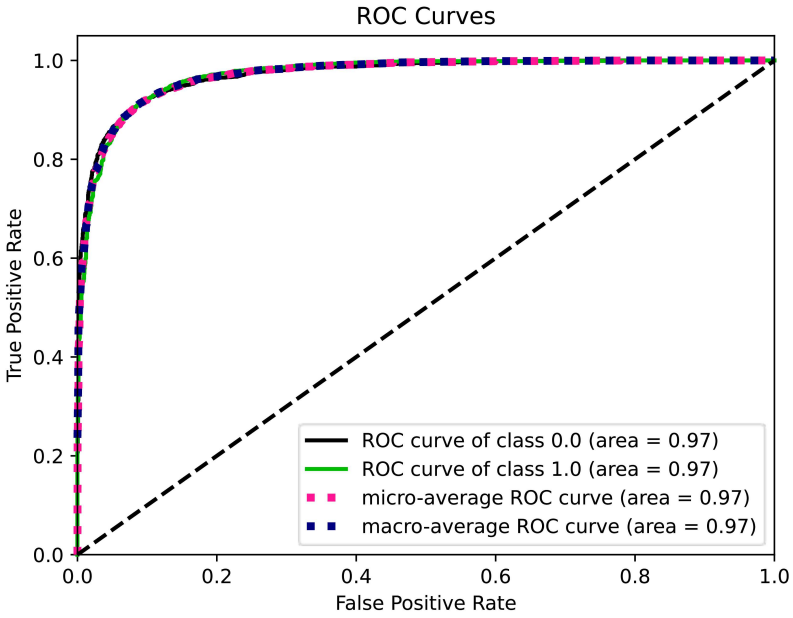
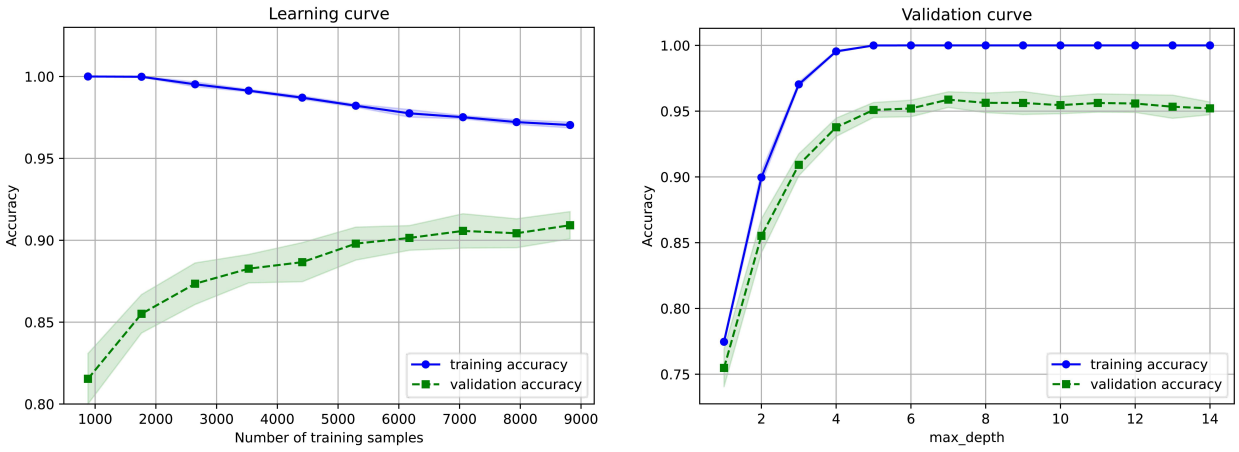


Figure E.3: Example ROC curve computed for the same classifier used in Figure E.1. For the definitions of macro- and micro-averaged ROC, see https://scikit-learn.org/stable/auto_examples/model_selection/plot_roc.html.



(a) (b)

Figure E.4: (a) Example learning curve computed for the same classifier used in Figure E.1. (b) Validation curve for the same classifier, obtained as a function of the `max_depth` hyperparameter.

References

[1] J. Elster and H. Geitel. "Über Elektricitätszerstreuung in der Luft". *Ann. Phys.* 307.7 (1900), pp. 425–446. DOI: https://doi.org/10.1002/andp.19003070702.

[2] C. T. R. Wilson. "On the ionisation of atmospheric air". *Proc. R. Soc. Lon.* 68.442-450 (1901), pp. 151–161. DOI: 10.1098/rspl.1901.0032.

[3] R. G. A. Fricke and K. Schlegel. "Julius Elster and Hans Geitel – Dioscuri of physics and pioneer investigators in atmospheric electricity". *Hist. Geo-Space Sci.* 8.1 (2017), pp. 1–7. DOI: 10.5194/hgss-8-1-2017.

[4] V. F. Hess. "Über Beobachtungen der durchdringenden Strahlung bei sieben Freiballonfahrten". *Phys. Z.* 13 (1912), pp. 1084–1091.

[5] V. F. Hess. *On the Observations of the Penetrating Radiation during Seven Balloon Flights*. Translated and commented by A. De Angelis and C. Arcaro b. Schultz. 2018. arXiv: 1808.02927 [physics.hist-ph].

[6] M. S. Longair. *High Energy Astrophysics*. 3rd ed. Cambridge University Press, 2011.

[7] S. Navas et al. "Review of particle physics". *Phys. Rev. D* 110.3 (2024), p. 030001. DOI: 10.1103/PhysRevD.110.030001.

[8] S. Mollerach and E. Roulet. "Progress in high-energy cosmic ray physics". *Prog. Part. Nucl. Phys.* 98 (2018), pp. 85–118. ISSN: 0146-6410. DOI: https://doi.org/10.1016/j.ppnp.2017.10.002.

[9] W. L. Kraushaar and G. W. Clark. "Search for Primary Cosmic Gamma Rays with the Satellite Explorer XI". *Phys. Rev. Lett.* 8 (3 Feb. 1962), pp. 106–109. DOI: 10.1103/PhysRevLett.8.106.

[10] G. W. Clark, G. P. Garmire, and W. L. Kraushaar. "Observation of High-Energy Cosmic Gamma Rays". *Astrophys. J. Lett.* 153 (Sept. 1968), p. L203. DOI: 10.1086/180252.

[11] W. L. Kraushaar et al. "High-Energy Cosmic Gamma-Ray Observations from the OSO-3 Satellite". *Astrophys. J.* 177 (Nov. 1972), p. 341. DOI: 10.1086/151713.

[12] C. E. Fichtel et al. "High-energy gamma-ray results from the second Small Astronomy Satellite." *Astrophys. J.* 198 (May 1975), pp. 163–182. DOI: 10.1086/153590.

[13] G. F. Bignami et al. "The COS-B experiment for gamma-ray astronomy." *Space Sci. Instrum.* 1 (Aug. 1975), pp. 245–268.

[14] N. Gehrels, E. Chipman, and D. Kniffen. "The Compton Gamma Ray Observatory". *Astrophys. J. Suppl. Ser.* 92 (June 1994), p. 351. DOI: 10.1086/191978.

[15] C. Winkler et al. "The INTEGRAL mission". *Astron. Astrophys.* 411.1 (2003), pp. L1–L6. DOI: 10.1051/0004-6361:20031288.

[16] M. Tavani et al. "The AGILE Mission". *Astron. Astrophys.* 502.3 (2009), pp. 995–1013. DOI: 10.1051/0004-6361/200810527.

[17] W. B. Atwood et al. "The Large Area Telescope on the *Fermi* Gamma-Ray Space Telescope Mission". *Astrophys. J.* 697.2 (May 2009), p. 1071. DOI: 10.1088/0004-637X/697/2/1071.

[18] C. Meegan et al. "The *Fermi* Gamma-Ray Burst Monitor". *Astrophys. J.* 702.1 (Aug. 2009), p. 791. DOI: 10.1088/0004-637X/702/1/791.

[19] L. Singer and J. Racusin. "General Coordinates Network (GCN): NASA's Next Generation Time-Domain and Multimessenger Astronomy Alert System". *Bull. Am. Astron. Soc.* 55.2 (Jan. 2023). https://baas.aas.org/pub/2023n2i108p02.

[20] A. A. Abdo et al. "*Fermi*/Large Area Telescope Bright Gamma-Ray Source List". *Astrophys. J. Suppl. Ser.* 183.1 (July 2009), pp. 46–66. DOI: 10.1088/0067-0049/183/1/46.

[21] A. A. Abdo et al. "*Fermi* Large Area Telescope First Source Catalog". *Astrophys. J. Suppl. Ser.* 188.2 (May 2010), p. 405. DOI: 10.1088/0067-0049/188/2/405.

[22] P. L. Nolan et al. "*Fermi* Large Area Telescope Second Source Catalog". *Astrophys. J. Suppl. Ser.* 199.2 (Mar. 2012), p. 31. DOI: 10.1088/0067-0049/199/2/31.

[23] F. Acero et al. "*Fermi* Large Area Telescope Third Source Catalog". *Astrophys. J. Suppl. Ser.* 218.2 (June 2015), p. 23. DOI: 10.1088/0067-0049/218/2/23.

[24] S. Abdollahi et al. "*Fermi* Large Area Telescope Fourth Source Catalog". *Astrophys. J. Suppl. Ser.* 247.1 (Mar. 2020), p. 33. DOI: 10.3847/1538-4365/ab6bcb.

[25] J. Ballet et al. *Fermi Large Area Telescope Fourth Source Catalog Data Release 2*. 2020. arXiv: 2005.11208 [astro-ph.HE].

[26] S. Abdollahi et al. "Incremental *Fermi* Large Area Telescope Fourth Source Catalog". *Astrophys. J. Suppl. Ser.* 260.2 (June 2022), p. 53. DOI: 10.3847/1538-4365/ac6751.

[27] J. Ballet et al. *Fermi Large Area Telescope Fourth Source Catalog Data Release 4 (4FGL-DR4)*. 2024. arXiv: 2307.12546 [astro-ph.HE].

[28] F. Aharonian et al. "High energy astrophysics with ground-based gamma ray detectors". *Rep. Prog. Phys.* 71.9 (Aug. 2008), p. 096901. DOI: 10.1088/0034-4885/71/9/096901.

[29] A. M. Hillas. "Evolution of ground-based gamma-ray astronomy from the early days to the Cherenkov Telescope Arrays". *Astropart. Phys.* 43 (2013). Seeing the High-Energy Universe with the Cherenkov Telescope Array - The Science Explored with the CTA, pp. 19–43. ISSN: 0927-6505. DOI: https://doi.org/10.1016/j.astropartphys.2012.06.002.

[30] R. Mirzoyan. "Brief history of ground-based very high energy gamma-ray astrophysics with atmospheric air Cherenkov telescopes". *Astropart. Phys.* 53 (2014). Centenary of cosmic ray discovery, pp. 91–99. ISSN: 0927-6505. DOI: https://doi.org/10.1016/j.astropartphys.2013.11.004.

[31] P. Chadwick. "35 Years of Ground-Based Gamma-ray Astronomy". *Universe* 7.11 (2021). ISSN: 2218-1997. DOI: 10.3390/universe7110432.

[32] D. Bose et al. "Ground-based gamma-ray astronomy: history and development of techniques". *Eur. Phys. J. Spec. Top.* 231.1 (Jan. 2022), pp. 3–26. ISSN: 1951-6401. DOI: 10.1140/epjs/s11734-021-00396-3.

[33] R. Mirzoyan. "Technological Novelties of Ground-Based Very High Energy Gamma-Ray Astrophysics with the Imaging Atmospheric Cherenkov Telescopes". *Universe* 8.4 (2022). ISSN: 2218-1997. DOI: 10.3390/universe8040219.

[34] P. A. Cherenkov. "Visible luminescence of pure liquids under the influence of γ-radiation". *Dokl. Akad. Nauk SSSR* 2.8 (1934), pp. 451–454. DOI: 10.3367/UFNr.0093.196710n.0385.

[35] I. M. Frank and I. E. Tamm. "Coherent visible radiation of fast electrons passing through matter". *Compt. Rend. Acad. Sci. URSS* 14.3 (1937). Ed. by V. L. Ginzburg, B. M. Bolotovsky, and I. M. Dremin, pp. 109–114. DOI: 10.3367/UFNr.0093.196710o.0388.

[36] L. D. Landau, E. M. Lifshitz, and L. P. Pitaevskii. *Electrodynamics of Continuous Media*. 2nd ed. Vol. 8. Course of Theoretical Physics. Butterworth-Heinemann, 1984. ISBN: 9780750626347.

[37] M. de Naurois and D. Mazin. "Ground-based detectors in very-high-energy gamma-ray astronomy". *C. R. Phys.* 16.6-7 (2015), pp. 610–627. DOI: 10.1016/j.crhy.2015.08.011.

[38] W. Galbraith and J. Jelley. "Light Pulses from the Night Sky associated with Cosmic Rays". *Nature* 171.4347 (Feb. 1953), pp. 349–350. ISSN: 1476-4687. DOI: 10.1038/171349a0.

[39] W. Galbraith and J. Jelley. "Light-pulses from the night sky and Čerenkov radiation: Part I". *J. Atmos. Terrestr. Phys.* 6.1 (1955), pp. 250–262. ISSN: 0021-9169. DOI: https://doi.org/10.1016/0021-9169(55)90038-6.

[40] J. Jelley and W. Galbraith. "Light pulses from the night sky and Čerenkov radiation: Part II". *J. Atmos. Terrestr. Phys.* 6.1 (1955), pp. 304–312. ISSN: 0021-9169. DOI: https://doi.org/10.1016/0021-9169(55)90047-7.

[41] G. G. Fazio et al. "Detection of High-Energy Gamma Rays from the Crab Nebula". *Astrophys. J. Lett.* 175 (Aug. 1972), p. L117. DOI: 10.1086/180998.

[42] K. E. Turver and T. C. Weekes. "Gamma-ray astronomy from 10 to 100 GeV". *Il Nuovo Cimento B* 45.1 (May 1978), pp. 99–108. ISSN: 1826-9877. DOI: 10.1007/BF02904077.

[43] K. E. Turver and T. C. Weekes. "Gamma-rays above 100 GeV". *Philos. Trans. R. Soc. Lond.* Series A, Mathematical and Physical Sciences 301.1462 (1981), pp. 615–628. DOI: 10.1098/rsta.1981.0140.

[44] T. C. Weekes et al. "Observation of TeV Gamma Rays from the Crab Nebula Using the Atmospheric Cerenkov Imaging Technique". *Astrophys. J.* 342 (July 1989), p. 379. DOI: 10.1086/167599.

[45] A. M. Hillas. "Cerenkov Light Images of EAS Produced by Primary Gamma Rays and by Nuclei". *19th International Cosmic Ray Conference* (*ICRC19*). Ed. by F. C. Jones. Vol. 3. International Cosmic Ray Conference. Aug. 1985, p. 445.

[46] M. J. Lang et al. "TeV observations of the Crab Nebula and other Plerions in the Epoch 1988-91". *22nd International Cosmic Ray Conference* (*ICRC22*). Vol. 1. International Cosmic Ray Conference. Aug. 1991, p. 204.

[47] M. Punch et al. "Detection of TeV photons from the active galaxy Markarian 421". *Nature* 358.6386 (Aug. 1992), pp. 477–478. ISSN: 1476-4687. DOI: 10.1038/358477a0.

[48] J. Quinn et al. "Detection of Gamma Rays with $E > 300$ GeV from Markarian 501". *Astrophys. J.* 456.2 (Jan. 1996), p. L83. DOI: 10.1086/309878.

[49] M. Bott-Bodenhausen. "Ultra High Energy Gamma Ray Astronomy at the Observatorio del Roque de los Muchachos on La Palma". *Astrophys. Lett. Comm.* 28 (Jan. 1991), p. 195.

[50] G. Pühlhofer et al. "The technical performance of the HEGRA system of imaging air Cherenkov telescopes". *Astropart. Phys.* 20.3 (2003), pp. 267–291. ISSN: 0927-6505. DOI: https://doi.org/10.1016/j.astropartphys.2003.06.001.

[51] D. Alexandreas et al. "The CLUE experiment operating with 4 telescopes in La Palma". *Nucl. Inst. Meth. A* 409.1 (1998), pp. 488–491. ISSN: 0168-9002. DOI: https://doi.org/10.1016/S0168-9002(98)00133-8.

[52] R. Enomoto et al. "Design study of CANGAROO-III, stereoscopic imaging atmospheric Cherenkov telescopes for sub-TeV γ-ray detection". *Astropart. Phys.* 16.3 (2002), pp. 235–244. ISSN: 0927-6505. DOI: https://doi.org/10.1016/S0927-6505(01)00112-8.

[53] A. Kohnle. "HESS - The High Energy Stereoscopic System". *26th International Cosmic Ray Conference* (*ICRC26*). Ed. by D. Kieda, M. Salamon, and B. Dingus. Vol. 5. International Cosmic Ray Conference. Jan. 1999, p. 239.

[54] W. Benbow and H.E.S.S. Collaboration. "The Status and Performance of H.E.S.S." *AIP Conf. Proc.* 745.1 (Feb. 2005), pp. 611–616. ISSN: 0094-243X. DOI: 10.1063/1.1878471.

[55] M. Punch. "HESS II: Expansion of HESS for higher sensitivity and lower energy". *7th Workshop on Towards a Network of Atmospheric Cherenkov Detectors 2005*. Apr. 2005, pp. 379–392.

[56] Y. Becherini, M. Punch, and H.E.S.S. Collaboration. "Performance of HESS-II in multi-telescope mode with a multi-variate analysis". *AIP Conf. Proc.* 1505.1 (Dec. 2012), pp. 741–744. ISSN: 0094-243X. DOI: 10.1063/1.4772366.

[57] H.E.S.S. Collaboration et al. "The H.E.S.S. Galactic plane survey". *Astron. Astrophys.* 612 (2018), A1. DOI: 10.1051/0004-6361/201732098.

[58] R. Mirzoyan. "17m Diameter MAGIC telescope project for sub-100 GeV gamma ray astronomy". *Nucl. Phys. B Proc. Suppl.* 54.3 (1997), pp. 350–361. ISSN: 0920-5632. DOI: https://doi.org/10.1016/S0920-5632(97)00134-5.

[59] E. Lorenz. "Status of the 17 m ⌀ MAGIC telescope". *New Astron. Rev.* 48.5 (2004). 2nd VERITAS Symposium on the Astrophysics of Extragalactic Sources, pp. 339–344. ISSN: 1387-6473. DOI: https://doi.org/10.1016/j.newar.2003.12.059.

[60] D. Borla Tridon et al. "The MAGIC-II gamma-ray stereoscopic telescope system". *Nucl. Inst. Meth. A* 623.1 (2010). 1st International Conference on Technology and Instrumentation in Particle Physics, pp. 437–439. ISSN: 0168-9002. DOI: https://doi.org/10.1016/j.nima.2010.03.028.

[61] J. Aleksić et al. "The major upgrade of the MAGIC telescopes, Part I: The hardware improvements and the commissioning of the system". *Astropart. Phys.* 72 (2016), pp. 61–75. ISSN: 0927-6505. DOI: https://doi.org/10.1016/j.astropartphys.2015.04.004.

[62] J. Aleksić et al. "The major upgrade of the MAGIC telescopes, Part II: A performance study using observations of the Crab Nebula". *Astropart. Phys.* 72 (2016), pp. 76–94. ISSN: 0927-6505. DOI: https://doi.org/10.1016/j.astropartphys.2015.02.005.

[63] T. Weekes et al. "VERITAS: the Very Energetic Radiation Imaging Telescope Array System". *Astropart. Phys.* 17.2 (2002), pp. 221–243. ISSN: 0927-6505. DOI: https://doi.org/10.1016/S0927-6505(01)00152-9.

[64] N. Park. "Performance of the VERITAS experiment ". *Proceedings of The 34th International Cosmic Ray Conference — PoS(ICRC2015)*. Vol. 236. 2016, p. 771. DOI: 10.22323/1.236.0771.

[65] H. Anderhub et al. "Design and operation of FACT – the first G-APD Cherenkov telescope". *JINST* 8.06 (June 2013), P06008. DOI: 10.1088/1748-0221/8/06/P06008.

[66] C. Borwankar et al. "Observations of the Crab Nebula with MACE (Major Atmospheric Cherenkov Experiment)". *Astropart. Phys.* 159 (2024), p. 102960. ISSN: 0927-6505. DOI: https://doi.org/10.1016/j.astropartphys.2024.102960.

[67] Z. Cao. "EAS Arrays at High Altitudes Start the Era of UHE γ-ray Astronomy". *Universe* 7.9 (2021). ISSN: 2218-1997. DOI: 10.3390/universe7090339.

[68] A. Borione et al. "A large air shower array to search for astrophysical sources emitting γ-rays with energies $\geq 10^{14}$ eV". *Nucl. Inst. Meth. A* 346.1 (1994), pp. 329–352. ISSN: 0168-9002. DOI: https://doi.org/10.1016/0168-9002(94)90722-6.

[69] M. Amenomori et al. "Search for steady emission of 10-TeV gamma rays from the Crab Nebula, Cygnus X-3, and Hercules X-1 using the Tibet air shower array". *Phys. Rev. Lett.* 69 (17 Oct. 1992), pp. 2468–2471. DOI: 10.1103/PhysRevLett.69.2468.

[70] M. Amenomori et al. "Observation of PeV Gamma Rays from the Monogem Ring with the Tibet Air Shower Array". *Astrophys. J.* 635.1 (Nov. 2005), p. L53. DOI: 10.1086/499335.

[71] M. Amenomori et al. "Search for Gamma Rays above 100 TeV from the Crab Nebula with the Tibet Air Shower Array and the 100 m^2 muon Detector". *Astrophys. J.* 813.2 (Nov. 2015), p. 98. DOI: 10.1088/0004-637X/813/2/98.

[72] M. Takita. "Highlights from the Tibet ASγ experiment". *Proceedings of 38th International Cosmic Ray Conference — PoS(ICRC2023)*. Vol. 444. 2023, p. 213. DOI: 10.22323/1.444.0213.

[73] G. D'Alì Staiti. "The ARGO-YBJ experiment in Tibet". *Nucl. Inst. Meth. A* 588.1 (2008). Proceedings of the First International Conference on Astroparticle Physics, pp. 7–13. ISSN: 0168-9002. DOI: https://doi.org/10.1016/j.nima.2008.01.019.

[74] G. B. Yodh. "The MILAGRO gamma ray observatory". *Nucl. Phys. B Proc. Suppl.* 52.3 (1997), pp. 264–268. ISSN: 0920-5632. DOI: https://doi.org/10.1016/S0920-5632(96)00902-4.

[75] R. Atkins et al. "Observation of TeV Gamma Rays from the Crab Nebula with Milagro Using a New Background Rejection Technique". *Astrophys. J.* 595.2 (Oct. 2003), p. 803. DOI: 10.1086/377498.

[76] A. U. Abeysekara et al. "Observation of the Crab Nebula with the HAWC Gamma-Ray Observatory". *Astrophys. J.* 843.1 (June 2017), p. 39. DOI: 10.3847/1538-4357/aa7555.

[77] P. Abreu et al. *The Southern Wide-Field Gamma-Ray Observatory (SWGO): A Next-Generation Ground-Based Survey Instrument for VHE Gamma-Ray Astronomy*. Astro2020 APC White Paper. 2019. arXiv: 1907.07737 [astro-ph.IM].

[78] P. Huentemeyer. "SWGO: A Next-generation Ground-based Survey Instrument for Gamma-ray Astronomy". *Proceedings of 39th International Cosmic Ray Conference — PoS(ICRC2025)*. Vol. 501. 2025, p. 686. DOI: 10.22323/1.501.0686.

[79] X.-H. Ma et al. "Chapter 1 LHAASO Instruments and Detector technology". *Chin. Phys. C* 46.3 (Mar. 2022), p. 030001. DOI: 10.1088/1674-1137/ac3fa6.

[80] LHAASO collaboration. "A future project at Tibet: the Large High Altitude Air Shower Observatory (LHAASO)". *Chin. Phys. C* 34.2 (Feb. 2010), p. 249. DOI: 10.1088/1674-1137/34/2/018.

[81] H. He. "Design of the LHAASO detectors". *Radiat. Detect. Technol. Met.* 2.1 (Feb. 2018), p. 7. ISSN: 2509-9949. DOI: 10.1007/s41605-018-0037-3.

[82] Z. Cao et al. "Discovery of the Ultrahigh-energy Gamma-Ray Source LHAASO J2108+5157". *Astrophys. J. Lett.* 919.2 (Sept. 2021), p. L22. DOI: 10.3847/2041-8213/ac2579.

[83] M. Actis et al. "Design concepts for the Cherenkov Telescope Array CTA: an advanced facility for ground-based high-energy gamma-ray astronomy". *Exp. Astron.* 32.3 (Dec. 2011), pp. 193–316. ISSN: 1572-9508. DOI: 10.1007/s10686-011-9247-0.

[84] B. Acharya et al. "Introducing the CTA concept". *Astropart. Phys.* 43 (2013). Seeing the High-Energy Universe with the Cherenkov Telescope Array - The Science Explored with the CTA, pp. 3–18. ISSN: 0927-6505. DOI: https://doi.org/10.1016/j.astropartphys.2013.01.007.

[85] G. Dubus et al. "Surveys with the Cherenkov Telescope Array". *Astropart. Phys.* 43 (2013). Seeing the High-Energy Universe with the Cherenkov Telescope Array - The Science Explored with the CTA, pp. 317–330. ISSN: 0927-6505. DOI: https://doi.org/10.1016/j.astropartphys.2012.05.020.

[86] A. Donini et al. "Performance study update of observations in divergent mode for the Cherenkov Telescope Array". *Proceedings of 38th International Cosmic Ray Conference — PoS(ICRC2023)*. Vol. 444. 2023, p. 840. DOI: 10.22323/1.444.0840.

[87] J. Cortina and M. Teshima. "Status of the Cherenkov Telescope Array Large Size Telescopes". *Proceedings of The 34th International Cosmic Ray Conference — PoS(ICRC2015)*. Vol. 236. 2016, p. 943. DOI: 10.22323/1.236.0943.

[88] D. Mazin et al. "Large size telescope report". *AIP Conf. Proc.* 1792.1 (Jan. 2017), p. 080001. ISSN: 0094-243X. DOI: 10.1063/1.4969022.

[89] A. Moralejo. "LST-1, the Large-Sized Telescope prototype of CTA. Status and first observations". *J. Phys. Conf. Ser.* 2156.1 (Dec. 2021), p. 012089. DOI: 10.1088/1742-6596/2156/1/012089.

[90] S. Abe et al. "Multiwavelength study of the galactic PeVatron candidate LHAASO J2108+5157". *Astron. Astrophys.* 673 (2023), A75. DOI: 10.1051/0004-6361/202245086.

[91] H. Abe et al. "Observations of the Crab Nebula and Pulsar with the Large-sized Telescope Prototype of the Cherenkov Telescope Array". *Astrophys. J.* 956.2 (Oct. 2023), p. 80. DOI: 10.3847/1538-4357/ace89d.

[92] K. Abe et al. "A detailed study of the very high-energy Crab pulsar emission with the LST-1". *Astron. Astrophys.* 690 (2024), A167. DOI: 10.1051/0004-6361/202450059.

[93] K. Abe et al. "Detection of RS Oph with LST-1 and modelling of its HE/VHE gamma-ray emission". *Astron. Astrophys.* 695 (2025), A152. DOI: 10.1051/0004-6361/202452447.

[94] K. Abe et al. "Detection of the Geminga pulsar at energies down to 20 GeV with the LST-1 of CTAO". *Astron. Astrophys.* 698 (2025), A283. DOI: 10.1051/0004-6361/202554350.

[95] K. Abe et al. "GRB 221009A: Observations with LST-1 of CTAO and Implications for Structured Jets in Long Gamma-Ray Bursts". *Astrophys. J. Lett.* 988.2 (July 2025), p. L42. DOI: 10.3847/2041-8213/ade4cf.

[96] K. Abe et al. "Constraining the TeV gamma-ray emission of SN 2024bch, a possible type IIn-L from a red supergiant progenitor - Multiwavelength observations and analysis of the progenitor". *Astron. Astrophys.* 702 (2025), A125. DOI: 10.1051/0004-6361/202554721.

[97] K. Abe et al. "VHE γ-ray observations of bright BL Lacs with the Large-Sized Telescope prototype (LST-1) of the CTAO". *Mon. Not. R. Astron. Soc.* 544.1 (Oct. 2025), pp. 669–686. ISSN: 0035-8711. DOI: 10.1093/mnras/staf1728.

[98] J. Cortina and CTAO LST Collaboration. "First detection of VHE gamma-ray emission from FSRQ OP 313 with LST-1". *The Astronomer's Telegram* 16381 (Dec. 2023).

[99] J. Baxter. "Pushing the VHE Frontier: LST-1's Inaugural Detection of the Distant Quasar OP 313". *Proceedings of 39th International Cosmic Ray Conference — PoS(ICRC2025)*. Vol. 501. 2025, p. 569. DOI: 10.22323/1.501.0569.

[100] H. Abe et al. "Performance of the joint LST-1 and MAGIC observations evaluated with Crab Nebula data". *Astron. Astrophys.* 680 (2023), A66. DOI: 10.1051/0004-6361/202346927.

[101] J. M. Davies and E. S. Cotton. "Design of the quartermaster solar furnace". *Sol. Energy* 1.2 (1957), pp. 16–22. ISSN: 0038-092X. DOI: https://doi.org/10.1016/0038-092X(57)90116-0.

[102] J.-F. Glicenstein. "NectarCAM: a camera for the medium size telescopes of the Cherenkov Telescope Array ". *Proceedings of The 34th International Cosmic Ray Conference — PoS(ICRC2015)*. Vol. 236. 2016, p. 937. DOI: 10.22323/1.236.0937.

[103] G. Puehlhofer et al. "FlashCam: a fully-digital camera for the medium-sized telescopes of the Cherenkov Telescope Array". *Proceedings of The 34th International Cosmic Ray Conference — PoS(ICRC2015)*. Vol. 236. 2016, p. 1039. DOI: 10.22323/1.236.1039.

[104] G. Pühlhofer. "The medium size telescopes of the Cherenkov telescope array". *AIP Conf. Proc.* 1792.1 (Jan. 2017), p. 080002. ISSN: 0094-243X. DOI: 10.1063/1.4969023.

[105] F. Bradascio. "Status of the Medium-Sized Telescopes for the Cherenkov Telescope Array Observatory". *Proceedings of 38th International Cosmic Ray Conference — PoS(ICRC2023)*. Vol. 444. 2023, p. 859. DOI: 10.22323/1.444.0859.

[106] V. Vassiliev, S. Fegan, and P. Brousseau. "Wide field aplanatic two-mirror telescopes for ground-based γ-ray astronomy". *Astropart. Phys.* 28.1 (2007), pp. 10–27. ISSN: 0927-6505. DOI: https://doi.org/10.1016/j.astropartphys.2007.04.002.

[107] C. Adams et al. "Detection of the Crab Nebula with the 9.7 m prototype Schwarzschild-Couder telescope". *Astropart. Phys.* 128 (2021), p. 102562. ISSN: 0927-6505. DOI: https://doi.org/10.1016/j.astropartphys.2021.102562.

[108] L. Tibaldo et al. "The gamma-ray Cherenkov telescope for the Cherenkov telescope array". *AIP Conf. Proc.* 1792.1 (Jan. 2017), p. 080004. ISSN: 0094-243X. DOI: 10.1063/1.4969025.

[109] M. C. Maccarone. "ASTRI for the Cherenkov Telescope Array". *Proceedings of 35th International Cosmic Ray Conference — PoS(ICRC2017)*. Vol. 301. 2017, p. 855. DOI: 10.22323/1.301.0855.

[110] S. Lombardi et al. "First detection of the Crab Nebula at TeV energies with a Cherenkov telescope in a dual-mirror Schwarzschild-Couder configuration: the ASTRI-Horn telescope". *Astron. Astrophys.* 634 (2020), A22. DOI: 10.1051/0004-6361/201936791.

[111] R. White et al. "The Small-Sized Telescopes for the Southern Site of the Cherenkov Telescope Array". *Proceedings of 37th International Cosmic Ray Conference — PoS(ICRC2021)*. Vol. 395. 2021, p. 728. DOI: 10.22323/1.395.0728.

[112] S. Scuderi et al. "The ASTRI Mini-Array of Cherenkov telescopes at the Observatorio del Teide". *JHEAP* 35 (2022), pp. 52–68. ISSN: 2214-4048. DOI: https://doi.org/10.1016/j.jheap.2022.05.001.

[113] C. Alispach et al. "The SST-1M imaging atmospheric Cherenkov telescope for gamma-ray astrophysics". *JCAP* 2025.02 (Feb. 2025), p. 047. DOI: 10.1088/1475-7516/2025/02/047.

[114] A. De Angelis, G. Galanti, and M. Roncadelli. "Transparency of the Universe to gamma-rays". *Mon. Not. R. Astron. Soc.* 432.4 (May 2013), pp. 3245–3249. ISSN: 0035-8711. DOI: 10.1093/mnras/stt684.

[115] K. Bernlöhr et al. "Monte Carlo design studies for the Cherenkov Telescope Array". *Astropart. Phys.* 43 (2013). Seeing the High-Energy Universe with the Cherenkov Telescope Array - The Science Explored with the CTA, pp. 171–188. ISSN: 0927-6505. DOI: https://doi.org/10.1016/j.astropartphys.2012.10.002.

[116] T. Hassan et al. "Monte Carlo performance studies for the site selection of the Cherenkov Telescope Array". *Astropart. Phys.* 93 (2017), pp. 76–85. ISSN: 0927-6505. DOI: https://doi.org/10.1016/j.astropartphys.2017.05.001.

[117] A. Acharyya et al. "Monte Carlo studies for the optimisation of the Cherenkov Telescope Array layout". *Astropart. Phys.* 111 (2019), pp. 35–53. ISSN: 0927-6505. DOI: https://doi.org/10.1016/j.astropartphys.2019.04.001.

[118] D. Heck et al. *CORSIKA: A Monte Carlo code to simulate extensive air showers*. Tech. rep. FZKA-6019. Forschungszentrum Karlsruhe, Feb. 1998.

[119] K. Bernlöhr. "Simulation of imaging atmospheric Cherenkov telescopes with CORSIKA and sim_telarray". *Astropart. Phys.* 30.3 (2008), pp. 149–158. ISSN: 0927-6505. DOI: https://doi.org/10.1016/j.astropartphys.2008.07.009.

[120] Cherenkov Telescope Array Observatory and Cherenkov Telescope Array Consortium. *CTAO Instrument Response Functions - prod5 version v0.1*. Version v0.1. Zenodo, Sept. 2021. DOI: 10.5281/zenodo.5499840.

[121] L. A. Antonelli. "The CTA LST South as part of the CTA+ program". *Proceedings of 38th International Cosmic Ray Conference — PoS(ICRC2023)*. Vol. 444. 2023, p. 755. DOI: 10.22323/1.444.0755.

[122] S. Loporchio. "CTA+: an Italian program to enhance the Southern Cherenkov Telescope Array Observatory". *J. Phys. Conf. Ser.* 3053.1 (July 2025), p. 012020. DOI: 10.1088/1742-6596/3053/1/012020.

[123] Cherenkov Telescope Array Observatory and Cherenkov Telescope Array Consortium. *CTAO Instrument Response Functions - version prod3b-v2*. Version prod3b-v2/v1.0.0. Zenodo, Apr. 2016. DOI: 10.5281/zenodo.5163273.

[124] The CTA Consortium. *Science with the Cherenkov Telescope Array*. World Scientific, 2019. DOI: 10.1142/10986.

[125] A. Acharyya et al. "Sensitivity of the Cherenkov Telescope Array to a dark matter signal from the Galactic centre". *JCAP* 2021.01 (Jan. 2021), p. 057. DOI: 10.1088/1475-7516/2021/01/057.

[126] S. Abe et al. "Prospects for a survey of the galactic plane with the Cherenkov Telescope Array". *JCAP* 2024.10 (Oct. 2024), p. 081. DOI: 10.1088/1475-7516/2024/10/081.

[127] A. Acharyya et al. "Sensitivity of the Cherenkov Telescope Array to TeV photon emission from the Large Magellanic Cloud". *Mon. Not. R. Astron. Soc.* 523.4 (May 2023), pp. 5353–5387. ISSN: 0035-8711. DOI: 10.1093/mnras/stad1576.

[128] F. Acero et al. "Sensitivity of the Cherenkov Telescope Array to spectral signatures of hadronic PeVatrons with application to Galactic Supernova Remnants". *Astropart. Phys.* 150 (2023), p. 102850. ISSN: 0927-6505. DOI: https://doi.org/10.1016/j.astropartphys.2023.102850.

[129] K. Abe et al. "Prospects for γ-ray observations of the Perseus galaxy cluster with the Cherenkov Telescope Array". *JCAP* 2024.10 (Oct. 2024), p. 004. DOI: 10.1088/1475-7516/2024/10/004.

[130] H. Abdalla et al. "Sensitivity of the Cherenkov Telescope Array for probing cosmology and fundamental physics with gamma-ray propagation". *JCAP* 2021.02 (Feb. 2021), p. 048. DOI: 10.1088/1475-7516/2021/02/048.

[131] K. Abe et al. "Galactic transient sources with the Cherenkov Telescope Array Observatory". *Mon. Not. R. Astron. Soc.* 540.1 (Apr. 2025), pp. 205–238. ISSN: 0035-8711. DOI: 10.1093/mnras/staf655.

[132] Planck Collaboration et al. "Planck 2018 results - VI. Cosmological parameters". *Astron. Astrophys.* 641 (2020), A6. DOI: 10.1051/0004-6361/201833910.

[133] E. Kolb and M. Turner. *The Early Universe*. Frontiers in Physics. Addison-Wesley, 1990. ISBN: 9780201116038.

[134] M. Cirelli et al. "PPPC 4 DM ID: a poor particle physicist cookbook for dark matter indirect detection". *JCAP* 2011.03 (Mar. 2011), p. 051. DOI: 10.1088/1475-7516/2011/03/051.

[135] J. Einasto. "On the Construction of a Composite Model for the Galaxy and on the Determination of the System of Galactic Parameters". *Trudy Inst. Astrofiz. Alma-Ata* 5 (Jan. 1965), pp. 87–100.

[136] J. F. Navarro, C. S. Frenk, and S. D. M. White. "A Universal Density Profile from Hierarchical Clustering". *Astrophys. J.* 490.2 (Dec. 1997), p. 493. DOI: 10.1086/304888.

[137] K. Abe et al. "Prospects for dark matter observations in dwarf spheroidal galaxies with the Cherenkov Telescope Array Observatory". *Mon. Not. R. Astron. Soc.* 544.3 (Oct. 2025), pp. 2946–2986. ISSN: 0035-8711. DOI: 10.1093/mnras/staf1798.

[138] S. Abe et al. "Dark matter line searches with the Cherenkov Telescope Array". *JCAP* 2024.07 (July 2024), p. 047. DOI: 10.1088/1475-7516/2024/07/047.

[139] G. Breit and J. A. Wheeler. "Collision of Two Light Quanta". *Phys. Rev.* 46 (12 Dec. 1934), pp. 1087–1091. DOI: 10.1103/PhysRev.46.1087.

[140] A. Franceschini, G. Rodighiero, and M. Vaccari. "Extragalactic optical-infrared background radiation, its time evolution and the cosmic photon-photon opacity". *Astron. Astrophys.* 487.3 (2008), pp. 837–852. DOI: 10.1051/0004-6361:200809691.

[141] J. D. Finke, S. Razzaque, and C. D. Dermer. "Modeling the extragalactic background light from stars and dust". *Astrophys. J.* 712.1 (Feb. 2010), p. 238. DOI: 10.1088/0004-637X/712/1/238.

[142] A. Domínguez et al. "Extragalactic background light inferred from AEGIS galaxy-SED-type fractions". *Mon. Not. R. Astron. Soc.* 410.4 (Jan. 2011), pp. 2556–2578. ISSN: 0035-8711. DOI: 10.1111/j.1365-2966.2010.17631.x.

[143] R. C. Gilmore et al. "Semi-analytic modelling of the extragalactic background light and consequences for extragalactic gamma-ray spectra". *Mon. Not. R. Astron. Soc.* 422.4 (May 2012), pp. 3189–3207. ISSN: 0035-8711. DOI: 10.1111/j.1365-2966.2012.20841.x.

[144] A. Franceschini and G. Rodighiero. "The extragalactic background light revisited and the cosmic photon-photon opacity". *Astron. Astrophys.* 603 (2017), A34. DOI: 10.1051/0004-6361/201629684.

[145] A. Saldana-Lopez et al. "An observational determination of the evolving extragalactic background light from the multiwavelength HST/CANDELS survey in the Fermi and CTA era". *Mon. Not. R. Astron. Soc.* 507.4 (Aug. 2021), pp. 5144–5160. ISSN: 0035-8711. DOI: 10.1093/mnras/stab2393.

[146] Y. Kobayashi et al. "Camera Calibration of the CTA-LST prototype". *Proceedings of 37th International Cosmic Ray Conference — PoS(ICRC2021)*. Vol. 395. 2021, p. 720. DOI: 10.22323/1.395.0720.

[147] C. Fruck. "The galactic center resolved with MAGIC and a new technique for atmospheric calibration". PhD thesis. Munich University of Technology, Germany, Jan. 2015.

[148] F. Aharonian et al. "Observations of the Crab nebula with HESS". *Astron. Astrophys.* 457.3 (2006), pp. 899–915. DOI: 10.1051/0004-6361:20065351.

[149] E. Aliu et al. "Improving the performance of the single-dish Cherenkov telescope MAGIC through the use of signal timing". *Astropart. Phys.* 30.6 (2009), pp. 293–305. ISSN: 0927-6505. DOI: https://doi.org/10.1016/j.astropartphys.2008.10.003.

[150] J. Ćelić et al. "A novel approach to optimizing the image cleaning performance of Imaging Atmospheric Cherenkov Telescopes: Application to a time-based cleaning for H.E.S.S." *Astron. Astrophys.* 699 (2025), A96. DOI: 10.1051/0004-6361/202554824.

[151] J. Aleksić et al. "Observations of the Crab pulsar between 25 and 100 GeV with the MAGIC I telescope". *Astrophys. J.* 742.1 (Nov. 2011), p. 43. DOI: 10.1088/0004-637X/742/1/43.

[152] R. Bock et al. "Methods for multidimensional event classification: a case study using images from a Cherenkov gamma-ray telescope". *Nucl. Instrum. Meth.* A516.2 (2004), pp. 511–528. ISSN: 0168-9002. DOI: https://doi.org/10.1016/j.nima.2003.08.157.

[153] J. Albert et al. "Implementation of the Random Forest method for the Imaging Atmospheric Cherenkov Telescope MAGIC". *Nucl. Instrum. Meth.* A588.3 (2008), pp. 424–432. ISSN: 0168-9002. DOI: https://doi.org/10.1016/j.nima.2007.11.068.

[154] S. Ohm, C. van Eldik, and K. Egberts. "γ/hadron separation in very-high-energy γ-ray astronomy using a multivariate analysis method". *Astropart. Phys.* 31.5 (2009), pp. 383–391. ISSN: 0927-6505. DOI: https://doi.org/10.1016/j.astropartphys.2009.04.001.

[155] T. K. Ho. "The random subspace method for constructing decision forests". *IEEE Transactions on Pattern Analysis and Machine Intelligence* 20.8 (1998), pp. 832–844. DOI: 10.1109/34.709601.

[156] L. Breiman. "Random Forests". *Machine Learning* 45.1 (Oct. 2001), pp. 5–32. ISSN: 1573-0565. DOI: 10.1023/A:1010933404324.

[157] S. Raschka and V. Mirjalili. *Python Machine Learning, 2nd Ed.* 2nd ed. Birmingham, UK: Packt Publishing, 2017. ISBN: 978-1787125933.

[158] J. Aleksić et al. "Performance of the MAGIC stereo system obtained with Crab Nebula data". *Astropart. Phys.* 35.7 (2012), pp. 435–448. ISSN: 0927-6505. DOI: https://doi.org/10.1016/j.astropartphys.2011.11.007.

[159] D. Nieto Castaño et al. "CTLearn: Deep Learning for Gamma-ray Astronomy". *Proceedings of 36th International Cosmic Ray Conference — PoS(ICRC2019)*. Vol. 358. 2019, p. 752. DOI: 10.22323/1.358.0752.

[160] J. L. Contreras et al. "Data model issues in the Cherenkov Telescope Array project". *Proceedings of The 34th International Cosmic Ray Conference — PoS(ICRC2015)*. Vol. 236. 2016, p. 960. DOI: 10.22323/1.236.0960.

[161] C. Nigro, T. Hassan, and L. Olivera-Nieto. "Evolution of Data Formats in Very-High-Energy Gamma-Ray Astronomy". *Universe* 7.10 (2021). ISSN: 2218-1997. DOI: 10.3390/universe7100374.

[162] C. Deil et al. "Open high-level data formats and software for gamma-ray astronomy". *AIP Conf. Proc.* 1792.1 (Jan. 2017), p. 070006. ISSN: 0094-243X. DOI: 10.1063/1.4969003.

[163] D. C. Wells, E. W. Greisen, and R. H. Harten. "FITS - a Flexible Image Transport System". *Astron. Astrophys. Suppl.* 44 (June 1981), p. 363.

[164] K. Abe et al. "ctapipe - Prototype Open Event Reconstruction Pipeline for the Cherenkov Telescope Array". *Proceedings of 38th International Cosmic Ray Conference — PoS(ICRC2023)*. Vol. 444. 2023, p. 703. DOI: 10.22323/1.444.0703.

[165] R. López-Coto et al. "lstchain: An Analysis Pipeline for LST-1, the First Prototype Large-Sized Telescope of CTA". *ASP Conf. Ser.* 532 (2022), p. 357.

[166] S. Abe et al. "Standardised formats and open-source analysis tools for the MAGIC telescopes data". *JHEAP* 44 (2024), pp. 266–278. ISSN: 2214-4048. DOI: https://doi.org/10.1016/j.jheap.2024.09.011.

[167] C. P. Walther et al. "Tools and Advancements towards Data Standardization of the MAGIC Collaboration". *Proceedings of 39th International Cosmic Ray Conference — PoS(ICRC2025)*. Vol. 501. 2025, p. 875. DOI: 10.22323/1.501.0875.

[168] R. Bird et al. *V2DL3 - VERITAS (VEGAS and Eventdisplay) to DL3 Converter.* Version v0.8.0. Sept. 2025. DOI: 10.5281/zenodo.17165882. URL: https://doi.org/10.5281/zenodo.17165882.

[169] H.E.S.S. Collaboration. *H.E.S.S. first public test data release*. Zenodo, Sept. 2018. DOI: 10.5281/zenodo.1421099. URL: https://doi.org/10.5281/zenodo.1421099.

[170] A. Albert et al. "Validation of standardized data formats and tools for ground-level particle-based gamma-ray observatories". *Astron. Astrophys.* 667 (2022), A36. DOI: 10.1051/0004-6361/202243527.

[171] A. Donath et al. "Gammapy: A Python package for gamma-ray astronomy". *Astron. Astrophys.* 678 (2023), A157. DOI: 10.1051/0004-6361/202346488.

[172] M. Nievas Rosillo et al. "Unified multiwavelength data analysis workflow with gammapy - Constraining the broadband emission of the flat-spectrum radio quasar OP 313". *Astron. Astrophys.* 693 (2025), A287. DOI: 10.1051/0004-6361/202452349.

[173] D. Berge, S. Funk, and J. Hinton. "Background modelling in very-high-energy γ-ray astronomy". *Astron. Astrophys.* 466.3 (2007), pp. 1219–1229. DOI: 10.1051/0004-6361:20066674.

[174] G. Cowan. *Statistical data analysis*. Oxford University Press, USA, 1998.

[175] T.-P. Li and Y.-Q. Ma. "Analysis methods for results in gamma-ray astronomy." *Astrophys. J.* 272 (Sept. 1983), pp. 317–324. DOI: 10.1086/161295.

[176] J. Knödlseder et al. "Analysis of the H.E.S.S. public data release with ctools". *Astron. Astrophys.* 632 (2019), A102. DOI: 10.1051/0004-6361/201936010.

[177] C. K. Seyfert. "Nuclear Emission in Spiral Nebulae." *Astrophys. J.* 97 (Jan. 1943), p. 28. DOI: 10.1086/144488.

[178] B. E. Markarian. "On the Nature of the Galaxies with Anomalous Spectral Features for Their Type". *Commun. Byurakan Astrophys. Obs.* 34 (Jan. 1963), pp. 3–18.

[179] D. W. Weedman. "A Photometric Study of Markarian Galaxies". *Astrophys. J.* 183 (July 1973), pp. 29–40. DOI: 10.1086/152205.

[180] E. Y. Khachikian and D. W. Weedman. "An atlas of Seyfert galaxies." *Astrophys. J.* 192 (Sept. 1974), pp. 581–589. DOI: 10.1086/153093.

[181] M. Schmidt. "3C 273: A Star-Like Object with Large Red-Shift". *Nature* 197.4872 (Mar. 1963), pp. 1040–1040. ISSN: 1476-4687. DOI: 10.1038/1971040a0.

[182] A. Sandage. "The Existence of a Major New Constituent of the Universe: the Quasistellar Galaxies." *Astrophys. J.* 141 (May 1965), p. 1560. DOI: 10.1086/148245.

[183] A. S. Wilson and E. J. M. Colbert. "The Difference between Radio-loud and Radio-quiet Active Galaxies". *Astrophys. J.* 438 (Jan. 1995), p. 62. DOI: 10.1086/175054.

[184] P. Padovani. "The faint radio sky: radio astronomy becomes mainstream". *Astron. Astrophys. Rev.* 24.1 (Sept. 2016), p. 13. ISSN: 1432-0754. DOI: 10.1007/s00159-016-0098-6.

[185] B. L. Fanaroff and J. M. Riley. "The Morphology of Extragalactic Radio Sources of High and Low Luminosity". *Mon. Not. R. Astron. Soc.* 167.1 (Apr. 1974), 31P–36P. ISSN: 0035-8711. DOI: 10.1093/mnras/167.1.31P.

[186] P. Padovani et al. "Active galactic nuclei: what's in a name?" *Astron. Astrophys. Rev.* 25.1 (Aug. 2017), p. 2. ISSN: 1432-0754. DOI: 10.1007/s00159-017-0102-9.

[187] R. Antonucci. "Unified Models for Active Galactic Nuclei and Quasars". *Annu. Rev. Astron. Astrophys.* 31.Volume 31, 1993 (1993), pp. 473–521. ISSN: 1545-4282. DOI: https://doi.org/10.1146/annurev.aa.31.090193.002353.

[188] C. M. Urry and P. Padovani. "Unified Schemes for Radio-Loud Active Galactic Nuclei". *Publ. Astron. Soc. Pac.* 107.715 (Sept. 1995), p. 803. DOI: 10.1086/133630.

[189] The Event Horizon Telescope Collaboration et al. "First M87 Event Horizon Telescope Results. I. The Shadow of the Supermassive Black Hole". *Astrophys. J. Lett.* 875.1 (Apr. 2019), p. L1. DOI: 10.3847/2041-8213/ab0ec7.

[190] J. L. Schmitt. "BL Lac identified as a Radio Source". *Nature* 218.5142 (May 1968), pp. 663–663. ISSN: 1476-4687. DOI: 10.1038/218663a0.

[191] P. Madau, G. Ghisellini, and M. Persic. "Beaming in blazars". *Mon. Not. R. Astron. Soc.* 224.1 (Jan. 1987), pp. 257–264. ISSN: 0035-8711. DOI: 10.1093/mnras/224.1.257.

[192] P. Padovani. "Is there a relationship between BL Lacertae objects and flat-spectrum radio quasars?" *Mon. Not. R. Astron. Soc.* 257.3 (Aug. 1992), pp. 404–414. ISSN: 0035-8711. DOI: 10.1093/mnras/257.3.404.

[193] E. Prandini and G. Ghisellini. "The Blazar Sequence and Its Physical Understanding". *Galaxies* 10.1 (2022). ISSN: 2075-4434. DOI: 10.3390/galaxies10010035.

[194] G. Ghisellini et al. "The Fermi blazar sequence". *Mon. Not. R. Astron. Soc.* 469.1 (Apr. 2017), pp. 255–266. ISSN: 0035-8711. DOI: 10.1093/mnras/stx806.

[195] A. A. Abdo et al. "The spectral energy distribution of *Fermi* bright blazars". *Astrophys. J.* 716.1 (May 2010), p. 30. DOI: 10.1088/0004-637X/716/1/30.

[196] P. Padovani and P. Giommi. "The Connection between X-Ray– and Radio-selected BL Lacertae Objects". *Astrophys. J.* 444 (May 1995), p. 567. DOI: 10.1086/175631.

[197] L. Costamante et al. "Extreme synchrotron BL Lac objects - Stretching the blazar sequence". *Astron. Astrophys.* 371.2 (2001), pp. 512–526. DOI: 10.1051/0004-6361:20010412.

[198] G. Fossati et al. "A unifying view of the spectral energy distributions of blazars". *Mon. Not. R. Astron. Soc.* 299.2 (Sept. 1998), pp. 433–448. ISSN: 0035-8711. DOI: 10.1046/j.1365-8711.1998.01828.x.

[199] D. Donato et al. "Hard X-ray properties of blazars". *Astron. Astrophys.* 375.3 (2001), pp. 739–751. DOI: 10.1051/0004-6361:20010675.

[200] C. D. Dermer and G. Menon. *High Energy Radiation from Black Holes: Gamma Rays, Cosmic Rays, and Neutrinos*. Princeton University Press, Oct. 2009. ISBN: 978-0-691-14408-5.

[201] M. Cerruti. "Leptonic and Hadronic Radiative Processes in Supermassive-Black-Hole Jets". *Galaxies* 8.4 (2020). ISSN: 2075-4434. DOI: 10.3390/galaxies8040072.

[202] M. Boettcher. *Modeling the Spectral Energy Distributions and Variability of Blazars*. 2012 Fermi & Jansky Proceedings. 2012. arXiv: 1205.0539 [astro-ph.CO].

[203] M. Böttcher et al. "Leptonic and hadronic modeling of *Fermi*-detected blazars". *Astrophys. J.* 768.1 (Apr. 2013), p. 54. DOI: 10.1088/0004-637X/768/1/54.

[204] O. Klein and Y. Nishina. "Über die Streuung von Strahlung durch freie Elektronen nach der neuen relativistischen Quantendynamik von Dirac". *Z. Physik* 52.11 (Nov. 1929), pp. 853–868. ISSN: 0044-3328. DOI: 10.1007/BF01366453.

[205] H. Bethe and W. Heitler. "On the stopping of fast particles and on the creation of positive electrons". *Proc. R. Soc. Lon. A* 146.856 (1934), pp. 83–112. DOI: 10.1098/rspa.1934.0140.

[206] The IceCube Collaboration et al. "Multimessenger observations of a flaring blazar coincident with high-energy neutrino IceCube-170922A". *Science* 361.6398 (2018), eaat1378. DOI: 10.1126/science.aat1378.

[207] The IceCube Collaboration et al. "Neutrino emission from the direction of the blazar TXS 0506+056 prior to the IceCube-170922A alert". *Science* 361.6398 (2018), pp. 147–151. DOI: 10.1126/science.aat2890.

[208] S. Garrappa et al. "Investigation of Two Fermi-LAT Gamma-Ray Blazars Coincident with High-energy Neutrinos Detected by IceCube". *Astrophys. J.* 880.2 (July 2019), p. 103. DOI: 10.3847/1538-4357/ab2ada.

[209] M. G. Aartsen et al. "Time-Integrated Neutrino Source Searches with 10 Years of IceCube Data". *Phys. Rev. Lett.* 124 (5 Feb. 2020), p. 051103. DOI: 10.1103/PhysRevLett.124.051103.

[210] IceCube Collaboration et al. "Evidence for neutrino emission from the nearby active galaxy NGC 1068". *Science* 378.6619 (2022), pp. 538–543. DOI: 10.1126/science.abg3395.

[211] A. Neronov, D. Savchenko, and D. V. Semikoz. "Neutrino Signal from a Population of Seyfert Galaxies". *Phys. Rev. Lett.* 132 (10 Mar. 2024), p. 101002. DOI: 10.1103/PhysRevLett.132.101002.

[212] G. Sommani et al. "Two 100 TeV Neutrinos Coincident with the Seyfert Galaxy NGC 7469". *Astrophys. J.* 981.2 (Mar. 2025), p. 103. DOI: 10.3847/1538-4357/adb031.

[213] E. T. Meyer et al. "Collective evidence for inverse Compton emission from external photons in high-power blazars". *Astrophys. J. Lett.* 752.1 (May 2012), p. L4. DOI: 10.1088/2041-8205/752/1/L4.

[214] J. D. Finke, C. D. Dermer, and M. Böttcher. "Synchrotron Self-Compton Analysis of TeV X-Ray-Selected BL Lacertae Objects". *Astrophys. J.* 686.1 (Oct. 2008), p. 181. DOI: 10.1086/590900.

[215] M. Cerruti, C. Boisson, and A. Zech. "Constraining the parameter space of the one-zone synchrotron-self-Compton model for GeV-TeV detected BL Lacertae objects". *Astron. Astrophys.* 558 (2013), A47. DOI: 10.1051/0004-6361/201220963.

[216] F. A. Aharonian. "TeV gamma rays from BL Lac objects due to synchrotron radiation of extremely high energy protons". *New Astron.* 5.7 (2000), pp. 377–395. ISSN: 1384-1076. DOI: https://doi.org/10.1016/S1384-1076(00)00039-7.

[217] H. Sol, G. Pelletier, and E. Asséo. "Two-flow model for extragalactic radio jets". *Mon. Not. R. Astron. Soc.* 237.2 (Mar. 1989), pp. 411–429. ISSN: 0035-8711. DOI: 10.1093/mnras/237.2.411.

[218] G. Ghisellini, F. Tavecchio, and M. Chiaberge. "Structured jets in TeV BL Lac objects and radiogalaxies - Implications for the observed properties". *Astron. Astrophys.* 432.2 (2005), pp. 401–410. DOI: 10.1051/0004-6361:20041404.

[219] W. J. Potter and G. Cotter. "New constraints on the structure and dynamics of black hole jets". *Mon. Not. R. Astron. Soc.* 453.4 (Sept. 2015), pp. 4070–4088. ISSN: 0035-8711. DOI: 10.1093/mnras/stv1657.

[220] W. J. Potter and G. Cotter. "Synchrotron and inverse-Compton emission from blazar jets – I. A uniform conical jet model". *Mon. Not. R. Astron. Soc.* 423.1 (May 2012), pp. 756–765. ISSN: 0035-8711. DOI: 10.1111/j.1365-2966.2012.20918.x.

[221] W. J. Potter and G. Cotter. "Synchrotron and inverse-Compton emission from blazar jets – II. An accelerating jet model with a geometry set by observations of M87". *Mon. Not. R. Astron. Soc.* 429.2 (Dec. 2012), pp. 1189–1205. ISSN: 0035-8711. DOI: 10.1093/mnras/sts407.

[222] W. J. Potter and G. Cotter. "Synchrotron and inverse-Compton emission from blazar jets – III. Compton-dominant blazars". *Mon. Not. R. Astron. Soc.* 431.2 (Mar. 2013), pp. 1840–1852. ISSN: 0035-8711. DOI: 10.1093/mnras/stt300.

[223] W. J. Potter and G. Cotter. "Synchrotron and inverse-Compton emission from blazar jets – IV. BL Lac type blazars and the physical basis for the blazar sequence". *Mon. Not. R. Astron. Soc.* 436.1 (Oct. 2013), pp. 304–314. ISSN: 0035-8711. DOI: 10.1093/mnras/stt1569.

[224] K. Asada and M. Nakamura. "The Structure of the M87 Jet: A Transition from Parabolic to Conical Streamlines". *Astrophys. J. Lett.* 745.2 (Jan. 2012), p. L28. DOI: 10.1088/2041-8205/745/2/L28.

[225] R. D. Blandford and R. L. Znajek. "Electromagnetic extraction of energy from Kerr black holes". *Mon. Not. R. Astron. Soc.* 179.3 (July 1977), pp. 433–456. ISSN: 0035-8711. DOI: 10.1093/mnras/179.3.433.

[226] V. S. Beskin and E. E. Nokhrina. "The effective acceleration of plasma outflow in the paraboloidal magnetic field". *Mon. Not. R. Astron. Soc.* 367.1 (Mar. 2006), pp. 375–386. ISSN: 0035-8711. DOI: 10.1111/j.1365-2966.2006.09957.x.

[227] A. A. Abdo et al. "Bright active galactic nuclei source list from the first three months of the *Fermi* Large Area Telescope all-sky survey". *Astrophys. J.* 700.1 (July 2009), p. 597. DOI: 10.1088/0004-637X/700/1/597.

[228] J. R. P. Angel and H. S. Stockman. "Optical and Infrared Polarization of Active Extragalactic Objects". *Annu. Rev. Astron. Astrophys.* 18.Volume 18, 1980 (1980), pp. 321–361. ISSN: 1545-4282. DOI: https://doi.org/10.1146/annurev.aa.18.090180.001541.

[229] M. Böttcher. "Progress in Multi-Wavelength and Multi-Messenger Observations of Blazars and Theoretical Challenges". *Galaxies* 7.1 (2019). ISSN: 2075-4434. DOI: 10.3390/galaxies7010020.

[230] M. de Naurois. "H.E.S.S. detection of a strong VHE activity from the blazar 3C 279". *The Astronomer's Telegram* 11239 (Jan. 2018), p. 1.

[231] Z. Shah et al. "Study on temporal and spectral behaviour of 3C 279 during 2018 January flare". *Mon. Not. R. Astron. Soc.* 484.3 (Jan. 2019), pp. 3168–3179. ISSN: 0035-8711. DOI: 10.1093/mnras/stz151.

[232] J. Albert et al. "Variable Very High Energy γ-Ray Emission from Markarian 501". *Astrophys. J.* 669.2 (Nov. 2007), p. 862. DOI: 10.1086/521382.

[233] F. Aharonian et al. "An Exceptional Very High Energy Gamma-Ray Flare of PKS 2155–304". *Astrophys. J.* 664.2 (July 2007), p. L71. DOI: 10.1086/520635.

[234] L. Dondi and G. Ghisellini. "Gamma-ray-loud blazars and beaming". *Mon. Not. R. Astron. Soc.* 273.3 (Apr. 1995), pp. 583–595. ISSN: 0035-8711. DOI: 10.1093/mnras/273.3.583.

[235] M. C. Begelman, A. C. Fabian, and M. J. Rees. "Implications of very rapid TeV variability in blazars". *Mon. Not. R. Astron. Soc. Lett.* 384.1 (Feb. 2008), pp. L19–L23. ISSN: 1745-3925. DOI: 10.1111/j.1745-3933.2007.00413.x.

[236] G. Henri and L. Saugé. "The Bulk Lorentz Factor Crisis of TeV Blazars: Evidence for an Inhomogeneous Pileup Energy Distribution?" *Astrophys. J.* 640.1 (Mar. 2006), p. 185. DOI: 10.1086/500039.

[237] G. Ghisellini and F. Tavecchio. "Rapid variability in TeV blazars: the case of PKS 2155−304". *Mon. Not. R. Astron. Soc. Lett.* 386.1 (May 2008), pp. L28–L32. ISSN: 1745-3925. DOI: 10.1111/j.1745-3933.2008.00454.x.

[238] F. Tavecchio et al. "On the origin of the γ-ray emission from the flaring blazar PKS 1222+216". *Astron. Astrophys.* 534 (2011), A86. DOI: 10.1051/0004-6361/201117204.

[239] M. J. Valtonen et al. "The 2005 November Outburst in OJ 287 and the Binary Black Hole Model". *Astrophys. J.* 643.1 (May 2006), p. L9. DOI: 10.1086/505039.

[240] M. J. Valtonen et al. "Predicting the Next Outbursts of OJ 287 in 2006-2010". *Astrophys. J.* 646.1 (July 2006), p. 36. DOI: 10.1086/504884.

[241] S. Abdollahi et al. "Periodic Gamma-Ray Modulation of the Blazar PG 1553+113 Confirmed by Fermi-LAT and Multiwavelength Observations". *Astrophys. J.* 976.2 (Nov. 2024), p. 203. DOI: 10.3847/1538-4357/ad64c5.

[242] B.-K. Zhang et al. "Optical quasi-periodic oscillation and color behavior of blazar PKS 2155–304". *Res. Astron. Astrophys.* 14.8 (Aug. 2014), p. 933. DOI: 10.1088/1674-4527/14/8/004.

[243] P.-f. Zhang et al. "Revisiting Quasi-periodic Modulation in γ-Ray Blazar PKS 2155-304 with Fermi Pass 8 Data". *Astrophys. J.* 835.2 (Feb. 2017), p. 260. DOI: 10.3847/1538-4357/835/2/260.

[244] "H.E.S.S. Collaboration" et al. "Characterizing the γ-ray long-term variability of PKS 2155−304 with H.E.S.S. and Fermi-LAT". *Astron. Astrophys.* 598 (2017), A39. DOI: 10.1051/0004-6361/201629419.

[245] J. Chevalier et al. "Variability studies and modelling of the blazar PKS 2155−304 in the light of a decade of multi-wavelength observations". *Mon. Not. R. Astron. Soc.* 484.1 (Jan. 2019), pp. 749–759. ISSN: 0035-8711. DOI: 10.1093/mnras/stz027.

[246] A. A. Abdo et al. "The First Catalog of Active Galactic Nuclei Detected by the *Fermi* Large Area Telescope". *Astrophys. J.* 715.1 (May 2010), pp. 429–457. DOI: 10.1088/0004-637X/715/1/429.

[247] M. Ackermann et al. "The Second Catalog of Active Galactic Nuclei Detected by the *Fermi* Large Area Telescope". *Astrophys. J.* 743.2, 171 (Dec. 2011), p. 171. DOI: 10.1088/0004-637X/743/2/171.

[248] M. Ackermann et al. "The Third Catalog of Active Galactic Nuclei Detected by the *Fermi* Large Area Telescope". *Astrophys. J.* 810.1 (Aug. 2015), p. 14. DOI: 10.1088/0004-637X/810/1/14.

[249] M. Ajello et al. "The Fourth Catalog of Active Galactic Nuclei Detected by the *Fermi* Large Area Telescope". *Astrophys. J.* 892.2 (Apr. 2020), p. 105. DOI: 10.3847/1538-4357/ab791e.

[250] B. Lott, D. Gasparrini, and S. Ciprini. *The Fourth Catalog of Active Galactic Nuclei Detected by the Fermi Large Area Telescope – Data Release 2*. 2020. arXiv: 2010.08406 [astro-ph.HE].

[251] M. Ajello et al. "The Fourth Catalog of Active Galactic Nuclei Detected by the *Fermi* Large Area Telescope: Data Release 3". *Astrophys. J. Suppl. Ser.* 263.2 (Nov. 2022), p. 24. DOI: 10.3847/1538-4365/ac9523.

[252] M. Ackermann et al. "The First *Fermi*-LAT Catalog of Sources above 10 GeV". *Astrophys. J. Suppl. Ser.* 209.2 (Nov. 2013), p. 34. DOI: 10.1088/0067-0049/209/2/34.

[253] M. Ackermann et al. "2FHL: The Second Catalog of Hard *Fermi*-LAT Sources". *Astrophys. J. Suppl. Ser.* 222.1 (Jan. 2016), p. 5. DOI: 10.3847/0067-0049/222/1/5.

[254] M. Ajello et al. "3FHL: The Third Catalog of Hard *Fermi*-LAT Sources". *Astrophys. J. Suppl. Ser.* 232.2 (Sept. 2017), p. 18. DOI: 10.3847/1538-4365/aa8221.

[255] S. P. Wakely and D. Horan. "TeVCat: An online catalog for Very High Energy Gamma-Ray Astronomy". *Proceedings of the 30th International Cosmic Ray Conference* 3 (2008), pp. 1341–1344.

[256] J. Biteau and D. A. Williams. "The extragalactic background light, the Hubble constant, and anomalies: conclusions from 20 years of TeV gamma-ray observations". *Astrophys. J.* 812.1 (Oct. 2015), p. 60. DOI: 10.1088/0004-637X/812/1/60.

[257] J. P. van den Berg et al. "Systematic Physical Characterization of the γ-Ray Spectra of 2FHL Blazars". *Astrophys. J.* 874.1 (Mar. 2019), p. 47. DOI: 10.3847/1538-4357/aafdfd.

[258] E. Massaro et al. "Log-parabolic spectra and particle acceleration in blazars - III. SSC emission in the TeV band from Mkn 501". *Astron. Astrophys.* 448.3 (2006), pp. 861–871. DOI: 10.1051/0004-6361:20053644.

[259] A. Tramacere, E. Massaro, and A. M. Taylor. "Stochastic Acceleration and the Evolution of Spectral Distributions in Synchro-Self-Compton Sources: A Self-consistent Modeling of Blazars' Flares". *Astrophys. J.* 739.2 (Sept. 2011), p. 66. DOI: 10.1088/0004-637X/739/2/66.

[260] F. D'Ammando and M. Orienti. "Fermi LAT detection of increased gamma-ray emission from PKS 0736+01". *The Astronomer's Telegram* 6731 (Nov. 2014), p. 1.

[261] M. Cerruti et al. "Target of opportunity observations of blazars with H.E.S.S." *AIP Conf. Proc.* 1792.1 (Jan. 2017), p. 050029. ISSN: 0094-243X. DOI: 10.1063/1.4968975.

[262] D. Donato. "Fermi LAT observed another strong GeV flare from 4C 21.35 (PKS 1222+21)". *The Astronomer's Telegram* 2584 (Apr. 2010), p. 1.

[263] M. Mariotti. "MAGIC detects a VHE flare from 4C +21.35 (PKS 1222+21)". *The Astronomer's Telegram* 2684 (June 2010), p. 1.

[264] C. C. Cheung, D. Gasparrini, and S. Buson. "Fermi LAT detection of GeV flaring activity from blazar Ton 599 (4C +29.45)". *The Astronomer's Telegram* 10931 (Nov. 2017), p. 1.

[265] R. Mukherjee and VERITAS Collaboration. "VERITAS Detection of VHE Emission from Ton 599". *The Astronomer's Telegram* 11075 (Dec. 2017), p. 1.

[266] C. Bartolini et al. "Fermi-LAT detection of renewed gamma-ray activity from the FSRQ OP 313, and enhanced gamma-ray activity from the FSRQ ON 393". *The Astronomer's Telegram* 16356 (Dec. 2023), p. 1.

[267] S. Ciprini and Fermi Large Area Telescope Collaboration. "Fermi-LAT detection of hard spectrum and highest-level gamma-ray outburst from the distant blazar PKS 1502+106". *The Astronomer's Telegram* 7801 (July 2015), p. 1.

[268] F. D'Ammando and D. Gasparrini. "Fermi LAT detection of a very intense and rapid gamma-ray flare from the blazar PKS 1510-089". *The Astronomer's Telegram* 3473 (July 2011), p. 1.

[269] R. Mirzoyan. "MAGIC detects exceptionally high activity from PKS 1510-089 at very high energy gamma-rays". *The Astronomer's Telegram* 9105 (June 2016), p. 1.

[270] R. Ojha, P. van Zyl, and Fermi Large Area Telescope Collaboration. "Fermi LAT detection of renewed strong GeV activity from the FSRQ 3C 279". *The Astronomer's Telegram* 11542 (Apr. 2018), p. 1.

[271] R. Mirzoyan. "MAGIC detection of increased activity from FSRQ 3C 279 at very-high-energy gamma rays". *The Astronomer's Telegram* 11545 (Apr. 2018), p. 1.

[272] S. Wagner, B. Rani, and H. E. S. S. Collaboration. "Enhanced HE and VHE gamma-ray activity from the FSRQ PKS 0346-27". *The Astronomer's Telegram* 15020 (Nov. 2021), p. 1.

[273] M. Wood et al. "Fermipy: An open-source Python package for analysis of Fermi-LAT Data". *35th International Cosmic Ray Conference (ICRC2017)*. Vol. 301. International Cosmic Ray Conference. July 2017, 824, p. 824. DOI: 10.22323/1.301.0824. arXiv: 1707.09551 [astro-ph.IM].

[274] C. B. Adams et al. "Variability and Spectral Characteristics of Three Flaring Gamma-Ray Quasars Observed by VERITAS and Fermi-LAT". *Astrophys. J.* 924.2 (Jan. 2022), p. 95. DOI: 10.3847/1538-4357/ac32bd.

[275] J. D. Scargle et al. "Studies in Astronomical Time Series Analysis. VI. Bayesian Block Representations". *Astrophys. J.* 764.2 (Feb. 2013), p. 167. DOI: 10.1088/0004-637X/764/2/167.

[276] Astropy Collaboration et al. "Astropy: A community Python package for astronomy". *Astron. Astrophys.* 558, A33 (Oct. 2013), A33. DOI: 10.1051/0004-6361/201322068.

[277] Astropy Collaboration et al. "The Astropy Project: Building an Open-science Project and Status of the v2.0 Core Package". *Astrophys. J.* 156.3, 123 (Sept. 2018), p. 123. DOI: 10.3847/1538-3881/aabc4f.

[278] Astropy Collaboration et al. "The Astropy Project: Sustaining and Growing a Community-oriented Open-source Project and the Latest Major Release (v5.0) of the Core Package". *Astrophys. J.* 935.2, 167 (Aug. 2022), p. 167. DOI: 10.3847/1538-4357/ac7c74.

[279] K. Yoshida et al. "Flare Duty Cycle of Gamma-Ray Blazars and Implications for High-energy Neutrino Emission". *Astrophys. J.* 954.2 (Sept. 2023), p. 194. DOI: 10.3847/1538-4357/acea74.

[280] D. J. Eisenstein and P. Hut. "HOP: A New Group-finding Algorithm for N-Body Simulations". *Astrophys. J.* 498.1 (May 1998), p. 137. DOI: 10.1086/305535.

[281] M. Meyer, J. D. Scargle, and R. D. Blandford. "Characterizing the Gamma-Ray Variability of the Brightest Flat Spectrum Radio Quasars Observed with the Fermi LAT". *Astrophys. J.* 877.1 (May 2019), p. 39. DOI: 10.3847/1538-4357/ab1651.

[282] S. M. Wagner et al. "Statistical properties of flux variations in blazar light curves at GeV and TeV energies". *Proceedings of 37th International Cosmic Ray Conference — PoS(ICRC2021)*. Vol. 395. 2021, p. 868. DOI: 10.22323/1.395.0868.

[283] F. Acero et al. *Gammapy: Python toolbox for gamma-ray astronomy*. Version v1.3. Jan. 2025. DOI: 10.5281/zenodo.14760974. URL: https://doi.org/10.5281/zenodo.14760974.

[284] N. Sugiura. "Further analysis of the data by Akaike's information criterion and the finite corrections". *Communications in Statistics - Theory and Methods* 7.1 (1978), pp. 13–26. DOI: 10.1080/03610927808827599.

[285] K. P. Burnham and D. R. Anderson. "Multimodel Inference: Understanding AIC and BIC in Model Selection". *Sociol. Methods Res.* 33.2 (2004), pp. 261–304. DOI: 10.1177/0049124104268644.

[286] R. F. Streater and A. S. Wightman. *PCT, spin and statistics, and all that*. Princeton University Press, 1989. ISBN: 978-0-691-07062-9.

[287] T. D. Lee and C. N. Yang. "Question of Parity Conservation in Weak Interactions". *Phys. Rev.* 104 (1 Oct. 1956), pp. 254–258. DOI: 10.1103/PhysRev.104.254.

[288] C. S. Wu et al. "Experimental Test of Parity Conservation in Beta Decay". *Phys. Rev.* 105 (4 Feb. 1957), pp. 1413–1415. DOI: 10.1103/PhysRev.105.1413.

[289] J. H. Christenson et al. "Evidence for the 2π Decay of the K_2^0 Meson". *Phys. Rev. Lett.* 13 (4 July 1964), pp. 138–140. DOI: 10.1103/PhysRevLett.13.138.

[290] M. Pospelov and A. Ritz. "Theta vacua, QCD sum rules, and the neutron electric dipole moment". *Nucl. Phys. B* 573.1 (2000), pp. 177–200. ISSN: 0550-3213. DOI: https://doi.org/10.1016/S0550-3213(99)00817-2.

[291] C. Abel et al. "Measurement of the Permanent Electric Dipole Moment of the Neutron". *Phys. Rev. Lett.* 124 (8 Feb. 2020), p. 081803. DOI: 10.1103/PhysRevLett.124.081803.

[292] R. D. Peccei and H. R. Quinn. "CP Conservation in the Presence of Pseudoparticles". *Phys. Rev. Lett.* 38 (25 June 1977), pp. 1440–1443. DOI: 10.1103/PhysRevLett.38.1440.

[293] S. Weinberg. "A New Light Boson?" *Phys. Rev. Lett.* 40 (4 Jan. 1978), pp. 223–226. DOI: 10.1103/PhysRevLett.40.223.

[294] F. Wilczek. "Problem of Strong P and T Invariance in the Presence of Instantons". *Phys. Rev. Lett.* 40 (5 Jan. 1978), pp. 279–282. DOI: 10.1103/PhysRevLett.40.279.

[295] T. W. Donnelly et al. "Do axions exist?" *Phys. Rev. D* 18 (5 Sept. 1978), pp. 1607–1620. DOI: 10.1103/PhysRevD.18.1607.

[296] J. E. Kim. "Weak-Interaction Singlet and Strong CP Invariance". *Phys. Rev. Lett.* 43 (2 July 1979), pp. 103–107. DOI: 10.1103/PhysRevLett.43.103.

[297] M. Shifman, A. Vainshtein, and V. Zakharov. "Can confinement ensure natural CP invariance of strong interactions?" *Nucl. Phys. B* 166.3 (1980), pp. 493–506. ISSN: 0550-3213. DOI: https://doi.org/10.1016/0550-3213(80)90209-6.

[298] M. Dine, W. Fischler, and M. Srednicki. "A simple solution to the strong CP problem with a harmless axion". *Phys. Lett. B* 104.3 (1981), pp. 199–202. ISSN: 0370-2693. DOI: https://doi.org/10.1016/0370-2693(81)90590-6.

[299] A. R. Zhitnitsky. "On Possible Suppression of the Axion Hadron Interactions. (In Russian)". *Sov. J. Nucl. Phys.* 31 (1980), p. 260.

[300] L. Di Luzio et al. "The landscape of QCD axion models". *Phys. Rep.* 870 (2020). The landscape of QCD axion models, pp. 1–117. ISSN: 0370-1573. DOI: https://doi.org/10.1016/j.physrep.2020.06.002.

[301] I. G. Irastorza and J. Redondo. "New experimental approaches in the search for axion-like particles". *Prog. Part. Nucl. Phys.* 102 (2018), pp. 89–159. ISSN: 0146-6410. DOI: https://doi.org/10.1016/j.ppnp.2018.05.003.

[302] E. Massó and R. Toldrà. "Light spinless particle coupled to photons". *Phys. Rev. D* 52 (4 Aug. 1995), pp. 1755–1763. DOI: 10.1103/PhysRevD.52.1755.

[303] A. Arvanitaki et al. "String axiverse". *Phys. Rev. D* 81 (12 June 2010), p. 123530. DOI: 10.1103/PhysRevD.81.123530.

[304] A. Ringwald. "Searching for axions and ALPs from string theory". *J. Phys. Conf. Ser.* 485.1 (Mar. 2014), p. 012013. DOI: 10.1088/1742-6596/485/1/012013.

[305] J. Jaeckel and A. Ringwald. "The Low-Energy Frontier of Particle Physics". *Annual Review of Nuclear and Particle Science* 60.Volume 60, 2010 (2010), pp. 405–437. ISSN: 1545-4134. DOI: https://doi.org/10.1146/annurev.nucl.012809.104433.

[306] A. Ringwald. "Exploring the role of axions and other WISPs in the dark universe". *Phys. Dark Universe* 1.1 (2012). Next Decade in Dark Matter and Dark Energy, pp. 116–135. ISSN: 2212-6864. DOI: https://doi.org/10.1016/j.dark.2012.10.008.

[307] C. O'Hare. *cajohare/AxionLimits: AxionLimits*. Version v1.0. July 2020. DOI: 10.5281/zenodo.3932430. URL: https://doi.org/10.5281/zenodo.3932430.

[308] G. Raffelt and L. Stodolsky. "Mixing of the photon with low-mass particles". *Phys. Rev. D* 37 (5 Mar. 1988), pp. 1237–1249. DOI: 10.1103/PhysRevD.37.1237.

[309] W. Rindler. *Introduction to Special Relativity*. Clarendon Press, 1991.

[310] W. Heisenberg and H. Euler. "Folgerungen aus der Diracschen Theorie des Positrons". *Z. Phys.* 98 (1936). [English translation in arXiv: 9905030 [physics.hist-ph]], pp. 714–732. DOI: 10.1007/BF01343663.

[311] S. L. Adler. "Photon splitting and photon dispersion in a strong magnetic field". *Ann. Phys.* 67.2 (1971), pp. 599–647. ISSN: 0003-4916. DOI: https://doi.org/10.1016/0003-4916(71)90154-0.

[312] A. Cotton and H. Mouton. "Sur le phénomène de Majorana". *C. R. Acad. Sci.* 141 (1905), pp. 317–319.

[313] A. Mirizzi, G. G. Raffelt, and P. D. Serpico. "Photon-Axion Conversion in Intergalactic Magnetic Fields and Cosmological Consequences". *Axions: Theory, Cosmology, and Experimental Searches*. Ed. by M. Kuster, G. Raffelt, and B. Beltrán. Berlin, Heidelberg: Springer Berlin Heidelberg, 2008, pp. 115–134. ISBN: 978-3-540-73518-2. DOI: 10.1007/978-3-540-73518-2_7. URL: https://doi.org/10.1007/978-3-540-73518-2_7.

[314] A. Dobrynina, A. Kartavtsev, and G. Raffelt. "Photon-photon dispersion of TeV gamma rays and its role for photon-ALP conversion". *Phys. Rev. D* 91 (2015), p. 083003. DOI: 10.1103/PhysRevD.91.083003. [Erratum: *Phys. Rev. D* **95**, 109905 (2017)].

[315] T. K. Kuo and J. Pantaleone. "Neutrino oscillations in matter". *Rev. Mod. Phys.* 61 (4 Oct. 1989), pp. 937–979. DOI: 10.1103/RevModPhys.61.937.

[316] N. Bassan, A. Mirizzi, and M. Roncadelli. "Axion-like particle effects on the polarization of cosmic high-energy gamma sources". *JCAP* 2010.05 (May 2010), p. 010. DOI: 10.1088/1475-7516/2010/05/010.

[317] G. Galanti and M. Roncadelli. "Axion-like Particles Implications for High-Energy Astrophysics". *Universe* 8.5 (2022). ISSN: 2218-1997. DOI: 10.3390/universe8050253.

[318] L. Mastrototaro et al. "Constraining axion-like particles with the diffuse gamma-ray flux measured by the Large High Altitude Air Shower Observatory". *Eur. Phys. J. C* 82.11 (Nov. 2022), p. 1012. ISSN: 1434-6052. DOI: 10.1140/epjc/s10052-022-10979-6.

[319] P. Sikivie. "Experimental Tests of the "Invisible" Axion". *Phys. Rev. Lett.* 51 (16 Oct. 1983), pp. 1415–1417. DOI: 10.1103/PhysRevLett.51.1415.

[320] R. Bähre et al. "Any light particle search II – Technical Design Report". *J. Instrum.* 8.09 (Sept. 2013), T09001. DOI: 10.1088/1748-0221/8/09/T09001.

[321] A. Ringwald. "Axion interpretation of the PVLAS data?" *J. Phys. Conf. Ser.* 39.1 (May 2006), p. 197. DOI: 10.1088/1742-6596/39/1/050.

[322] K. Altenmüller et al. "New Upper Limit on the Axion-Photon Coupling with an Extended CAST Run with a Xe-Based Micromegas Detector". *Phys. Rev. Lett.* 133 (22 Nov. 2024), p. 221005. DOI: 10.1103/PhysRevLett.133.221005.

[323] E. Armengaud et al. "Physics potential of the International Axion Observatory (IAXO)". *JCAP* 2019.06 (June 2019), p. 047. DOI: 10.1088/1475-7516/2019/06/047.

[324] N. Du et al. "Search for Invisible Axion Dark Matter with the Axion Dark Matter Experiment". *Phys. Rev. Lett.* 120 (15 Apr. 2018), p. 151301. DOI: 10.1103/PhysRevLett.120.151301.

[325] A. Álvarez Melcón et al. "First results of the CAST-RADES haloscope search for axions at 34.67 μeV". *JHEP* 2021.10 (Oct. 2021), p. 75. ISSN: 1029-8479. DOI: 10.1007/JHEP10(2021)075.

[326] C. P. Salemi et al. "Search for Low-Mass Axion Dark Matter with ABRACADABRA-10 cm". *Phys. Rev. Lett.* 127 (8 Aug. 2021), p. 081801. DOI: 10.1103/PhysRevLett.127.081801.

[327] P. Brun et al. "A new experimental approach to probe QCD axion dark matter in the mass range above 40 μeV". *EPJ C* 79.3 (Mar. 2019). ISSN: 1434-6052. DOI: 10.1140/epjc/s10052-019-6683-x.

[328] A. De Angelis, G. Galanti, and M. Roncadelli. "Relevance of axionlike particles for very-high-energy astrophysics". *Phys. Rev. D* 84 (10 Nov. 2011), p. 105030. DOI: 10.1103/PhysRevD.84.105030.

[329] L. D. Landau and E. M. Lifshitz. *Quantum Mechanics: Non-Relativistic Theory*. 3rd ed. Vol. 3. Course of Theoretical Physics. Butterworth-Heinemann, 1981. ISBN: 9780750635394.

[330] C. Evoli et al. "Reionization during the dark ages from a cosmic axion background". *JCAP* 2016.05 (May 2016), p. 006. DOI: 10.1088/1475-7516/2016/05/006.

[331] F. Schiavone et al. "Axion-like particles from primordial black holes shining through the Universe". *JCAP* 2021.08 (Aug. 2021), p. 063. DOI: 10.1088/1475-7516/2021/08/063.

[332] M. C. Begelman, R. D. Blandford, and M. J. Rees. "Theory of extragalactic radio sources". *Rev. Mod. Phys.* 56 (2 Apr. 1984), pp. 255–351. DOI: 10.1103/RevModPhys.56.255.

[333] M. A. Sánchez-Conde et al. "Hints of the existence of axionlike particles from the gamma-ray spectra of cosmological sources". *Phys. Rev. D* 79 (12 June 2009), p. 123511. DOI: 10.1103/PhysRevD.79.123511.

[334] M. Meyer, D. Montanino, and J. Conrad. "On detecting oscillations of gamma rays into axion-like particles in turbulent and coherent magnetic fields". *JCAP* 2014.09 (Sept. 2014), p. 003. DOI: 10.1088/1475-7516/2014/09/003.

[335] F. Tavecchio, M. Roncadelli, and G. Galanti. "Photons to axion-like particles conversion in Active Galactic Nuclei". *Phys. Lett. B* 744 (2015), pp. 375–379. ISSN: 0370-2693. DOI: https://doi.org/10.1016/j.physletb.2015.04.017.

[336] G. Galanti et al. "Blazar VHE spectral alterations induced by photon–ALP oscillations". *Mon. Not. R. Astron. Soc.* 487.1 (Apr. 2019), pp. 123–132. ISSN: 0035-8711. DOI: 10.1093/mnras/stz1144.

[337] J. Davies, M. Meyer, and G. Cotter. "Relevance of jet magnetic field structure for blazar axionlike particle searches". *Phys. Rev. D* 103 (2 Jan. 2021), p. 023008. DOI: 10.1103/PhysRevD.103.023008.

[338] M. Meyer, J. Davies, and J. Kuhlmann. "gammaALPs: An open-source python package for computing photon-axion-like-particle oscillations in astrophysical environments". *Proceedings of 37th International Cosmic Ray Conference — PoS(ICRC2021)*. Vol. 395. 2021, p. 557. DOI: 10.22323/1.395.0557.

[339] R. Jansson and G. R. Farrar. "A New Model of the Galactic Magnetic Field". *Astrophys. J.* 757.1 (Aug. 2012), p. 14. DOI: 10.1088/0004-637X/757/1/14.

[340] F. Govoni and L. Feretti. "Magnetic fields in clusters of galaxies". *Int. J. Mod. Phys. D* 13.08 (2004), pp. 1549–1594. DOI: 10.1142/S0218271804005080.

[341] A. Bonafede et al. "The Coma cluster magnetic field from Faraday rotation measures". *Astron. Astrophys.* 513 (2010), A30. DOI: 10.1051/0004-6361/200913696.

[342] A. De Angelis, O. Mansutti, and M. Roncadelli. "Axion-like particles, cosmic magnetic fields and gamma-ray astrophysics". *Phys. Lett. B* 659.5 (2008), pp. 847–855. ISSN: 0370-2693. DOI: https://doi.org/10.1016/j.physletb.2007.12.012.

[343] D. Horns et al. "Hardening of TeV gamma spectrum of active galactic nuclei in galaxy clusters by conversions of photons into axionlike particles". *Phys. Rev. D* 86 (7 Oct. 2012), p. 075024. DOI: 10.1103/PhysRevD.86.075024.

[344] M. Meyer and J. Conrad. "Sensitivity of the Cherenkov Telescope Array to the detection of axion-like particles at high gamma-ray opacities". *JCAP* 2014.12 (Dec. 2014), p. 016. DOI: 10.1088/1475-7516/2014/12/016.

[345] R. Beck. "Magnetic fields in spiral galaxies". *Astron. Astrophys. Rev.* 24.1 (Dec. 2015), p. 4. ISSN: 1432-0754. DOI: 10.1007/s00159-015-0084-4.

[346] M. S. Pshirkov et al. "Deriving the Global Structure of the Galactic Magnetic Field from Faraday Rotation Measures of Extragalactic Sources". *Astrophys. J.* 738.2 (Aug. 2011), p. 192. DOI: 10.1088/0004-637X/738/2/192.

[347] M. Unger and G. R. Farrar. "The Coherent Magnetic Field of the Milky Way". *Astrophys. J.* 970.1 (July 2024), p. 95. DOI: 10.3847/1538-4357/ad4a54.

[348] D. Grasso and H. R. Rubinstein. "Magnetic fields in the early Universe". *Phys. Rep.* 348.3 (2001), pp. 163–266. ISSN: 0370-1573. DOI: https://doi.org/10.1016/S0370-1573(00)00110-1.

[349] A. Neronov and D. V. Semikoz. "Sensitivity of γ-ray telescopes for detection of magnetic fields in the intergalactic medium". *Phys. Rev. D* 80 (12 Dec. 2009), p. 123012. DOI: 10.1103/PhysRevD.80.123012.

[350] M. Ackermann et al. "The Search for Spatial Extension in High-latitude Sources Detected by the Fermi Large Area Telescope". *Astrophys. J. Suppl. Ser.* 237.2 (Aug. 2018), p. 32. DOI: 10.3847/1538-4365/aacdf7.

[351] J. Aleksić et al. "Search for an extended VHE γ-ray emission from Mrk 421 and Mrk 501 with the MAGIC Telescope". *Astron. Astrophys.* 524 (2010), A77. DOI: 10.1051/0004-6361/201014747.

[352] H.E.S.S. Collaboration: et al. "Search for extended γ-ray emission around AGN with H.E.S.S. and Fermi-LAT". *Astron. Astrophys.* 562 (2014), A145. DOI: 10.1051/0004-6361/201322510.

[353] S. Archambault et al. "Search for Magnetically Broadened Cascade Emission from Blazars with VERITAS". *Astrophys. J.* 835.2 (Feb. 2017), p. 288. DOI: 10.3847/1538-4357/835/2/288.

[354] Planck Collaboration et al. "Planck 2015 results - XIX. Constraints on primordial magnetic fields". *Astron. Astrophys.* 594 (2016), A19. DOI: 10.1051/0004-6361/201525821.

[355] A. Mirizzi and D. Montanino. "Stochastic conversions of TeV photons into axion-like particles in extragalactic magnetic fields". *JCAP* 2009.12 (Dec. 2009), p. 004. DOI: 10.1088/1475-7516/2009/12/004.

[356] D. Montanino et al. "Enhancing the Spectral Hardening of Cosmic TeV Photons by Mixing with Axionlike Particles in the Magnetized Cosmic Web". *Phys. Rev. Lett.* 119 (10 Sept. 2017), p. 101101. DOI: 10.1103/PhysRevLett.119.101101.

[357] D. Hooper and P. D. Serpico. "Detecting Axionlike Particles with Gamma Ray Telescopes". *Phys. Rev. Lett.* 99 (23 Dec. 2007), p. 231102. DOI: 10.1103/PhysRevLett.99.231102.

[358] A. Mirizzi, G. G. Raffelt, and P. D. Serpico. "Signatures of axionlike particles in the spectra of TeV gamma-ray sources". *Phys. Rev. D* 76 (2 July 2007), p. 023001. DOI: 10.1103/PhysRevD.76.023001.

[359] I. Batković et al. "Axion-like Particle Searches with IACTs". *Universe* 7.6 (2021). ISSN: 2218-1997. DOI: 10.3390/universe7060185.

[360] G. Galanti. "Axion-like Particle Effects on Photon Polarization in High-Energy Astrophysics". *Universe* 10.8 (2024). ISSN: 2218-1997. DOI: 10.3390/universe10080312.

[361] W. A. Rolke and A. M. López. "Confidence intervals and upper bounds for small signals in the presence of background noise". *Nucl. Inst. Meth. A* 458.3 (2001), pp. 745–758. ISSN: 0168-9002. DOI: https://doi.org/10.1016/S0168-9002(00)00935-9.

[362] W. A. Rolke, A. M. López, and J. Conrad. "Limits and confidence intervals in the presence of nuisance parameters". *Nucl. Inst. Meth. A* 551.2 (2005), pp. 493–503. ISSN: 0168-9002. DOI: https://doi.org/10.1016/j.nima.2005.05.068.

[363] S. S. Wilks. "The Large-Sample Distribution of the Likelihood Ratio for Testing Composite Hypotheses". *Ann. Math. Statist.* 9.1 (1938), pp. 60–62. DOI: 10.1214/aoms/1177732360.

[364] M. Ajello et al. "Search for Spectral Irregularities due to Photon–Axionlike-Particle Oscillations with the Fermi Large Area Telescope". *Phys. Rev. Lett.* 116 (16 Apr. 2016), p. 161101. DOI: 10.1103/PhysRevLett.116.161101.

[365] H. Abe et al. "Constraints on axion-like particles with the Perseus Galaxy Cluster with MAGIC". *Phys. Dark Universe* 44 (2024), p. 101425. ISSN: 2212-6864. DOI: https://doi.org/10.1016/j.dark.2024.101425.

[366] C. B. Adams et al. "Constraints on axionlike particles from VERITAS observations of a flaring radio galaxy in the Perseus cluster". *Phys. Rev. D* 112 (10 Nov. 2025), p. 103044. DOI: 10.1103/jydc-npy6.

[367] G. Cowan et al. "Asymptotic formulae for likelihood-based tests of new physics". *Eur. Phys. J. C* 71.2 (Feb. 2011), p. 1554. ISSN: 1434-6052. DOI: 10.1140/epjc/s10052-011-1554-0.

[368] S. Jacobsen, T. Linden, and K. Freese. "Constraining axion-like particles with HAWC observations of TeV blazars". *JCAP* 2023.10 (Oct. 2023), p. 009. DOI: 10.1088/1475-7516/2023/10/009.

[369] J. Davies, M. Meyer, and G. Cotter. "Constraints on axionlike particles from a combined analysis of three flaring *Fermi* flat-spectrum radio quasars". *Phys. Rev. D* 107 (8 Apr. 2023), p. 083027. DOI: 10.1103/PhysRevD.107.083027.

[370] A. Abramowski et al. "Constraints on axionlike particles with H.E.S.S. from the irregularity of the PKS 2155 − 304 energy spectrum". *Phys. Rev. D* 88 (10 Nov. 2013), p. 102003. DOI: 10.1103/PhysRevD.88.102003.

[371] A. Caputo and G. Raffelt. "Astrophysical Axion Bounds: The 2024 Edition". *Proceedings of 1st General Meeting and 1st Training School of the COST Action COSMIC WISPers — PoS(COSMICWISPers)*. Vol. 454. 2024, p. 041. DOI: 10.22323/1.454.0041.

[372] M. S. Turner. "Axions from SN1987A". *Phys. Rev. Lett.* 60 (18 May 1988), pp. 1797–1800. DOI: 10.1103/PhysRevLett.60.1797.

[373] A. Payez et al. "Revisiting the SN1987A gamma-ray limit on ultralight axion-like particles". *JCAP* 2015.02 (Feb. 2015), p. 006. DOI: 10.1088/1475-7516/2015/02/006.

[374] C. A. Manzari et al. "Supernova Axions Convert to Gamma Rays in Magnetic Fields of Progenitor Stars". *Phys. Rev. Lett.* 133 (21 Nov. 2024), p. 211002. DOI: 10.1103/PhysRevLett.133.211002.

[375] S. Sahu et al. "Extreme HBL-like Behavior of Markarian 421 and Its Two-zone Photohadronic Interpretation". *Astrophys. J.* 914.2 (June 2021), p. 120. DOI: 10.3847/1538-4357/abfd9a.

[376] M. L. Ahnen et al. "Extreme HBL behavior of Markarian 501 during 2012". *Astron. Astrophys.* 620 (2018), A181. DOI: 10.1051/0004-6361/201833704.

[377] MAGIC Collaboration et al. "Broadband characterisation of the very intense TeV flares of the blazar 1ES 1959+650 in 2016". *Astron. Astrophys.* 638 (2020), A14. DOI: 10.1051/0004-6361/201935450.

[378] M. Will. "Atmospheric Monitoring at the Site of the MAGIC Telescopes". *EPJ Web Conf.* 144 (2017), p. 01002. DOI: 10.1051/epjconf/201714401002.

[379] R. Zanin et al. "MARS, The MAGIC Analysis and Reconstruction Software". *International Cosmic Ray Conference*. Vol. 33. International Cosmic Ray Conference. Jan. 2013, p. 2937.

[380] R. Brun and F. Rademakers. "ROOT: An object oriented data analysis framework". *Nucl. Instrum. Meth. A* 389 (1997). Ed. by M. Werlen and D. Perret-Gallix, pp. 81–86. DOI: 10.1016/S0168-9002(97)00048-X.

[381] A. Aguasca-Cabot et al. *Gammapy: Python toolbox for gamma-ray astronomy*. Version v1.1. June 2023. DOI: 10.5281/zenodo.8033275. URL: https://doi.org/10.5281/zenodo.8033275.

[382] F. Tavecchio et al. "TeV BL Lac objects at the dawn of the Fermi era". *Mon. Not. R. Astron. Soc.* 401.3 (Jan. 2010), pp. 1570–1586. ISSN: 0035-8711. DOI: 10.1111/j.1365-2966.2009.15784.x.

[383] L.-Q. Gao et al. "Impact of parameters in the toroidal blazar jet magnetic field model on axion-like particle constraints". *JCAP* 2025.01 (Jan. 2025), p. 031. DOI: 10.1088/1475-7516/2025/01/031.

[384] F. Landgraf. "The effect of the Milky Way magnetic field on photon-axion conversions". Bachelor thesis. Universität Hamburg, Germany, Sept. 2024. URL: https://raw.githubusercontent.com/axion-alp-dm/axion-alp-dm.github.io/main/Theses/BA_Landgraf.pdf.

[385] N. Sahakyan et al. "Markarian Multiwavelength Data Center (MMDC): A Tool for Retrieving and Modeling Multitemporal, Multiwavelength, and Multimessenger Data from Blazar Observations". *Astron. J.* 168.6 (Nov. 2024), p. 289. DOI: 10.3847/1538-3881/ad8231.

[386] F. Aharonian et al. "Simultaneous multiwavelength observations of the second exceptional γ-ray flare of PKS 2155–304 in July 2006". *Astron. Astrophys.* 502.3 (2009), pp. 749–770. DOI: 10.1051/0004-6361/200912128.

[387] F. Acero et al. *Gammapy: Python toolbox for gamma-ray astronomy*. Version v1.0.1. Mar. 2023. DOI: 10.5281/zenodo.7734804. URL: https://doi.org/10.5281/zenodo.7734804.

[388] P. Virtanen et al. "SciPy 1.0: Fundamental Algorithms for Scientific Computing in Python". *Nat. Methods* 17 (2020), pp. 261–272. DOI: 10.1038/s41592-019-0686-2.

[389] T. Chen and C. Guestrin. "XGBoost: A Scalable Tree Boosting System". *Proceedings of the 22nd ACM SIGKDD International Conference on Knowledge Discovery and Data Mining*. KDD '16. ACM, Aug. 2016, pp. 785–794. DOI: 10.1145/2939672.2939785. URL: http://dx.doi.org/10.1145/2939672.2939785.

[390] F. Day and S. Krippendorf. "Accelerating the search for axion-like particles with machine learning". *JCAP* 2020.03 (Mar. 2020), pp. 046–046. ISSN: 1475-7516. DOI: 10.1088/1475-7516/2020/03/046.

[391] F. Pedregosa et al. "Scikit-learn: Machine Learning in Python". *J. Mach. Learn. Res.* 12 (2011), pp. 2825–2830.

[392] K. Kohri and H. Kodama. "Axion-like particles and recent observations of the cosmic infrared background radiation". *Phys. Rev. D* 96 (5 Sept. 2017), p. 051701. DOI: 10.1103/PhysRevD.96.051701.

[393] C. Dessert, D. Dunsky, and B. R. Safdi. "Upper limit on the axion-photon coupling from magnetic white dwarf polarization". *Phys. Rev. D* 105 (10 May 2022), p. 103034. DOI: 10.1103/PhysRevD.105.103034.

[394] D. Noordhuis et al. "Novel Constraints on Axions Produced in Pulsar Polar-Cap Cascades". *Phys. Rev. Lett.* 131 (11 Sept. 2023), p. 111004. DOI: 10.1103/PhysRevLett.131.111004.

[395] P. Bhattacharjee et al. *Probing the Parameter Space of Axion-Like Particles Using Simulation-Based Inference*. 2026. arXiv: 2509.20578 [astro-ph.HE].

[396] F. James and M. Roos. "Minuit - a system for function minimization and analysis of the parameter errors and correlations". *Comput. Phys. Commun.* 10.6 (1975), pp. 343–367. ISSN: 0010-4655. DOI: https://doi.org/10.1016/0010-4655(75)90039-9.

[397] W. Cash. "Parameter estimation in astronomy through application of the likelihood ratio". *Astrophys. J.* 228 (Mar. 1979), pp. 939–947. DOI: 10.1086/156922.

Acknowledgements

Starting a PhD in experimental astrophysics coming from a theoretical particle physics and cosmology background can be a bit of a daunting experience, and there were many times when the quote *"You can only trust yourself and the first six Black Sabbath albums."*, hanging over my office desk, sounded very true. Nevertheless, I was not alone during this path, and I feel the need to mention some of the people that made it possible.

I would first like to thank my supervisor Francesco Giordano for the freedom and trust he gave me in conducting my research project, and my co-supervisor Leo Di Venere for helping me navigate its most tricky practical aspects. Thanks to Michele Doro, to Giacomo D'Amico and to my sister-in-ALPs Ivana Batković for letting me join their MAGIC/LST-1 analysis team, for all the meetings and conferences we attended together, and for introducing me to their awesome group in Padova. Thanks to my dear friend Chiara Bartolini for inviting me to join her project on FSRQ simulations, and to Reshmi Mukherjee and Elina Lindfors for supporting it. I acknowledge all the precious feedback from members of the CTAO, LST and MAGIC collaborations, gathered during the various presentations I gave at working group and collaboration meetings. Thanks to Alessandro Mirizzi, who was my supervisor during my master thesis, for his continued interest in my work and his useful advice. Finally, I would like to thank Javier Rico and Miguel Angel Sánchez-Conde for kindly reviewing my thesis and helping improve its quality with their insightful comments.

Thanks to the Gamma Group in Bari for welcoming me since the start of this PhD. A few special mentions go to: Celeste, Chiara, Mario and Riccardo, who have been my office mates since the first day and with whom I've shared many many things inside and outside of work; Davide 1, Leo, and Serena, the "young seniors", for mentoring a whole generation of students (including myself); Davide 2, for the days spent traveling, the nights taming the MAGIC telescopes, and for somehow always knowing the right thing to do; Davide 3, for accepting the crazy idea of becoming my keyboardist besides being my colleague; Tonuccio, always a shoulder to lean on, discussing our common and often not-so-happy worldview and our weird music taste; Aldana, por todo el mate, el té y las *conversaciones filósoficamente profundas en español*. Many more colleagues and friends helped making my lunch and (frequent) tea breaks beautiful occasions to chat, discuss and relax together. The list would be way too long, and I would certainly miss somebody, but hopefully you will recognize yourselves in these lines: you all hold a place somewhere in my heart.

I was lucky enough to visit the Roque de los Muchachos Observatory in La Palma four times during these years. I truly consider La Palma and the ORM to be among the most beautiful places in the world, and they never fail to fill me with a feeling of deep peace that is hard to describe. I am thankful to the LST and MAGIC shift crews for all the time

spent observing, cooking and exploring the island together, and to all the locals who made our working conditions the best possible. I had many more occasions to travel for schools, meetings and conferences, learning that any place in the world can feel much closer than it seems. Each of these experiences has been a great opportunity of meeting new colleagues, collaborators and forming real friendships that lasted beyond work. I am very grateful for them.

Finally, thanks to my family, my friends, my cats and my bandmates in Prometheo[1] for the continued support and for putting up with my long absences, both physical and mental. I love you all!

— Francesco, May 2026

[1] Go check us out! https://prometheoband.bandcamp.com/